Non-Invasive Blood Glucose Monitoring Using Electromagnetic Sensors

by

Ala Eldin Omer

A thesis
presented to the University of Waterloo
in fulfillment of the
thesis requirement for the degree of
Doctor of Philosophy
in
Electrical and Computer Engineering

Waterloo, Ontario, Canada, 2022

Examining Committee Membership

The following served on the Examining Committee for this thesis. The decision of the Examining Committee is by majority vote.

External Examiner	Dr. Ali Fathy Professor Electrical Engineering and Computer Science University of Tennessee
Supervisor(s)	Dr. George Shaker Adjunct Associate Professor Electrical and Computer Engineering Mechanical & Mechatronics Engineering
	Dr. Kankar Bhattacharya Professor and University Research Chair Electrical and Computer Engineering
Internal Member	Dr. Raafat Mansour Professor Electrical and Computer Engineering
	Dr. Karim Sallaudin Karim Professor Electrical and Computer Engineering
Internal-external Member	Dr. Richard Hughson Professor Kinesiology and Health Sciences

Author's Declaration

I hereby declare that I am the sole author of this thesis. This is a true copy of the thesis, including any required final revisions, as accepted by my examiners.

I understand that my thesis may be made electronically available to the public.

Abstract

Monitoring glycemia levels in people with diabetes has developed rapidly over the last decade. A broad range of easy-to-use systems of reliable accuracies are now deployed in the market following the introduction of the invasive self-monitoring blood glucose meters (i.e., Glucometers) that utilize the capillary blood samples from the fingertips of diabetic patients. Besides, semi-invasive continuous monitors (CGM) are currently being used to quantify the glucose analyte in interstitial fluids (ISF) using an implantable needle-like electrochemical sensors. However, the limitations and discomforts associated with these finger-pricking and implantable point-of-care devices have established a new demand for complete non-invasive pain-free and low-cost blood glucose monitors to allow for more frequent and convenient glucose checks and thereby contribute more generously to diabetes care and prevention. Towards that goal, researchers have been developing alternative techniques that are more convenient, affordable, pain-free, and can be used for continuous non-invasive blood glucose monitoring.

In this research, a variety of electromagnetic sensing techniques were developed for reliably monitoring the blood glucose levels of clinical relevance to diabetes using the non-ionizing electromagnetic radiations of no hazards when penetrating the body. The sensing structures and devices introduced in this study were designed to operate in specific frequency spectrums that promise a reliable and sensitive glucose detection from centimeter- to millimeter-wave bands. Particularly, three different technologies were proposed and investigated at the Centre for Intelligent Antenna and Radio Systems (CIARS): Complementary Split-Ring Resonators (CSRRs), Whispering Gallery Modes (WGMs) sensors, and Frequency-Modulated Continuous-Wave (FMCW) millimeter-Wave Radars. Multiple sensing devices were developed using those proposed technologies in the micro/millimeter-wave spectrums of interest. A comprehensive study was conducted for the functionality, sensitivity, and repeatability analysis of each sensing device. Particularly, the sensors were thoroughly designed, optimized, fabricated, and practically tested in the laboratory with the desired glucose sensitivity performance. Different topologies and configurations of the proposed sensors were studied and compared in sensitivity using experimental and numerical analysis tools. Besides, machine learning and signal processing tools were intelligently applied to analyze the frequency responses of the sensors and reliably identify different glucose levels. The developed glucose sensors were coupled with frequency-compatible radar boards to realize small mobile glucose sensing systems of reduced cost.

The proposed sensors, beside their impressive detection capability of the diabetes-spectrum glucose concentrations, are endowed with favourable advantages of simple fabrication, low-power consumption, miniaturized compact sizing, non-ionizing radiation, and minimum health risk or impact for human beings. Such attractive features promote the proposed sensors as possible candidates for development as mobile, portable/wearable gadgets for affordable non-invasive blood glucose

monitoring for diabetes. The introduced sensing structures could also be employed for other vital sensing applications such as liquid type/quantity identification, oil adulteration detection, milk quality control, and virus/bacteria detection.

Another focus of this thesis is to investigate the electromagnetic behavior of the glucose in blood mimicking tissues across the microwave spectrum from 200 MHz to 67 GHz using a commercial characterization system (DAK-TL) developed by SPEAG. This is beneficial to locate the promising frequency spectrums that are most responsive to slight variations in glucose concentrations, and to identify the amount of change in the dielectric properties due to different concentrations of interest. Besides, the effect of the blood typing and medication was also investigated by measuring the dielectric properties of synthetic "artificial" as well as authentic "human" blood samples of different ABO-Rh types and with different medications. Measured results have posed for other factors that may impact the developed microwave sensors accuracy and sensitivity including the patient's blood type, pre-existing medical conditions, or other illnesses.

Acknowledgments

I would take this opportunity to express my sincere gratitude to those who supported me throughout the four years of this research. With a grievous heart, I dedicate this work to the soul of my supervisor, Prof. Safieddin Safavi-Naeini, who passed away in the last days before completing this thesis. His mighty legacy will stay alive, and he will live in our hearts and memories forever. Indeed, I am grateful to him, and my co-supervisor, Prof. George Shaker, who shared their valuable knowledge, and provided the necessary guidance, motivation, and support throughout my PhD studies at University of Waterloo. I'm deeply beholden for their kindness, assistance, constructive criticism, worthy discussion, and dignified advice. Their accompaniment for four years was a precious credit to my career and professional development, and I am proud that I have been their student.

My special thanks extend to Dr. Suren Gigoyan for his support and help in some of the lab measurements. My sincere thanks to Prof. Hamid Kokabi, Georges Alquié, and Frédérique Deshours, from Sorbonne University and Prof. Raed Shubair from New York University Abu Dhabi for their fruitful collaborations and reviews. I am also thankful to the committee members, Prof. Richard Hughson, Prof. Raafat Mansour, Prof. Karim Karim, and Prof. Ali Fathy (external examiner) for their valuable comments and perceptive reflection on this research outcomes.

I express my thanks to the researchers at the Centre for Intelligent and Antenna Radio Systems (CIARS), Wireless Sensors and Devices Lab (WSDL) at Schlegel-UW Research Institute for Aging (RIA), and Group of electrical engineering Paris (GeePs), UMR CNRS-CentraleSupelec – University Paris-Saclay – Sorbonne University, for their collaboration and friendship. Also, I am thankful to Ms. Chris Schroeder for her help in editing some of my research publications.

Special thanks to the Electrical and Computer Engineering department at University of Waterloo for granting me the International Doctoral Student (IDS) Award and Faculty of Engineering Graduate Awards that helped supporting my financial status while studying. I would like to acknowledge the National Science and Engineering Research Council of Canada (NSERC), and CREATE NSERC for funding this research, and for offering a unique training program in global biomedical technology research and innovation. My thanks to the Erasmus+ for funding my Summer 2019 exchange research study at Sorbonne University.

Lastly, I would send my sincere gratitude to my family: parents, brothers and sisters for their kindness, ultimate support, and motivation along the postgraduate journey. They would remain the spirit for all success in my life.

Dedication

To my parents, brothers, and sisters…

To my fiancée…

To my teachers…

To my country …

To the martyrs of the Sudanese revolution …

To the souls of my grandparents …

To the soul of Prof. Safieddin Safavi-Naeini …

Table of Contents

List of Figures

List of Tables

List of Abbreviations

ADC:	Analog-to-Digital converter
BGL:	Blood Glucose Level
CGM:	Continuous Glucose Monitors
CIARS:	Centre for Integrated Antenna and Radio Systems
CSRR:	Complementary Split-Ring Resonator
DDR:	Dielectric Disc Resonator
DIG:	Dielectric Image Waveguide
DRR:	Dielectric Ring Resonator
EM:	Electromagnetics
FDA:	Food and Drug Administration
GOx:	Glucose Oxidase
HCI:	Human Computer Interface
HRS:	High Resistivity Silicon
IDF:	International Diabetes Federation
ISF:	Interstitial Fluid
ISM:	Industrial, Scientific, and Medical
mmWave:	Millimeter Wave
MUT:	Material Under Test
NIR:	Near Infra-Red
OCT:	Optical coherence tomography
PDMS:	Polydimethylsiloxane
PEC:	Perfect Electric Conductor
PLL:	Phase Lock Loop
POD:	Point of Care Devices
PPG:	Photoplethysmography
PSD:	Power Spectral Density
RBC:	Red Blood Cells
SMA:	SubMiniature version A
SNR:	Signal-to-Noise Ratio
SUT:	Sample Under Test
VCO:	Voltage Controlled Oscillator
VNA/PNA:	Vector Network Analyzer
WHO:	World Health Organization

Chapter 1. Introduction

1.1 Overview

Recent technologies have established a growing demand for agile sensing devices that are affordable, sustainable, miniature, selective, and highly sensitive to be employed in a variety of applications in healthcare, biomedical, pharmaceutical, food processing and gas industry. Advanced assessment of treatment progress, instant clinical diagnosis, and continuous monitoring entail the need for fast and accurate real-time measurement of electrolytes and other physiological biomarkers in bodily fluids [1]. This is particularly important for some common disastrous diseases such as diabetes that is increasingly prevalent among human beings especially among communities of stationary lifestyle and of high obesity rates. Over 400 million people worldwide suffer from Diabetes and the number is growing rapidly at an unpredictable rate year-by-year according to the International Diabetes Federation (IDF) report [2]. A considerable 8.5% of the world population in 2014 lived with diabetes according to the World Health Organization (WHO) report [3]. In North America, 37.0 million people have been with diabetes while in Canada about 5.0 million Canadians (i.e., about 15% of the population) are expected to be with diabetes by 2025 according to the WHO [3].

Diabetes is described as a metabolic disorder that is caused by the malfunction of steady hormone insulin production by the pancreas, thus degenerating the body-cells' vitality in glucose absorption from the circulating blood as caloric energy due to insulin shortage and resistance. Diabetes generally happens due to some genetic factors or excessive eating habits. Generally, it is classified into two categories: Type-1 (insulin-dependent), caused by the immune-supportive destruction of the beta cells in the pancreas, thus inhibiting or shortening the insulin production by the pancreas, and Type-2 (non-insulin-dependent), where the produced hormone insulin is not properly utilized by the biological system of the body that exhibits no sufficient response. Diabetes is addressed based on the glucose level which cannot be physiologically maintained and standardized for the diabetic patient within the desired normal range, thus indicating the need for the patient to undergo regular medical inspection [3], [4].

Typical glucose levels in humans' blood for Type-2 diabetes – which is widespread among 90% of the diabetics' community – normally vary in the range from 72 to 126 mg/dL (milligrams per decilitre) before having a meal and remains less than 153 mg/dL within 1 – 2 hours after a meal [5]. Negligence to preserve certain glycemic targets would probably put the patient at the risk of experiencing the extreme events of hyperglycemia (> 230 mg/dL) resulting into serious health complications such as heart attack, stroke, kidney failure, blindness, amputation, etc. [2]. Alternatively, for very low glycemia levels, patients would encounter hypoglycemia (< 65 mg/dL) that could rapidly lead to life-threating events such as coma or death [2]. Moreover, an increase of about 30 – 40% is seen among diabetics of smoking habits leading to an increased risk of kidney- and heart-disease complications that affect the patient health, worsen quality of life, and increase the death rate by 50%.

These drastic effects of diabetes could be averted by having an early diagnosis and following a treatment plan that involves renovated lifestyle, continuous glucose monitoring (CGM), and regular medical care with the proper medication.

1.2 Importance of Glucose Monitoring

The complex procedure of managing diabetes frequently requires a multidisciplinary approach to assist in controlling the blood glucose level (BGL). Modifications to lifestyle and therapy-assisted control of BGLs may both be beneficial, however they can also be a bit overwhelming. Abundant evidence points to clinical benefits following frequent self-monitoring and control of blood glucose in Type-1, insulin and non-insulin treated Type-2 diabetes; to help reducing its progression and avert any potential complications [4], [6]. Particularly, through glucose monitoring, symptoms of diabetes are properly managed, responses to remedies are better evaluated, glycemic targets set by physicians are closely achieved, and progressive complications are prevented. This is also presented in the WHO 2016 report, indicating that regular diabetes monitoring via frequent glucose measurement is an essential preventive method to protect diabetic patients, beside the scaled-up prevention and enriched care [3]. To meet the glycemic targets, patients of Type-1 should check up their BGL in accordance with the insulin intake four to ten times a day, while Type-2 patients should check two to four times a day as recommended by the Canadian Diabetes Association [7]. Self-monitoring of blood glucose is not only recommended in accordance with the insulin regimens but also at certain circumstances such as before and after meals/snacks, before exercising, before all focus-based tasks (e.g., driving, operating heavy machinery), before sleeping, and when symptoms are generally observed especially those of hypoglycemia and hyperglycemia. Patients of good compliance to self-monitoring will not only avoid the disease complications but also will see a great reduction in their glycated hemoglobin A1c (HbA1c) [8].

Figure 1.1: Finger pricking methodology for BGL testing using Glucometer devices. **1.** Lancet needle, **2.** Transfer the extracted blood sample to test strip, and **3.** Processing and displaying the resulting BGL on the screen.

The leading methodology currently available in the market and reliably used by diabetics is the invasive glucometer based on the capillary blood sampling (Fig. 1.1), where a drop of blood sample is taken from the fingertip via a lancet and analyzed on a strip of test paper that is chemically pre-treated [9].

The glucose concentration then induces a low-level electrical current after a set of chemical reactions where different principles are applied such as enzymatic glucose-oxidase, glucose-molecules binding, glucose spectral properties, colour reflectance, etc. The first-generation of such glucose biosensors were proposed back in 1962 by Clark and Lyons [10], where the enzyme glucose oxidase (GOx) was adopted as the enzymatic basis in the electrochemical approach of the sensor [11]. GOx was more favorable than other enzymes of hexokinase, glucose-1-dehydrogenase, etc. due to its high glucose selectivity and good tolerance for rapid changes in ionic strength, temperature, and pH [9].

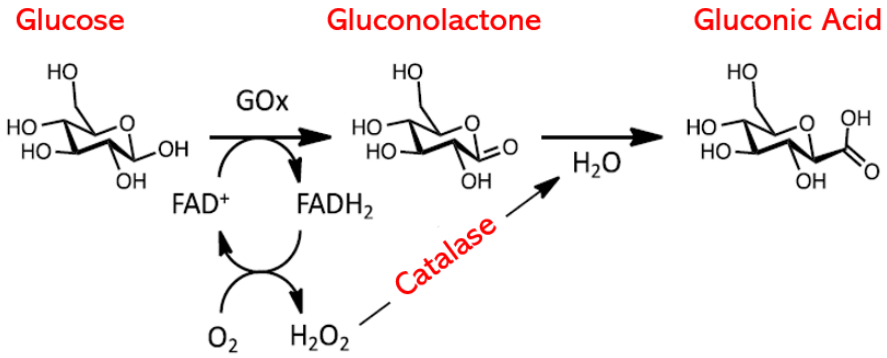

Figure 1.2: Chemical process of glucose oxidation where the glucose molecules are converted to gluconic acid (Adapted from [9])

As depicted in Fig. 1.2, in the presence of oxygen, the GOx catalyses the oxidation of glucose to gluconolactone, whilst the hydrogen peroxide (H_2O_2) and water (H_2O) are produced as by-products, (H_2O_2 is produced, and H_2O is consumed) [11]. Another reaction happens for the resulting gluconolactone to produce the gluconic carboxylic acid by the end. In that first design, a thin layer of the GOx was placed on a platinum electrode (via a semipermeable dialysis membrane), and the glucose concentrations were indirectly quantified proportionally by measuring the decrease in O_2 and the release of H_2O_2 [10]. However, the interference of other electroactive substances in blood (e.g., urea and ascorbic acid, etc.), was a challenge for this approach [11]. Therefore, it was further improved to quantify glucose concentrations directly using the amperometry detection of H_2O_2, and thereby become the first successfully commercialized GOx-based sensor in 1975 [11]. The usage of this version, however, was restricted to some clinical settings due to the costly platinum electrode incorporated and the need for high operating potential to acquire the desired electrochemical signal. Additionally, significant errors arose from the tension variations and other defects of O_2 when used as the electron-acceptor [12]. To overcome these limitations, the second-generation emerged in 1980 where synthetic electron redox was employed instead of O_2 [9]. This was further evolved to have a palm-size glucometer and enzyme-based test strips. Each strip has a miniature printed window housing the reference and working electrodes where the later was encased with the desired sensing pieces such as GOx, redox mediator, stabilizer, and linking agent [13].

This finger-pricking procedure is painful, invasive, risky for infection, and costly to the users who must prick their fingers multiple times a day to draw blood and constantly purchase a fresh supply of control solutions, alcohol swabs, and test papers to analyze the samples. Additionally, such invasive devices could only provide BGL measurements at a specific time spot by the time of testing. Therefore, their readings will not reflect any long-term patterns or trends in glucose fluctuations due to specific lifestyles, diet regimes, or medication intake. The maximum glucose level that can be measured by the currently available glucometers is 600 mg/dL [14] with error rates that are relatively high ~10% – 20%, yet still meeting the standards for BGL monitoring [15]. Apparently, the pain, burden, expenses, commitment, overthinking, and inconvenience associated with the current self-monitoring technology can lead to patient noncompliance and insufficient number of daily measurements, thus limiting the benefits of self-monitoring of BGLs [16].

1.3 Continuous Blood Glucose Monitoring

Continuous glucose monitoring is a paradigm shift in the assessment methods of glycemia levels. It is well-suited to diabetics of Type-1 and Type-2 with intense insulin therapy to assure the safety and efficacy of the diabetes treatment [8]. Currently, the most marketable forms of continuous glucose monitors (CGMs) (e.g., Dexcom, FreeStyle Libre by Abbott, Guardian Connect by Medtronic, etc.) are based on the electrochemical technology where the glucose levels are continuously measured in the interstitial fluid (ISF) of the subcutaneous tissue using tiny sensors implanted under the skin [17], therefore enabling diabetics to optimize their glucose control in the target range for longer time and further improving their HbA1c. These CGMs are described to be minimally-invasive since the blood vessels are not actually punctured but rather a sensor is put into contact subcutaneously with the ISF by pushing a tiny needle into the arm or abdominal wall. ISF is the fluid that surrounds the tissue cells just under the skin, and usually the glucose molecules move from the blood vessels into the ISF as illustrated in Fig. 1.3.

Accordingly, these sensors estimate the glucose level in ISF every few minutes via measuring the current flowing through a very thin wire to the external transmitter [17]. This current is produced proportionally to the amount of glucose being oxidized in a chemical reaction in the presence of specific enzymes (e.g., GOx). A transmitter is attached external to the implanted sensor to send the measurements frequently via wireless signals to a remotely located receiving device that processes the data and displays the glucose readings. To ensure accurate readings for practical use, currently available CGMs need to be externally calibrated based on the unique characteristics of the individual user several times a day. Particularly, the diabetic patient is required to use multiple readings from a finger-pricking device after fasting or some time postprandial to properly calibrate the CGM. An average of 2 – 4 invasive readings per day for the real time BGL are commonly used as input data to calibrate the CGM system. However, diabetics are not advised to take any therapeutic actions based on the CGM readings if an abnormality is reported unless an invasive glucometer is referenced for more precise decisions.

Despite being quite valuable, most of the current minimally invasive CGMs have issues in accuracy and sustainability resulted from having the sensor implanted inside the body, and hence a periodic replacement is recommended for the consumables to avoid any tissue fibrosis or inflammation on the long term. Nevertheless, some deformations were observed in the body parts where the measuring device is attached. Additionally, the total expense for the end users is relatively high and sometimes is not affordable on a frequent basis [18].

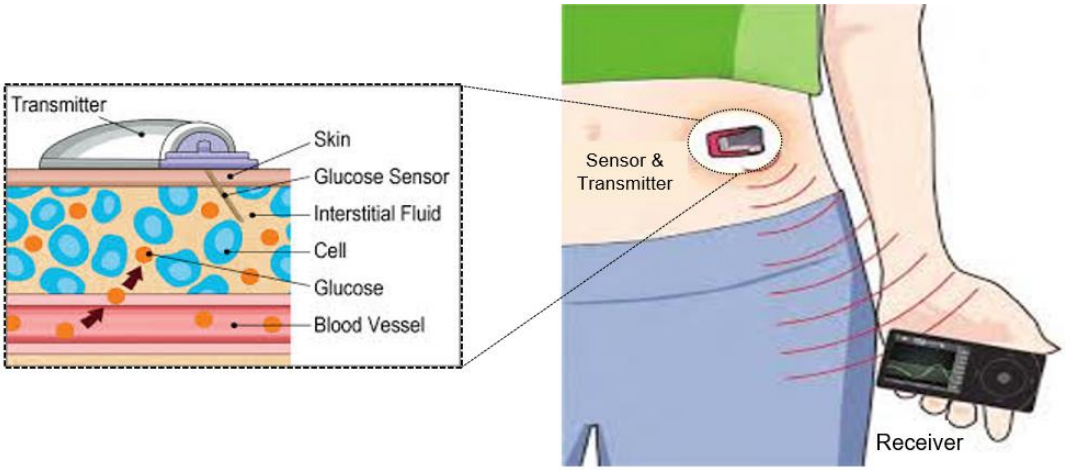

Figure 1.3: Continuous BGL monitoring using an implanted electrochemical sensor under the skin.

1.4 Non-invasive Blood Glucose Monitoring

Accordingly, there have been a growing demand for complete non-invasive pain-free glucose monitors that would guarantee more affordable, careful, and comfortable control of BGLs with no replacement over the long term [19]. To meet that demand and cope with these discomforts and limitations, significant number of researchers have been investigating the development of alternative, more innovative non-invasive (NI) glucose detection systems where different technologies are applied [19]. Most of these systems are based on optical methods where the scattering of light at several wavelengths is used to detect the glucose concentrations by measuring some optical parameters such as Raman spectroscopy [20], optical coherence tomography (OCT) [21], photoacoustic [22], impedance [23], fluorescence measurements, photoplethysmography (PPG), and mid/near infra-red (NIR) spectroscopy [24]. However, bulky, power-hungry, and expensive instruments are commonly required to conduct these optical measurements at short wavelengths. In addition, these techniques are known to have low signal-to-noise ratio (SNR) and large errors inherent from the calibration drift, thermal noise, and vulnerability to physiological (e.g., body temperature) and environmental (e.g., humidity) conditions [25]. The accessible biological fluids such as tears [26], [27], [28], saliva [29], sweat [30], [31] and breath condensation [32], have been utilized in numerous enzyme-based electrochemical techniques to correlate their glucose content to the glycemia levels. Despite being quite innovative, a lagging correlation is shown to the physical BGL variations, in addition to their susceptibility to metabolic changes. Likewise, the transdermal techniques where reverse iontophoresis methods are used to extract

and measure the BGL from ISF, are shown to be very expensive, deteriorating over time, and uncomfortable for injecting electrical current through the skin [33], [34].

Several devices have recently been developed by equipment manufacturing companies using the aforesaid techniques with promising preliminary results. Table 1.1 summarizes some of these devices alongside their respective manufacturers, merits, demerits, and their varying development status whether a proof-of-concept, waiting for regularity approval, or even been to the market while continuing to improve the technology [17]. Many other devices were released earlier but did not last long in the market for some commercial difficulties. For instance, GlucoWatch based on the reverse iontophoresis technique, was approved by the FDA for its reasonable accuracy in clinical and home trials, however it was dropped due to some issues in reliability and consistency. Another example is Pendra (based on impedance spectroscopy) was CE approved and marketed for short period then dropped later for its poor accuracy. Some other devices did not initially reach the market for lacking funds to finalize their designs (e.g., C8 Medisensors based on Raman spectroscopy) [17]. The NBM-200G by OrSense is also dropped for similar reasons [35].

Table 1.1: Non-invasive glucose monitoring devices currently available in the market, close to release, or withdrawn

Device/Company	**Technique**	**Placement**	**Needs**	**Attributes**
NovioSense (Noviosense BV) [36]	Electrochemical enzymatic-based tear analysis	Lower eye lid (inferior conjunctival fornix)	Continuous monitoring provided a sample	Compact, painless, flexible, wireless power, smartphone connected for data analysis
Smart Contact Lens (Novartis & Google) [37]	Electrochemical enzymatic-based tear analysis	Eye	Continuous monitoring provided a sample	Painless, power efficient, portable, low relief, hazardous when overheated, withdrawn from market
iQuicklt Saliva Analyzer (Quick LLC) [38]	Saliva analysis	Saliva of the mouth	Intermittent monitoring provided a sample	Portable, convenient to use, accurate, time efficient (real-time readings), under development and clinical trials
TensorTip Combo Glucometer (Cnoga Medical [39] - [40]	NIR spectroscopy, photometric and photography-based techniques	Fingertip	Intermittent monitoring without a sample	Convenient to use, accurate when calibrated on individual-basis, smartphone compatible, battery operated (rechargeable), cost-effective, certified
Glucosense (Glucosense Diagnostic Ltd) [41]	Low-powered laser sensors that use photonic technology (infrared light)	Fingertip	Intermittent monitoring without a sample	Convenient to use, portable, affordable, power-efficient, time efficient (30 s), performed one clinical trial; aiming for more after further development
Groves's Device (Groves Instrument Inc) [42]	NIR spectroscopy	Fingertip or earlobe	Intermittent monitoring without a sample	Fast processed readings, time-efficient (20 s), compact, portable, uses capillary-level blood, less accurate due to lacking subjective calibration
HELO Extense (World Global Network) [43]	photoplethysmogram (PPG)	Fingertip	Intermittent monitoring	Portable, reliable, should be paired with a smartphone with the sugar trend software, requires a calibration (2 – 3 times/day), CE approved (class 1 medical device)
GlucoTrack (Integrity Applications) [44]	Thermal, ultrasonic, and microwave EM technology	Earlobe	Intermittent monitoring without a sample	Affordable, convenient to use, high accuracy due to earlobe placement, unit-connected for results processing/display, complex processing, FDA approved, commercialized in Europe
GlucoWise (MediWise) [45]-[46]	RF/Microwave	Amid fingers (thumb and forefinger)	Intermittent monitoring without a sample	Convenient to use, affordable, accurate, Bluetooth-based data transmission, compact, integrable with insulin pumps, uses capillary-level blood, time-efficient, fast

				readings (10 s), hurtful due to localized energy usage, under development!
SugarBEAT (Nemaura Medical) [47]	Reverse iontophoresis (Electric current)	Upper Arm	Continuous monitoring	Waiting for CE approval
Wizmi (Wear2b Ltd) [48]	NIR spectroscopy	Arm wrist	Continuous monitoring	Proof of concept

1.5 RF/Microwave Sensing

Out of the many investigated non-invasive methods, the radio frequency (RF)/microwave sensing techniques [49], [50], [51], [52], [53], [54], [55], [56], [57], [58], [59], [60], [61], [62], [63], [64], [65], [66], [67] have shown to be more promising among the aforementioned methods due to the non-destructive nature of the electromagnetic (EM) waves when penetrating inside the biological tissues unlike other ionizing radiation (e.g., X-rays) that might incur dicey effects. Specifically, they do not alter the sample or the tissue under test neither by chemical nor mechanical procedures. Such sensing techniques are principally based on the theory of material characterization with the fact that the glucose level in a person's blood affects the EM properties of the blood (i.e., dielectric permittivity and conductivity) [60], and therefore seek for a promising correlation between the measured EM properties of blood and its glucose content. Essentially, the EM waves radiated from the microwave sensors penetrate into the body and interact with it. The reflected and transmitted versions of the EM waves are affected by the underlying tissues and therefore valuable information of their dielectric properties and glucose fluctuations could be extracted by monitoring the variations in the attributes of those modulated scattering signals.

Measurements of the dielectric properties of blood biological tissues at subjective glucose concentrations similar to diabetics have become particularly important for developing an accurate non-invasive microwave sensor for BGL monitoring. A variety of methods have been developed for characterizing materials (i.e., measuring their complex permittivity) in the RF/microwave spectrum using transmission and/or reflection techniques. These methods include transmission-lines, free-space methods, near-field probes, resonant methods, etc. [50], [68], [69]. A method is chosen properly depending on the operating frequency, physical state (solid or liquid) of the sample, its losses and volume. A popular method for measuring the complex permittivity for liquids is using an open-ended coaxial probe as a near-field sensor by placing the sample under test (SUT) right at the opening and measuring the reflection coefficient S_{11} which is then related to the dielectric properties through a complex mathematical model [70], [71]. Such probes can be used for measurements in a convenient laboratory setup, yet not suitable for practical non-invasive glucose sensing due to their high cost, bulky nature, high error rates (up to 5%), and limited penetration depth depending on the probe diameter [72]. They also become quite inaccurate in measurements for any asymmetries in the SUT surface, that increase the model complexity [70], [73]. On the other hand, SUT needs to be carefully prepared to

adapt to the shape of the transmission-line (e.g., coaxial-line) used for testing [74]. Waveguides enable only a limited bandwidth and therefore allows for narrow-band characterization.

Among those RF/microwave dielectric characterization techniques, the resonant methods have earned a popularity for the different sensing applications (e.g., biomedical, industrial, safety, etc.). This is due to their great advantages on reliable sensing accuracy and precision with less susceptibility to noises and other measurement losses, as opposed to non-resonance techniques which suffer from several limitations [75]. They feature instant measurement of the dielectric permittivity of liquids over a narrowband using simple, low-power, and cost-effective structures [56]. Particularly, they employ various types of microwave resonators (e.g., classical box, transmission-line, circular/ring, etc.) and in different forms of metal cavities, dielectric cavities, planar metamaterials resonant structures [76] [77]. For the measurement recipe, a unique resonance characteristic (resonant frequency, amplitude, width, or quality coefficient) is noted when the resonator is unloaded. Interestingly, a noticeable change in the resonator response is detected when a fluid sample is placed nearby the resonator due to its field interactions with the tissue under test at the operating frequency. The dielectric properties of biological tissues can be calculated indirectly by carefully analyzing these changes in the resonance behaviour [78]. Nevertheless, this method is found to be more suitable for characterizing the materials of low loss over a narrow band, yet the harmonic resonance frequencies could be of great use for wideband characterization. Table 1.2 summarizes some of the most popular dielectric characterization and the pros and cons of each. Based on these techniques, a variety of reflection and/or transmission methods have been developed to measure the dielectric constant and loss of blood glucose in superficial vessels using different setups of resonators [79], antennas [80] or waveguides [53] while relying on costly and bulky vector network analyzers (VNAs) [81]. Remarkably, a distinct correlation has been demonstrated between the measured blood properties and its glucose content. However, most of these RF systems are not practicable for immediate in-house usage by diabetics due to their cost, complexity, size, and weight. This makes the systems impractical for large-scale deployment. Besides, their limit of detection for the glucose is way beyond the practical range of BGLs seen at the different diabetes conditions. Some state-of-the-art techniques recently proposed for non-invasive glucose detection are listed in Table 1.3.

Table 1.2: The microwave-based dielectric characterization techniques with their respective pros and cons

Characterization Technique	**Examples**	**Pros**	**Cons**
Free-Space Methods	MUT between two horn antennas connected to VNA (reflection/transmission based)	• Non-destructive (preserve the MUT integrity) • Contactless (easy sample preparation) • Wideband characterization	• Need for large samples (large wavelength) to avoid diffraction on sample sides/edges • High cost for lenses and antenna equipment

Transmission-Line Methods	MUT inside a transmission line (e.g., waveguide or coaxial line) (reflection/transmission based)	• Cheaper (no need for lenses) • MUT characterized in the unimodal propagation band of the device • Wideband characterization • Wider bandwidth at low frequencies (coaxial cables) • Simple MUT preparation (rectangular or circular inside waveguides)	• Sample must be carefully prepared and adapted to the device shape (coaxial cables) • Allowing narrow bandwidth and characterization is valid for a limited frequency range (waveguides)
Near-Field Sensors	Open-ended coaxial lines (Reflection based)	• Inexpensive	• Less accurate (affected by asymmetries in sample surface). • Mathematical model complexity
Resonance Methods	• Ring resonator coupled to a transmission line • Cavity resonator (Quality-factor and resonance frequency based)	• Reliable accuracy especially for MUT with low losses.	• Mainly for narrowband, harmonic resonances can be used for wideband characterization • Precise fabrication for resonator and sample preparation • Limited by the size and physical state of the sample

Table 1.3: Some state-of-the-art techniques for non-invasive glucose detection

Ref	Technique	Main items	Sensing parameter	Pros	Cons
[82]	OCT	Light source + coupler + interferometer	OCT slope	• Good resolution images with high SNR	• Affected by pressure and temperature • Compromise between resolution and penetration depth • Time consuming for glucose estimation
[83]	Optical/thermal spectroscopy + photoacoustic	Microphone + laser diode	Change in optical absorption coefficient and pressure	• Compact size • Improved sensitivity	• Affected by pressure and temperature
[84]	NIR + PPG + ANN	Photo diode + LED	Difference in optical density	• Reduced cost • Fast FPGA implementation • Good accuracy	• PPG is affected by noise, motion, fatty tissues • Increased complex processing • Time consuming • Filtering overhead
[85]	Photoacoustic + NIR + MEMS	IR + ultrasonic micro-electro-micro mechanical (MEMS) sensors	Acoustic pressure and absorption	• Compact size • Efficient power • Accurate and sensitive • Deep penetration in earlobe area	• Affected by pressure, temperature, and humidity • Performance dependency on surface
[86]	NIR + photoacoustic	Piezoelectric sensor + pulsed laser diode (PLD)	Change in pressure (Photoacoustic amplitude)	• Good sensitivity • Limited scattering • User friendly	• Non-uniform absorption • Affected by pressure and temperature • Time consuming • Power inefficient
[87]	NIR	Thermal/laser sensors + spectroscope	Change in power output of the transmitted light beam	• Not expensive • Harmless	• Data limitation • Less accurate
[88]	ECG + ML	Compumedics ECG leads	Heart rate and QT interval	• Fast processing • Converged computation • Detecting hypoglycemia and hyperglycemia	• ECG signal parameters possibly affected by abnormal heart condition (e.g., arrhythmia)
[89]	RF/Microwave	Microstrip patch antenna (spiral)	Shift in resonance frequency	• Compact size • Affordable cost • High Q-factor	• Affected by noises in atmosphere • Not validated for glucose sensing using real measurements

					• Loss parameters not considered in simulation
[90]	RF/Microwave	PNA + antenna + Cole-Cole model	Shift in resonant frequency	• Good correlation with glucometer when calibrated	• Affected by environmental changes (sweat, temperature, pressure, etc.) • Subject-based calibration
[91]	RF/Microwave	Microstrip patch antenna (triangular)	Shift in resonance frequency	• Cost effective • Miniaturized size • Linear	• Not demonstrated for different glucose levels detection
[64]	RF/Microwave	Patch resonator	Changes in input impedance	• Miniaturized size • Good sensitivity • Tested on wideband tissue mimicking phantom	• Large error margin • Phantom simulated with non-dispersive dielectric properties
[45]	Millimeter-wave Antenna	Two patch antennas (Glucowise)	Changes in transmission coefficient S_{21}	• Portable • Less susceptible by interference	• Possible harmful effects due to localized energy
[92]	RF/Microwave	Planar ring resonator	Shift in resonant frequency	• Compact size • Accurate (Resonant-based)	• Affected by environment status • Low sensitivity • Tested on impractical glucose ranges

Beyond glucose biosensing, there has been a growing interest over the recent years in those micro/millimeter wave sensing devices for accurate characterization of materials for numerous applications in various fields especially in the healthcare, industry, agriculture, and food processing such as dielectric characterization [93], liquid identification [94], oil quality monitoring [67], biomolecular sensing [95], gas detection [96], etc. The affordability and portability of such devices along with their non-invasive, non-destructive, uncontaminated, and rapid responses, make the micro/mm-wave sensing technology apropos for many industries to develop effective wireless sensing systems that are easily configurable at different frequencies to meet the requirements of the specific application while facilitating the automated and computerized processes.

One interesting field is food quality control where the quality control procedures are applied on characterising the food products and monitoring their quality in a rapid non-destructive fashion exploiting the recent advances on the Internet-of-Things (IoT) technologies [97]. Among different foods, the milk and oil products that contain composite blend of saturated, polyunsaturated, and monounsaturated fats where various carbon chain lengths are incorporated [98]. Monitoring the quality of oils is paramount not only during their production, transportation, and storage phases but also, more importantly, for controlling their authenticity by the regulatory authorities. Extra virgin olive oil (EVOO), for instance, is massively prone to frequent fraudulent activities in the oil industry [99]. To lower the cost of production, fake olive oils are currently produced from mixing cheap and low-quality edible or botanical oils like soybean, sunflower, and canola types with the virgin olive oil of high quality and cost [99]. Those added vegetable oils are composed of similar fatty acids at different proportions [100]. The adulteration results into modulating the composition of the fatty acids and compounds while removing many of the EVOO flavour-related features of much desirability. In addition, such

adulteration would reduce the associated health benefits and may raise health issues for customers who are allergic to some supplements such as peanut proteins [101]. Therefore, advanced EM sensing techniques could be effectively used in oil fraud detection to rapidly identify different oil types and their quality status through their EM fingerprints in the micro/mm-wave spectrum of frequency domain [102]. They could also be used to detect any impurity presents in oils through capturing the tiny modifications in their EM properties over a narrow band of interest.

Milk products, on the other hand, are massively produced every year with constraints that both satisfy the consumer's quality standard and meet the health safety standards. The global milk production has almost multiplied from 482 million tons in 1982 to 906 million tons in 2020 [103]. This is clearly reflecting how crucial the milk and dairy industry in the economy status of many countries. Milk is a nutrient-rich liquid of short shelf-life that is highly susceptible to spoilage due to bacterial growth and other microorganisms [104]. Therefore, its processing becomes of pivotal importance for longer-period preservation at the actual quality of raw milk. Traditionally, milk gets transported in tankers to dairy manufacturing plants. Next, milk gets separated into cream and skim milk in a centrifuge, which are then blended together to create a desired concentration of butterfat in the final product. After that milk gets pasteurized and homogenized in a processing machine before packaging. During the manufacturing process, composition issues can arise as a result of various factors such as physical/liquid contaminants, piping system issues, products changeover, accidental flaws, etc., that can result in poor quality products with potentially massive consequences on the manufacturing efficiencies and the company's brand. Unfortunately, traditional quality control tools do not provide timely information that could prevent any subsequent losses. Innovative non-invasive sensing techniques could be developed to rapidly assess the quality status of milk products through identifying their EM fingerprints that correlate to their butterfat content. Such a new continuous, fast, and automated quality control device can address the underlying problems in the milk industry at multiple levels of the supply chain hierarchy with a significant economic impact.

1.6 Research Objectives and Contributions

Driven by the developing interest in realizing non-invasive blood glucose monitoring devices to conveniently serve the diabetic's society, in this research multiple compact low-cost portable electromagnetic sensors working in the micro/mm-wave frequencies are proposed for the purpose of non-invasively monitoring the glucose concentration levels for diabetes. The sensing structures were developed to operate in certain frequency spectrums of interest based on three different technologies, namely, Complementary Split-Ring Resonators (CSRRs), Whispering Gallery Modes (WGMs) Resonators, and FMCW mm-wave Radars. The primary objective of the developed sensors is to detect the glucose concentrations of clinical relevance to Type-1 and Type-2 diabetes. Particularly, the narrow range of normal diabetes condition 70 – 200 mg/dL as well as those of extreme events (Hypoglycemia

< 70 mg/dL and Hyperglycemia > 200 mg/dL). Comprehensive theoretical and experimental studies were conducted probing the functionality, sensitivity, and repeatability of each sensing device. Particularly, the EM sensors were thoroughly designed, numerically simulated, and analyzed for optimal sensing. Additionally, proof-of-concept prototypes were fabricated and practically tested and verified in the microwave laboratory for blood glucose monitoring with the desired sensitivity performance. Different topologies and configurations of the proposed sensors were also studied and compared in terms of sensitivity using experimental testing and numerical analysis tools. The research focused on achieving high sensitivity for detecting the practical glucose levels for diabetes by experimenting with the developed sensors for blood mimicking materials (e.g., aqueous solutions, synthetic blood, etc.) of varying glucose concentrations typical to the diabetes condition.

Towards this goal, the dielectric complex permittivity behavior of glucose-loaded samples was first studied across the frequency spectrum from 200 MHz to 67 GHz using a dielectric characterization system. The objective was to determine whether varying the amount of dissolved glucose in blood affects its dielectric EM properties, and to what extent. Furthermore, we aimed at determining the portion of the frequency spectrum that is most responsive to slight variations in glucose concentrations, and to identify the amount of change in the EM property due different concentrations of interest. The extracted dielectric properties were then used to numerically analyze the scattering behaviour of the lossy blood mimicking solutions at varying concentrations, and optimally design the underlying sensors for high sensitivity. A portable sensor prototype was developed by interconnecting a small low-cost and -power radar as a driving source and tested in-vivo for tracking the blood glucose levels pre- and post-prandial.

The proposed EM sensors, beside their excellent detection for the diabetes-related glucose levels, they are featured in terms of the compact size, simple fabrication, affordable cost, non-ionizing nature, and minimum health risk or impact. Such favorable attributes promote the proposed sensors as possible candidates for continuous glucose monitors that enable efficient diabetes management. Beside the primary intention for blood glucose monitoring, the EM sensing structures introduced in this research have demonstrated their potential in other pivotal sensing applications such as liquid identification/quantification, oil adulteration detection, milk quality control monitoring, and viral pathogens detection.

The chapters of this thesis are organized as follows:

- **In Chapter 2**, the Debye dispersive model was presented, and the EM characterization of the glucose-varying aqueous solutions was discussed from the available literature both at low and high frequency bands. Additionally, the dielectric complex properties of blood mimicking solutions of concentrations relevant to diabetes conditions were measured over the wideband spectrum 200 MHz – 67 GHz using a commercial coaxial probe kit (DAK-TL) with two probes

for low- and high-frequency bands. The broadband testing fixture was also used to investigate the effect of blood typing and medication on the dielectric properties of blood.

- **In Chapter 3**, novel planar sensors were developed in the low-frequency band 1 – 6 GHz using advanced metamaterial-inspired resonators based on mutually coupled Complementary Split Ring Resonators (CSRRs). In these microstrip structures, different configurations of the CSRRs were designed, numerically analyzed, and optimized in geometry for the desired performance. Numerical models for the targeted glucose tissues were integrated into the CSRRs to study and improve the sensitivity with respect to changes in blood permittivity. Machine learning algorithms were applied to enhance the resolution of the CSRRs scattering signals. The functional behaviour of the CSRR structure was electrically modelled using an optimized lumped-element electrical model. Proof-of-concept CSRRs were fabricated in-house using the PCB laser manufacturing, and their sensitivity performance for glucose detecting was experimentally verified in the practical measurements.
- **In Chapter 4**, the motivation for glucose monitoring in the millimeter-wave band was thoroughly discussed. The Whispering Gallery Mode (WGM) technique was then utilized for BGL monitoring at multiple frequency points in the mm-wave spectrum. Several resonant structures supporting travelling-wave higher-order WGMs were designed in different configurations using disc and ring resonators made of materials of desired properties such as Aluminum, Silicon, and Ferrites. The first WGM structure was developed in the mm-wave range 50 – 70 GHz using a Silicon-made disc resonator coupled to a dielectric image waveguide. Second, a novel WGM sensing platform based on changing the conductivity of the Silicon-made dielectric resonator using near-infrared radiation (NIR) was introduced and experimented for monitoring the varying glucose levels. Lastly, a nonreciprocal WGM sensor was developed for glucose monitoring in the sub-centimeter and millimeter wavelengths using a Ferrite-made ring resonator integrated with a permanent magnet in a microstrip substrate. All the proposed WGM structures were numerically modelled, analyzed for optimal sensing, and simulated for sensitive glucose detection using 3D full-wave simulation tools. Proof-of-concept prototypes were also fabricated and experimentally verified in the lab for glucose monitoring using blood mimicking samples of practical concentrations.
- **In Chapter 5**, radar sensing and signal processing were applied for identifying the glucose levels in synthetic blood samples of varying glucose concentrations typical to the diabetes condition. A novel sensing technique for BGL monitoring was introduced where a low-power millimeter-wave radar system, operating in the range 57 – 64 GHz, was used to non-invasively differentiate synthetic bloods of diabetes-related concentrations. The radar sensing structure, its working principle, and the experimental approach for glucose detection were all discussed in detail. The capability of the radar sensor for non-invasive glucose monitoring was

demonstrated by testing blood samples in clinical test tubes at a definite distance from the radar inside a 3D-printed fixture. The raw data, representing the reflected mm-waves, collected from the multi-channels of the radar was then analyzed using signal processing techniques to accurately identify the corresponding glucose concentrations in tested bloods. Next, the chapter presents the portable prototypes/devices of the low- and high-band glucose sensors where been connected to low-profile radar boards instead of the bulky and expensive VNA instrument.

- **In Chapter 6**, insightful conclusions were discussed, and the future works were outlined.

Chapter 2. Dielectric Properties of Glucose Solutions

The presence of glucose in host medium (i.e., blood or any mimicking tissue) would modulate the EM properties (i.e., complex permittivity) of the sample to some extent depending on the dissolved concentrations. In all EM-based systems, the blood glucose sensing is realized by measuring changes in the intrinsic responses of the sensor due to the contrast in EM properties of blood as induced by the glucose concentration changes. Therefore, development of an accurate model for measuring the complex permittivity of blood biological tissues, at subjective glucose concentrations similar to diabetes, is a major and fundamental step to properly design our targeted wireless glucose sensors. In this chapter, we measured the complex permittivity, in terms of dielectric constant and loss tangent, of water-based glucose-loaded samples of varying concentrations related to diabetes conditions over the broadband frequency spectrum from 200 MHz to 67 GHz using a commercial coaxial probe called Dielectric Assessment kit (DAK-TL). The objective is to determine the portion of the frequency spectrum that is most responsive and sensitive to slight variations in glucose concentrations and to identify the amount of change in complex permittivity due to different concentrations of interest. Measured dielectric parameters were used to model the BGL monitoring process in the different proposed EM sensing structures. Other factors that affect the dielectric properties of blood such as blood typing and medications were also discussed.

2.1 Debye Relaxation Model

The behaviour of any EM waves propagating through a material is essentially governed by the dielectric properties of that material. Such properties should primarily be considered when designing any RF/microwave structure [105]. For preliminary investigations on non-invasive glucose detection using RF sensors, aqueous glucose solutions (where a dextrose powder is added to pure distilled water) can be utilized in the RF experiments to mimic the blood behaviour at disparate glucose concentrations, and therefore overcome the challenges and complexity of using real blood tissues while ensuring sufficient repeatability of the measurements [79], [106], [107]. This approximation is valid since water contributes a high percentage (≈ 50%) of the entirety volume of human blood that contains other vital constituents at varying proportions (e.g., Sodium ‘Na’, Calcium ‘Ca’, Magnesium ‘Mg’, Potassium ‘K’, Chloride ‘Cl’, etc.). These minerals are present at lower concentrations compared to the dominant glucose whereby the blood dielectric properties are dominantly affected [105], [108], [49], [109]. In particular, compared to the broad range of glucose concentrations in blood; other minerals only vary in limited ranges, Na: 310 – 333 mg/dL, Cl: 337 – 372 mg/dL, Mg: 1.8 – 3.4 mg/dL, Ca: 8.5 – 10.5 mg/dL, K: 13.6 – 21.4 mg/dL) [109], and other components in blood like the lactic acids, have also very small concentrations (normal range is 4.5 – 19.8 mg/dL or 0.5 – 2.2 mmol/L) when compared to the dominant glucose. Sodium and Chloride that exist in larger order of magnitudes compared to other minerals would mostly influence the conductivity properties of the blood. This is shown very clear in the study by Erdem *et al* [49], [109]

where the laboratory tests revealed for 10 different blood samples collected from adults of 18 – 40 years old have shown that the mineral concentrations do not vary significantly from one individual to another as shown in Table 2.1 [109]. Additionally, the measurements collected between 500 MHz and 20 GHz using the Agilent open-ended coaxial dielectric probe kit, have shown that the dielectric properties of the respective 10 blood plasmas were considerably dependent on the glucose concentrations and that other minerals have negligible effects.

Table 2.1: Laboratory test results of the minerals quantities in blood plasma of ten subjects [109]

Mineral (mmol/L)	**S1**	**S2**	**S3**	**S4**	**S5**	**S6**	**S7**	**S8**	**S9**	**S10**
Na	138	137	138	139	138	137	139	136	139	140
K	6.8	9.0	5.9	7.8	9.8	9.7	6.4	7.1	7.2	4.7
Cl	101	101	101	103	101	102	102	100	101	102
Ca	9.1	8.8	9.2	9.0	8.8	8.7	9.1	8.2	8.9	9.2

Liquids of high-water contents (e.g., blood, aqueous solutions, etc.) introduce dispersion to the EM waves propagating through their media at different frequencies, and hence they are described as dispersive media whose EM properties depend on frequency. Essentially, exposing EM fields to polar liquids would cause some rotations and polarization to their molecular dipoles after a definite amount of time called relaxation time. This would consequently lead to an increase in the energy stored in the polarized molecules as well as some energy loss due to the intermolecular friction and heat from molecular vibrations, stretching, and rotations [110]. The resulting liquid permittivity is therefore displayed as a complex quantity due to the phase lagging between the polarization of the dielectric and the applied electric field. The real part of the permittivity represents the polarization component in line with the electric-field, while the imaginary part represents the other component in quadrature with the electric-field [111]. Therefore, liquids tend to be lossy with attenuation introduced to the EM waves propagating through their media due to the damping of vibrating dipole moments. Providing an accurate mathematical model is necessary to describe this frequency dependency for the liquid EM properties.

The dielectric response in the frequency domain of tissues having high water content can be characterized by the Debye Relaxation Model [112], which describes the reorientation of molecules that could involve translational and rotational diffusion, hydrogen bond arrangement, and structural rearrangement. The relative permittivity for aqueous solutions is designated as a function of the angular frequency $\omega = 2\pi f$ and the concentration ξ of any hydrophilic substance (i.e., a molecule or other molecular entity that is attracted to water molecules and tends to be dissolved by water) by

$$\epsilon_r(\omega, \xi) = \epsilon_r'(\omega, \xi) - j\epsilon_r''(\omega, \xi), \tag{2.1}$$

where $\epsilon_r(\omega, \xi)$ is the complex permittivity of the aquatic solution of ξ solute concentration at angular frequency ω, $\epsilon_r'(\omega, \xi)$ is the dielectric constant that represents the energy stored in the solution when exposed to an external electric-field (i.e., the easier the molecules are to polarize, the higher the

dielectric constant) and $\epsilon_r''(\omega,\xi)$ symbolizes the dielectric loss for the total attenuated and absorbed energy due the ionic conduction $\epsilon_{r\sigma}''$ and dipole rotation ϵ_{rd}'' loss mechanisms that are dominant at specific RF/microwave frequencies [113].

$$\epsilon_r''(\omega,\xi) = \epsilon_{rd}'' + \epsilon_{r\sigma}'' = \epsilon_{rd}''(\omega,\xi) + \frac{\sigma}{\omega\epsilon_o}, \tag{2.2}$$

where σ is the ionic/dc conductivity of the material in S/m and ϵ_o is the reference free-space permittivity (8.854×10^{-12} F/m) [108]. The ratio between dissipated and stored energy in the material is labeled as loss tangent (or dissipation factor)

$$\tan\delta = \epsilon_r''/\epsilon_r', \tag{2.3}$$

According to the first order Debye relaxation model, the complex permittivity $\epsilon_r(\omega,\xi)$ of a dispersive material, such as glucose-water solutions, can be calculated using Eq. (2.4) with the knowledge of four parameters denoted as static permittivity ϵ_{stat}, infinity permittivity ϵ_∞, relaxation time τ (for the dispersion region), and the static conductivity σ_s. However, the last term can be neglected for low-conductive solutions of no dissociated ions such as the non-electrolyte glucose. The real and imaginary parts are extracted using Eq. (2.5) and (2.6). The permittivity could also be modelled using the Cole-Cole model that is very similar to the Debye model yet with the term $j\omega\tau$ raised to power $1-\alpha$, where α represents the broad distribution of τ.

$$\epsilon_r(\omega,\xi) = \epsilon_\infty(\xi) + \left(\frac{\epsilon_{stat}(\xi) - \epsilon_\infty(\xi)}{1 + j\omega\tau(\xi)}\right) + \frac{\sigma_s}{j\omega\epsilon_o}, \tag{2.4}$$

$$\epsilon_r'(\omega) = \epsilon_\infty + \left(\frac{\epsilon_{stat} - \epsilon_\infty}{1 + (\omega\tau)^2}\right) \tag{2.5}$$

$$\epsilon_r''(\omega) = -\left(\frac{\omega\tau\,(\epsilon_\infty - \epsilon_{stat})}{1 + (\omega\tau)^2}\right) \tag{2.6}$$

2.2 Dielectric Properties of Glucose Solutions at Low Frequencies

Many studies have focused on extracting the permittivity measurements for liquid samples of relatively high glucose concentrations in the low frequency range using different setups. For instance, the relative permittivity and conductivity for adults' blood samples were measured in the frequency range 0.5 – 20 GHz using an open-ended coaxial probe [49]. The collected measurements were then fitted to a single-pole Cole-Cole model. The studies in [50] [114] used resonant cavity structures in the frequency range 2 – 3 GHz for measuring glucose solutions in the range 0 – 3600 mg/dL. Open waveguide structures were used in [53] for frequencies up to 20 GHz where a 12° phase difference was observed for a 500 mg/dL glucose change in aqueous solutions.

Different setups with *antenna* sensors were used in [51] and [52] for the frequency ranges 1.0 – 2.5 GHz and 5.0 – 8.5 GHz, respectively. U-shape antenna was utilized in [51] to track the 1000 – 4000 mg/dL glucose variations in aqueous solutions, while a patch antenna was tested in [52] for the 50 – 500 mg/dL glucose range. The 1.5 – 3 GHz reflection response of a monopole antenna was observed to slightly shift when testing blood mimicking phantoms [115] [116]. However, such wideband responses of antennas have lower sensitivity to small dielectric property changes in lossy medium or liquids. Besides, the omnidirectional radiation of this antenna type will significantly disturb the glucose precise measurements by the uncontrolled environment around the antenna. A 1.4 GHz planar dipole antenna was used to monitor BGL when strapped on a food-fed diabetic's hand by tracking the S_{11} or return loss resonance on the VNA every 15 seconds [117]. The measured frequency shifts were observed to correlate with the actual BGL readings taken by an invasive glucometer. However, the study has not discussed the antenna and glucose experiment designs in details. A pair of ultra-wideband slot antenna of 12.5 GHz bandwidth (3.5 – 15 GHz) were simulated on two sides of an earlobe to monitor its BGL using the S_{21} parameter [118]. The proposed sensing approach was practically validated on earlobe phantoms filled with aqueous solutions of 0 – 4000 mg/dL glucose concentrations, where a regular trend was observed in the S_{21} signals around 6.5 GHz.

A microstrip patch resonator with two-coupled feedings strips operating around 2.45 GHz was tested with the in-house made mimicking phantom of four layers (skin, fat, blood, and muscle tissues). The miniaturized prototype was realized on Rogers 3210 substrate with high dielectric constant while connecting the patch to the ground using two shorting vias. Blood layers with varying dextrose 0, 7, 9, and 12 mmol/dL (~ 0, 1260, 1620, and 2160 mg/dL) were tested, and the corresponding input impedances were extracted from the resulting S-parameters. Slight changes with limited sensitivity were observed in the real and imaginary impedances following the varying glucose in the blood layer [64] [119]. A 2.45 – 5.8 GHz patch antenna with FR4 superstrate was tested for glucose solutions that were noticed to change its matching in a non-linear scale at the different levels from 200 mg/dL to 1500 mg/dL [120]. Two layers of FR4 were stacked together to form a thick layer of superstrate thereby preventing the direct contact between the radiating parts of the antenna and liquids inside the container. Another 5 GHz patch antenna was simulated with 0 – 500 mg/dL glucose-liquid phantoms, and linear shifts in the S_{11} resonant frequency were observed. However, no correlation or trend was seen in practical measurements possibly due to temperature or volume differences between samples [121]. A near-field antenna operating at 4.8 GHz was numerically analysed for glucose monitoring using a four-layer fingertip model. The blood layer was simulated with a Debye model at varying glucose levels from 0 to 2000 mg/dL, and slight frequency shifts in the S_{11} resonance were captured. However, no frequency shifts were observed when testing the antenna on actual fingertips possibly due to the weak sensitivity of the structure that is limited by the loss mechanism of the tested biological tissues [122]. A correlation between the varying dextrose (18, 54, 90, 126, and 450 mg/dL) in a sodium chloride solution and frequency signal of the complex S_{11} was demonstrated between 1.4 GHz and 1.7 GHz

using a conic horn probe with conical coaxial conductor. However, the size of the bulky sensing setup sounds impractical for BGL monitoring [123]. A recent study proposed two multiband systems, slot antenna and reject filter, operating in 500 MHz – 3 GHz for BGL monitoring. The slots design was inspired by the vascular anatomy of the back palm and lower arm of the body. A good correlation was observed in the sensing parameters while tracking the BGLs [124].

A study by Choi *et al.* proposed a pair of split-ring *resonators* operating at 1.4 GHz for sensing blood glucose. One resonator was used for sensing the glucose sample and the other was set as a reference to revoke the temperature effects. The study concluded that the sensor bandwidth response, and hence the blood complex permittivity, was primarily affected by the glucose concentrations, and that other constituents in blood had negligible effects [60]. The resonating system was found to be much more sensitive to glucose than other sugars of similar structure (i.e., maltose, fructose, and galactose). The system also has shown no response to variations in metabolites (e.g., uric acids) and vitamins (e.g., ascorbic acids). Clinical tests were performed on a non-diabetic subject; therefore, a very narrow range of blood glucose levels was studied. An extended clinical study was performed on 24 subjects (8 healthy, 4 Type-1 and 12 Type-2) using the two fabricated resonators where a correlation was noticed between the microwave readings and reference glucometer. However, the two similar resonators have shown different variations that are either physiological- or fabrication-related [125].

A dielectric resonator with high quality-factor *Q* was used in [79] to design a microwave biosensor that detects different glucose concentrations in aquatic solution at 1.68 GHz. The authors had the capability of detecting glucose concentrations down to 5 mg/ml resolution at 25^{o}C temperature by tracing the reflection coefficient S_{11} of the microwave sensor and the shift in resonance frequency using a VNA. A two-port spiral microstrip line was tested on five human thumbs after consuming soda drinks, and the S_{21} amplitudes were monitored in the 100 MHz – 5 GHz range. A custom fixture was designed to accommodate the tested thumbs while integrating a pressure sensor underneath to ensure consistent pressure applied in each measurement trial. However, the resulting scattering data were not explicitly reported or discussed in terms of repeatability [126]. Another open-ended spiral resonator was tested on mimicking phantoms and the resulting S_{11} responses were processed to retrieve the permittivity properties around 600 MHz. Three versions of an open-loop microstrip resonator operating between 2 – 7 GHz were analyzed in [63] for testing small volumes 5 – 25 µL of highly concentrated glucose aqueous solutions 1250 – 10000 mg/dL inside a dielectric liquid holder pasted onto their gaps. The *Q*-factor and maximum $|S_{21}|$ magnitudes were used as primary sensing parameters. However, reported measurements have shown very limited sensitivity inadequate for practical blood glucose monitoring in diabetes. A 5.8 GHz resonator composed of an interdigitated capacitor and spiral inductor was tested for aqueous solutions and blood plasma with varying glucose levels 25 – 500 mg/dL [127]. The S_{11} resonant frequency was noticed to increase with the increased glucose at a sensitivity of about 199 MHz/[mg/dL]. Another 6.53 GHz stepped-impedance resonator made on GaAs substrate was

experimented for 2 μL watery solutions with varying glucose (75 – 500 mg/dL) directly injected onto the sensing region by tracking the S_{11} response that was observed to shift upwards with increased glucose levels [128]. A tag-reader sensor operating around 3 GHz was proposed for glucose sensing from ISF. Both parts, reader, and tag, were designed as split ring resonators on Rogers 5880 PTFE composite and Rogers RO4450 substrates, respectively. The sensor was tested for detecting 90 – 720 mg/dL glucose-water solutions with a low sensitivity of about 4.17 KHz/[mg/dL]. However, glucose measurements from ISF are not practically favored due to the time delay effect discussed earlier [129].

The EM properties measured for the blood plasmas with different glucose concentrations (0 – 16,000 mg/dL) in [49] were fitted using a single-pole Cole-Cole equation in Eq. (2.7) with parameters of quadratic polynomials given by Eq. 2.6 – 2.9 [49]. According to this model, both ϵ_r' and σ decrease with the increased glucose level, however the amount of change in both is very small (~ 0.2 units and 0.1 S/m, respectively) for the realistic BGL change from 72 mg/dL to 600 mg/dL [105]

$$\epsilon_r(w,\xi) = \epsilon_\infty(\xi) + \left(\frac{\Delta\epsilon(\xi)}{1 + (j\omega\tau(\xi))^{1-\alpha}}\right) + \frac{\sigma_i(\xi)}{j\omega\epsilon_o}, \tag{2.7}$$

where the parameters are

$$\epsilon_\infty(\xi) = (0.99 \times 10^{-2}).\xi^2 + (0.47 \times 10^{-1}).\xi + 2.3, \tag{2.8}$$

$$\Delta\epsilon(\xi) = (0.93 \times 10^{-2}).\xi^2 - (0.21).\xi + 71.0, \tag{2.9}$$

$$\tau(\xi) = (0.12 \times 10^{-2}).\xi^2 + (0.23).\xi + 8.7, \tag{2.10}$$

$$\sigma_i(\xi) = (0.63 \times 10^{-2}).\xi^2 - (0.14).\xi + 2.0, \tag{2.11}$$

A two-pole Cole-Cole model was used in [115] to fit the dielectric property measurements of authentic blood samples with varying glucose 79 – 330 mg/dL. Twenty samples were drawn at 3 mL volume from 12 healthy and 8 diabetic persons (2 samples per subject). The samples were then measured in a 5-mL dish using the Agilent dielectric probe kit. The dielectric constant was observed to decrease for increasing BGL from 80 to 140 mg/dL. However, the measured results were not much reliable due to the associated noise caused by using small sample size of relatively lower thickness than the probe volume. The number of repeatable measurements were also not reported. An analytical method was used in [130] to extract the dielectric properties of phantoms replicating the lossy medium of human body. However, reduced sensitivity, increased bandwidth, and associated noise were direct results of the loss introduced in the developed phantoms.

The dielectric properties of blood mimicking phantoms of 0 – 216 mg/dL were characterized using an open-ended coaxial probe kit [64]. Each phantom was measured 20 times, and the median measurements were fitted using a single-pole Cole-Cole model where the fitting accuracy was assessed using Euclidean distance metric. The behaviour of the modelled permittivity was consistent with the previously reported results showing a decrease in ϵ_r' with the increased glucose concentrations.

Glucose-water solutions 0 – 16,000 mg/dL were characterized at 25°C using an in-house fabricated open-ended coaxial probe. The complex permittivity values were extracted from the measured reflection coefficients (S_{11}) using an artificial neural network, then fitted to a Debye model with glucose-dependent parameters formulated as second-order polynomial equations as given below [122]

$$\epsilon_\infty(\xi) = (-8.214 \times 10^{-8}).\xi^2 + (2.148 \times 10^{-3}).\xi + 8.722, \quad (2.12)$$

$$\epsilon_s(\xi) = (2.318 \times 10^{-9}).\xi^2 - (-2.793 \times 10^{-4}).\xi + 81.015, \quad (2.13)$$

$$\tau(\xi) = (-8.37 \times 10^{-9}).\xi^2 + (5.15 \times 10^{-4}).\xi + 8.776, \quad (2.14)$$

The permittivity parameters of binary glucose-water solutions of 100 mg/dL – 500 mg/dL concentrations (in steps of 100 mg/dL) were extracted in [78] using a manufactured open-ended coaxial probe connected to a VNA in the frequency range 1 – 8 GHz. In these measurements it was observed that, an increase in the glucose concentration would result in a decrease in the dielectric constant (real part) and an increase in the dielectric loss (imaginary part). The complex permittivity values were computed from the measured scattering parameters and fitted to the Debye model with the proposed parameters shown in Table. 2.2. In a similar research, a different set of Debye parameters were proposed by Hofmann *et al* in [69] [131] where the influence of increasing the glucose concentrations in aqueous solutions was investigated by measuring the complex permittivity of watery solutions of 50, 250, 1000, and 2000 mg/dL glucose concentrations using a commercial coaxial probe kit connected to VNA in a frequency range up to 40 GHz. The permittivity dependency in concentrations was modelled by fitting the measured data to a single-pole Debye model with the parameters of first-order polynomial shown in Table 2.2.

Table 2.2: Debye coefficients proposed by [78] and [129]

Debye Parameter	[78]	[131]
$\epsilon_\infty(\xi)$	$4.076 + (5.048 \times 10^{-5}).\xi$	$5.38 + (30 \times 10^{-3}).\xi$
$\epsilon_s(\xi)$	$80.769 - (0.439 \times 10^{-3}).\xi$	$80.68 - (0.207 \times 10^{-3}).\xi$
$\tau(\xi)$	$8.008 + (0.275 \times 10^{-3}).\xi$	$9.68 + (0.23 \times 10^{-3}).\xi$

2.3 Dielectric Properties of Glucose Solutions at High Frequencies

The literature is not well-established with measurements that address the EM behavior of glucose in liquid materials at high frequencies in contrast to the case at lower frequencies up to 10 GHz [132]. In fact, measurements in higher frequency bands are challenged by the strict tolerances in manufacturing the RF measuring tools that often require very high accuracy, and hence their costly deployment in large-scale. However, a few research studies have focused on extracting the permittivity measurements for liquid samples of relatively high glucose concentrations at higher frequency ranges. In [81] a *waveguide* transmission probe was clamped onto the ear of a live anesthetized rat in order to conceive the glucose-varying effect from the continuous readings on the VNA. The authors noted a correlation

between blood glucose concentrations and the absorption/reflection coefficients of the mm-wave transmitted in the Ka band (27 – 40 GHz) during the 0.5 mL intraperitoneal (IP) injection of glucose and insulin into the rat under experiment. Particularly, three trends of increased transmission, decreased transmission, and no change were observed following the glucose, insulin, and saline injections, respectively. The same authors tested their mm-wave system (Ka band waveguide probes) for detecting the D- and L-glucose variations [133] and on healthy human subjects where a 30 – 40 mins delay in measurements was observed [134]. The authors in [132] were able to demonstrate a clear linear correlation between the transmitted EM energy in the mm-wave band (50 – 75 GHz) and the glucose concentrations in watery and salty solutions. Two open-ended V-band waveguides (WR-15) connected to VNA were used to track the dielectric properties by measuring the reflection (S_{11}) and transmission (S_{21}) coefficients. The tested samples had different types of glucose concentrations in a clinically relevant range between 0.025 wt.% and 5 wt.% (0.25 – 50 mg/ml). Transmission data has shown better results compared to the reflection one especially in the 59 – 64 GHz and 69 – 73 GHz frequency ranges. However, the setup sounds bulky and tricky to interconnect.

The dielectric properties of glucose solutions varying from 0 mg/dL to 108,000 mg/dL in 18,000 mg/dL increments were measured in the 500 MHz – 67 GHz spectrum at 37°C using Agilent's open-ended coaxial probe [135]. A small decrease was observed in ϵ_r' with increased glucose levels at lower frequencies, nevertheless the ϵ_r' behaviour was quite contrary at higher frequencies. Additionally, the conductivity was observed to change in smaller units than ϵ_r'. However, the glucose increments of 18,000 mg/dL considered in this study were much higher than the practical BGL variations for diabetics. Different sensing techniques of both reflection and transmission modes were used in [69] to collect the permittivity measurements for aqueous glucose solutions in a frequency range up to 40 GHz for highly concentrated glucose from 1.5 – 5 mg/ml (0.15 wt.% up to 0.5 wt.%). The study in [136] considered the 50 – 75 GHz band for measuring the reflection coefficients using saline solutions of high concentrations 5 – 30 mg/ml (0.5 wt.% and 3 wt.%). A correlation between these concentrations and the reflected coefficients was not sufficiently strong even at the high glucose levels. Another study [137] over the 28 – 93 GHz frequency range used the mm-wave spectroscopy in reflection mode to detect sugar in watery solutions, blood imitators (physiological solution: 0.9% NaCl in water), and actual blood, while checking the sensitivity of their dielectric properties to glucose content at levels ranging from 5 – 50 mg/ml (0.5 to 5 wt.%). A recent study in [55] proposed a mm-wave antenna system that consists of a pair of 60 GHz microstrip patches of 1.5 mm × 1.5 mm placed across the interrogated blood sample. Measurements of the transmission coefficients on healthy male subjects were shown to be highly affected by changes in the permittivity along the signal path due to BGL variations.

2.4 Spectroscopy Dielectric Measurements using DAK-TL

Following the aforesaid efforts, we aimed at investigating which frequency band would have the most sensitivity to glucose changes in the hosting tissue while understanding the underlying dielectric behavior related to glucose at different frequencies as reflected by the corresponding spectroscopy measurements. For this purpose, the commercially-available dielectric assessment kit (DAK-TL) was utilized with the most updated software version 2.4.1.144 to measure the EM dielectric properties of water-based glucose-loaded samples of concentrations 70 – 120 mg/dL in four distinct frequency bands using two probes for low- and high-frequency bands with an overlapped bandwidth. Aqueous glucose solutions were utilized in these characterization experiments to approximate the behaviour of the actual blood at disparate glucose concentrations while ensuring the stability and repeatability of the dielectric measurements.

DAK-TL is a broadband measuring tool that is used to precisely measure the dielectric properties of thin material layers on the millimeter and sub-millimeter scale and of liquids available in small volumes (5 – 50 ml). It has a wideband operation over the frequency range from 200 MHz to 67 GHz. The system is featured with full automation and controlled software; the automated sample platform brings the material under test to the probe and measures the sample thickness with micrometer precision. The applied force can be precisely controlled to enable high measurement repeatability for soft samples such as leather or soft plastic. DAK-TL system could be used for a variety of applications including the evaluation of raw PCB materials or small biological samples (e.g., human skin or tumor tissue samples), analysis of dielectric materials used in electronic component (e.g., resonators, coils, and capacitors), characterization of dielectric substrates, antenna/lens materials, and small quantities of liquids (e.g., precious pharmaceutical samples).

The DAK testing fixture is based on the open-ended coaxial probe technique commonly used for non-destructive sensing where a probe flange is pressed against the sample (SUT) and the complex reflection coefficient S_{11} is measured with the VNA. The complex dielectric properties of the SUT are then calculated from this reflection coefficient, the probe dimensions (diameters, bead permittivity), and the sample thickness. The probes are constructed from open-ended sections of 50 Ω coaxial transmission cable, where contact with the dielectric material occurs at one cut end (Fig. 2.1). The DAK base system accommodates the automated sample platform with built-in controlling electronics for automatic thickness measurement. The sample is placed on the sample platform, which brings it to the probe for measurement of the sample thickness with micrometer precision. To ensure reproducible conditions for testing of dielectric materials, the base system is also equipped with a force sensor where up to 1000 N can be specified when moving the sample platform upward. The base system is connected to a computer machine (or PC) via a Universal Serial Bus (USB) and is fully automated and software controlled. The base system is designed for use with three DAK-TL probes supporting different frequency bands.

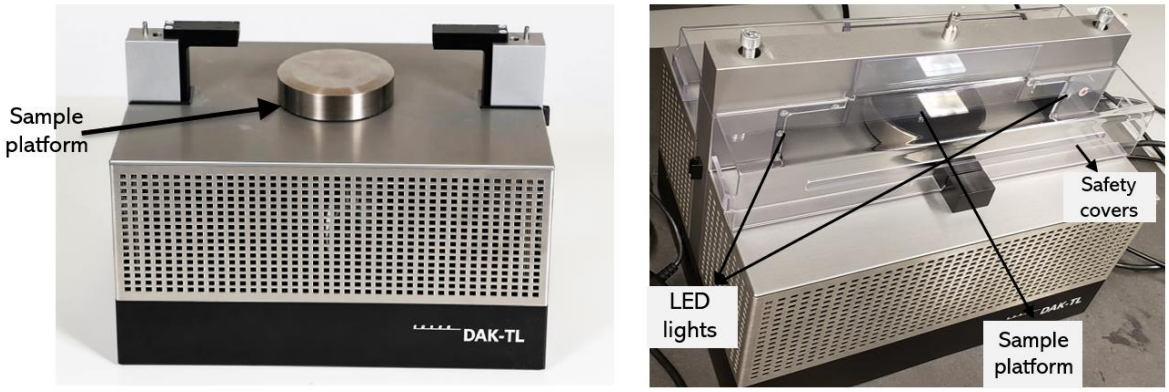

Figure 2.1: Different parts of the DAK-TL system.

DAK-TL uses a precise and fast numerical algorithm that can solve the improper integrals of complex functions and the equation inverse. This key algorithm is based on the equations formulated in [70] by Baker-Jarvis *et al*, and it is run simultaneously while acquiring the S-parameters in order to calculate and plot the dielectric measurements in real time during the continuous sweep process. The material under test by the DAK-TL should be homogeneous, isotropic, and large enough for the sample boundaries to not contribute to the reflected signal (i.e., assumed to extend to infinity in the radial direction). Despite being non-destructive, such techniques have some limitations in predicting the accurate value of the permittivity if there is an air gap at the interface between the probe and SUT. This is due to the large error possibly caused by any discontinuity in the normal component of the electric-field (field at the probe flange has two components E_z and E_ρ). Therefore, it is necessary to secure a good contact between the probe and the liquid sample in order to achieve stable accurate dielectric measurements.

When using the DAK-TL, the probe is connected to the VNA using a coaxial cable for measuring the complex reflection coefficient (S_{11}) at the probe end as displayed on the Smith chart sub-window of the interface. The S_{11} is calibrated to the reference plane of the probe flange (i.e., the interface of the probe with the MUT), and the dielectric parameters are calculated thereafter. The embedded Smith chart graphically represents the measured S_{11} as a vector $\Gamma = (\bar{Z} - 1)/(\bar{Z} + 1)$ where $\bar{Z} = Z_L/Z_o$ is the normalized complex load impedance and Z_o is the 50 Ω line impedance. The normalized impedance is represented as $\bar{Z} = \bar{R} + j\bar{X}$, where $\bar{R} = R/Z_o$ is the normalized resistance, and $\bar{X} = X/Z_o$ is the normalized reactance. Accordingly, on the Smith chart, lines of constant $\bar{R}$ are represented by circles on a scale from 0 to ∞ as displayed on the horizontal line through the centre of the chart. Lines of constant $\bar{X}$ are represented as circular arcs on the top half of the chart for $\bar{X} > 0$ (inductive reactance) or on the bottom half of the chart for $\bar{X} < 0$ (capacitive reactance). The reactance scale is shown on the outermost circle of the chart. Dielectric materials are of capacitance reactance; therefore, their associated dielectric measurements are shown in the bottom half of the Smith chart. The reflection coefficient (Γ) magnitude varies from 0 (i.e., no reflection) to 1 (i.e., full reflection). Hence, according to the design of the Smith chart, $\Gamma = 0$ is represented at the centre of Smith chart ($\bar{R} = 1, \bar{X} = 0$), $\Gamma =$

-1 is the short circuit appears at the leftmost point of the circle ($\bar{R} = 0, \bar{X} = 0$), while the ideal open circuit has a value of $\Gamma = 1$ located at the rightmost point ($\bar{R} = \infty, \bar{X} = 0$).

2.4.1 Samples Preparation

The samples of aqueous glucose solutions were first prepared precisely with disparate glucose content at the following concentrations: 0.7, 0.8, 0.9, 1.0, 1.1, and 1.2 mg/ml, using a micropipette device in the laboratory. The dilution equation $C_1V_1 = C_2V_2$ was used to calculate the volume V_1 added from the standard glucose solution of C_1 = 10 mg/ml, to achieve the desired concentrations for the prepared samples of volume V_2 = 20 ml. The glucose concentrations of these samples were confirmed by testing a hemoglobin-mixed (or fake blood) version of these samples on a reference glucometer device. First, a 1:1 ratio was used to prepare these mixed solutions, thereby the glucometer reading should be half of the original concentrations. However, the glucometer readings were much higher than expected as a result of testing concentrations at the very low end of the dynamic range of the glucometer. Alternatively, the relative amount of blood glucose in the test solution was increased using a 3:2 glucose solution to fake blood resulting into right expectations for the values of the measured concentrations as listed in Table. 2.3 for all the concentration readings of the prepared glucose-water samples using the reference glucometer device.

Table 2.3: Glucometer readings for the prepared glucose samples.

Glucose samples (mg/ml)	Glucometer reading (mg/ml)	
	(1:1 ratio)	(3:2 ratio)
0.7	0.93	0.83
0.8	1.14	0.95
0.9	1.34	1.03
1.0	1.6	1.06
1.1	1.84	1.08
1.2	1.86	1.30

2.4.2 Experimental Setup of DAK-TL Measurements

The basic system setup that interconnects the DAK-TL, VNA and PC is shown in Fig. 2.2. After matching the probe beam to the physical setup of the frequency of interest, the DAK-TL base system is connected to one port of the VNA via coaxial cable, while connected to the PC via USB to have the testing fixture fully automated and software controlled. The VNA is connected to the computer using LAN/Ethernet cable. DAK-TL is switched on and the appropriate settings are chosen in the setup window by selecting the VNA address, probe beam, range of frequencies, resolution and the standard liquid used for calibration at the convenient room temperature. Particularly, the VNA intermediate frequency (IF) Bandwidth is set to 100 Hz to achieve measurements at a convenient speed with reduced noise, VNA output source power (O/P) = 0 dBm for all probes DAK 3.5/1.2E used in the glucose measurements, and the averaging reset is tuned to 3 VNA traces to reduce the noise and errors in the

reported results. However, for a warmed up VNA that exhibits stable operation, trace averaging would not be a necessary adjustment. Specifications for both probe beams used in the glucose concentration characterization are detailed in Table 2.4.

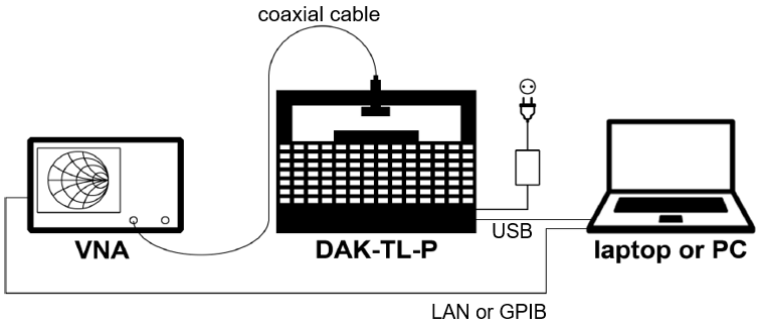

Figure 2.2: Schematic diagram of the DAK-TL connections in a full setup.

Table 2.4: Specifications of the DAK-TL probe beams

Item	**Specification**	
	DAK 3.5-TL probe beam	**DAK 3.5-TL probe beam**
Frequency Range	200 MHz – 20 GHz	5 GHz – 67 GHz
Dielectric bead material	Eccostock ($\varepsilon' = 2.54$)	EPO-TEK OG142 ($\varepsilon' = 3.08$)
Diameter of dielectric bead	3.5 mm	1.2 mm
Diameter of flange	48 mm	48 mm
Impedance	50	50 Ω
Operating Temperature	0 – 50 °C	0 – 50 °C
Beam Dimension	40 × 30 × 350 mm	40 × 30 × 350 mm

2.4.3 Glucose Measurements Using DAK-TL

To achieve precise reproducible measurements, the DAK-TL setup (shown in Fig. 2.3) is calibrated by means of a port extension using the standard Open-Short-Load method to normalize the magnitude and phase changes of the probe flange and coaxial cable so that the reflection coefficient measured by the VNA is normalized to the reference plane at the interface of the probe with the MUT. The calibration routine is explained in detail in Appendix I. Distilled water is used as a reference liquid for calibration at the room temperature of about 20°C. The dielectric measurements for the glucose samples 0.7, 0.8, 0.9, 1.0, 1.1, and 1.2 mg/ml were then performed on four distinct frequency intervals: 200 MHz – 10 GHz using the DAK 3.5-TL probe beam at 50 MHz resolution (197 points) while the DAK 1.2E-TL was used for measurements at the other three intervals 10 – 20 GHz (200 MHz resolution, 51 points), 20 – 50 GHz (200 MHz resolution, 151 points), and 50 – 67 GHz (200 MHz resolution, 86 points). Before starting the measurements in each interval, a careful calibration was performed following the steps detailed in the previous subsection and repeated multiple times until a good match was achieved

between the measured and target data for Saline 0.1M at 20°C. The large metallic petri-dish of 12 mL capacity shown in Fig. 2.3 was used to hold the glucose sample for measurements.

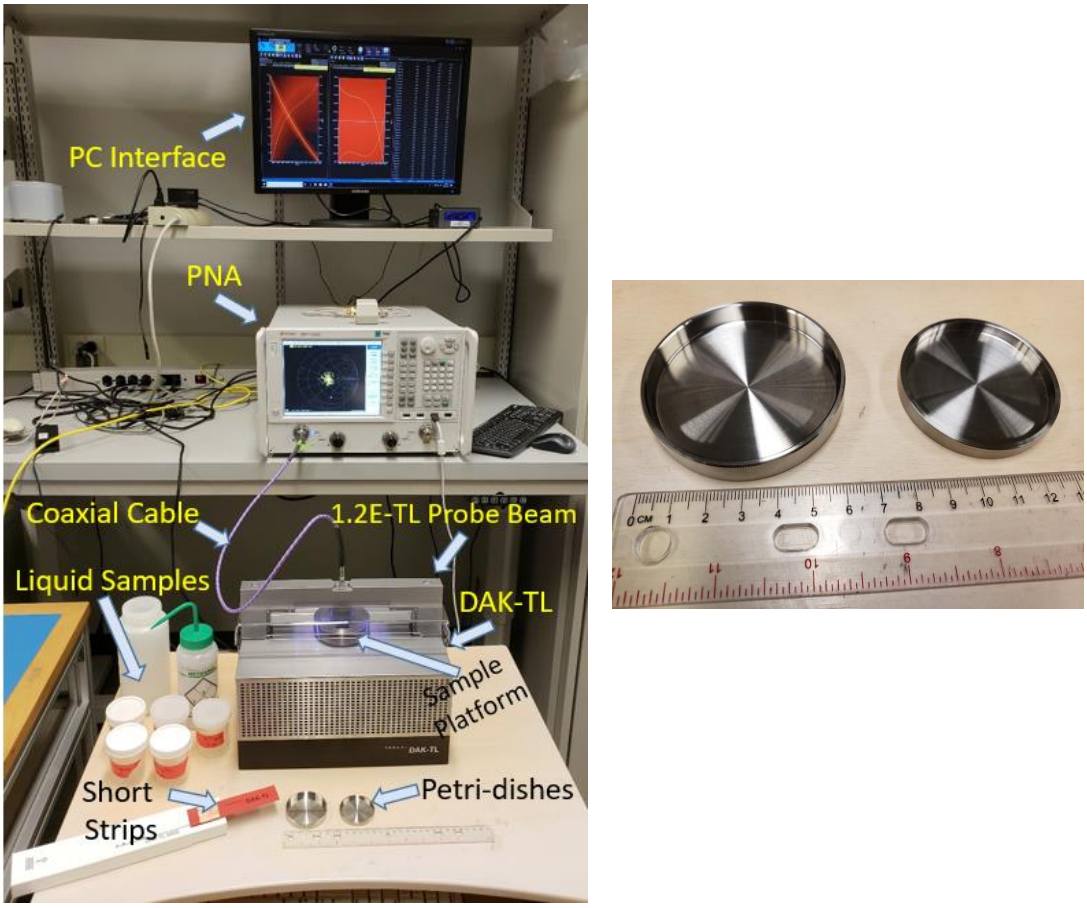

Figure 2.3: Experimental setup of the DAK-TL system for dielectric measurements of the aqueous glucose solutions, and the petri dishes of different sizes used in the experiments.

First, we investigated the DAK system accuracy in measurements at different volumes of the tested samples. Particularly, we measured the dielectric properties of the standard distilled water in the spectrums 200 MHz – 10 GHz and 10 – 20 GHz at three different volumes 2, 5, and 10 mL while considering the target data as a reference for comparison. Stable and repeatable data were collected for each water sample of a certain volume; however, small differences in properties values were observed when testing the same sample at different volumes. Experiments have shown that volumes of 10 mL and 5 mL were almost very close in measurements to the exact data while the 2 mL sample was slightly off due to its small volume insufficient to mitigate the reflections at the boundaries. The same investigative experiment was repeated for a glucose-water solution of 0.7 mg/ml concentration to test the volume effect in DAK measurements when the glucose was added. This time the accuracy of the EM measurements was compared for two volumes of the tested sample (5 mL and 10 mL) while checking the influence of the exact touching point between the sensing probe and the liquid under test. The resulting relative permittivity, conductivity, and loss tangent were all compared for four different

cases of volume and distance settings. Considering that the sensing probe can go to different distances from 0 to 10 mm (at zero distance the probe becomes in touch with the sample platform while at 10 mm distance the probe is fully off), better results would be achieved if a sample of volume 10 mL for example is tested at a probe distant of 3 – 5 mm that results into a sufficient contact compared to the 2 mm case where the probe immerses deeper inside the liquid. This observation was also confirmed for a sample of volume 5 mL at two different touching points 1 and 0.5 mm, where 1 mm was shown to be better.

The same experiment was repeated for different volumes (1, 2, 5, and 10 mL) of distilled water at higher frequency bands (i.e., 20 – 50 GHz, and 50 – 67 GHz). Results have confirmed our finding, more volume of a tested sample in the petri-dish is desirable to achieve more accurate and stable measurements. Besides, more deviations in the measured dielectric properties were experienced when testing lower volumes (e.g., 1 and 2 mL) compared to the deviation seen at lower frequencies. DAK results have shown that testing samples of smaller volumes (e.g., 5 and 2 mL) at higher mm-wave frequencies is challenging (i.e., needs to be repeated multiple times) and results into less accurate measurements compared to those obtained using larger volumes (e.g., 10 mL). Additionally, low-volume measurements were not fully stable with some ripples observed at some higher frequencies (e.g., 59 – 64 GHz) as caused by the volumetric resonances due to the limited sample volume.

Next, the dielectric measurements for the different glucose samples 0.7 – 1.2 mg/ml were kicked off. In each experiment a 10 mL volume from each glucose concentration was placed in the petri-dish and tested in the targeted frequency band for five times to confirm the repeatability. MATLAB was used to compute the average of the extracted dielectric properties (ϵ_r' and $tan\delta$) in each spectrum (200 MHz – 10 GHz), (10 – 20 GHz), (20 – 50 GHz), and (50 – 67 GHz) as plotted in Fig. 2.4(a) – 2.4(h), respectively.

In the low-band up to 20 GHz, for all glucose concentrations, both parameters change with the frequency almost linearly with decreasing dielectric constant and increasing loss tangent with the increased frequency as shown in Fig. 2.4(a) – 2.4(d). However, the change trends of both ϵ_r' and $tan\delta$ with frequency is not influenced by the glucose concentration. Glucose samples are more dispersive towards lower frequencies (200 MHz – 2 GHz). Additionally, a slight decrease in the dielectric constant and, conversely, a tenuous increase in the loss tangent were observed with the increased glucose concentration up to 10 GHz. Beyond 10 GHz, a decreased loss tangent is observed with the increasing glucose levels as depicted in Fig. 2.4(d). The trend of both characteristic parameters with varying glucose levels is sometimes jumbled at certain frequencies possibly due to a residual calibration issue when measuring the glucose properties that change in the third decimal digit. However, the mixed patterns were very much minimized after recalibrating the DAK system multiple times.

As for the high-band dielectric measurements of the prepared 0.7 – 1.2 mg/ml aqueous glucose samples, the extracted dielectric permittivity and loss tangents have shown some variations that are not entirely linear as depicted in Fig. 2.4(e) – 2.4(h). Additionally, it is demonstrated that our concentrations

of interest are better distinguishable in the higher mm-wave region 50 – 67 GHz as depicted in Fig. 2.4(g) – 2.4(h). It is observed that with an increased frequency in this interval, ϵ_r' of the glucose samples gradually decreases (Fig. 2.4(g)) and the loss tangent increases in a nearly exponential pattern before starting to gradually decay after 60 GHz (Fig. 2.4(h)). With an increased glucose content in water, the dielectric permittivity and loss tangent both decrease in larger resolution compared to those observed at lower bands. The collected dielectric measurements are generally following the Debye pattern similar to that of the pure distilled water (decreasing real part of the permittivity due to the dipole moment of water molecules) but with minor shifts due to the dissolved glucose content that would increase the inertia of the binary solution and decrease the sample viscosity in consequence. Therefore, the bonded glucose molecules become harder to rotate leading to lower polarization and lower energy stored in the solution. The dipolar/orientational polarization dominates mostly in the low frequencies than in the higher bands. Glucose characterization was performed in a controlled temperature environment of ~22±1°C, yet both ϵ_r' and *tanδ* are expected to decrease proportionally with increasing temperature.

To confirm the previous results, measurements for the different glucose concentrations were repeated using smaller sample sizes (2, 3, 4, and 5 mL). Volumes of 5 and 4 mL were tested using the large petri-dish, while the smaller fabricated stainless dish was used to hold the 3- and 2-mL volumes. Results have shown that, glucose varying samples of volume 5 and 4 mL can still be differentiated with a preserved trend similar to that revealed in the 10 mL testing case. Nevertheless, this trend was almost missing when the glucose samples were tested at lower volumes of 3 and 2 mL where the measurements for the 1.0, 1.1 and 1.2 mg/ml glucose concentrations were troubled with no plain trend observed. To confirm the pattern of both ϵ_r' and *tanδ* with respect to varying glucose, aqueous solutions of very high concentrations 400 – 800 mg/ml (40 wt.% and 80 wt.%) were measured across the frequencies 30 – 67 GHz and plotted against the pure water of zero concentration in Fig. 2.5(a) and 2.5(b), respectively. The dielectric properties become less dispersive when the glucose dominates more content in the aqueous solutions. Very high glucose levels start decreasing the max loss notably at higher frequencies beyond 30 GHz as depicted in Fig. 2.5(b) where observed a linearly decreased loss with the increasing frequency.

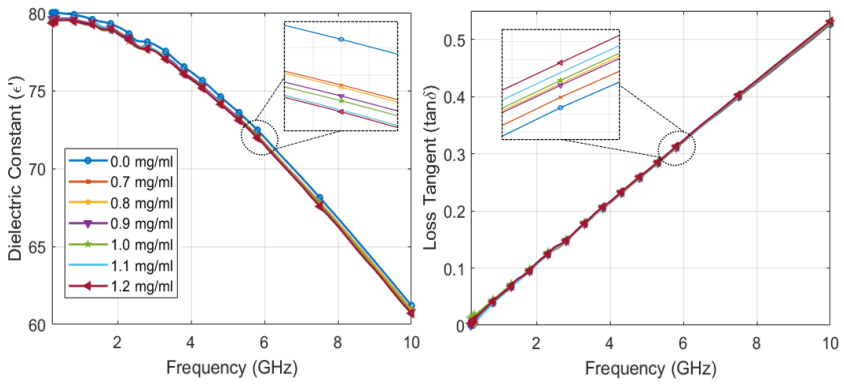

(a) (b)

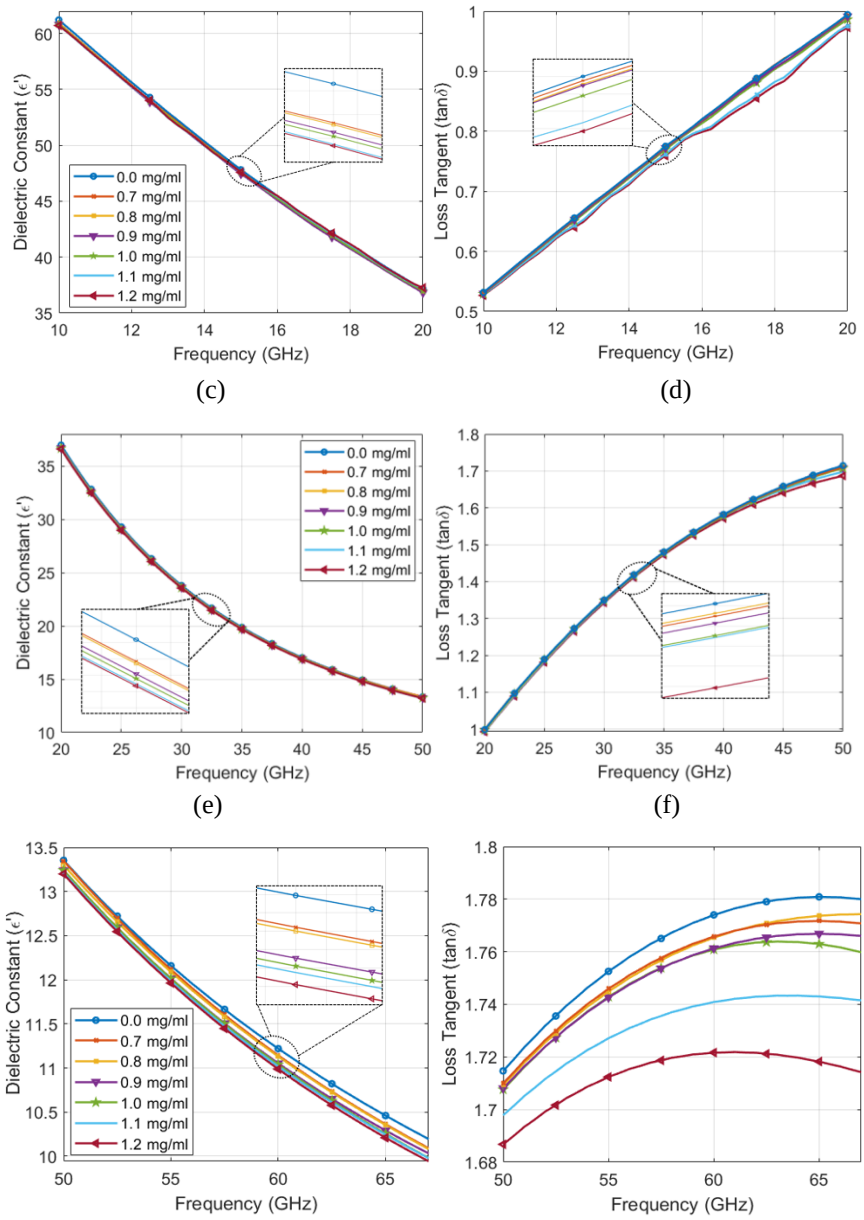

Figure 2.4: Dielectric measurements (dielectric constant and loss tangent) of glucose-loaded solutions at different frequency bands: (a) and (b) 200 MHz - 10 GHz, (c) and (d) 10 - 20 GHz, (e) and (f) 20 - 50 GHz, (g) and (h) 50 - 67 GHz.

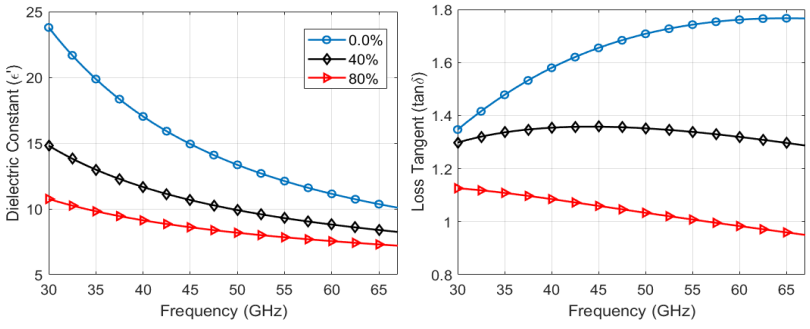

Figure 2.5: Dielectric properties of large glucose varying solutions (a) dielectric constant, and (b) loss tangent

2.4.4 Results Analysis and Discussion

In the DAK-TL 200 MHz – 67 GHz spectroscopy for the glucose-loaded solutions, it is observed that the low-band dielectric properties change in lower resolution from one glucose level to another. However, the loss tangent is of smaller values that allow for higher penetration depths inside the biological tissues. On the other hand, the mm-waves range has shown to be promising for glucose monitoring where higher sensitivity to the dielectric constant and loss tangents of glucose samples can be acquired because of the stronger interaction between the glucose molecules and EM waves in this spectrum. Particularly, with an increased glucose concentration, both dielectric constant and loss properties change in a decreasing pattern of larger resolutions. However, the loss becomes relatively higher at this spectrum especially for smaller concentrations related to the Type-2 diabetes. This outcome conforms with the results reported in [69] [136] where the measurements were performed using a simple scheme that indicated a decreasing trend among the dielectric constants extracted from the measured reflection coefficient at the minimum resonant frequency for the reflected mm-wave signal. However, the trend of the glucose-varying properties contradicts the conclusions reported in [132] [138] [139] that show an increased dielectric constant and decreased loss tangent with increasing levels of glucose.

By comparing the DAK-TL dielectric measurements at low frequency bands to those in the literature, it is found that some researchers were able to observe trends among glucose concentrations in such low frequencies but for higher glucose concentrations than those considered in this research (i.e., relevant to diabetes). For instance, the authors in [78] extracted the complex permittivity measurements for binary glucose-water solutions of concentrations in the range 1.0 – 5.0 mg/ml in the frequency band 1 – 8 GHz. Despite the non-linearity depicted in some variations of the collected data, a trend was observed at some frequencies posing a decrease in the dielectric constant and increase in the loss factor for an increased glucose level. The same trend could be observed when applying the Cole-Cole model parameters proposed in [49] for the glucose-dependent EM properties of blood plasma to the glucose-water of 1 – 5 mg/ml concentrations. However, the changes depicted in the real and imaginary units of the permittivity were quite small in terms of ± 0.02 unit between various glucose concentrations. Interestingly, the Debye coefficients proposed in [69], [131] suggested a different varying trend in the dielectric parameters of such concentrations. Particularly, an increased dielectric constant and decreased loss factor over the frequency spectrum were recorded for increasing the glucose levels.

When compared against the extracted dielectric properties in lower-frequency bands, it is observed that the difference in dielectric constant and loss tangent between various glucose concentrations is increasing beyond 50 GHz. This would imply a difficulty in detecting the tiny differences between the dielectric properties of the respective glucose samples in the lower microwave frequency ranges. Seemingly, 50 – 67 GHz is a promising detection region where an appreciable

complex permittivity contrast between small glucose concentrations is evidenced. A dispersive relaxation model could be formulated by fitting the collected dielectric measurements in this mm-wave range using the first order (~single-pole) Debye relaxation model. To do so, the real $\epsilon_r{}'$ and imaginary $\epsilon_r{}''$ parts of the measured permittivity for each glucose sample of a definite concentration are fitted to the theoretical Debye model defined by Eq. (2.5) and (2.6), respectively. The mm-wave range is also favored for other reasons: its reduced interference, enhanced security, non-ionizing nature, good penetration depths inside the bio-tissues, and the good resolution feature for their relatively small wavelength compared to EM radiations at lower microwave frequencies. However, measurements in such high frequencies are very challenging due to the strict tolerances in manufacturing their appropriate measuring devices that often require very high accuracy. In addition, the literature is not well-established with measurements that address the EM behavior of glucose-containing liquids in such higher frequencies in contrast to lower frequency range up to 10 GHz [132].

The choice of operating frequency for glucose sensing depends not only on the sensitivity to the respective dielectric properties, but also on the depth of penetration *D* inside the underlying tissue. In fact, any electromagnetic wave transmitted into a lossy medium will be attenuated after a certain penetration depth where the field intensity is 1/e of its source value. This depth is dependent on the SUT properties and decreases with increasing the frequency as follows [140]

$$D = \frac{\lambda_o}{2\pi\sqrt{2\epsilon_r'}} \frac{1}{\sqrt{1+\left(\frac{\epsilon_r''}{\epsilon_r'}\right)^2}-1} \tag{2.15}$$

where λ_o, ϵ_r', and ϵ_r'' are the free-space wavelength, real and imaginary parts of the complex permittivity of the underlying tissue, respectively. From this expression, $D \propto 1/f$ since $f \propto 1/\lambda_o$, and therefore EM waves are easily capable of penetrating the skin, fat, and muscle layers at frequencies lower than 0.1 GHz. However, at frequencies higher than 20 GHz, the EM wave could barely penetrate the skin, fat, and muscle layers [105]. Because of the high loss tangent of water (even deionized water) in the mm-wave band on account of the Debye relaxation of the water molecules, the mm-wave penetration into the biological tissues is likely to be less than one to two millimeters (i.e., predominantly in the skin) [141]. Maximum power density occurs at the skin, and the transmitted power decreases nearly exponentially in the skin as a function of depth. Above 30 GHz, the absorbed power is superficial with a penetration depth of around 1 mm or less. While the penetration depth at 60 GHz is around 0.5 mm, which is limited to the superficial layers of the human skin where most of the power is absorbed [142]. Under normal incidence, around 40% of the incident power is reflected by the skin. For normally incident plane wave at the air/skin interface the penetration depths are shown in Table 2.7 for some mm-wave frequencies [141].

Table 2.5: Penetration depth at mm-wave frequencies

Frequency (GHz)	30	60	74	84
Penetration depth (mm)	0.78	0.48	0.42	0.39

As part of this study, we also probed into the DAK-TL accuracy in measurements at different volumes of the tested liquid samples to conclude the lowest volume of liquid that could be used for acquiring stable and precise measurements. In particular, the dielectric properties of standard distilled water were measured in four different frequency bands at different volumes of 10, 5, 3, 2 and 1 mL using two petri-dishes of different capacities. By comparing the collected measurements at each volume against the reference target data provided in the DAK-TL database, measurements on the 10 mL volume were observed to be relatively close to the exact data of distilled water while other volumes were slightly off. In that event, all the dielectric measurements of glucose aqueous solutions were collected using the DAK-TL system at volume V = 10 mL to desire stable and precise dielectric parameters. The results have also revealed the challenge for testing samples of smaller volumes at higher frequency bands that probably needs to be repeated multiple times. Besides, it would result into less accurate measurements with few ripples appeared towards higher frequencies (59 – 66 GHz) due to the volumetric resonances. Similarly, the influence of the exact touching point between the sensing probe and the tested sample was investigated for different testing volumes.

More in-depth dielectric measurements were performed using DAK-TL testing fixture to address how ABO-Rh blood types and other medical conditions may impact the blood EM properties at different frequency bands. Both synthetic and authentic bloods of different types and medications were characterized across the microwave spectrum 500 MHz to 67 GHz using the DAK-TL coaxial probes. Measured results have indicated an appreciable contrast in the dielectric properties of various blood types across the spectrum especially at the mm-wave range 50 – 67 GHz where the differences are quite visible. A similar behaviour was observed for blood samples exposed to medications. Such variances in the blood dielectric properties would advocate the suggestion of calibrating any proposed microwave blood glucose monitors on individual basis to respect the physiological differences among the diabetic patients. Detailed experimentation and analysis about this study can be found in Appendix II.

Chapter 3. Glucose Levels Sensing using Complementary Split Ring Resonators in the Centimeter-Wave Band

3.1 Introduction

Resonators are widely used as precise instruments for determining the properties of materials such as complex permittivity and permeability in an electromagnetic environment at microwave frequencies. Among the different resonance-based microwave devices, metamaterial-inspired resonators of small electrical size (i.e., larger dimension is very small compared to the excitation wavelength) such as split-ring resonator (SRR) and its complementary (CSRR) are more favorable in the sensing and characterization applications. This is because such resonators combine the accuracy of the classic large resonators, are highly sensitive and can be miniaturized, simply fabricated, and easily integrated into a system [143], [56], [58]. They have been utilized for many applications in dielectric characterization [93], bimolecular sensing [95], [144], bioassay sensing [145], and microfluidic sensing [146], [147]. The concept of the SRR resonant structures was first introduced by J. B. Pendry *et al*. in 1999; for constructing materials with properties not naturally accessible (i.e., negative refractive index) [148].

In this chapter, the resonant CSRR-based microwave sensing approach is adopted for developing viable planar microwave biosensors for glucose monitoring and other applications in biomolecules detection and liquid identification. This choice for CSRR is driven by its suitability for sensing the complex permittivity of SUT using low power consumption with a simple, flexible design and affordable fabrication process. The sensing approach is fully compliant to the green form of technology that features non-invasive measurements in non-destructive fashion using non-ionizing EM radiation that penetrates inside the skin. Therefore, no hazards or risks to the human health when developed as wearables for continuous blood glucose monitoring. More importantly, compared to the SRRs where the electric field is confined in a small dielectric split, CSRRs are more responsive and sensitive to the permittivity changes for localizing highly concentrated electric fields in a relatively larger sensing region of the resonator, thus oblige more interactions with the SUT. Consequently, this will boost for an improved sensitivity and imaging capability necessary to characterize lossy liquid samples at microwave frequencies. The electrical size of the sensor is relatively small compared to the guided wavelength ($< \lambda_g/10$), which allows for a compact miniaturized realization and integration with other microwave components in embedded sensors and systems-on-chip. Lastly, the unlimited reusability and good accuracy throughout the sensor lifespan. This would eliminate the need for any replacement as in the case of the implanted sensors, patches or devices that use chemical reactions or fluid transfer through the skin.

The aforesaid features would facilitate the development of a portable, low-cost, miniaturized, non-invasive sensor for monitoring blood glucose levels in real-time. Therefore, in this chapter, we propose different CSRR-based sensors operating in the low centimeter-wave band 1 – 6 GHz that favors

sufficient penetration depth (~ 0.4 – 3 cm) and interaction of the EM waves with the epidermis/dermis tissues of human body [105], [65], while allowing for sizing smaller sensing structure. The developed sensors are inspired from the basic geometry of split-rings resonators with localized elements where different configurations of multiple coupled CSRRs are engraved on a copper ground plane of a dielectric substrate. Different layouts of the CSRR-based sensors were designed, simulated using the finite element simulator (ANSYS HFSS), and fabricated using the low-cost laser-incorporated PCB technology. The sensitivity performance of the fabricated prototypes for detecting the glucose concentrations of interest was practically analyzed and demonstrated by the in-lab experimental measurements using convenient VNA setups.

3.2 Perturbation Sensing Approach for Planar Microwave Resonators

Generally, the structure of SRRs is composed of one or more concentric annular slits of metal nested inside each other and etched on a dielectric substrate. The loop of each ring ends in a dielectric slot that is etched on the opposite sides for the respective rings as depicted in Fig. 3.1(a). Contrariwise, CSRRs are based on the "Babinet's principle" where consist of one or more dielectric slits in the form of concentric interrupted rings nested within each other and engraved in the plane of copper mass. In other words, the whole conductor (the rings) and the dielectric part (slots) of the SRR are respectively replaced by dielectric slits and metal slots in the case of the CSRR. That would be simply created by engraving the concentric rings inside a conductive surface as illustrated in Fig. 3.1(a).

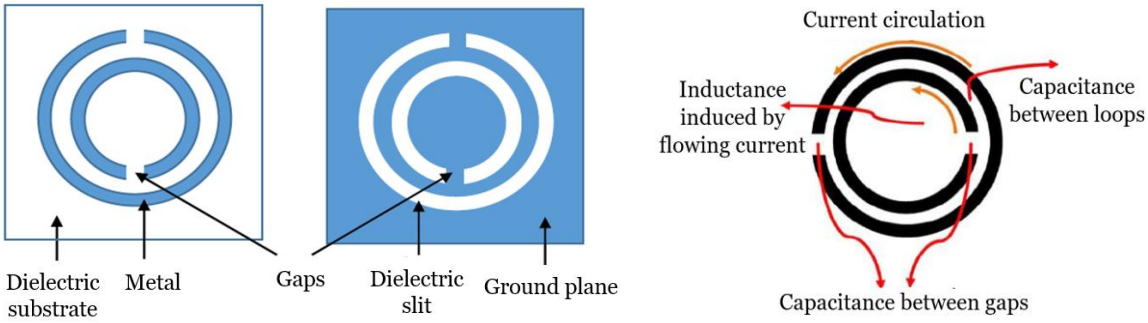

Figure 3.1: (a) Comparison between SRR and CSRR structures, (b) illustration of the electromagnetic behavior of the CSRR resonator.

SRRs and CSRRs both behave like a resonant magnetic and electric dipole, respectively, and hence they could be modelled as an *RLC* resonant circuit when a current circulates inside the patterned conductive/dielectric loops. Particularly, the winding of the rings acts as inductance *L*, the gaps and spacings of the rings create a parallel capacitance *C*, and the conductive and dielectric losses are modelled by a resistance *R*. Therefore, such structures resonate at specific frequency when both oscillating electric and magnetic energies stored in the inductances and capacitances are balanced. The stored electric and/or magnetic energy interact with the surrounding medium, and therefore, its permittivity and permeability can be related to the created effective capacitance and inductance of the resonant structures, respectively. In fact, CSRRs are found to be more responsive to the permittivity

changes as it is easy for the SUT to interact with the electric field widely spread in the sensing area of the resonator while having the magnetic field straitened between the slit traces. This tendency for the fields is inversed in the case of SRRs; and therefore, they are better reacting for variations in permeability of the surrounding medium [149].

Following the last point, the sensing method herein is based on the resistance and capacitive perturbation of the resonator (i.e., disturbing the field distribution) and thereby the modification of one or all of its intrinsic resonance attributes in the presence of the sample to be characterized, generally called the "superstrate", which is the glucose tissue in our case. This superstrate is placed on the surface of the resonator in a region where the electric field is highly concentrated to achieve the most interaction between the coupled electric field and the tested tissue at the operating frequency. Figure 3.2 illustrates the resulting electric field distributions on top of the single-pole CSRR when loaded with samples of different dielectric constants and loss tangent. Particularly, Fig. 3.2(a) depicts the electric field distribution when no SUT is introduced onto the sensor, while Fig. 3.2(b), 3.2(c), and 3.2(d) represent the field distributions for loading the sensor with SUT 1 (ϵ'= 10, $tan\delta$ = 0.2), SUT 2 (ϵ'= 20, $tan\delta$ = 0.2), and SUT 3 (ϵ'= 20, $tan\delta$ = 1), respectively. The resulting changes in resonance profile are considered as a signature of the SUT's dielectric properties that could be indirectly calculated and correlated to the corresponding glucose level through careful analysis of the modified resonance behavior [78], [150], [151]. For instance, based on the experimental observations of the transmission response (insertion loss) of the resonator before and after loading with a sample, shifts in resonance frequencies are found dependent on the effective dielectric constant of the loaded sample, while changes in resonance depth and/or width (broadening or narrowing) are basically governed by its dielectric loss [77].

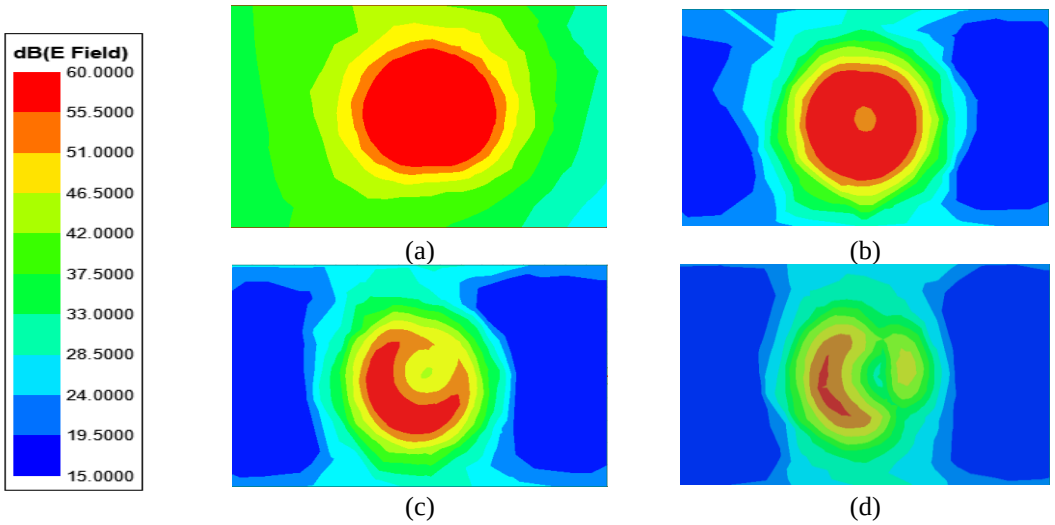

Figure 3.2: Electric field distribution on the surface of SP-CSRR, (a) unloaded, (b) SUT 1 (ϵ'= 10, $tan\delta$ = 0.2), (c) SUT 2 (ϵ'= 20, $tan\delta$ = 0.2), and (d) SUT 3 (ϵ'= 20, $tan\delta$ = 1)

The principle of resonance method can be illustrated by measuring the frequency difference (Δf) between the observed resonance peaks prior-loading (f_o) and post-loading (f_s) as well as their expansion or *Q*-

factor - related to the dielectric losses of the superstrate - from the insertion loss S_{21} experimental measurements. The relative displacement of each resonance is then given by [76]

$$\frac{\Delta f}{f_o} = \frac{f_s - f_o}{f_o} = 1 - \frac{\sqrt{\epsilon_e}}{\sqrt{\epsilon_{se}}}, \tag{3.1}$$

where ϵ_e and ϵ_{se} are the effective dielectric constants of the resonator when unloaded and loaded with a superstrate, respectively. From this relation, the resonance frequency of the loaded resonator f_s can be related to that of the unloaded state through the following relation

$$f_s = f_o \frac{\sqrt{\epsilon_e}}{\sqrt{\epsilon_{se}}}, \tag{3.2}$$

which clearly states the dependency of the shifted resonance f_s on the effective dielectric constant of the loaded sample but not its dielectric loss.

3.3 Inter-Resonator Coupling Approach for Improved Sensitivity

Significant research has investigated the SRR devices, the study in [150] developed a planar sensor based on microwave ring resonator operating at 1 GHz to characterize the biological tissues (e.g., meat, beef, chicken, etc.) and liquids (e.g., distilled water, ethanol, methanol, etc.) of high complex permittivity. Two different substrate materials (FR4 and RT-Duroid 5880) were used to compare the performance of the sensor in the frequency range 1 – 10 GHz. Another microstrip ring resonator operating at 1 GHz fundamental frequency [151] was developed with a winding conductor loop etched on the top surface of a dielectric substrate (Rogers RO4003C) and fed via the coplanar waveguide technology (CPW) on the ground plane to enhance its level of sensitivity. The sensor was used to characterize ex-vivo animal biological tissues of high dielectric permittivity and losses as extracted by optimization using the CST software. The authors in [152] suggested an SRR-based glucose sensing technique that fundamentally uses the changes in S-parameter magnitudes. Their system however requires large quantity of the tested specimen.

Two circular-shaped SRRs were integrated in [60], one resonator was used for sensing the glucose sample and the other was set as a reference to revoke the temperature effects. Another metamaterial resonator operating at 3 – 5 GHz was proposed in [61] for detecting the 68 – 150 mg/dL concentrations in small droplets of human serums. A closed-loop SRR operating in 2 – 5 GHz was recently proposed in [62] to detect 50 – 400 mg/dL aqueous glucose concentrations on the $|S_{11}|$ reflection response at a sensitivity of about 82 MHz/(mg/ml). Three versions of an open-loop microstrip resonator operating between 2 – 7 GHz were analyzed in [63] for testing small volumes 5 – 25 µL of highly concentrated glucose aqueous solutions 1250 – 10000 mg/dL inside a dielectric liquid holder pasted onto their gaps. The *Q*-factor and maximum $|S_{21}|$ magnitudes were used as primary sensing parameters. However, reported measurements have shown very limited sensitivity inadequate for practical blood glucose monitoring in diabetes.

The CSRRs have also been considered in many studies. A rectangular-shaped CSRR operating in the frequency range 0.8 – 1.3 GHz was proposed in [149] as a near-field sensor to characterize the solid materials of single layer with low-loss (e.g., air, Teflon, Rogers RO3003, etc.) by noticing the shift in the minimum transmission frequency. A similar study in [66] proposed a planar square-shaped CSRR operating in the frequency band 1.8 – 2.8 GHz for the purpose of measuring the dielectric constant and loss tangents of materials. This is done by first observing the transmission response, both the absolute magnitude and resonance frequency, of the CSRR under loading condition, then the sample properties were extracted using the equivalent *RLC* circuit model. The functionality of the proposed sensor was tested for measuring the complex permittivity of low-loss solid materials such as FR4, Rogers (5880, 4003, and 6010) with 7.6% and 22% errors in ϵ_r' and $tan\,\delta$, respectively. The work in [153] presented three different structures for CSRRs that resonate around 2.4 GHz, namely, square, circular, and hexagonal. The proposed CSRRs were used to characterize the animal tissues (e.g., beef, chicken, veal, etc.) of different thicknesses (~2 – 8 mm) by extracting their dielectric properties using the optimization function in HFSS and CST simulation software programs. The study in [154] used a ring-and-horn complementary structure of 2.074 GHz resonance frequency to detect the glucose concentrations in the range 2000 – 10000 mg/dL, which is way beyond the practical range for diabetes.

Nevertheless, the enhanced field localization nature in conventional CSRR sensors is not fully and efficiently exploited to increase their sensitivity. CSRR cells in such structures are basically coupled to the MTL quasi-TEM mode of high intensity within a confined area of the attached dielectric substrate (host material). This will restrict any ground defect design for the CSRR to be positioned in a small region within the hosting MTL for proper excitation. Accordingly, the achieved sensitivity would be weak; primarily due to the limited interaction between the induced fields and the loaded SUT. To alleviate this limitation, we chose to integrate multiple resonating cells of CSRR and exploit the induced inter-cell mutual coupling to intensify the fields over a larger sensing area, thus enhancing the overall sensitivity of the biosensor. Additionally, the proposed sensing schema of multiple coupled CSRRs would confine the resonating electric fields with steeper resonance depth over a wider bandwidth compared to the single-CSRR design of limited sensitivity. This would allow for extracting more resonant data at multiple frequencies upon loading the resonating cells symmetrically with one dielectric glucose sample. This wideband scattering response increases the sensitivity and decreases the prediction error due to the background noise, variant ambient temperature, etc. Consequently, the liquid samples and blood glucose levels would be reliably identified by collecting more information at many frequency points and extracting unique sets of critical resonant features adequate to drive an efficient machine learning prediction model. Another advantage of the broadband response is featured when developing the sensor as a wearable device for blood glucose monitoring; is to provide a wide range of penetration depths. Therefore, the sensor could be easily adapted for different users' physiological needs (e.g. age and gender) by selecting the appropriate set of sensing frequencies.

3.4 Multiple-Pole CSRR-based Sensor

3.4.1 Sensor Configuration

Three resonating cells of double-loop CSRR are loaded onto a microstrip structure and arranged in a series configuration in the ground plane of a thin dielectric substrate along the MTL (i.e., line of symmetry orthogonal to the MTL) to support longitudinal coupling parallel to the propagation direction (Fig. 3.3(a)). This cascaded configuration is favored to properly excite the CSRR cells with a single MTL passing through their centre islands, thus guaranteeing stronger CSRRs-MTL coupling as compared to the parallel arrangement used in [155], [156] for a pair of coupled CSRRs. The preceding solution is more efficient and practical compared to other sophisticated solutions such as embedding a channel inside the MTL substrate to increase the field interaction with the loaded SUT [157]. The CSRRs in this proposed design are positioned in very close electrical distance to engender a significant inter-resonator coupling that enhances the sensitivity for glucose characterization. This sensing approach is different from other works in [155] and [158] where the two resonators (placed sufficiently apart) were loaded asymmetrically with a SUT and a reference sample; resulted into splitting the transmission zero into two notches and diminishing the sensitivity accordingly.

Mutual coupling occurs across the plane where the CSRR cells are installed in the direction of wave propagation along the MTL. Therefore, the sensor (named TP-CSRR or MC-CSRR) exhibits a broadband reject filter behaviour at multiple transmission resonances in the centimeter-wave band 1 – 6 GHz when loaded symmetrically with dielectric liquid tissues over the sensing zone. Three CSRR cells are favored in the proposed design to realize a larger sensing region of about 36×9 mm^2 adequate for integrating a rectangular fluidic channel that supports liquid volumes in the range 400 – 1200 µL. Such an area is also quite adequate for finger placement when adapting the sensor as a wearable for non-invasive blood glucose monitoring. Figure 3.3(b) shows the layout integrating the plexiglass rectangular channel with the CSRRs sensor. Illustration of the finger placement along the sensing region for continuous BGL monitoring is shown in Fig. 3.3(c).

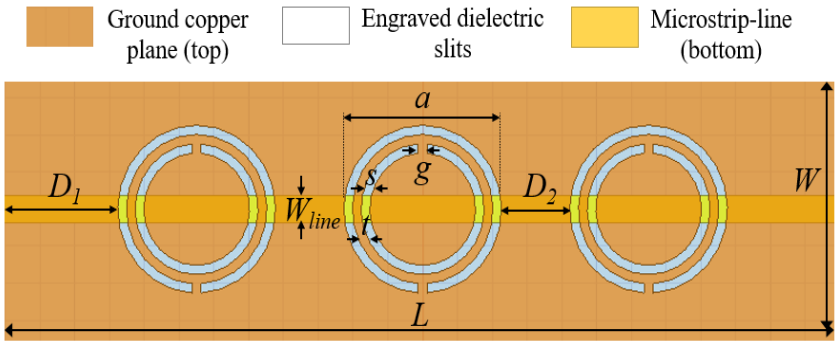

(a)

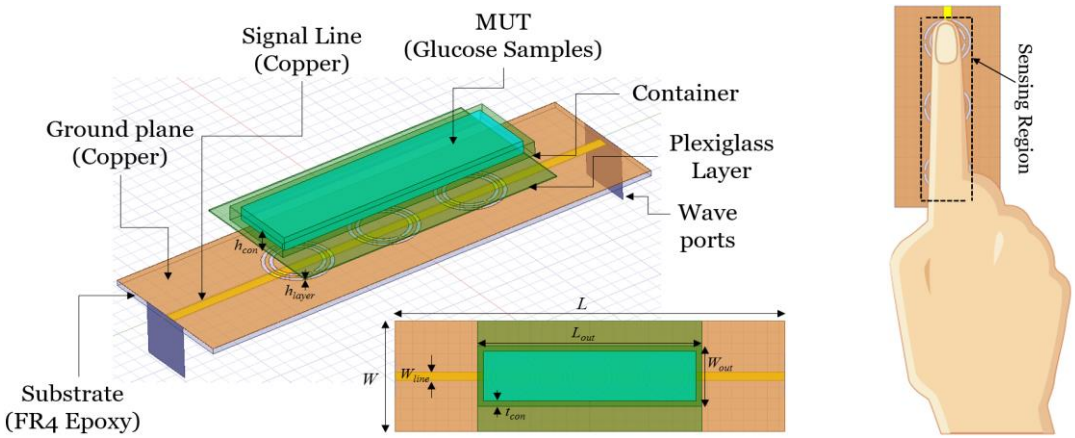

Figure 3.3: (a) Configuration of the CSRR poles in the ground plane (top view), (b) geometrical schematic model of the TP-CSRR integrated with the vein-resembling channel (top view of the integrated sensor is enclosed), and (c) sensor application for continuous glucose monitoring from the finger.

The sensor structure implements the metamaterial technology in the form of three identical cells of circular-shape of complementary split-ring resonators placed horizontally on the top layer of a dielectric substrate of length *L*, width *W*, and thickness *h* as shown in Fig. 3.3(a). The first cell is located at distance D_1 from the input port. The CSRR cells are spatially detached with D_2 distance ranges from one cell boundary to another. Each CSRR cell is composed of two tightly coupled concentric split-rings of dielectric slits nested inside each other and engraved in the copper ground layer. The double split-rings are designed in the form of two circular-shaped annular loops with a gap *t* between each. The loop of each ring ends in a metallic slot of width *g*. To achieve the broadband response upon loading the sensor symmetrically, a two-ports feeding line (MTL) is implemented with cross section L_{line} x W_{line} on the bottom face of the dielectric substrate to excite the resonating cells from a coupled RF power supply.

When an EM power is triggered from the input port (attached at distance D_1 from the first cell), charges and currents are induced inside the dielectric slit of each cell. As such, the microstrip TP-CSRRR structure exhibits a bandgap resonance at certain frequency when the electric and magnetic energies (stored in capacitors and inductances, respectively) are balanced. The TP-CSRR sensor has so many design parameters that affect its bandgap response (resonant frequency, depth, and quality-factor) and performance when used for sensing lossy dielectrics (i.e., liquid glucose samples). In specific, the resonance profile is dependent on the sensor physical dimensions, substrate specifications [66], sample permittivity, and the geometry of each CSRR cell in the integrated structure including diameters of both outer ring *a* and inner rings *b*, inter-distance or coupling gap *t*, ring width *s*, and split gap *g*, in addition to the distances D_1 and D_2 that correspond to the input and in-between MTL delays, respectively. The resonance strength is enhanced with the mutual coupling originated between the adjacent cells as controlled by D_2. The resonant cells (of an *RLC* circuit behaviour) are capacitively and resistively perturbed when the intrinsic electric field distributed over the sensor surface is disturbed by the loaded

glucose sample. The latter strongly interacts with the electric field stored in each cell, yielding the sensor response (resonance frequency and/or amplitude) very responsive to any permittivity changes in the glucose sample due to a change of concentration.

3.4.2 Design Perspectives and Numerical Analysis

As previously shown, the EM dispersive properties of blood tissues (ϵ_r' and $tan\delta$) change very slightly for the varying-level glucose spectrum of diabetics (60 – 300 mg/dL). For instance, the single-pole Debye model in [131] suggests that for a 10 mg/dL glucose change at 2.3 GHz, the percent change in $tan\delta$ is about 0.8% while that in ϵ_r' is around 0.01%. Therefore, for blood glucose monitoring applications, we need to optimize the design of the proposed sensing structure in terms of the geometric parameters defining the planar MTL and the CSRR resonating cells; in order to maximize the resonance strength and perfectly confine the resonating electric fields within the permittivity sensing region. This is pivotal to acquire higher sensitivity capable of capturing the small contrast in blood glucose dielectric properties. In what follows, the choice of integrating three cells and other design specifications are explored following thorough investigation of the sensitivity performance at different number of CSRR cells, resonator order (i.e., single or double loop), excitation schemes, substrate thickness, and CSRR geometries. The HFSS numerical simulator was used in these numerical analysis and modelling.

3.4.2.1 CSRR orientation or excitation method. The integrated CSRRs could be either electrically excited when their magnetic walls (line of symmetry) are orthogonal to the coupling MTL, or possibly triggered by a combined electric/magnetic excitation when the magnetic walls are in parallel alignment with the MTL strip. Numerical analysis revealed a better sensitivity performance for the sensor when the CSRRs are oriented perpendicularly to the MTL strip. This would guarantee an electric excitation for the resonance with time-varying electric field between the MTL and the ground plane.

3.4.2.2 Substrate thickness and dielectric properties. In the sensor structure of MTL coupled with the CSRRs, the plugged electric field polarizes a portion of the dielectric substrate and a portion of the loaded glucose sample. The sensor sensitivity to variations in glucose levels could be enhanced by increasing the dependency of the minimum transmission resonant frequency on the loaded sample permittivity (i.e., C_M). This is achieved by increasing the polarized portion of the loaded sample and decreasing the field confinement into the substrate by reducing its respective thickness h and dielectric properties (ϵ_r' and $tan\delta$). Lower substrate thickness of h = 0.8 mm has achieved better sensitivity compared to the 1.6 mm thickness.

3.4.2.3 CSRR cell geometry. In addition to the substrate specifications, the resonant characteristics of the TP-CSRR sensor (f_o and Q) are also dependent on the geometrical parameters of each CSRR cell (i.e., diameters of both inner and outer rings a, coupling gap t, ring width s, and split gap g). HFSS was used to investigate the primary influence of each of these parameters on f_o. The pole diameters a and b are proportionate to the effective length of the dielectric slits; larger inductance L_R

would be resulted for increased pole diameters, thus reducing the overall f_o as shown in Fig. 3.4(a) for the case of a changing from 8.88 to 9.28 mm. Fig. 3.4(b) depicts how f_o is shifted upward when increasing the split-gap g (reducing C_R) from 0.1 to 0.5 mm. Similar behavior with larger shifts in f_o is observed in Fig. 3.4(d) for increasing the slits-coupling distance t in 0.1, 0.3, and 0.5 mm. Fig. 3.4(c) also shows the slight decrease in f_o with an increased ring-width s that is directly proportional to L_R. On the contrast, both slots-coupling distance t and split-gap g tend to establish an inverse proportionality to C_R, therefore increasing these parameters would probably increase f_o. The cells geometry has been optimized to reduce the combined reactive elements L_R and C_R in each cell and increase the minimum transmission frequency f_o towards 2.3 GHz, so that to realize more dependence on the loaded SUT permittivity (i.e. C_M).

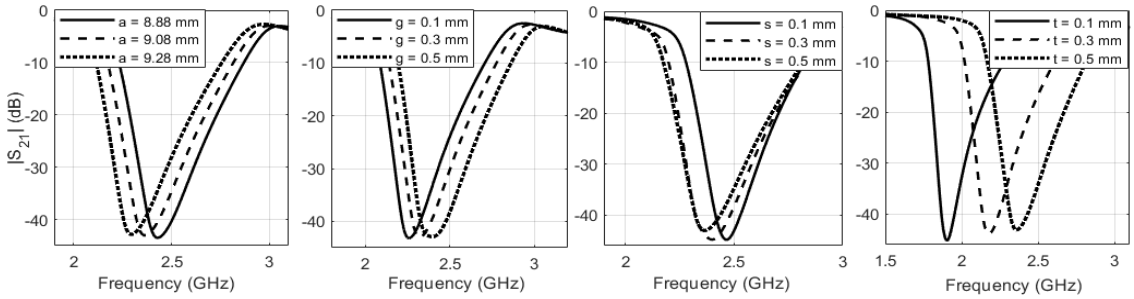

Figure 3.4: Simulated transmission coefficients of unloaded TP-CSRR at different (a) outer diameter a, (b) split-gap g, (c) ring-width s, and (d) slots-coupling distance t

3.4.2.4 Input line-delay D_1. The effect of the input delay D_1 (distance from the feeding port to the cell boundary) on the resonance profile was investigated numerically and experimentally to set it accordingly in the TP-CSRR design for utmost sensitivity. Two SP-CSRRs with different input delays D_1 = 15.46 mm and D_1 = 28.46 mm were compared, when unloaded, in terms of the transmission coefficients and phases as functions of frequency as plotted in Fig. 3.5. Increasing D_1 enables the exciting signal to have sufficient propagation within and around the spatial extent of the MTL before coupling the resonator. Noticeably, D_1 does not have any effect on the transmission resonance frequency, which is shown in Fig. 3.5(a) to be around 2.295 GHz for both types. However, D_1 has an obvious effect on the resonance peak in the transmission mode where a 5 dB difference is recorded between the long (solid black) and short (dash-dotted red) SP-CSRRs. The effect of D_1 is more apparent in the transmission phase response that tends to shift toward lower frequencies for larger D_1 as shown in Fig. 3.5(b).

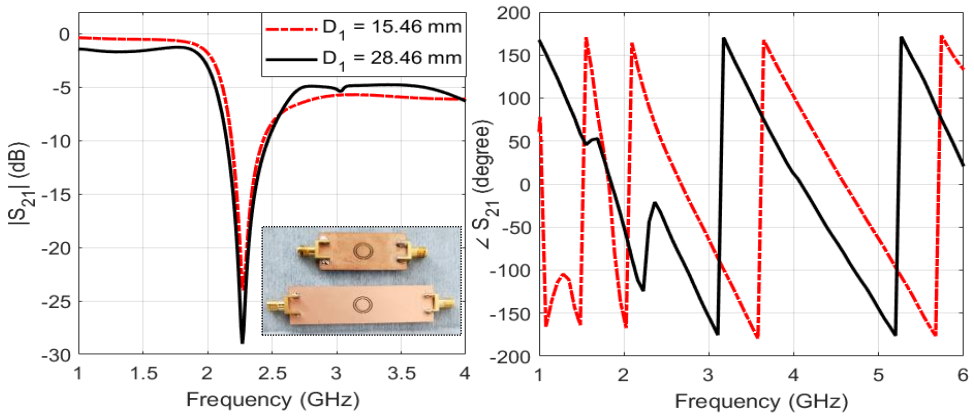

(a) (b)

Figure 3.5: Measured transmission coefficients (a) magnitude and (b) phase of the short and long SP-CSRRs.

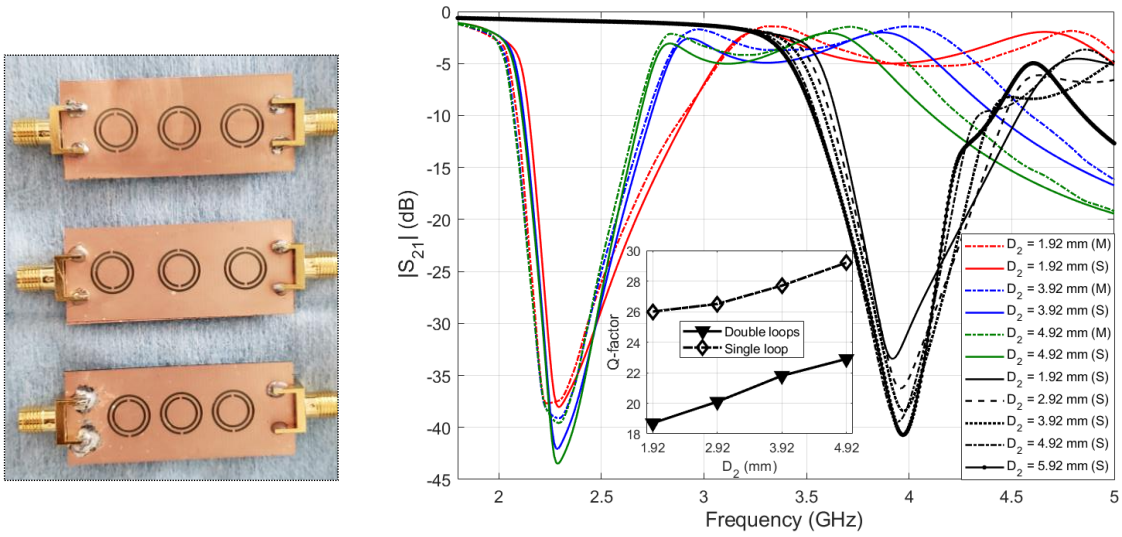

(a) (b)

Figure 3.6: (a) Fabricated prototypes with different D_2 (1.92 mm, 3.92 mm, and 4.92 mm), (b) Measured (M) and simulated (S) transmission coefficients of single and double-loop TP-CSRRs with different in-between line-delay D_2

3.4.2.5 In-between line-delay D_2. Similarly, to examine how the resonance profile of the TP-CSRR is correlated to the delay parameter D_2 that represents edge-to-edge distance between adjacent poles, three TP-CSRRs (Fig. 3.6(a)) with different delays D_2: 1.92, 3.92, and 4.92 mm, were numerically analyzed by comparing their transmission coefficients in the unloading state as shown in Fig. 3.6(b). Apparently, D_2 would not affect the frequency of the minimum transmission response. However, increasing D_2 to some extent results into deeper resonance amplitude/depth, narrower 3-dB bandwidth, and a higher Q-factor for the TP-CSRR, thus benefiting a higher sensitivity for glucose detection as will be shown later. This behavior is attributed to the inter-resonator coupling established between the adjacent poles. Similar behaviour was also demonstrated for the single-loop version that

resonates around 3.9 GHz as shown in Fig. 3.6(b). It is also observed that TP-CSRR of single-loop excels the double-loop type in terms of the *Q*-factor as depicted in the enclosed graph.

3.4.2.6 Number of CSRR cells. The performance of the TP-CSRR sensor was analyzed both experimentally and numerically and compared to that of the conventional SP-CSRR. First, before loading any glucose sample, the transmission coefficients $|S_{21}|$ of the bare structures for both SP-CSRR and TP-CSRR were measured and simulated as plotted in Fig. 3.7(a). Both sensors exhibit unloaded resonances around f_o = 2.3 GHz. However, TP-CSRR has shown a steeper resonance peak/depth of about -46 dB amplitude compared to -24 dB for the case of SP-CSRR. In addition, the 3-dB bandwidth is more broadening in the TP-CSRR resonance than its corresponding on the SP-CSRR. Integrating multiple resonators will increase the bandwidth and depth of the bandgap as shown in Fig. 3.7(a) (red curves). Measurements and numerical simulations are in good agreement with minor differences due to fabrication tolerances.

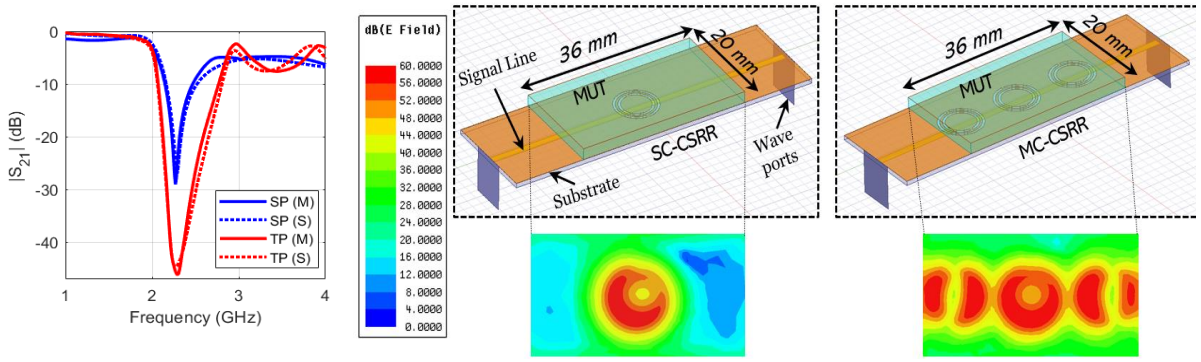

(a) (b)

Figure 3.7: (a) Measured and simulated transmission coefficients of SP-CSRR and TP-CSRR prior-loading (resonance around 2.3 GHz), (b) simulating a dielectric MUT on top of SP-CSRR and TP-CSRR and depicting the electric field distribution at 1 mm height across the MUT surface.

Second, both sensing structures were numerically analyzed for detecting changes in EM properties (dielectric permittivity and loss tangent) of a loaded MUT with rectangular dimension 36×20 mm^2 and 2 mm thickness as depicted in Fig. 3.7(b) and 3.7(c). To exploit the full benefits of the resonance induced by the CSRR cells, the MUT is loaded on the most sensitive region of the sensor surface as identified by the numerical simulations of the electric field distribution in both cases. Figure 3.7(b) and 3.7(c) also compare the magnitude of the simulated electric field in the resonance state at 1 mm height across the MUT (ϵ' = 20, $tan\delta$ = 0.1) for the SC-CSRR and MC-CSRR, respectively. Remarkably, MC-CSRR realizes larger sensing zone with highly concentrated electric field that extends longitudinally across the CSRRs plane. This most sensitive region on the sensor surface would be used for loading the glucose tissues to achieve the most interaction with the coupled electric field at the resonant frequency and boost the detection sensitivity.

The parametric sweep function in HFSS was used to vary the ϵ' between 10, 20, and 30, while varying the *tanδ* between 0.01, 0.1, and 0.2. $|S_{21}|$ was used to monitor the change in the sensor response since it shows the effect of the sample permittivity more predominantly, compared to S_{11}. Resulted responses have shown broadband rejection signals with multiple resonance modes (fundamental and harmonics) induced in the frequency range 1 – 6 GHz. Fig. 3.8(a) and 3.8(b) depict the resulting resonant frequencies and peak amplitudes for the simulated dielectric properties at the fundamental and harmonic resonance modes, respectively. Loading dielectric samples of relatively higher permittivity than air (ϵ' = 1), will increase the effective capacitance in each resonating cell. Therefore, both sensors respond to the increase in ϵ' by shifting the resonance frequencies towards lower bands (i.e. decreasing f_r) with similar frequency resolution (i.e. percentage change in minimum transmission frequency). For instance, the two sensors resonate around 1.15 GHz when loaded with an MUT of ϵ'= 30 resulting into $\Delta f = \left(\frac{|f_{MUT} - f_{air}|}{f_{air}}\right)$ of about 0.5 in each. The sensors also exhibit variations in the resonance peak amplitudes to reflect the changes in *tanδ* of the loaded MUT. Resonant amplitudes decrease gradually with an increased *tanδ.* However, MC-CSSR shows an appreciably higher sensitivity to variations in *tanδ* compared to that of SC-CSRR as inferred from the resonant peaks depicted in Fig. 3.8(a) and 3.8(b).

To illustrate this superiority, we evaluated the amplitude resolution at the fundamental mode at f_r = 1.35 GHz where both sensors resonate when loaded with an MUT of ϵ'= 20. Herein, the minimum amplitude variation per unit change in *tanδ* $\left(\frac{\Delta|S_{21}|}{\Delta|tan\delta|}\right)$ was calculated as 56.4 dB for MC-CSRR compared to 14.1 dB for SC-CSRR. Therefore, an MUT with lossy characteristics such as glucose aqueous solutions could be detected with higher amplitude resolution on top of the MC-CSRR sensor. In addition, this amplitude resolution is higher in the harmonic mode compared to the fundamental mode, thus enabling a higher sensitivity detection at higher frequencies. For instance, for an MUT of dielectric constant of 30 and loss tangent of 0.2, the resonant peak is -14.88 dB at the harmonic mode at f_r = 3.06 *GHz* compared to that of -5.48 dB at the fundamental mode recorded at f_r = 1.15 *GHz*. Resonant amplitude in MC-CSRR varies in 4.31 dB when *tanδ* changes from 0.1 to 0.2, while for the same change in *tanδ* a 1.29 dB is recorded by the SC-CSRR. This numerical analysis demonstrates the higher sensitivity of the multiple-cell sensor (in both modes) for detecting the loss property changes of a loaded MUT compared to the single-cell case.

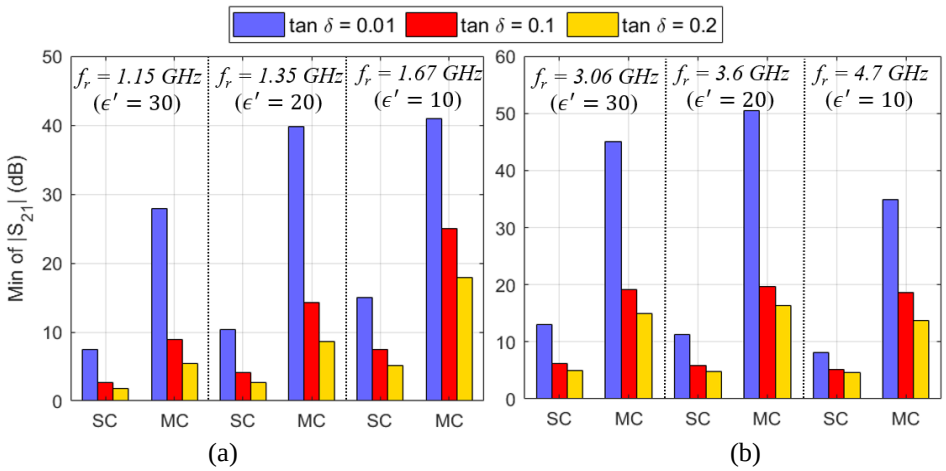

Figure 3.8: Numerical analysis for the sensitivity behaviour of SC-CSRR and MC-CSRR for variations in dielectric properties of the loaded MUT at (a) fundamental and (b) harmonic resonance modes.

3.4.3 Design Specifications

The sensor with three CSRRs exhibits higher sensitivity with a steeper resonance peak/depth of around -46 dB amplitude at f = 2.3 GHz compared to -35 dB and -24 dB for the case of the DP-CSRR (double-pole) and SP-CSRR (single-pole), respectively. Therefore, TP-CSRR would probably yield a better sensitivity for characterizing lossy materials of high $tan\delta$, which makes it ideal for adoption in our case to detect tiny variations in the loss tangent for various blood glucose concentrations of interest. Additionally, having three cells coupled together in the proposed sensor would allow for sensing the glucose tissues over a larger region of the CSRRs wherein the electric field is localized with high concentration, and therefore acquiring higher sensitivity for glucose monitoring. Lastly, the effective area of about 37×9 mm^2 for the respective sensing region (with three cells) is quite adequate to place the subject finger when the sensor is adapted for non-invasive BGL monitoring as a wearable device.

Following the abovementioned investigative studies, we used the FEM-based HFSS to design the proposed CSRR sensor in the triple-pole configuration. Specifically, three CSRRs were patterned on the upper face of an FR4 dielectric substrate (ϵ_r' = 4.4 and $tan\delta$ = 0.02) of length L = 66 mm, width W = 20 mm, and thickness h = 0.8 mm. The exterior ring of each CSRR cell was designed with outer diameter a = 9.08 mm, ring width s = 0.5 mm, and split gap g = 0.5 mm. Similar values were used for designing s and g in the interior ring of 8.08 mm outer diameter. The inter-distance t that considerably controls the coupling between the exterior and interior rings was optimized to 0.5 mm. The distances D_1 and D_2 were set to 15.46 mm and 3.92, respectively. The MTL was sized with a length of L_{line} = 66 mm and a width of W_{line} = 1.5 mm in order to realize a characteristic impedance of 50 Ω around 2.3 GHz that matches the internal input impedance of the feeding ports. A rectangular plexiglass container (ϵ_r' = 3.9 and $tan\delta$ = 0.001) was integrated on top of the CSRRs surface to hold the blood glucose samples. This would also simulate the practical scenario of the blood flow inside the blood vessels. The container has an outer length L_{out} = 37 mm, inner length L_{in} = 36 mm, outer width W_{out} = 10 mm, inner

width W_{in} = 9 mm, wall thickness t_{con} = 0.5 mm, and height h_{con} = 2 mm. Additionally, a glass layer of slim thickness t_{layer} = 0.15 mm was introduced between the channel and CSRRs in order to evade short-circuiting the dielectric slots in each pole. Therefore, the damping effect on the reflection/transmission resonances can be significantly reduced when lossy glucose samples of moist nature are loaded on top. As a result, the resonance peaks remain indicative for the perturbation introduced when the blood glucose samples are loaded. All the design and geometrical parameters of the integrated sensor are listed in Table 3.1.

Table 3.1: Geometrical parameters of the integrated TP-CSRR sensor

Parameter	a	g	t	s	D_1	D_2	W	L	L_{line}
Value (mm)	9.08	0.5	0.5	0.5	15.46	3.92	20	66	66
Parameter	W_{line}	L_{out}	W_{out}	L_{in}	W_{in}	h_{con}	t_{con}	h	t_{layer}
Value (mm)	1.5	38	11	36	9.0	2.0	1.0	0.8	0.15

3.4.4 Fabrication of the Sensor Prototype

Several prototypes of the TP-CSRR sensor were fabricated on an FR4 PCB substrate of 35 µm copper layers on both sides using the laser micromachining (LPKF ProtoLaser U4) shown in Fig. 3.9(a). The DipTracer PCB layout software was used to generate the Gerber files (.gbr) from the DXF HFSS design files for the intended CSRR structures. A sample of the Gerber file for an SP-CSRR design is shown in Fig. 3.9(b). First, a few fiducial points were added to the design to ease the alignment of top and bottom parts in fabrication as shown in Fig. 3.9(c). Some other settings were adjusted accordingly including the design template, material type and height, contour configuration, laser power, etc.

The proto-laser machine was used to fabricate the CSRR devices while being controlled and guided via the CircuitPro software where the Gerber design files were imported. In this process, the scanning laser beam was initially used to etch three small holes as fiducials on the ground layer through the PCB to properly align top and bottom parts in the design. Next, the laser cutting was used to incise the outer and inner dielectric annular slits of each CSRR cell on the ground layer of the PCB as shown in Fig. 3.9(d). Lastly, the laser beam was used to pattern the MTL strip of 66 × 1.5 mm^2 cross section in the bottom layer after alignment with the fiducial markers (Fig. 3.9(e)). A pair of 50 Ω SMA coaxial connectors were soldered to both ends of the MTL to facilitate the measurements when connecting to the VNA. Figure. 3.9(f) and 3.9(g) shows both sides of the fabricated TP-CSRR prototype.

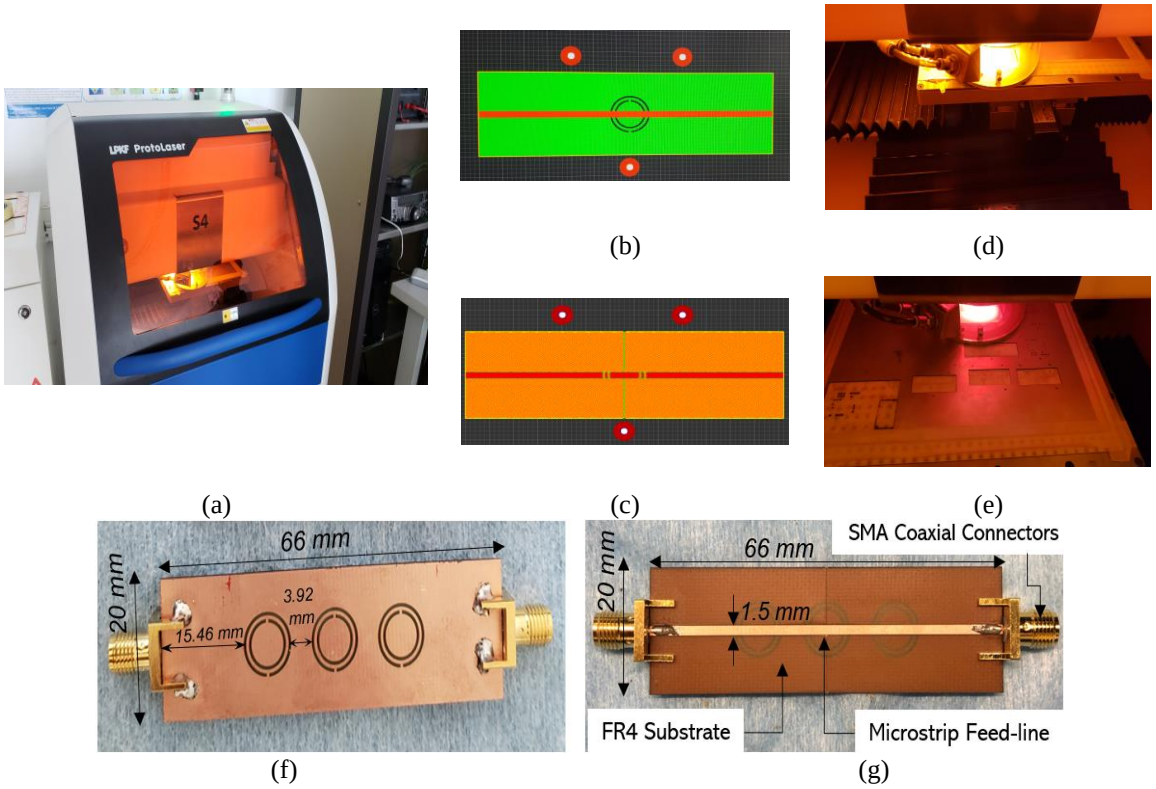

Figure 3.9: Fabrication process of the CSRR sensor prototypes using the laser technology (a) Proto-Laser machine, (b) Gerber file sample, (c) placing the fiducials, (d) engraving the CSRR poles on the ground plane, and (e) patterning the transmission line on the bottom side. Fabricated sensor prototype (f) top view showing the ground plane where the CSRR sensing elements are patterned, (g) bottom view showing the MTL used for exciting the CSRRs.

3.4.5 Integrating a Microfluidic Channel

A fluidic channel is integrated with the MC-CSRR sensor to allow for non-contact, reusable, consistent, and intact testing of the liquid samples. This would also benefit a more sensitive measurement compared to other conventional sensing elements used in the literature such as rectangular waveguide cavities [159] or substrate integrated waveguide (SIW) [160] that basically operate at fundamental modes (e.g., TE_{101}) or any dominant mode (e.g. TE_{110}). Other resonator modules that are being integrated with microfluidics include hairpin resonators [161], split ring resonators [146], [157], and interdigitated capacitors [162].

The fluidic channel was fabricated using standard soft lithography technique with polydimethylsiloxane (PDMS) suitable for usage in the biomedical environments due to its excellent features in biocompatibility, optical transparency, mechanical resistance, chemical inertness, and non-toxicity. The sensor design yields an entire sensing region of about 36×9 mm^2. To perform the sensing operation with higher sensitivity while consuming the minimum liquid volume, the master channel was designed with dimensions 33×8×3 mm^3 to be integrated on the most sensitive region along the centre islands of the coupled CSRRs where the electric field is highly concentrated. The supporting PDMS was designed with larger width and length to perfectly align the position of the master channel onto the

CSRR cells. The mold was designed as shown in Fig. 3.10(a) using OpenScad software and printed using the Form2 3D-printer (Formlabs).

PDMS mixed with the prepolymer curing agent (in ratio of 10:1) was poured over the mold and cured at 80°C for 2 hours. The mold was then peeled off and holes were punched through the PDMS at the inlet and outlet of the channel. The microfluidic channel was then covalently bonded to the glass chips containing the patterned electrodes by treating both the PDMS surface and the glass substrate with oxygen plasma at a radio frequency power of 30 W and a chamber pressure of 300 mTorr for 1 min. The resulting platform was heated at 80°C for 1 hour to help separating H_2O molecules from the glass/PDMS interface during bond formation. The resulting PDMS channel is shown in Fig. 3.10(b) with a total capacity of 500 μL. It was integrated on top of the MC-CSRR sensor in precise alignment with the sensing elements to acquire the most sensitivity when measuring the tested liquids (Fig. 3.10(c)). A transparent plexiglass sheet of slim thickness 0.15 mm was installed underneath the channel to avoid short-circuiting the dielectric slits of the CSRR cells and prevent any damping effect on the sensor's resonances due to the moist nature of the measured liquids flowing across the microfluidic channel.

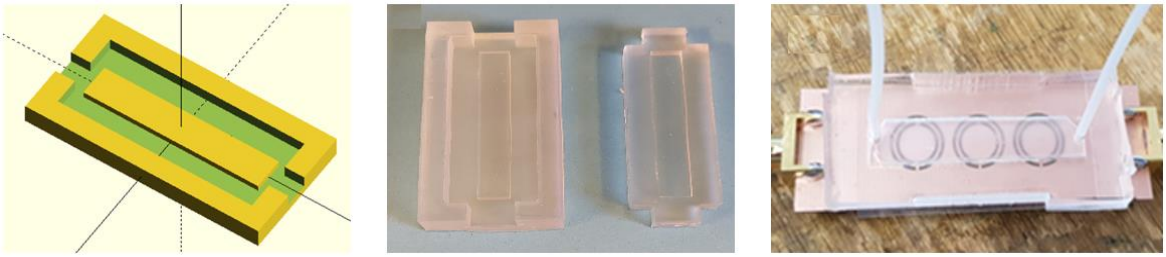

(a) (b) (c)

Figure 3.10: (a) Mold designed using OpenScad software, (b) printed mold and PDMS channel, and (c) final device layout where PDMS channel is integrated with MC-CSRR sensor.

3.4.6 Electrical Modeling

Simple quasi-static models of lumped elements can be used to describe the physical behavior of the CSRRs given their smaller dimensions compared to the guided wavelength (< λ_g/10) [163], [164]. To electrically model the TP-CSRR, a model common to different forms of resonators was developed for each pole (SP-CSRR) based on localized *RLC* elements in the equivalent electrical circuit shown in Fig. 3.11(a). The model consists of three parts, first, the signal line used for exciting the resonator is modelled by an inductance L_c to represent the magnetic coupling of the MTL strip when crossing the CSRR cell for excitation. The second part is the dielectric substrate that guides the EM fields from the MTL to couple the resonator in the ground plane. This part can be approximately modelled by a shunt capacitance C_c in parallel with a resistance R_c that quantifies both the dielectric losses of the substrate and the conductive losses of the metal ribbon. The last part in the model pertains the resonator alone and is modelled by *RLC* parallel resonant circuit where the winding of width *s* in the interior/exterior rings act as inductance L_R, the metallic gaps *g* and spacings *t* of the rings create a parallel capacitance C_R, and the

conductive and dielectric losses are modelled by a resistance R_R that takes into account the small inductive magnetic losses associated with L_R.

$$f_o = \frac{1}{2\pi\sqrt{L_R(C_R + C_c)}}, \tag{3.3}$$

$$Q = \frac{f_0}{\Delta f_{3dB}} = 2\pi f_o R_P (C_R + C_c), \tag{3.4}$$

Given this resonating structure, the transmission resonant frequency of the single cell is given by Eq. (3.3) and its loaded *Q*-factor by Eq. (3.4) where Δf_{3dB} is the 3-dB bandwidth of the resonance peak, and R_p is the equivalent resistance of paralleling the coupling-part R_c and resonator-part R_R. When an MUT (i.e., superstrate) is loaded onto the resonator, an *RC* parallel circuit is attached to the resonator part to model the EM properties (ϵ_r' and $tan\delta$) of the loaded sample. In specific, C_M is directly related to the relative permittivity of the sample while R_M is mainly dependent on its loss properties. In consequence, changes in the dielectric characteristics of the loaded MUT (i.e. glucose) would be reflected into f_o and Q through perturbing the CSRR effective capacitance C_e and resistance R_e. Therefore, when the integrated CSRR sensor is used for sensing a given sample, all the model parameters would be fixed in value except for the resonator part that is essentially controlled by the EM properties of the MUT. The model for SP-CSRR can be extended to TP-CSRR by modelling the input line-delays and in-between line-delays (inter-distance) between individual poles using the transmission-line model as shown in Fig. 3.11(b). Mutual coupling would take place between adjacent poles as represented by C_{M1} and C_{M2} capacitances.

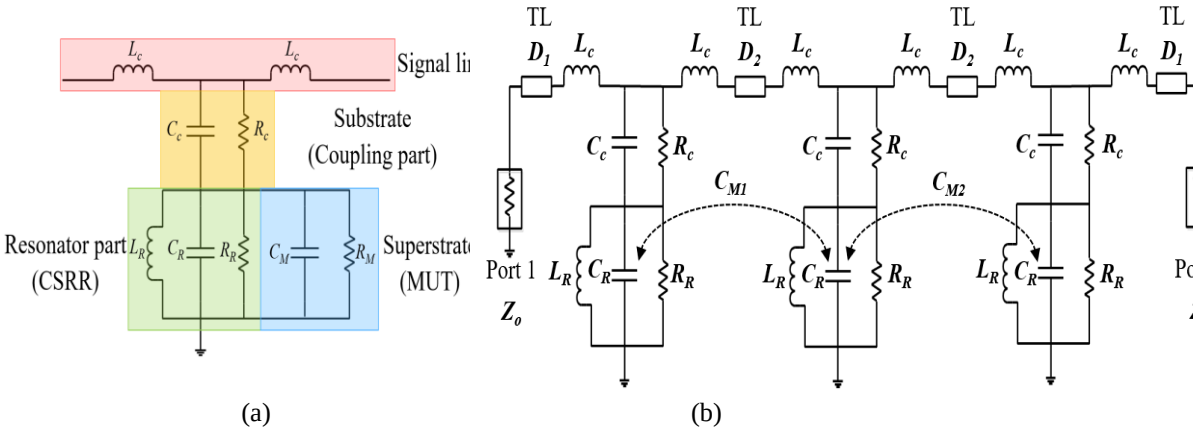

Figure 3.11: Equivalent electrical model of (a) single CSRR cell under loading condition, (b) unloaded triple-pole CSRR.

The delay of each MTL segment was estimated using the relation $T_D = \frac{\epsilon_{eff}}{\omega}$, where ϵ_{eff} is the effective permittivity of the MTL evaluated at the operating frequency ω based on the substrate specifications as well as the thickness, width and length of the MTL segment. For instance, to electrically model the line-delay of D_2 = 3.92 mm between adjacent cells, the Line-Calc module in ADS was used

to calculate the corresponding ϵ_{eff} and Z_o at ω = 2.3 GHz given the substrate specifications (h = 0.8 mm, ϵ_r' = 4.4, and $tan\delta$ = 0.02), thickness, width and length of the MTL segment (W_{seg} = 1.5 mm, t_{seg} = 35 µm and L_{seg} = 3.92 mm) resulting into ϵ_{eff} = 0.34 rad, Z_o = 50.31 Ω, and a delay value of 24.17 ps.

The methodology to extract the values of the reactive elements (C_C, L_C, C_R, L_R) in such an electrical model is based on measuring the S-parameters of the SP-CSRR when it is unloaded. The losses associated with the coupling and resonator (R_C and R_R) would be neglected at this stage. In this methodology, the reference plane is transferred from the conventional input plane used for measurements at the sensor connectors to that located right at the resonator boundary. This is done to determine the intrinsic S- and Z-parameters of the integrated set (CSRR coupled to MTL) at the reference plane of the resonator alone by de-embedding all the delay effects from the coaxial cables, connectors at feeding ports, and MTL. The measured S-parameters of the unloaded SP-CSRR are plotted in Fig. 3.12(a). It is observed that the reflection and transmission coefficients do not primarily change after de-embedding, however, their phases are dominantly affected as indicated by the variations in the Z_{11} response shown in Fig. 3.12(b). After de-embedding, four characteristic frequencies (f_s, f_o, f_R, and f_z) are observed in the frequency responses of parameters S_{11}, S_{21}, and Z_{11}, respectively. Particularly, f_s and f_o are the minimum resonance frequencies of the reflection $|S_{11}|$ and transmission $|S_{21}|$ coefficients, respectively. While the other two characteristic frequencies f_R and f_z are observed in the frequency variation of the input impedance Z_{11} as calculated from the measured S-parameters in the open circuit mode of the SP resonator. As depicted in Fig. 3.12(b), the Z_{11} response has a minimum value at frequency f_z and a peak value at frequency f_R that represents the resonance frequency of the parallel circuit equivalent to the resonator only.

Next, the values of the four reactive elements (C_C, L_C, C_R, L_R) were determined by solving five independent equations Eq. (3.3), (3.5), (3.6), (3.7), and (3.8) that relate the four reactive elements to the four characteristic frequencies (f_s, f_o, f_R, and f_z). Eq. (3.3) defines the transmission resonance frequency f_o, while that for the reflection resonance is given in Eq. (3.5) that shows its dependency on the characteristic impedance of the access-line Z_o, S_{21} resonance f_o, and other two frequencies f_R and f_c that are given by Eq. (3.6) and (3.7), respectively. The frequency f_R represents the resonance frequency of the resonator exclusively, and f_c is the resonant frequency of the circuit equivalent to the coupling between the feed-line and the resonator (i.e., LC series circuit). f_c is not directly observable on the collected measurements but is derived from frequency f_z as given in Eq. (3.8). The values of the four characteristic frequencies as well as those of the reactive elements obtained after resolving this system of equations for a single resonator are summarized in Table 3.2

$$f_s \approx \frac{1}{2\pi}\sqrt{\frac{2-(C_c Z_o^2/L_c)}{\frac{1}{(2\pi f_c)^2}+\frac{2}{(2\pi f_o)^2}-\frac{1}{(2\pi f_R)^2}\left(\frac{C_c Z_o^2}{L_c}\right)}}, \tag{3.5}$$

$$f_R = \frac{1}{2\pi\sqrt{L_R C_R}}, \tag{3.6}$$

$$f_c = \frac{1}{2\pi\sqrt{L_c C_c}}, \tag{3.7}$$

$$f_z \approx \frac{f_c}{\sqrt{1 + \left(\frac{f_c^2}{f_o^2}\right)}}, \tag{3.8}$$

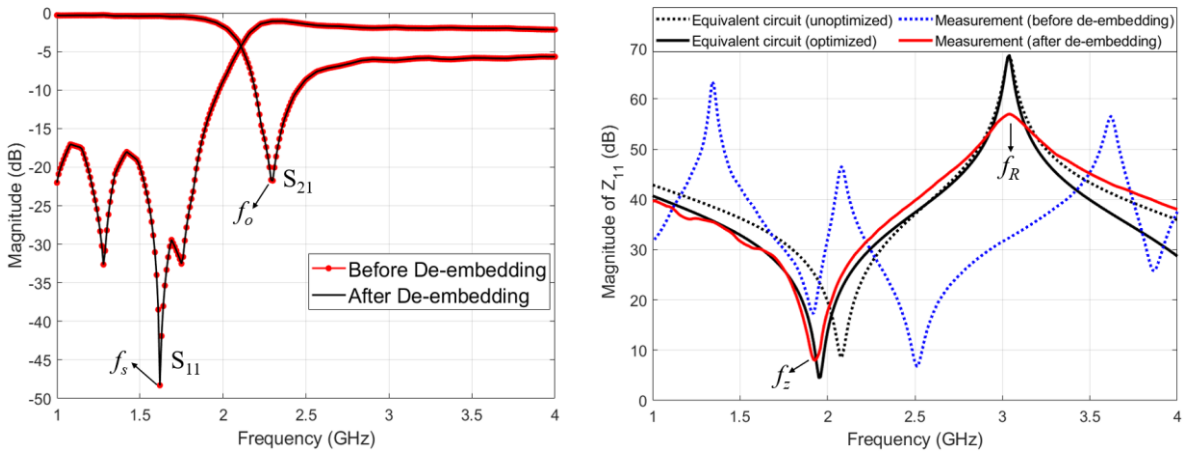

(a) (b)

Figure 3.12: (a) Measurements of the reflection S_{11} and transmission S_{21} responses of SP-CSRR before and after de-embedding in ADS. Resonance frequencies of reflection f_s and transmission f_o are also indicated, (b) Z_{11} response of the SP-CSRR extracted from measurements before and after de-embedding compared to that of the equivalent circuit model.

Table 3.2: Characteristic frequencies and calculated reactive elements of the SP-CSRR electrical model.

Parameter	f_o (GHz)	f_S (GHz)	f_R (GHz)	f_Z (GHz)	f_C (GHz)	L_R (nH)	C_R (pF)	L_C (nH)	C_C (pF)
Value	2.30	1.62	3.04	1.93	3.55	2.16	1.27	2.12	0.95

The lumped elements model was then implemented in ADS using the exact values in Table 3.2, and further optimized to match the S-parameter measurements collected via VNA for the unloaded SP-CSRR. The dielectric losses (resistive elements R_R and R_c) were first estimated by considering the loss tangent of the FR4 substrate and the value of corresponding capacity, then optimized from the amplitudes and widths of the reflection and transmission resonances. Ohmic losses associated with the resonant inductances have been neglected because they are very small in value. Figure 3.13(a) and 3.13(b), compare the results of simulating the electric schema of SP-CSRR before and after optimizing its respective elements in ADS to those experimentally measured when unloaded. The calculated and optimized values for the resistive and reactive elements of the electrical circuit are presented in Table 3.3. The differences between the estimated and optimized values remain in a reasonable range, thus validating the proposed electrical model and methodology. The analytical values of the exclusive SP-

CSRR part are integrated into the TP-CSRR model of Fig. 3.11(b) and further fine-tuned on the MTL delays from 128 to 140 ps (Fig. 3.14) to match the experimental TP-CSRR measurements of reflection and transmission coefficients as shown in Fig. 3.15(a) and 3.15(b), respectively. The optimized values of the lumped elements are shown in Table 3.4.

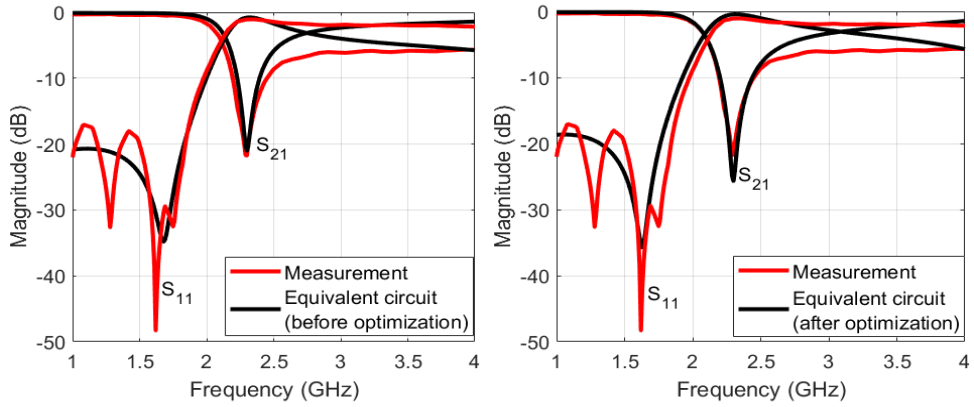

(a) (b)

Figure 3.13: Comparison of the S-parameters from VNA measurements and ADS electrical simulation for the model developed for SP-CSRR, (a) before optimization and (b) after optimization.

Table 3.3: Analytical values of the lumped elements model of the SP-CSRR.

Parameter	L_R (nH)	C_R (pF)	L_C (nH)	C_C (pF)	R_C $(\mathbf{k\Omega})$	R_R $(\mathbf{k\Omega})$
Calculated	2.16	1.27	2.12	0.95	4.4	3.0
Optimized	1.78	1.55	2.71	1.15	4.99	3.29

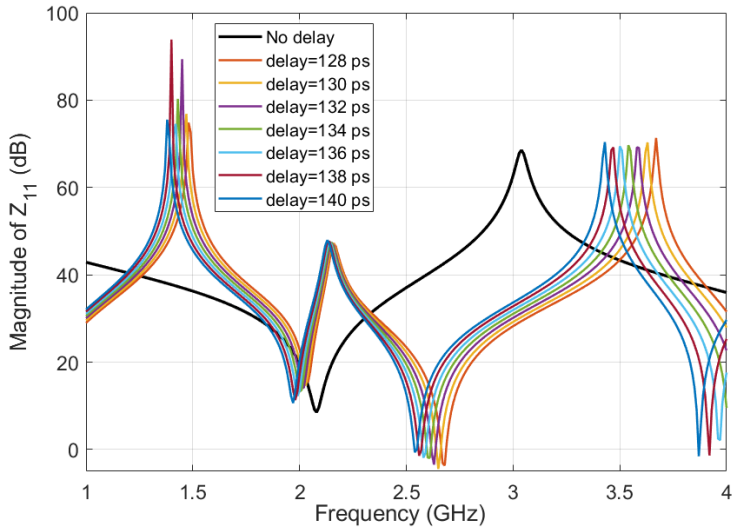

Figure 3.14: Magnitude of Z_{11} at different delays

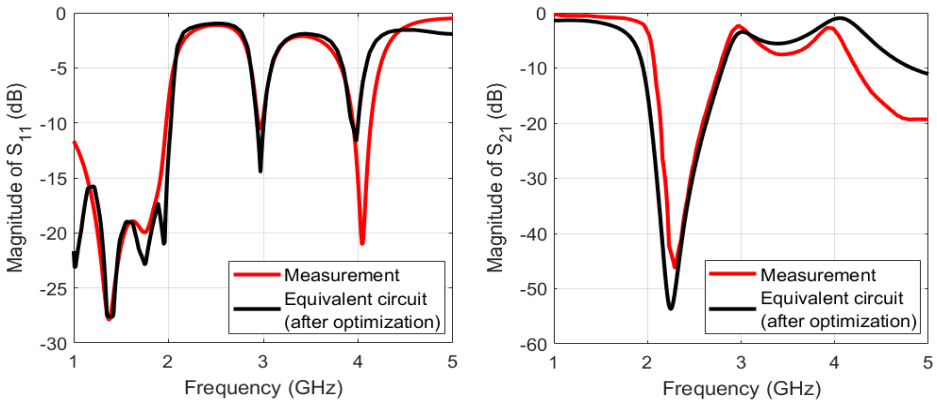

(a) (b)

Figure 3.15: Comparison of the S-parameters from VNA measurements and ADS electrical simulation for the TP-CSRR optimized model, (a) reflection and (b) transmission coefficients

Table 3.4: Optimized values of the lumped elements model for the TP-CSRR.

Parameter	L_R (nH)	C_R (pF)	L_C (nH)	C_C (pF)	R_C $(\mathbf{k\Omega})$	R_R $(\mathbf{k\Omega})$
Optimized	3.33	0.63	3.38	0.88	1.30	1.32

3.4.7 Numerical Simulations for Glucose Sensing

The performance of the developed TP-CSRR sensor was numerically analyzed for non-invasive blood glucose detection. Aqueous-glucose samples of concentrations in the range 60 – 300 mg/dL were simulated on top of the sensing region inside the plexiglass channel as depicted in Fig. 3.3(b) and 3.16(a). This was done via integrating their respective dielectric properties over the operating frequency of the TP-CSRR in the HFSS simulator. Specifically, the dielectric permittivity and loss tangent parameters for the glucose concentrations of interest were approximated at f = 2.3 GHz as listed in Table 3.5. This model was developed in [69] for the permittivity dependency in glucose concentrations by fitting the dielectric measurements - collected using a commercial coaxial probe kit connected to VNA - of watery solutions of 50, 250, 1000, and 2000 mg/dL to a first order Debye relaxation model with the parameters shown in Fig. 3.16(b). This is the most rational model to use for approximating the blood-glucose behaviour at the operating frequency range since no other mathematical model is yet developed for the dielectric properties of actual blood-glucose solutions.

Table 3.5: Extracted dielectric properties for G1 – G8 concentrations

Glucose samples	**G1**	**G2**	**G3**	**G4**	**G5**	**G6**	**G7**	**G8**
ϵ_r'	79.33	79.29	79.25	79.21	79.19	79.17	79.15	79.13
$tan\delta$	0.113	0.117	0.121	0.125	0.127	0.129	0.131	0.133

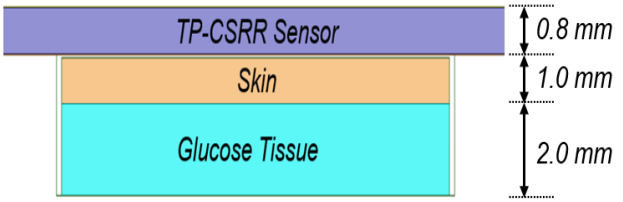

Debye parameter	Model
$\epsilon_\infty(\xi)$	$5.38 + (30 \times 10^{-3}).\xi$
$\epsilon_s(\xi)$	$80.68 - (0.207 \times 10^{-3}).\xi$
$\tau(\xi)$	$9.68 + (0.23 \times 10^{-3}).\xi$

(a) (b)

Figure 3.16: (a) Cross section of the simulation model of the TP-CSRR loaded with glucose tissues on top of a skin layer, (b) Debye coefficients as functions of glucose concentrations

Figure 3.17(a) and 3.17(b) show the simulated transmission responses for the different samples G1 – G8 loaded at volume 600 µL each. These responses were compared in Fig. 3.17(a) at different models of the in-between line-delay D_2 for the sensor to demonstrate the superiority of the proposed design at D_2 = 3.92mm as inferred from the higher amplitude resolutions $\frac{\Delta|S_{21}|}{\Delta|\epsilon_r'|}$ = 13.5 dB and $\frac{\Delta|S_{21}|}{\Delta|tan\delta|}$ = 135 dB compared to those of other models at D_2 = 0.92, 1.92, and 2.92 mm. The enclosed graphs show these resonant amplitude (min of $|S_{21}|$) variations at different glucose levels. To mimic the realistic scenario of placing a finger along the sensing region or when the sensor is revised as a wearable, another simulation model was performed where the glucose samples G1 – G8 of thickness 2 mm each were placed on top of a skin layer (ϵ_r' = 38.1 and $tan\delta$ = 0.28) [60] of thickness 1 mm as depicted in Fig. 3.16(a). The electric field distribution induced by the coupled CSRR cells at resonance is plotted across the sensing region at two levels, z = 0 at the interface between the CSRRs surface and skin layer (Fig. 3.18(a)), and z = 2 mm inside the glucose tissue (Fig. 3.18(b)). The sensor response was measured over the range 3 – 6 GHz as depicted in Fig. 3.17(b), where two resonances were induced at f = 3.3 GHz and f = 5.2 GHz. The corresponding amplitude resolutions for glucose level changes were enclosed in Fig. 3.17(b).

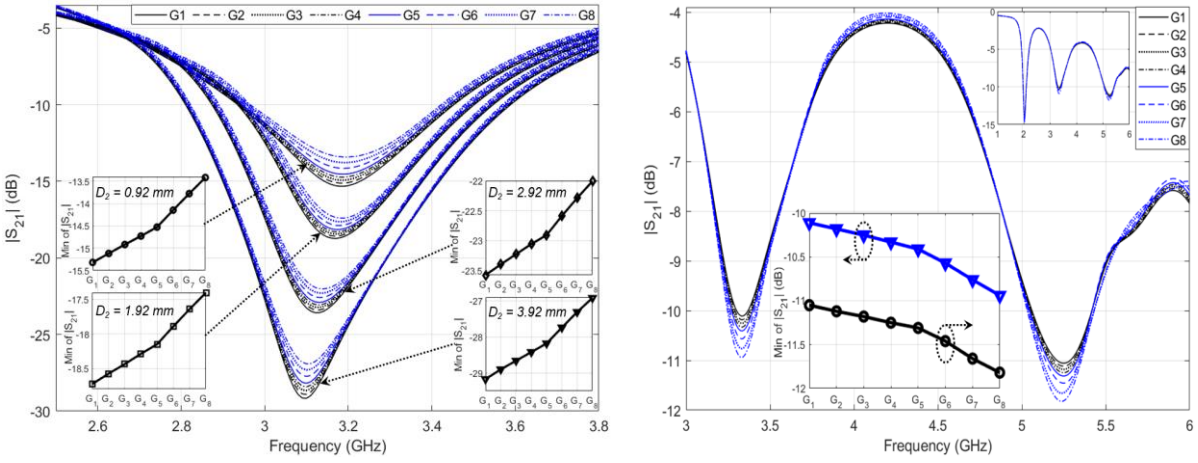

(a) (b)

Figure 3.17: Simulated transmission response of the TP-CSRR loaded with glucose concentrations G1 – G8 (a) at different D_2 models, (b) on top of a skin layer.

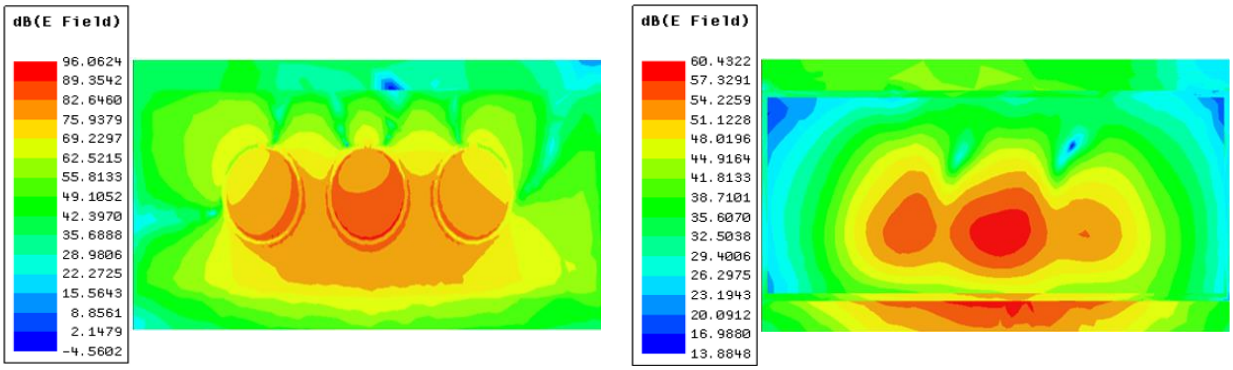

(a) (b)

Figure 3.18: Electric field distribution across the sensing region at the interface between (a) TP-CSRR and skin, (b) skin and glucose tissue.

3.4.8 Single-Loop Multiple-Coupled CSRRs

A modified version of the TP-CSRR sensing structure operating between 3 – 4 GHz is studied. It incorporates three identical resonators each of a single-loop complementary split-ring on the copper layer of a dielectric substrate as shown in Fig. 3.19(a). The annular loop of each resonator (of diameter *a*) ends in a *g*-width metallic slot. Similarly, the three resonators are coupled through the substrate with a two-port MTL of length L_{line} and width W_{line}. The resonating cells are configured in series at relatively close distance D_2 to enhance the inter-resonator coupling. The symmetry plane of the resonators is aligned orthogonally to the direction of field propagation along the MTL strip.

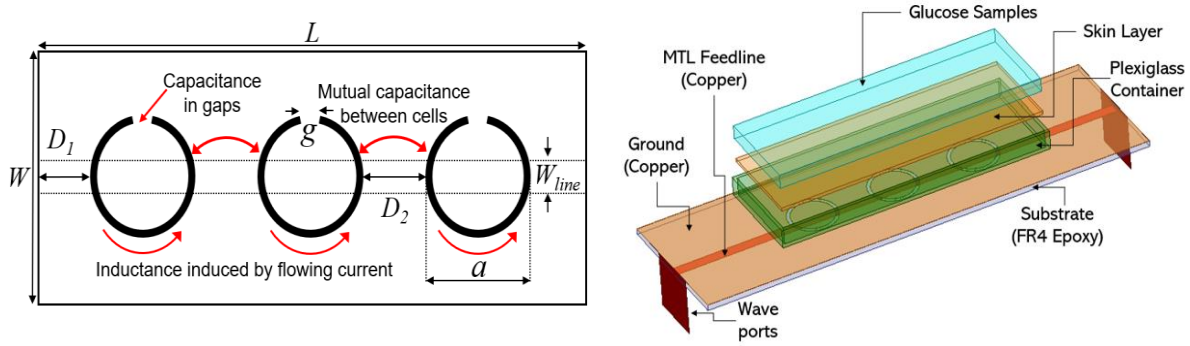

(a) (b)

Figure 3.19: (a) Layout of the metamaterial cells in the microstrip substrate, (b) sensor model loaded with glucose samples and skin layer inside a plexiglass container.

The geometry for each cell was chosen in the circular form not the rectangular or square that is conventionally used [156], [147]. Given the smaller circumference of the circles as compared to rectangles (of similar cross section), their associated lumped parameters (L_c, C_c, L_R, C_R) would be smaller [56], resulting in slightly higher f_o. Therefore, the circular CSRR is expected to have higher sensitivity for dielectrics compared to the rectangular type. Additionally, the average energy dissipation

per cycle (proportional to the tangential magnetic field H_t) is larger for the rectangular CSRR (~ due to its larger circumference) as compared to the circular resonator, and therefore the latter achieves higher *Q*-factor (Eq. (3.9)).

$$Q = \omega_0 \frac{W}{\mathrm{P}_L} = \frac{2}{\delta} \frac{\iiint |H|^2 \, dv}{\oiint |H_t|^2 \, ds} = \frac{f_o}{\Delta f_{3dB}} \approx 2\pi f_o R_P (C_r + C_c), \tag{3.9}$$

Lastly, implementing a single-loop in each cell would bring more sensitivity for the glucose permittivity measurements. This is expected since the double-loop has two concentric rings with a small gap between the inner and outer rings. This format would increase the effective capacitance C_R of each cell, and further reduces the dependence of the sensor minimum transmission response on the sample's equivalent capacitance or permittivity.

Table 3.6: Geometrical Parameters (in mm) of the Integrated Sensor

a	t	g	h	D_1	D_2	W	L	W_{line}
7.08	0.5	0.5	0.8	17.46	4.92	20	66	1.5

The HFSS simulator was used to design the proposed sensor on an FR4 substrate (ϵ' = 4.4 and *tanδ* = 0.02) with the specifications listed in Table 3.6, resulting in a transmission resonance of about -39.44 dB at f_o = 4 GHz. The impact of D_2 on the $|S_{21}|$ resonance profile was simulated at 1.92, 2.92, 3.92, 4.92, and 5.92 mm. With increased D_2, slight upshifts were observed in f_o, the resonance depth increases, and the 3-dB bandwidth decreases accordingly. A similar behaviour was demonstrated for the double-loop version of the sensor that resonates at lower frequency f_o = 2.3 GHz. The sensing performance of both sensors was numerically analyzed and compared for detecting changes in ϵ' and *tanδ* of a rectangular-shaped (36×20 mm^2) dielectric SUT of 2 mm thickness. The parametric sweep function was used to vary ϵ' in 10, 20, and 30, and for each, *tanδ* was changed in 0.01, 0.1, and 0.2, resulting into a total of 9 sensing instances. The resulted $|S_{21}|$ has shown a broadband scattering response with fundamental resonances induced between 1 – 3 GHz. In this spectrum, both sensors respond to the increase in ϵ' by lowering f_o, yet the single-loop device achieves a higher frequency resolution $\Delta f = |f_{SUT} - f_o|/f_o$ (i.e., percentage change in minimum transmission frequency) compared to the double-loop sensor as demonstrated in Table 3.7 for the three simulated cases of ϵ' (same resonant frequency for all *tanδ*). The sensors also modulate the resonance peaks to reflect the loss changes of the loaded SUT. However, the amplitude resolutions for varying *tanδ* are shown to be almost similar for both sensors.

Table 3.7: Sensitivity to dielectric constant changes in single- and double-loop CSRR

Sensor Type	$\Delta f = \left(\frac{\lvert f_{MUT} - f_r \rvert}{f_r}\right)$		
	$\epsilon' = 10$	$\epsilon' = 20$	$\epsilon' = 30$
Single-loop (TP-SL)	0.34	0.48	0.55
Double-loop (TP-DL)	0.27	0.41	0.50

The performance of the triple-pole single-loop (TP-SL) CSRR was numerically analyzed when the glucose concentrations of interest were loaded at volume 600 μL onto the sensing cells (inside a plexiglass container) as shown in Fig. 3.19(b). Mimicking glucose solutions of varying concentrations 40 – 600 mg/dL (denoted as G1 – G20) were integrated into the simulation using the first-order Debye model with the appropriate real and imaginary permittivity for each glucose sample at the operating spectrum 3 – 4 GHz.

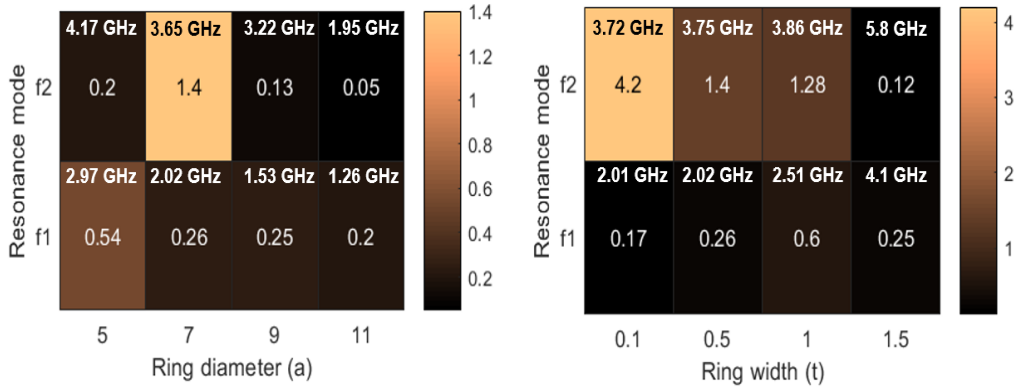

(a) (b)

Figure 3.20: Sensitivity analysis of the TC-SL CSRR at different (a) ring diameters, (b) ring widths.

The effect of the geometrical parameters (*a*, *t*, and *g*) of each resonant cell on the sensitivity performance of the TP-SL CSRR was studied by simulating a subset of the glucose samples on top of different configurations of the sensor cells. The ring diameter *a* represents the effective length of the dielectric slit, therefore increasing *a* from 5 mm to 11 mm (*g* and *t* were fixed at 0.5 mm) would increase L_r and decrease f_o from 2.97 GHz to 1.26 GHz (fundamental resonance) and from 4.17 GHz to 1.95 GHz (harmonic resonance) as demonstrated in Fig. 3.20(a). The heatmap also portrays the average amplitude resolution (in dB) at both resonance modes. A moderate cell size (a = 7 mm) has shown to bring the highest sensitivity (i.e., largest amplitude resolution of about 1.4 dB per 0.02 change in ϵ' and 0.002 change in $tan\delta$) for glucose detection around f = 3.65 GHz.

Next, the ring width *t* was varied from 0.1 mm to 1.5 mm as shown in Fig. 3.20(b) with *a* and *g* both fixed at 0.5 mm and 7 mm, respectively. The best amplitude resolutions in both first and second resonant modes was achieved at t = 0.5 mm. However, a 4.2 dB resolution was observed in the second resonance for the layout with t = 0.1 mm. Lastly, the metallic split-gap g for each cell is directly correlated to its induced capacitance C_r that decreases with an increased g, thereby increasing f_o accordingly. The structure was simulated at different split-gaps g = 0.25, 0.5, and 1 mm, yet no significant difference in the amplitude resolution was observed for the varying glucose levels.

A subset of glucose samples G1 – G8 were simulated onto different models of the sensor with D_2 varying between 1.92, 2.92, 3.92, and 4.92 mm. The resulting $|S_{21}|$ are plotted in Fig. 3.21(a-d) for the four respective cases in the 3.6 – 3.8 GHz range. The two models with D_2 = 1.92 mm (Fig. 3.21(a)) and 4.92 mm (Fig. 3.21(d)) show higher amplitude resolutions compared to other cases. Besides, their

resonant amplitudes (min of $|S_{21}|$) were observed to change non-linearly with increased glucose concentrations, and sometimes follow a non-monotonic pattern as depicted in the insets of Fig. 3.21(a) and 3.21(d).

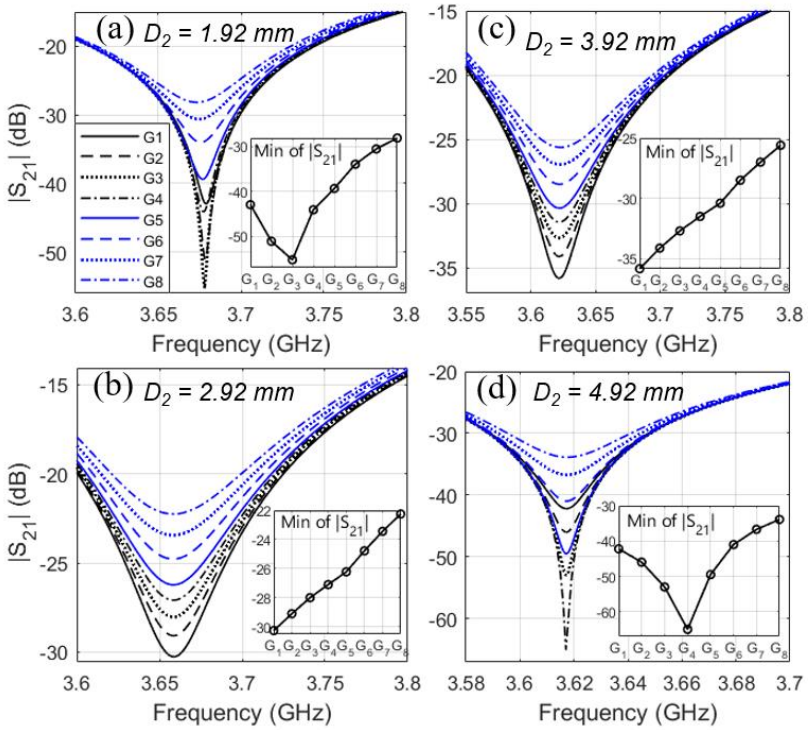

Figure 3.21: Simulated $|S_{21}|$ responses to glucose samples G1 – G8 at different configurations of (a) D_2 = 1.92 mm, (b) D_2 = 2.92 mm, (c) D_2 = 3.92 mm, (d) D_2 = 4.92 mm (without skin)

To imitate the realistic scenario of attaching the sensor to a specific body part (e.g., finger, earlobe, wrist, etc.) for non-invasive BGL monitoring, another simulation model was performed where a 0.5 mm skin layer was introduced between the sensor surface and samples G1 – G8 of thickness 2 mm each. This skin layer is a lossy medium (ϵ_r' = 38.1 and $tan\delta$ = 0.28) [165] that is expected to attenuate the electric field penetration to glucose tissues, and thereby weaken the sensing interaction. The model was implemented for the best two configurations D_2 = 1.92 and 4.92 mm as inferred from the previous analysis, and the responses are shown in Fig. 3.22(a) and 3.22(b), respectively. A lower amplitude resolution for the glucose property changes was observed at both cases due to the inclusion of the lossy skin tissue. However, the detection sensitivity with D_2 = 4.92 mm has shown to be relatively higher for the varying concentrations.

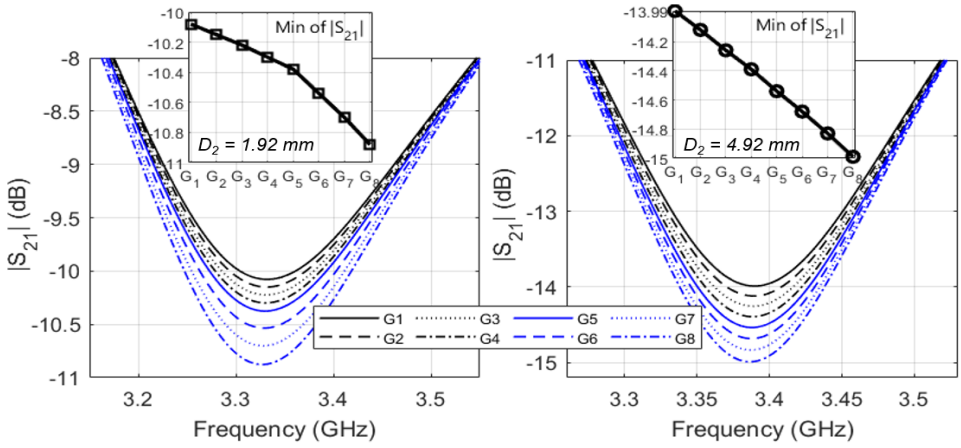

(a) (b)

Figure 3.22: Simulated $|S_{21}|$ responses to glucose samples G1 – G8 at different configurations of (a) D_2 = 1.92 mm, and (b) D_2 = 4.92 mm (with skin)

3.4.9 Machine Learning Analysis

Previous numerical analysis has shown that the TP-SL CSRR sensor could distinguish various glucose concentrations by tracking the transmission coefficients $|S_{21}|$ at the resonance frequency. However, these variations in resonant amplitude from one glucose level to another are noticed to be relatively small and sometimes tricky to trace especially for the case where the lossy skin layer is introduced. To help identifying various BGLs more precisely with a higher resolution, the principal component analysis (PCA) algorithm is applied to conclude the high dimensional data near resonance into fewer variables that identify various glucose levels more precisely without a prior domain knowledge about the most sensitive resonance data.

The PCA as a robust classification algorithm can be used to further analyze the raw data induced by the sensor for different glucose samples. Particularly, to enhance the small scattering differences between various glucose levels, the PCA algorithm is used to map the feature vectors (i.e., measured scattering data) for each glucose sample into a two-dimensional space where each glucose concentration is represented by only two indices called the principal components $\mathcal{K}$. This will help to bring a higher resolution when the sensor responses are correlated to different blood glucose levels. In other words, the PCA algorithm creates a mapping between 1) $X \in R^N$: the N-dimensional input variables' vector (also referred to as the features' vector) which corresponds to the measured $|S_{21}|$ or $\angle S_{21}$ obtained at the different frequencies over the operating frequency range and 2) $y \in R$: the outcome variable which corresponds to the estimated glucose level.

The theory of the PCA algorithm is based on the dimensionality reduction of the problem where a vector space transformation is performed [166]. Herein, the PCA is exploited to extract important features from the sensing data set of the sensor scattering responses and further to express this

information as a set of orthogonal variables called principal components [167]. Generally, these principal components are derived from the eigen-decomposition of positive semi-definite matrices and the singular value decomposition of rectangular matrices [167]. In this sense, original datasets of high dimensionality could be reduced to smaller number of distinctive features or variables via mathematical projection without missing much information to analyze patterns, tendencies, and anomalies.

The pseudocode in Algorithm 1 describes this classification routine when applied to the sensing data from measurements or simulations. In particular, the PCA algorithm would map the feature vectors or collected sensing data $|S_{21}|_{G_m}(f)$ over a range of frequency (indexed by $f = 1, 2, \dots, N$, where N is the total number of frequency points), for each glucose sample G_m ($m = 1, 2, \dots, M$, where M is the total number of glucose smaples) into a two-dimensional space where each glucose concentration is represented by only two indices or principal components $\mathcal{K}_{G_m}^1$ and $\mathcal{K}_{G_m}^2$.

Algorithm 1: PCA classification algorithm.

Input the feature vector (measured data) $x_{C_m}(n)$ of each glucose sample C_m, where $m = 1, 2, \dots, M$ (total number of glucose smaples), x could be either $|S_{21}|$ or $\angle S_{21}$, n is the index number for the frequency points that ranges $n = 1, 2, \dots, N$, N is the total number of frequency points.
Formulate the data matrix X (MxN) with feature vectors in each row. $X = [x_{C_1};\ x_{C_2};\ \dots; x_{C_M}]$
Perfom the feature normalization for each entry in X
Evaluate the Covariance matrix $Cov = \frac{1}{M}X'X$ (matrix of NxN dimension)
Perform the singular value decomposition $[\mathrm{U}, \mathrm{S}, \mathrm{V}] = \mathrm{svd}(\mathrm{Cov})$ to extract the U (NxN) matrix of N eigenvectors
Select the first K eigenvectors from matrix U: $u = U(:, 1{:}K)$
Perform the data projection $Z = Xu$ to reduce the number of features (dimensionality) for each glucose sample from N to K
Output the principal components $\mathcal{K}_{C_m}^i$ for each glucose sample C_m, $i = 1, 2, \dots, K$, where K is the total number of principal components

To demonstrate the efficacy of the PCA algorithm, it was applied to analyze the scattering data of the optimized TP-SL CSRR sensor (with D_2 = 4.92 mm) for the glucose concentrations G1 – G20 that range between 40 – 600 mg/dL covering the entire diabetes conditions spectrum (hypoglycemia, normal, and hypoglycemia). Figure 3.23(a) shows the linear regression model that correlates the resulting resonance amplitudes of the sensor to the simulated glucose concentrations G1 – G20. One feature vector was extracted for each glucose concentration G_m from the resulting frequency response in the range 3.3 – 3.5 GHz. These features represent not only the resonant amplitude at a single frequency f = 3.4 GHz (min of $|S_{21}|$), but rather the entire induced $|S_{21}|$ magnitudes at N = 201 frequency points spanning the range 3.3 – 3.5 GHz. This selected bandwidth near resonance (±0.1 GHz) show the most significant variations in the sensor response at different glucose levels.

The derived feature vectors for each G_m were normalized and arranged as rows in one data matrix $G\ (MxN) = [|S_{21}|_{G_1};\ |S_{21}|_{G_2};\ \ldots;|S_{21}|_{G_{20}}]$. Next, the covariance matrix $Cov\ (NxN) = \frac{1}{M}G'G$ was evaluated and decomposed to extract the $U\ (NxN)$ matrix of N eigenvectors. The dimensionality of each concentration's fetaure vector was reduced from $N = 201$ to $K = 2$ by projecting the sensing data $\mathcal{K} = G\ U(:,1{:}K)$ to extarct two principal components $\mathcal{K}^1_{G_m}$ and $\mathcal{K}^2_{G_m}$ for each glucose concentration $G_1 - G_{20}$ as plotted in Fig. 3.23(b). $\mathcal{K}^1_{G_m}$ explains 67.33% of the total variance in the sensing data, while $\mathcal{K}^2_{G_m}$ explains the remaining 32.67%. The simulated concentrations are shown to be mapped into the 2D space in a parabola pattern with higher spatial separation between each. This would thereby enhance the resolution of the scattering data that are correlated to different glucose concentrations.

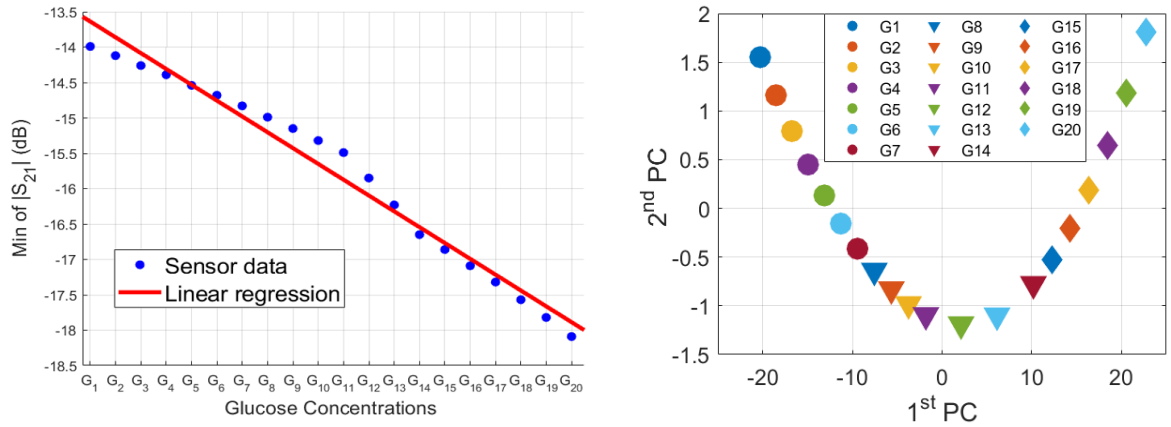

(a) (b)

Figure 3.23: (a) Linear regression model correlating the resulting resonant amplitudes to the varying glucose samples, (b) mapping the high dimensionality scattering responses of the TP-SL sensor into a two-dimensional space for each glucose concentration

3.4.10 Wearable Version (Reader/Tag)

An improved design of the TP-CSRR biosensor was developed in the tag/reader format for non-invasive blood glucose monitoring. This design configuration offers a sensing distance between the communicating reader and tag suitable for adapting the device as wearable as shown in Fig. 3.24(a). The passive tag is based on the CSRR technology that offers multiple features when used for sensing. The sensing structure comprises a groundless resonator that serves as a passive tag and a simple flexible antenna that works as a reader as depicted in Fig. 3.24(a). The tag sensing is composed of three similar cells of circular CSRRs patterned horizontally on the top layer of an FR4 dielectric substrate ($\epsilon'_r = 4.4$ and tanδ = 0.02) as depicted in Fig. 3.24(b). The sensing elements (three CSRRs) in the passive tag are coupled to the remote interrogator antenna at the operating frequency f = 2.3 GHz. This layout is different from the previous excitation method using an attached microstrip-line on the bottom face (i.e. ground plane) of the same dielectric substrate of the tag structure. The three CSRRs in the sensing tag were

configured similarly to the previous design to realize a larger sensing region of concentrated electric field, thus enabling a higher sensitivity for glucose detection.

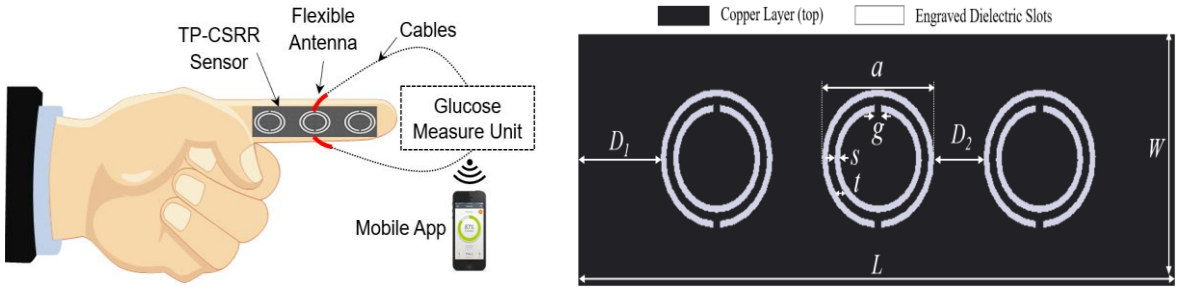

(a) (b)

Figure 3.24: (a) Illustration of the wearable sensing system (tag: TP-CSRR sensor and reader: flexible antenna) when attached to the subject finger, (b) configuration of the three CSRR cells in the copper layer of the sensing tag (top view).

Figure 3.24(a) illustrates the sensor realization as a wearable on the patient finger for continuous BGL monitoring. It could also be adapted as a wearable around the patient wrist. The reader part coupled with the sensing tag could be of any antenna type that conforms to the wearable standards. In fact, it is preferable for the wearable antenna structure to be of low-profile, low-cost, simple-geometry, and directional EM radiation pattern to enhance the performance efficiency of the integrated sensor when attached to the finger part [168]. When the tag is electrically coupled by the antenna radiation at the resonance frequency, an electric field of high localization and concentration will be generated along the tag surface in the near-field region, thus allowing the sensor to detect small variations in the EM properties that characterize the varying glucose levels in the underlying tissue. The attached finger would consequently perturb the distribution of the highly concentrated electric field in the tag, and further induce noticeable changes in the scattering response at the antenna port. The variations in the reflected signals are further analyzed to extract the signature of the measured blood glucose level.

The performance of the proposed sensor was numerically analyzed when used for non-invasive BGL monitoring using the HFSS FEM simulator. First, a $\lambda/2$ dipole antenna was designed using a perfect electric conductor (PEC) to couple the passive TP-CSRR tag at the operating frequency f = 2.3 GHz as shown in Fig. 3.25(a). The passive resonators in the tag will be electrically excited from distance d as shown in Fig. 3.25(b) and 3.25(c). Accordingly, the dipole antenna will act as an active reader that communicates from this sensing distance with the TP-CSRR tag when used for glucose sensing. The driven solution of each simulation model was set with the appropriate parameters of solution frequency = 2.3 GHz, maximum number of passes = 30, delta S for allowable variation between consecutive meshes = 0.005, and minimum converged passes = 4. The frequency solution was set with interpolation sweep in the range 1 – 4 GHz with 0.001 GHz resolution. The meshing sizes for the tag and dipole structures were chosen suitably to achieve the convergence criteria. A lumped-port was used for the dipole excitation and set with the appropriate size. Both antenna and tag were enclosed inside an airbox with

radiation boundary condition to imitate the free space into a finite domain. Thus, ensuring the maximum absorption for the radiated fields with minimum reflections from the surrounding surfaces.

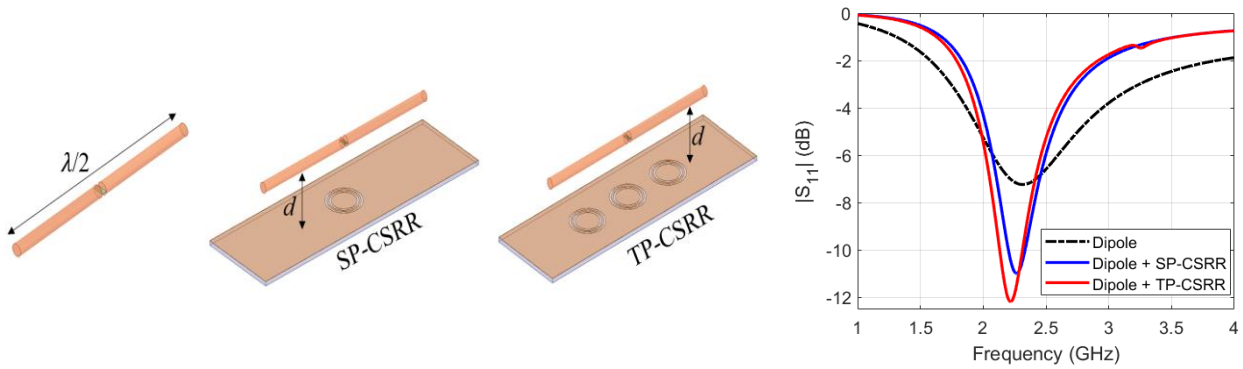

(a) (b) (c) (d)

Figure 3.25: (a) Dipole antenna used as a reader. Integrated sensor structure with (b) single-pole CSRR tag, (c) triple-pole CSRR tag, and (d) comparison of the simulated reflection coefficient response of the TP-CSRR integrated sensor to that of the bare dipole and SP-CSRR cases.

Before loading any glucose sample, the performance of the integrated sensor was compared to that of a bare dipole antenna (Fig. 3.25(a)) and when a single-pole CSRR is patterned in the tag (Fig. 3.25(b)). Figure 3.25(d) depicts the simulated reflection coefficients $|S_{11}|$ (return loss) over the frequency range 1 – 4 GHz for the three respective cases. The bare antenna has a wideband reflection response that resonates around f = 2.32 GHz with -7.23 dB return loss. The $|S_{11}|$ is shifted slightly towards lower frequencies when the passive tags are attached at distance d = 4 mm from the dipole. In particular, the scattering response is shifted to f = 2.27 GHz and f = 2.22 GHz for the SP-CSRR and TP-CSRR tags, respectively. Additionally, attaching the passive tag would strengthen the resonance perceived at the antenna port and narrow its 3-dB bandwidth. It is also observed that the TP-CSRR tag exhibits a steeper resonance peak/depth of about -12.18 dB compared to -11.36 dB for the case of SP-CSRR. Having three cells integrated together on the tag surface will relatively enhance the resonance strength and confine the resonating electric fields over a larger sensing region via exploiting the mutual coupling originated between the three resonating cells.

The sensor performance was analyzed when the glucose concentrations of interest, 60 – 500 mg/dL relevant to different diabetes conditions (normal, hypoglycemia, and hyperglycemia), were introduced in the sensing area on top of the tag as shown in Fig. 3.26(a). The glucose samples were modelled in a rectangular shape of 39 × 13 mm^2 and 2 mm height inside a plexiglass container as shown in Fig. 3.26(a). The sensing parameter used for tracking the glucose level variations was the reflection coefficient $|S_{11}|$ which represents the amplitude ratio of the reflected wave to the incident wave at the antenna port written with respect to frequency.

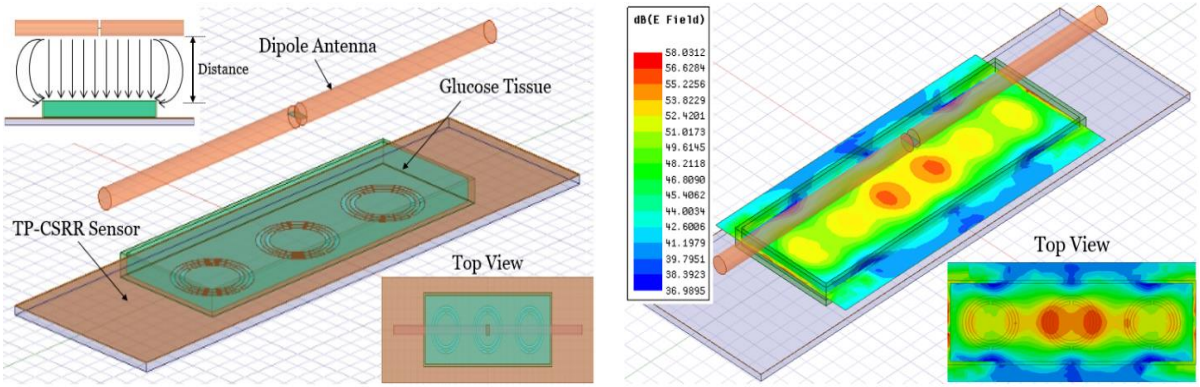

(a) (b)

Figure 3.26: (a) Simulation model of the glucose samples in the sensing region of the TP-CSRR tag. Enclosed plots show the top view of the loaded sensor (bottom right) and the EM coupling between the dipole and loaded-sensor at a specific distance (top left), (b) Electric field distribution at resonance across the G1 glucose sample loaded on top of the TP-CSRR tag at 5 mm distance from the antenna.

The first-order Debye model with the coefficients listed in Fig. 3.16(b) was used to approximate the dielectric properties of the blood mimicking samples at disparate glucose concentrations 60 – 500 mg/dL. The extracted model was integrated into the FEM simulator over the operating frequency range 1 – 4 GHz. The glucose samples were first simulated in proximity of the bare dipole antenna at d = 4 mm without the TP-CSRR tag to study the effect of the glucose level variations on the electric field induced by the interrogating antenna and its scattering response. The parametric sweep function in HFSS was used to vary the ϵ_r' and $\tan\delta$ parameters for the G1 – G8 samples. As expected, no significant change in the antenna $|S_{11}|$ was observed in reaction to the varying dielectric parameters of the glucose samples in the vicinity of the radiator. Apparently, detecting the small changes in the EM properties of the glucose samples requires a highly confined and concentrated electric field that is not afforded by the setup of the bare antenna wherein the radiated fields are dispersed around in the near- and far-field regions.

The full sensor structure with the TP-CSRR tag was analyzed for sensing the glucose concentrations inherent in the loaded samples G1 – G8 as shown in Fig. 3.26(a). The dipole antenna was placed at two sensing distances above the tag, 4 and 5 mm. The TP-CSRR has shown to be sensitive to the dielectric property changes of various glucose samples placed nearby the passive CSRR cells. This sensitivity to glucose dielectric contrast is translated to variations in the antenna reflection coefficient via the EM coupling between the dipole and the passive tag. As depicted in Fig. 3.26(b), the EM field variations around the passive TP-CSRR when loaded with different glucose concentrations will affect the input impedance of the antenna, and hence its reflection coefficient.

Figure 3.27(a) shows the simulated reflection coefficient $|S_{11}|$ of the dipole in the frequency range 1 – 4 GHz when the TP-CSRR tag was placed at d = 4 mm. Two resonances were observed around f = 2 GHz and f = 3.44 GHz. The resonant amplitude at both is varying in response to the glucose concentration changes G1 – G8 as depicted in Fig. 3.27(b) and 3.27(c), respectively. However, the

second resonance has shown more sensitivity with higher resolution to glucose level changes. In specific, the amplitude variation per unit change in ϵ_r' $\left(\frac{\Delta|S_{11}|}{\Delta|\epsilon_r'|} = 13.5 \text{ dB}\right)$ and $tan\delta$ $\left(\frac{\Delta|S_{11}|}{\Delta|tan\delta|} = 135 \text{ dB}\right)$ compared to those recorded at the first resonance 3.5 dB and 35 dB, respectively. Similarly, Fig. 3.28(a) shows the reflection responses for the case of d = 5 mm with two resonances at f = 2.04 GHz and f = 3.32 GHz. Notably, the first resonance strength has significantly increased at this distance, and therefore brings a higher amplitude resolution of about $\left(\frac{\Delta|S_{11}|}{\Delta|\epsilon_r'|} = 25 \text{ dB}\right)$ and $\left(\frac{\Delta|S_{11}|}{\Delta|\text{tan}\delta|} = 250 \text{ dB}\right)$ for identifying different glucose concentrations.

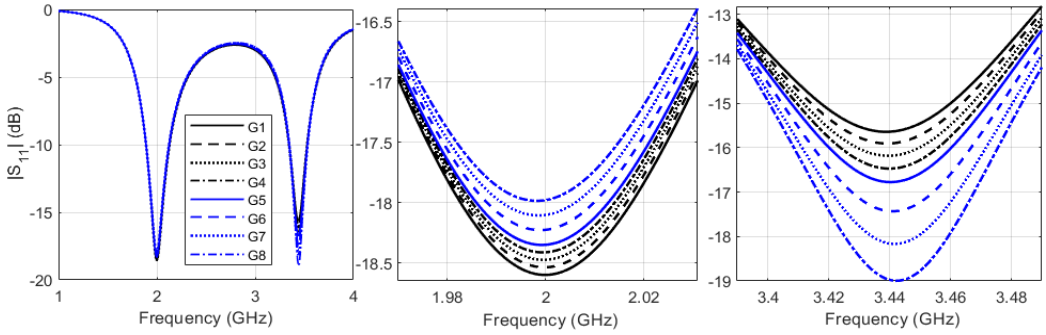

(a) (b) (c)

Figure 3.27: Simulated reflection responses at d = 4 mm between the dipole and loaded-TPCSRR, (a) over the frequency range 1 – 4 GHz, (b) resonant amplitudes at f = 2 GHz, (c) resonant amplitudes at f = 3.44 GHz

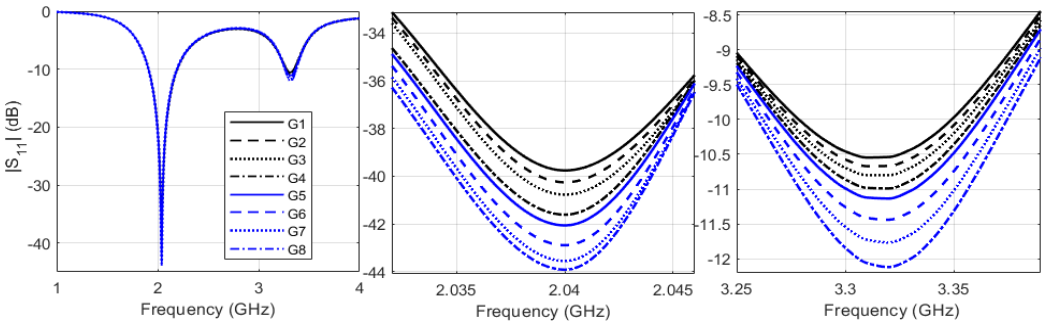

(a) (b) (c)

Figure 3.28: Simulated reflection responses at d = 5 mm between the dipole and loaded-TPCSRR, (a) over the frequency range 1 – 4 GHz, (b) resonant amplitudes at f = 2.04 GHz, (c) resonant amplitudes at f = 3.32 GHz

The glucose samples G1 – G8 were also numerically simulated on top of a passive tag of a single CSRR cell at d = 4 mm from the dipole to compare the glucose detection sensitivity to that of our proposed sensor that uses TP-CSRR tag. Figures 3.29(a) and 3.29(b) depict the resonant amplitude resolution at the varying glucose levels for both sensors. The minimum of $|S_{11}|$ at the first resonance around f = 2.06 GHz and f = 2.0 GHz for different glucose samples introduced onto the SP-CSRR and TP-CSRR tag, respectively, are shown in Fig. 3.29(a). Figure. 3.29(b) shows the same results at the second resonance around f = 3.19 GHz and f = 3.44 GHz, for the SP-CSRR and TP-CSRR, respectively. Clearly, the TP-CSRR tag realizes a larger amplitude resolution for tracking the glucose level changes. This is explained by Fig. 3.29(c) and 3.29(d) that portray the electric field distribution across the G1

sample at f = 2.3 GHz when loaded onto each sensor. As depicted in Fig. 3.29(d), the electric field is highly concentrated in the TP-CSRR tag with higher magnitudes along a larger sensing region wherein the glucose samples are loaded. However, the electric field in Fig. 3.29(c) is relatively restricted in a smaller region that corresponds to one cell of the SP-CSRR tag.

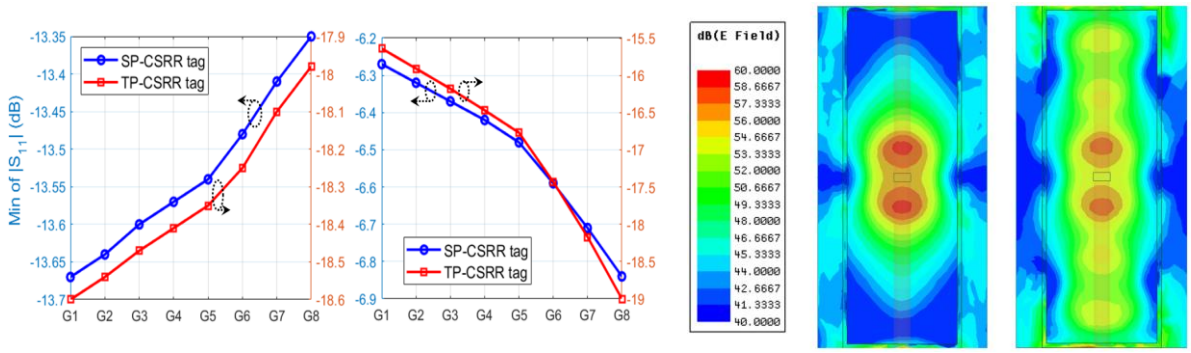

(a) (b) (c) (d)

Figure 3.29: Variations of the resonant amplitude at the two resonances ((a) first resonance, (b) second resonance) induced in the SP-CSRR and TP-CSRR sensors at the different glucose levels. Electric field distribution at f = 2.3 GHz across the G1 glucose sample when loaded on top of (c) SP-CSRR tag and (d) TP-CSRR tag at 4 mm from the antenna.

The sensitivity of the sensor was further studied when a skin layer (ϵ_r' = 38.1 and $tan\delta$ = 0.28) of thickness 1 mm was introduced between the tag and the glucose samples G1 – G8 as shown in Fig. 3.30. The dielectric parameters for the skin were reported from the database in [165] with dielectric constant = 38.1 and loss tangent = 0.28. This simulation model would provide some insights for the sensor performance in a practical scenario when the sensor is attached to the finger. The sensor response in the updated model was simulated over the frequency range 1 – 4 GHz as depicted in Fig. 3.31(a), with two resonances induced at f = 1.918 GHz (Fig. 3.31(b)) and f = 3.45 GHz (Fig. 3.31(c)). Both resonances exhibit remarkable amplitude variations for the glucose level changes, however, the detection sensitivity is much higher (larger amplitude resolution) at the second resonance compared to that of the first resonance as shown in Fig. 3.31(c) and Fig. 3.31(b), respectively. The sensor preserved the high sensitivity performance despite the inclusion of another lossy layer of the skin tissue.

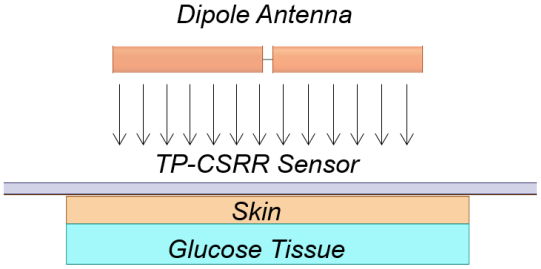

Figure 3.30: Front view of the integrated CSRR sensor when used for sensing the glucose samples under a skin layer

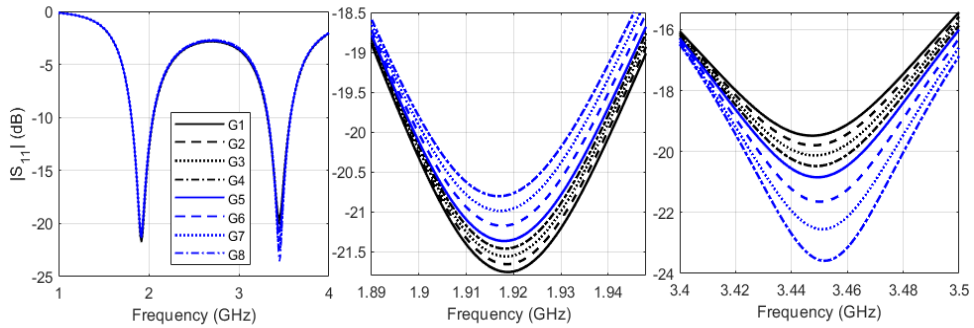

(a) (b) (c)

Figure 3.31: Simulated reflection responses at d = 5 mm between the dipole and TP-CSRR tag loaded with glucose and skin, (a) over the 1 – 4 GHz frequency range, (b) resonant amplitudes at f = 1.918 GHz, (c) resonant amplitudes at f = 3.45 GHz

3.4.11 Experimental Measurements

In this subsection, the fabricated TP-CSRR prototypes were practically experimented for detecting the glucose levels in two different tissues, aqueous solutions, and synthetic blood (hemoglobin-based).

3.4.11.1. Samples preparation. To mimic the practical condition of Type-2 diabetes, mimicking tissues were carefully prepared in small disparate glucose concentrations 80, 100, and 120 mg/dL at 10 mL volume each using a micropipette device in the laboratory. To do so, volume V_1 was drawn from the stock glucose solution of C_1 = 1000 mg/dL as calculated using the dilution equation $C_1V_1 = C_2V_2$ to synthesize glucose aqueous samples of volume V_2 = 10 mL each at the desired concentrations C_2 = 80, 100, and 120 mg/dL. Another set of hemoglobin-mixed samples were prepared at the desired concentrations C_2 following the same recipe by adding volume V_1 from the standard glucose solution to $V_2 – V_1$ of a pure fake blood instead of distilled water [169].

3.4.11.2. Glucose sensing on DL TP-CSRR. Measurements of the scattering responses of the TP-CSRR sensor (double-loop version) were performed using the Keysight Technologies PNA N5227A Network Analyzer by sweeping the frequency across the cm-wave band 1 – 6 GHz. Before connecting the sensor with the VNA, its full two-port calibration was performed using the standard Open-Short-Load technique to eliminate any undesired effects on the measurements, and hence accurate producible measurements would be achieved. The S-parameters data were recorded at 22ºC room temperature, 1600 frequency points resolution, 50 Hz IF BW, and -10 dB input power for the testing port. The channel-loaded TP-CSRR was connected via coaxial cables to the VNA power source as shown in the complete experimental setup in Fig. 3.32(a).

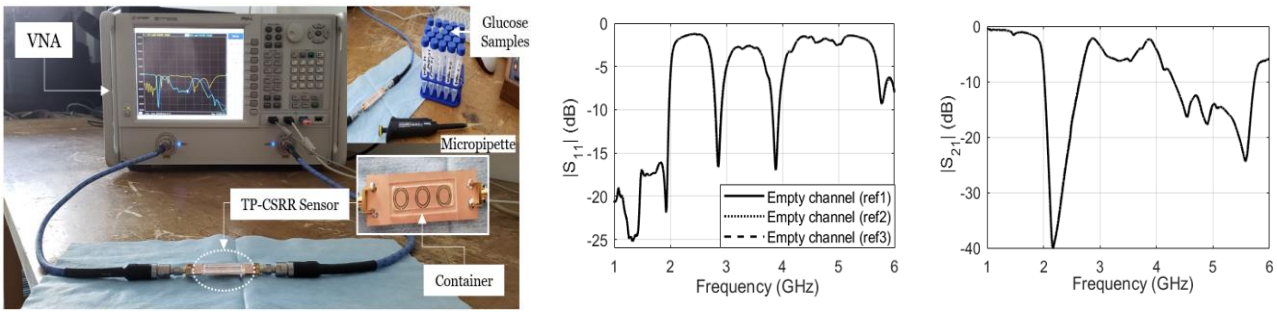

(a) (b) (c)

Figure 3.32: (a) Experimental setup for glucose sensing. Measured (b) reflection and (c) transmission coefficients over a broad band 1 – 6 GHz for the empty channel-loaded TP-CSRR sensor.

First, before loading any glucose sample, the reflection and transmission responses of the TP-CSRR were measured and verified as plotted in Fig. 3.32(b), and 3.32(c), respectively. Next, the TP-CSRR sensor was tested for detecting the glucose level in the three prepared aquatic glucose samples of 80, 100, and 120 mg/dL. In each trial of the subsequent measurements, the micropipette device was used to measure a precise volume of V = 600 µL from a given concentration sample and load it inside the channel in three consecutive batches of 200 µL each. After each drop of V = 200 µL, noticeable shifts in the reflection S_{11} and transmission S_{21} resonances were observed towards lower frequencies which imply a dependency of the resonance frequency on the sample volume. However, these resonances were perfectly converged to a lower frequency limit beyond the sample volume of 600 µL that enabled a homogenous distribution of the glucose sample inside the channel whereby the sensing area was entirely covered. Based on the last result, the stable volume of 600 µL was adopted as a constant volume for testing all the glucose samples in the subsequent measurements to minimize the measurement errors due to uncertainty in the sample volume.

Once a sample of given concentration was fully loaded then the corresponding reflection and transmission signals were recorded in the frequency band 1 – 6 GHz. The transmission response of the TP-CSRR loaded with an empty channel was considered as a reference for all measurements of glucose samples (Fig. 3.32(b)). A clean tissue paper was used after each measurement trial to completely remove the glucose sample in place before loading another concentration. This is important to reset the reference resonance at S_{21} before loading a new sample and hence guaranteeing precise measurements for fair comparisons. The S-parameters corresponding to the 80, 100, and 120 mg/dL glucose samples were measured to record the resonance frequencies as well as their minimal amplitudes in both modes of reflection and transmission. The glucose concentration changes were reflected more prominently as amplitude variations in the resonance peaks of the harmonic resonances established towards higher frequencies 4.8 – 5.8 GHz (reflection response in Fig. 3.33(a)) and 3.5 – 5.1 GHz (transmission response in Fig. 3.33(b)), thus demonstrating the sensor capability to detect the small variations in the loss properties of the tested glucose samples. For repeatability verification, each glucose sample measurement was repeated for three times while paying attention to restore the exact reference response

of the empty channel-loaded sensor after any sample removal as shown in Fig. 3.32(b) and 3.32(c). Each scattering plot is an average of three repeatable measurements for the respective glucose sample.

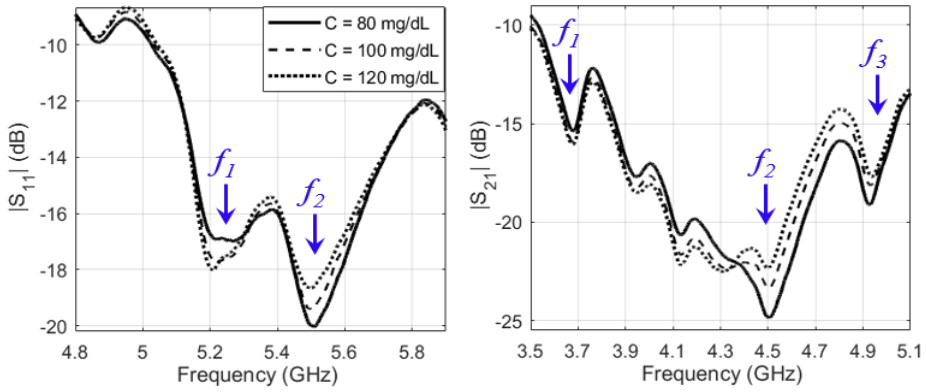

(a) (b)

Figure 3.33: Measured (a) reflection and (b) transmission coefficients for the tested glucose samples on the higher frequency regions.

To verify the detection functionality of the sensor, it was experimented again for hemoglobin samples of similar glucose concentrations 80, 100, 120 mg/dL using the setup in Fig. 3.34. The reflection and transmission responses of the sensor when loaded with blood samples of concentrations 80, 100, and 120 mg/dL were both measured and plotted in Fig. 3.35 and 3.36, respectively. In the reflection response depicted in Fig. 3.35, the two resonances recorded in the frequency range 2.75 – 3.25 GHz and 5 – 5.5 GHz change their depths in response to the varying glucose concentrations. Similarly, the three resonances captured in the transmission response in Fig. 3.36 were all responsive to the glucose level changes. The resonances around 1.5 – 1.7 GHz and 4.25 GHz shift their frequencies towards lower bands with an increased glucose level, while the last resonance around 5.1 GHz changes its resonant amplitude accordingly.

To avoid significant impact of any environmental and instrumental intakes onto the measurements, the sensing experiments were performed in an environment of controlled temperature 22±1°C mimicking indoor environments where such experiments are performed. However, small fluctuations in temperature will not significantly change the resonant amplitude readings of such CSRR structures (±0.03 – 0.09 dB/°C) [170]. Additionally, the tested glucose samples were all stored in the same room temperature of 22±1°C. This is necessary since the sensor scattering responses are enormously dependent on the glucose sample permittivity that is shown to be temperature dependent [170].

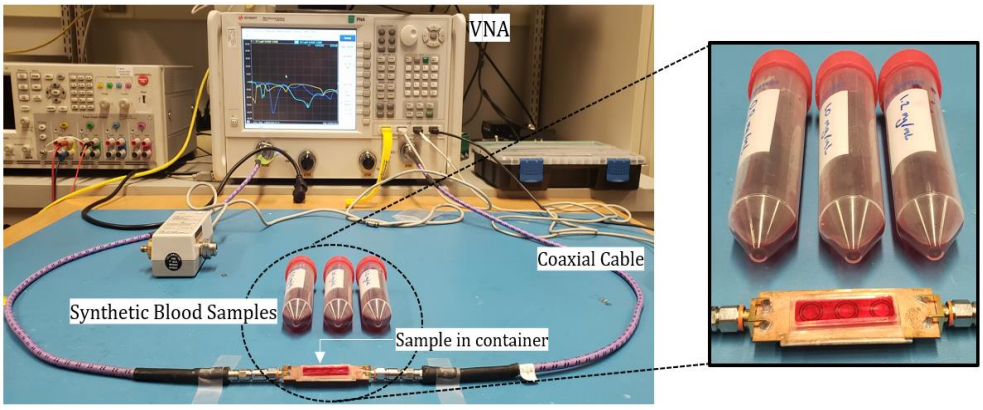

Figure 3.34: Experimental setup for testing synthetic blood samples

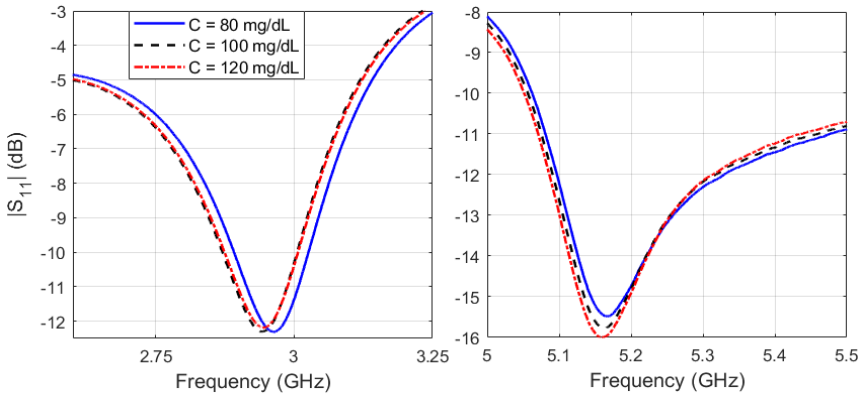

Figure 3.35: Measured reflection coefficients for the tested glucose samples

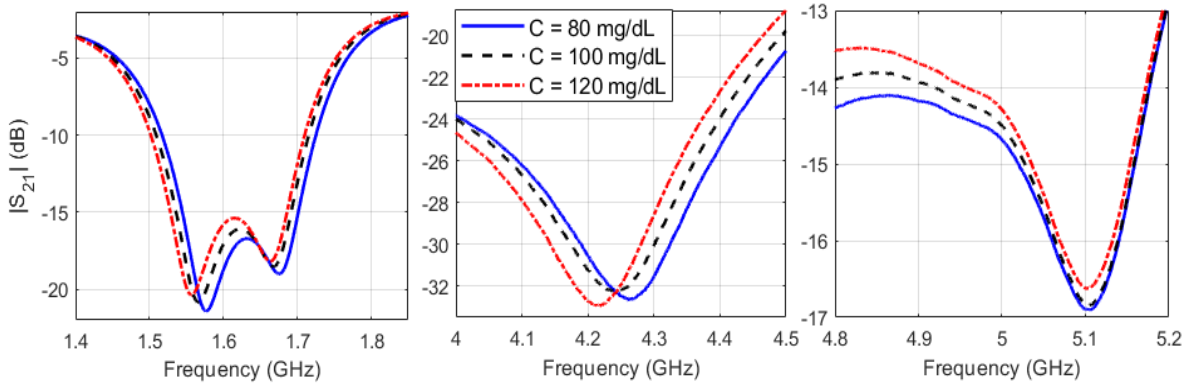

Figure 3.36: Measured transmission coefficients for the tested glucose samples.

The VNA experimental measurements of the S-parameters of the glucose-loaded TP-CSRR sensor have shown considerable variations in the peak amplitudes of the harmonic resonances of the S_{11} and S_{21} for varying the glucose levels between 80, 100, and 120 mg/dL. In what follows the sensitivity of the sensor is evaluated in terms of the absolute change in the magnitude of S_{21} or S_{11} (in dB) at any of the resonances corresponding to change in glucose concentration (in mg/ml). Two resonances f_1 = 5.21 GHz and f_2 = 5.51 GHz were recorded in the reflection response of the glucose-loaded sensor in the

frequency range 4.8 – 6.0 GHz as indicated by the blue arrows in Fig. 3.33(a). It is observed that the reflected magnitude at f_1 slightly increases while that at f_2 decreases with increased glucose level. The average sensitivity at the two resonances were calculated as 2.73 and 3.45 dB/(mg/ml), respectively. Similarly, three distinct resonances f_1 = 3.68 GHz, f_2 = 4.5 GHz, and f_3 = 4.92 GHz (indicated by arrows in Fig. 3.33(b)) were recorded in the S_{21} transmission response of the sensor when used for glucose detection. The amplitude variations in the transmission resonances are more significant compared to their reflection counterparts as illustrated in Fig. 3.37. The harmonic resonance at f_2 = 4.5 GHz is the most sensitive mode where the glucose concentration of a tested sample can be distinctly detected with a considerable sensitivity of about 6.2 dB/(mg/ml) in average.

In the operating frequency range of the sensor, the data sheet of the VNA measuring tool used in these experiments poses for higher uncertainties in the readings of the reflection coefficient $|S_{11}|$ compared to the transmission coefficient (≈ ±0.1 dB uncertainty at -20 – -25 dB transmission). This is also evidenced by the repeatability measurements that show ±0.2 dB variations in the resonant amplitudes of $|S_{11}|$ and ±0.1 dB for those in $|S_{21}|$. Therefore, magnitudes of resonance peaks in $|S_{21}|$ were adopted as more robust and reliable sensing parameters for the reported glucose measurements. By noting the resonant amplitudes recorded at the favorable $|S_{21}|$ resonance mode (f_2 = 4.5 GHz) of about -24.81 dB, -23.28 dB, and -22.33 dB amplitudes for the glucose concentrations 80, 100, and 120 mg/dL, respectively, thus yields a minimum resolution $\Delta|S_{21}|/\Delta|C|$ of about 0.05 dB/(mg/dL). Considering the ±0.1 dB uncertainty in the VNA readings, this would imply that concentration changes as small as ΔC_{min} = 3 mg/dL could be reasonably detected in the S_{21} signal using the proposed sensor when connected to the VNA. Therefore, larger glucose variations (>= ΔC_{min}) would be reliably identifiable in the current setup since their corresponding amplitude changes are beyond the VNA noise limitation.

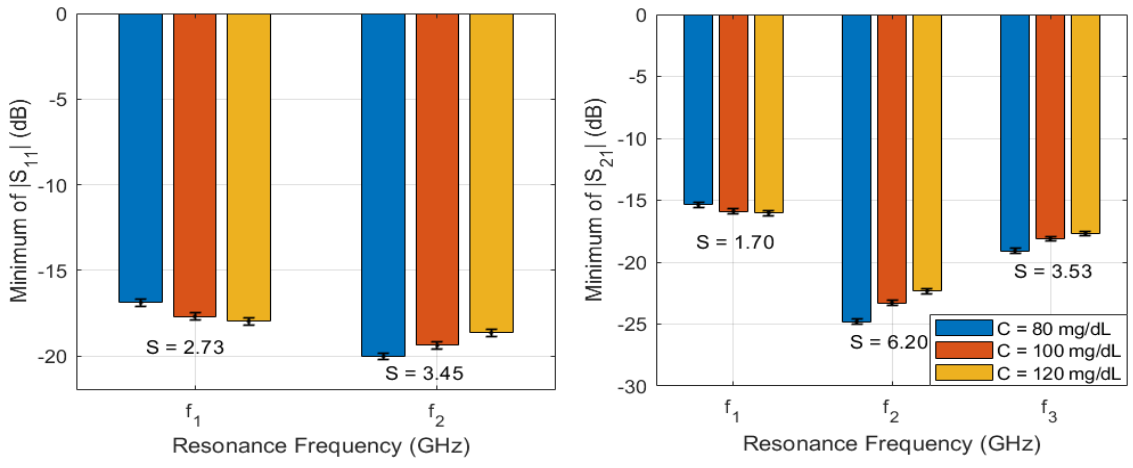

(a) (b)

Figure 3.37: Graphical illustration of the amplitude variations at each of the (a) reflection and (b) transmission resonances corresponding to glucose level changes. The sensitivity is shown for each resonance in dB/(mg/ml). Error bars are also attached to represent ±0.2 dB (reflection) and ±0.1 dB (transmission) variations in the three repeatable trials for each glucose sample.

Lastly, in what follows the sensitivity of the TP-CSRR sensor for glucose detection is compared to other microwave glucose sensors in the recent literature that adopted the resonant amplitude as a sensing parameter as shown in Table 3.8. Careful examination of Table 3.8 clearly demonstrates that the TP-CSRR sensor is outperforming with an average sensitivity of about 3.95 dB/[mg/ml].

Table 3.8: Comparison of TP-CSRR against other microwave glucose sensors

Ref	Sample volume (µL)	Concentration (mg/ml)	Operating frequency (GHz)	Sensing parameter	S (dB per mg/ml)
[171]	7500	0.78 – 50	1.4 – 1.9	$\|S_{11}\|$	0.18
[172]	–	0 – 4	2.4 – 2.9	$\|S_{21}\|$	0.0075
[173]	–	0.3 – 80	7.5	$\|S_{21}\|$	0.008
[159]	170	5 – 25	1.91	$\|S_{21}\|$	0.025
[152]	20	200 – 1000	3.02	$\|S_{21}\|$	0.007
[174]	20	40 – 200	2.5 – 6	$\|S_{21}\|$	0.01
[175]	1000	0 – 300	2.0 – 2.5	$\|S_{11}\|$	0.003
TP-CSRR	100 – 600	0.7 – 1.2	2.3 (unloaded) 1 – 6 (loaded)	$\|S_{11}\|/\|S_{21}\|$	1.7 – 6.2 (S_{21}) 0.6 – 3.45 (S_{11})

3.4.11.3. Glucose sensing on SL TP-CSRR. A preliminary prototype of the TP-CSRR (single-loop version) was tested for detecting the varying glucose levels 100 – 300 mg/dL in synthetic blood samples. The Keysight Technologies VNA N5227A was calibrated and used to measure the transmission responses of the sensor in the 3 – 5 GHz at 22±1°C controlled temperature with a resolution of 1 MHz using the setup in Fig. 3.38. The $|S_{21}|$ coefficients of the unloaded sensor were measured before loading any glucose sample as plotted (black curve) in Fig. 3.39(a). A 3D-printed ear phantom was fabricated using silicone rubber-carbon black composite to replicate the features of the human ear. Glucose samples were tested at constant volume 1 *mL* (loaded with syringes) in two different locations in the ear model, namely, the ear concha (Fig. 3.38(b)) and earlobe (Fig. 3.38(c)).

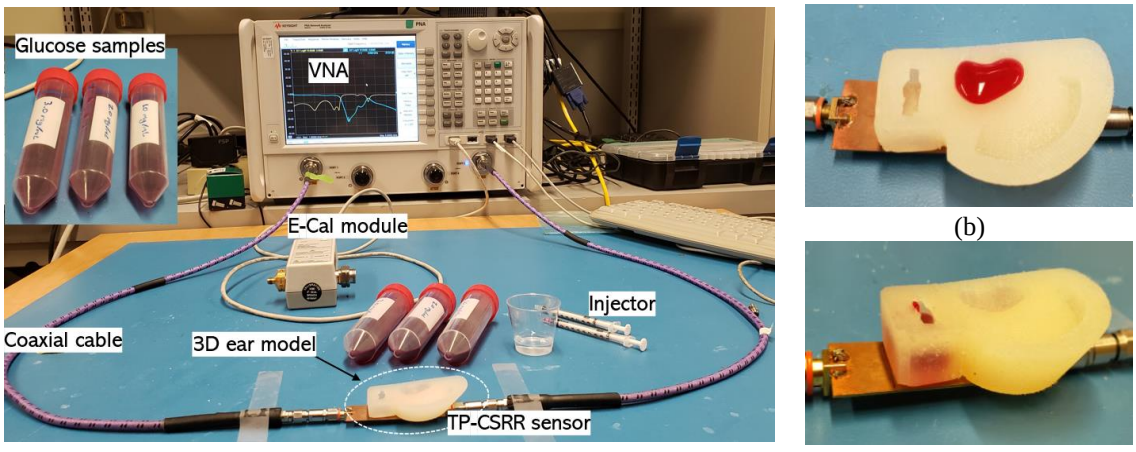

(a) (b) (c)

Figure 3.38: Blood glucose sensing experiment (a) experimental setup. Testing blood samples in the (b) concha and (c) earlobe areas.

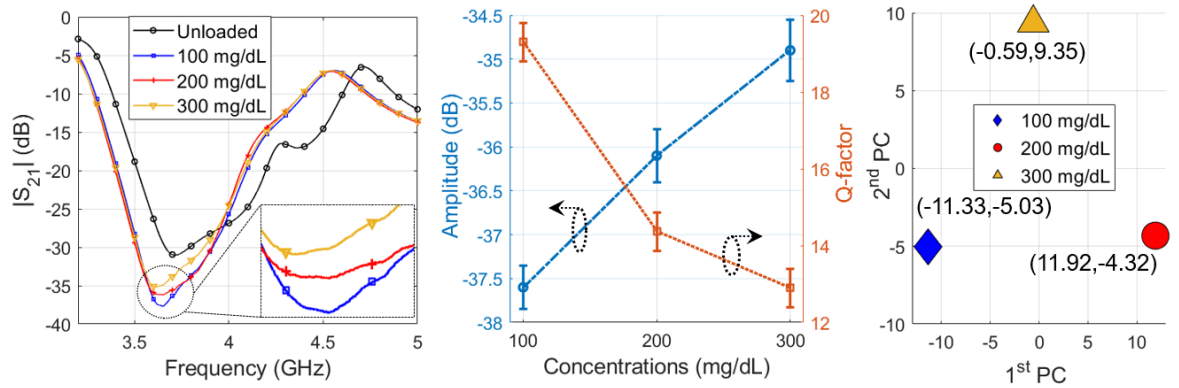

(a) (b) (c)

Figure 3.39: Glucose sensing results, (a) measured unloaded and ear-loaded sensor responses, (b) minimum resonant amplitudes, Q-factor, and repeatability errors, (c) PCA processing of the sensor data.

The samples were first measured in the concha area (Fig. 3.38(b)) of a larger thickness of about 10 mm where no significant change was observed in the $|S_{21}|$ response for the varying glucose concentrations due to the weak interaction of the coupled electric field with the glucose samples. To enable a stronger tissue interaction with the distributed electric field, the glucose samples were measured again at the earlobe area of thinner thickness of about 1.1 mm as shown in Fig. 3.38(c). The sensor responds to glucose loading by shifting its resonance frequency slightly towards f = 3.6 GHz. Additionally, it changes the resonance amplitudes in a decreasing pattern following the increased concentrations 100, 200, and 300 mg/dL as depicted in Fig. 3.39(a). The 3-dB bandwidth of the resonance was also observed to change following the varying glucose-levels as reflected by the computed *Q*-factors in Fig. 3.39(b). The resonant frequency at which the transmission is minimized is not substantially affected by changes in BGLs; similar to what predicted by the corresponding numerical analysis (Fig. 3.22).

Each glucose sample was measured three times with repeatability errors of about (± 0.25 – 0.35 dB) as indicated in Fig. 3.39(b). The average of three repeatable $|S_{21}|$ readings for each glucose sample are plotted in Fig. 3.39(a). The baseline (unloaded response of the sensor) in Fig. 3.39(a) was repeatedly restored before testing a different glucose sample. The TP-SL CSRR has proved better glucose sensitivity than SP-DL (single-pole double-loop) CSRR when tested for the same concentrations (Fig. 3.40(a)). Particularly, the resulting resonant amplitudes induced in 2.2 – 2.21 GHz for the SP-DL CSRR changed very little ~0.02 dB (compared to 1.25 dB for TP-SL CSRR) for every 100 mg/dL change (i.e., sensitivity of about 0.0125 dB/[mg/dL]) as depicted in Fig. 3.40(b). All the glucose sensing measurements were performed carefully with attention to the setup stabilization. A total of 201 sensing instances were collected from the $|S_{21}|$ responses for various concentrations in the spectrum 3.5 – 3.7 GHz, then processed by the PCA algorithm to extract the principal components representation as plotted in Fig. 3.39(c). The resulting measurements suggest the earlobe tissue as a promising region for BGL sensing due to its high blood content, smooth surface, thin thickness, and simple structure as compared

to other body parts. This would allow to acquire the scattering data with higher sensitivity and adequate penetration depth at the operating frequency.

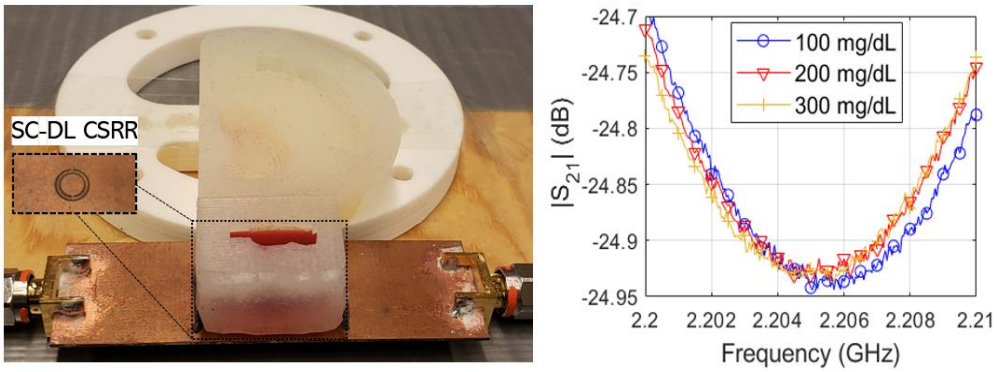

(a) (b)

Figure 3.40: (a) Testing the blood samples using SP-DL CSRR, and (b) $|S_{21}|$ results for different glucose concentrations.

3.4.11.4. Liquid and glucose sensing on microfluidic MP-CSRR. The performance of the microfluidic MP-CSRR sensor was analyzed experimentally using the stable setup in Fig. 3.41(a). The Keysight Technologies PNA N5227A Network Analyzer was used to stimulate the microwave sensor and monitor its scattering responses (both reflection $|S_{11}|$ and transmission $|S_{21}|$ coefficients) by sweeping the frequency in the cm-wave band (1 – 6 GHz). The resonance amplitude and frequency at the multiple resonances induced in the $|S_{11}|$ and $|S_{21}|$ responses would provide more sensing instances (data points) necessary for developing a robust machine learning model. More available data could be equipped using additional sensing parameters such as the line-width of the resonance or *Q*-factor.

The PNA was calibrated using the N4694A E-Cal module to acquire accurate producible measurements, then used to record the reflection and transmission scattering responses at 22^{o}C room temperature with a resolution of 10 MHz. The bare sensor has a transmission resonance at 2.3 GHz as shown in Fig. 3.41(b) (blue curve). Introducing the microfluidic channel on top of the MP-CSRR sensor introduced a 136 MHz shift from the fundamental S_{21} resonance at the unloading state as depicted in Fig. 3.41(b) (black curves). This empty channel-loaded response was considered as the baseline for all the subsequent measurements. The experimental platform was also equipped with a disposable syringe pump to inject the liquid samples into the microfluidic channel from the inlet and hence enabling an accurate volume flowing over the sensing area at a constant flow rate. All sensing experiments were performed in a controlled environment of 22±1^{o}C to reduce the environmental impact on the collected scattering data and maintain consistent operating conditions for all measurements.

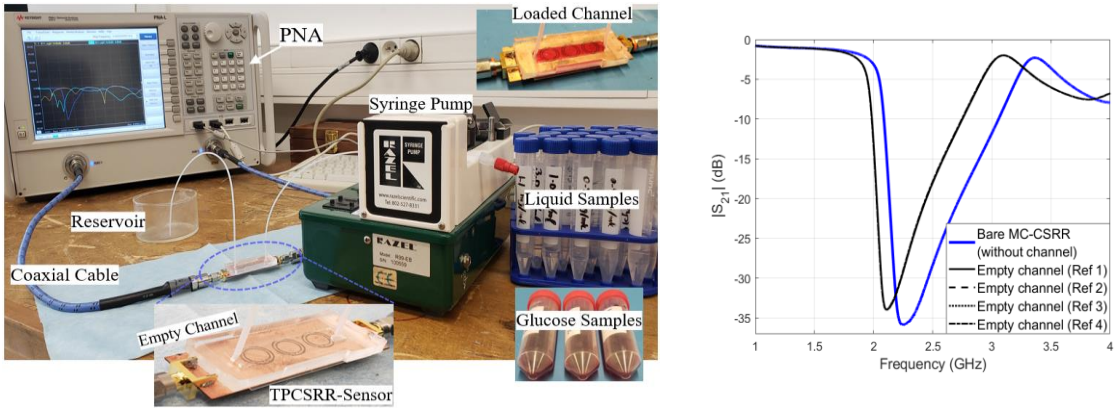

(a) (b)

Figure 3.41: (a) Complete experimental setup comprises PNA connected to fabricated microfluidic sensor via coaxial cables. Syringe pump delivers the liquid samples inside the channel. (b) Measured sensor responses before integrating the channel (blue curve), and when loaded with empty channel. The latter represents the reference response that is retrieved after testing each liquid sample (black curves).

To probe into the fabricated microfluidic sensor capabilities, and sensitivity for identifying different liquid samples, four samples of distilled water, bacteriostatic water, saline (0.9% NaCl), and methanol were tested onto the sensor. In each measurement trial a liquid sample was introduced inside the PDMS channel, and the scattering responses of the sensor were measured three times, once every 20 seconds over a course of 1 minute, to assure the stability of the sensing measurements. The integrated microfluidic channel allows for sensing liquids at 500 μL volume, however preliminary tests have shown the sensor capability to provide stable measurements for volumes as low as 400 μL whereby the loaded sample is consistently distributed over the entire sensing area. This would offer some scalability for the geometry of the attached channel to adjust the length, width, and height accordingly for a specific volume capacity.

A cleaning protocol for the microfluidic channel was followed to ensure acquiring independent sensing data from the subsequent measurements of different liquid samples. Each liquid measurement was repeated for three times to verify the repeatability of the measured sensor responses. Tested liquid sample was flushed out after each measurement trial with adequate air flow driven by the syringe pump, then the channel was rinsed with pure water and flushed out accordingly. This would result into retrieving the pre-loading sensing reference (i.e., baseline) to fairly conduct the next measurement. Next liquid sample was pumped continuously through the PDMS channel at a constant rate for about 15 seconds. Precautionary measures were also considered to prevent any air bubbles formation inside the PDMS channel that might impact the sensing measurements. Figure 3.41(b) shows the reference responses in black curves as retrieved after testing each liquid sample.

Two different sensor responses (reflection $|S_{11}|$ and transmission $|S_{21}|$) were recorded for each tested liquid as depicted in Fig. 3.42. These signals represent the average of three repeatable measurement trials for each liquid sample. The sensor's dependency on the EM properties (dielectric permittivity and loss tangent) of the liquid samples inside the channel was demonstrated by the

variations in resonance frequencies and amplitudes in both modes of reflection and transmission. Particularly, the liquid samples could be distinctly identified by monitoring changes in the resonant attributes at four distinct sensing resonances in the S_{11} signal occurring in the frequency intervals 1 – 2 GHz, 2 – 3 GHz, 3 – 4.5 GHz, and 4.8 – 6 GHz, as depicted in Fig. 3.42(a), 3.42(b), 3.42(c), and 3.42(d), respectively. Liquid samples were also featured by specific resonance characteristics in the transmission response of the sensor at two different intervals 1.3 – 2.5 GHz and 3.5 – 6 GHz as shown in Fig. 3.42(e) and 3.42(f), respectively. The measured data were validated by simulating the sensor response in HFSS for detecting the distilled water and methanol via integrating their dispersive EM properties in the frequency range 1 – 6 GHz as depicted in Fig. 3.42. Figure 3.43 demonstrates the sensor applicability for identifying different liquid samples at a given sensing mode in the reflection and transmission responses. Fig. 3.43(a) and 3.43(b) extract the mean resonance frequency and amplitude, respectively, of the $|S_{11}|$ signal for each liquid sample in the frequency interval 3 – 4.5 GHz. The same resonant features were extracted in Fig. 3.43(c) and 3.43(d), respectively, from the transmission response $|S_{21}|$ in the 1.5 – 2 GHz range for each liquid sample.

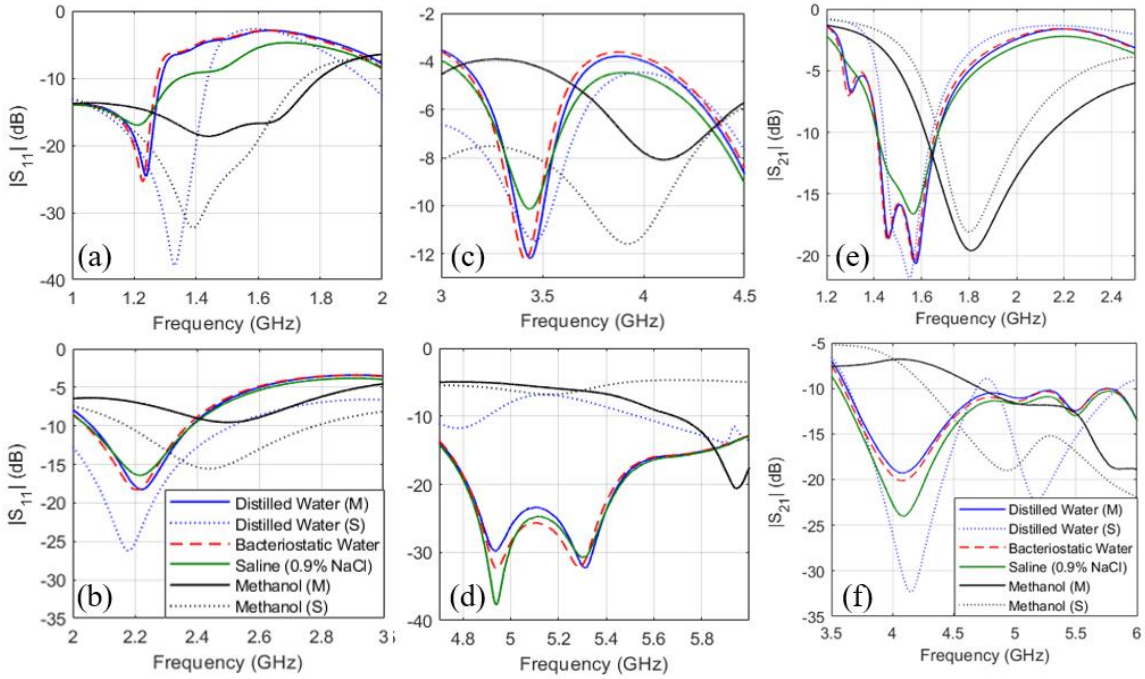

Figure 3.42: Measured (M) and simulated (S) reflection coefficients $|S_{11}|$ for different liquid samples (a) 1 – 2 GHz, (b) 2 – 3 GHz, (c) 3 – 4.5 GHz, and (d) 4.8 – 5.8 GHz. Measured (M) and simulated (S) transmission coefficients $|S_{21}|$ for different liquid samples (e) 1.3 – 2.5 GHz and (f) 3.5 – 6.0 GHz

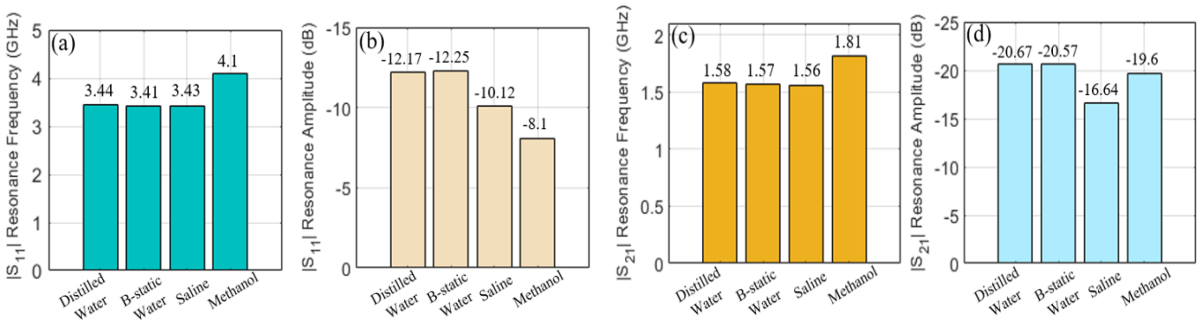

Figure 3.43: Extracted resonant features for tested liquid samples from the scattering responses at specific frequency bands, (a) resonant frequency and (b) resonant amplitude of S_{11} in the 3 – 4.5 GHz range, (c) resonant frequency and (d) resonant amplitude of S_{21} in the 1.5 – 2.0 GHz range.

Different liquids have distinct resonant features that reflects the contrast in their dielectric properties. Notably, the sensor could detect the differences between various liquid samples at different sensing modes due to its high sensitivity feature enabled through the metamaterial-inspired design of the CSRR cells. The sensor could also identify liquids with tiny differences in their dielectric attributes such as distilled water, bacteriostatic water, and saline. Distilled water is processed through steaming and condensation to release any minerals (e.g., NaCl, Ca, Fa). Bacteriostatic water is basically a sterile water containing 0.9% benzyl alcohol. It is basically used to dilute or dissolve medications for medical injection and the benzyl alcohol suppresses or stops the growth of most potentially contaminating bacteria. While saline contains 0.9% NaCl. Distilled water was detected in the reflection response at 3.44 GHz resonance frequency with -12.17 dB peak amplitude, while the bacteriostatic water was captured in the same response at 3.41 GHz and -12.25 dB resonant frequency and amplitude, respectively. Extracted resonant features could be used as potential inputs to a machine learning model to accurately identify the tested liquid.

Following the same recipe, the sensing functionality of the microfluidic sensor was tested for monitoring the glucose level changes 70 – 150 mg/dL in synthetic blood samples. The measured reflection and transmission responses of the sensor for different glucose concentrations 70, 100, and 150 mg/dL are shown in Fig. 3.44. Two harmonic resonances were recorded in the $|S_{11}|$ signal in the 4.9 – 5.4 GHz range as shown in Fig. 3.44(a). In these sensing modes both the resonant depth and frequency are changing in response to the varying glucose concentrations. It is noteworthy to mention, fundamental resonances at which the reflection is minimized in lower bands 1 – 4 GHz were not substantially affected by the change in glucose concentrations, only small changes in $|S_{11}|$ magnitudes were observed. Similarly, three sensing resonances were captured in the transmission response of the sensor. The resonance in 1.44 – 1.5 GHz shifts its frequency towards higher bands with an increased glucose level as depicted in Fig. 3.44(b), while the resonance frequency in the 1.55 – 1.6 GHz range decreases with an increased glucose level. The resonant depth is also changing at these two resonances following the change in glucose concentrations. The last transmission resonance in the 3.9 – 4.3 GHz

range shows only amplitude variations with an increasing pattern as the glucose level increases (Fig. 3.44(c)).

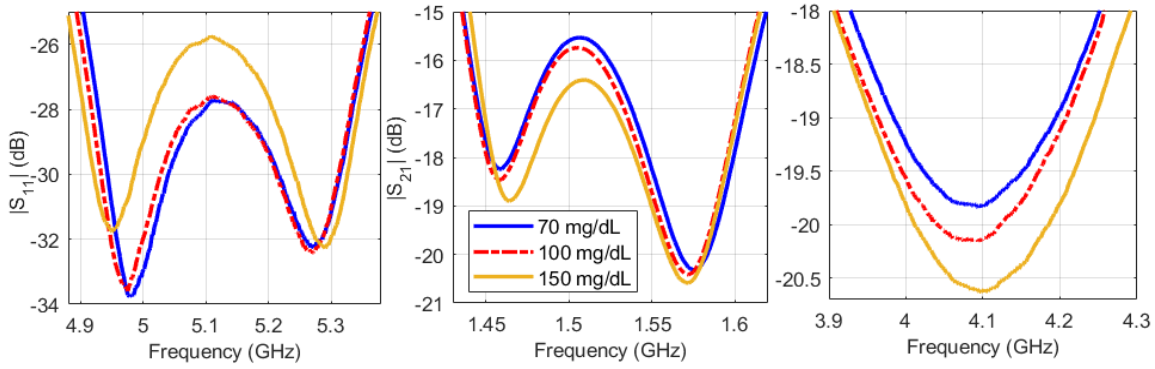

(a) (b) (c)

Figure 3.44: Glucose level monitoring at different sensing modes, (a) measured reflection response in the 4.9 – 5.4 GHz. Measured transmission response in (b) 1.44 – 1.6 GHz, and (c) 3.9 – 4.3 GHz.

The average sensitivity at each reflection and transmission resonance was calculated in dB/(mg/mL) and/or MHz/(mg/mL) as presented in Table 3.9. The reported amplitude and frequency sensitivities demonstrate the sensor capability to differentiate the varying-level glucose samples with adequate resolution for diabetes monitoring where the glycemic concentrations are relatively small. Additionally, glucose monitoring could be performed at multiple sensing modes enabling more robust measurements against additive noises from instruments, environment, or any other uncertainties. Reflection modes achieve higher frequency resolutions compared to their transmission counterparts. Mode 1 in both reflection and transmission responses obtains the highest amplitude resolution. The variations in the magnitude and frequency at this mode as a function of the glucose concentrations are depicted in Fig. 3.45(a) and 3.45(b), respectively.

Table 3.9: Sensitivity analysis of the sensor responses for glucose monitoring

Sensor Response	***Sensing mode***	***Frequency range (GHz)***	***Sensitivity MHz/(mg/mL)***	***Sensitivity dB/(mg/mL)***
Reflection (S_{11})	Mode 1	4.9 – 5.0	33.40	2.10
	Mode 2	5.2 – 5.3	27.40	0.50
Transmission (S_{21})	Mode 1	1.45 – 1.5	6.70	1.60
	Mode 2	1.55 – 1.6	7.00	0.30
	Mode 3	3.9 – 4.3	–	1.00

Non-linear regressions were performed on the sensing parameters of mode 1 in each response. The corresponding fitted curves for the frequency and magnitude data were obtained using the quadratic fitting that results into higher coefficient of determination R^2 as shown in Fig. 3.45. The fitting frequency and amplitude equations for the processed modes are shown in Table 3.10 along with the norm of residuals obtained in each case. The inverse models could be developed using appropriate functions (e.g., power or polynomial) to detect the glucose concentration of a new tested sample as predicted from the resulting resonant frequency and/or peak at specific sensing mode. The microfluidic

MP-CSRR is compared to the state-of-the-art microwave sensors based on diverse sensing mechanisms in Table 3.11. The developed MP-CSRR has the capability to conveniently detect, within the range of normal glycemia, small variations of glucose concentration with relatively high sensitivity of about 6.6 × 10^{-3} dB/[mg/dL] and 8.9 × 10^{-2} MHz/[mg/dL].

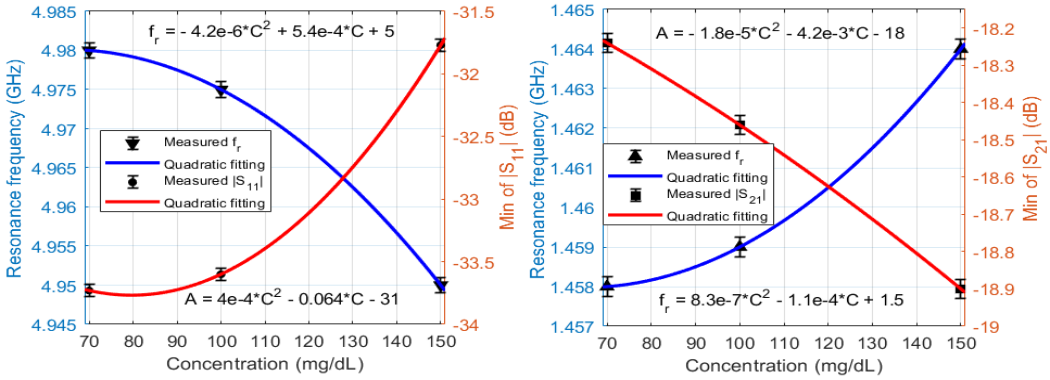

(a) (b)

Figure 3.45: Measured sensing parameters (resonant frequency f_r and amplitude A) for different glucose levels at (a) reflection sensing mode (4.9 – 5 GHz) and (b) transmission sensing mode (1.45 – 1.48 GHz). Quadratic fitting is incorporated for in-between concentrations. Error bars indicate a maximum repeatability error of about (±0.1 dB, ±1MHz) in (a) reflection readings, and (±0.05 dB, ±1MHz) in (b) transmission readings.

Table 3.10: Curve fitting for the frequency and magnitude sensing data

Sensor Response	***Sensing Parameter***	***Fitting equations***	***Norm of residuals***
Reflection (Mode 1)	f_r	$-4.2 \times 10^{-6}C^2 + 5.4 \times 10^{-4}C + 5$	2.176E-15
	$\|S_{11}\|^{min}$	$4 \times 10^{-4}C^2 - 6.4 \times 10^{-2}C - 31$	1.005E-14
Transmission (Mode 1)	f_r	$8.3 \times 10^{-7}C^2 - 1.1 \times 10^{-4}C + 1.5$	4.965E-16
	$\|S_{21}\|^{min}$	$-1.8 \times 10^{-5}C^2 - 4.2 \times 10^{-3}C - 18$	7.944E-15

Table 3.11: Comparative analysis between state-of-the-art microwave sensors for glucose level detection

Ref	**Sample volume (μL)**	**Concentration (mg/dL)**	**Operating frequency (GHz)**	**Sensing parameter**	**S (dB per mg/dL) (MHz per mg/dL)**
[171]	7500	78 – 5000	1.4 – 1.9	$\|S_{11}\|$	1.8E-3
[172]/ [170]	–	0 – 400	2.4 – 2.9	$\|S_{21}\|$	7.5E-5
[173]	–	30 – 8000	7.5	$\|S_{21}\|$	8.0E-5
[159]	43 – 170	500 – 2500	1.91	$\|S_{21}\|$ $f_r\,(S_{21})$	2.5E-4 4.00E-04
[174]	20	4000 – 20000	2.5 – 6	$\|S_{21}\|$	1.0E-4
[60]	600	504 – 3531	1.4	$f_r\,(S_{21})$	1.83E-04
[79]	5	5000 – 30000	1.68	$f_r\,(S_{11})$	2.00E-04
[176]	–	0 – 40000	6.5	$f_r\,(S_{21})$	1.88E-03
[154]	2	2000 – 10000	2.074	$f_r\,(S_{21})$	1.00E-02
[177]	125	100 – 1000	4.8	$f_r\,(S_{11})$	1.40E-02
[178]	–	0 – 34780	16	$f_r\,(S_{11})$	1.64E-02
[162]	2	0 – 8000	2.46	$f_r\,(S_{21})$	2.00E-02
[146]	–	0 – 5000	4.18	$f_r\,(S_{21})$	2.60E-02
[179]	–	1000 – 10000	1 – 3	$f_r\,(S_{21})$	2.11E-02
[180]	500	20 – 120 & 100 – 600	7.8	$\|S_{11}\|$	1.20E-02
Microfluidic MP-CSRR	400 – 1200	70 – 150	1 – 6	$\|S_{11}\|$ $\|S_{21}\|$ $f_r\,(S_{11})$ $f_r\,(S_{21})$	(5.0 – 21) E-3 (3.3 – 9.8) E-3 (2.74 – 3.34) E-1 (6.7 – 11) E-2

3.5 Honey-Cell Shaped CSRR Sensor

3.5.1 Sensor Description

Another microwave sensor was developed with the sensor element realized using a microstrip structure with an improved configuration of hexagonal CSRRs array engraved in copper ground plane in a honey-cell fashion as shown in Fig. 3.46(a). This honey-cell design is favored due to its capacity to alleviate the sensitivity limitations of the conventional SRR/CSRR structures by inducing an intensified electric field over a large sensing region adequate for fingertip or any fixture placement. Figure 3.46(b) sketches the corresponding electric field distribution on the honey-cell CSRR sensing surface at 3.0 GHz resonant frequency (prior-loading) and compares it against that of a single hexagonal CSRR. It is clearly observed the intense electric field coupled to the CSRRs area (14×19 mm^2) with higher magnitudes of about 10^5 V/m around the dielectric slits and the routes in-between. Having most of the energy accommodated by the CSRR elements is beneficial to enhance the sensitivity for characterizing the tiny variations in the dielectric properties of the targeted glucose concentrations when loaded onto the CSRRs surface.

The primary objective of the proposed biosensor is to non-invasively monitor the BGL for diabetics. Towards that goal, the sensor was primarily experimented to detect the change in the glucose levels in blood mimicking solutions of concentrations in the range of Type-1 and Type-2 diabetes. This was done by analyzing the sensor transmission signals as reflected on the radar receiving port using signal processing and machine learning techniques to identify different glucose levels. The detection capability of the sensor to the varying glucose levels was also demonstrated by the frequency shifts in the reflection and transmission resonances when tested using a conventional VNA setup. Different topologies of the CSRRs have been studied using experimental and numerical analysis to compare their sensitivity performance. The compact-layout of the honey-cell sensor has demonstrated greater resonant frequency deviation in response to changes in the glucose levels of interest. It scores an outstanding glucose sensitivity with frequency resolution of about 94 MHz/(mg/ml) outperforming other state-of-the-art microwave glucose sensors.

Realizing larger frequency shifts (higher resolution) enables our sensor to be more robust against additive noise and other measurement uncertainties. Additionally, the sensor would be able to achieve more precise, easy, and straightforward readings when integrated with any readout circuitry of wide dynamic ranges [181]. The improved CSRR sensor is capable of reproducibly detecting glucose concentrations ranging from 0 – 300 mg/dL in physiological solutions designed to mimic the practical diabetic condition with the precision of ~ 5 mg/dL which should provide sufficient sensitivity for accurate real-time monitoring of glycemia levels in patients with diabetes.

3.5.2 Sensor Design

The proposed biosensor was numerically designed to operate around 2.45 GHz when used for glucose detection. This was chosen to match the Industrial, Scientific, and Medical (ISM) band 2.4 – 2.5 GHz of the radar system to be integrated in a later phase [182]. In fact, operating in this range of frequency would also allow adequate penetration depth for the induced EM waves to reach the blood vessels in the fingertip. This penetration is to a certain extent maximized in our sensor given the concentrated energy of the sensing region where the fingertip is placed [105]. Additionally, at this frequency there is a higher possibility to identify different glucose concentrations of interest due to the small loss introduced ($tan\delta \sim 0.13$). Therefore, sensing at this frequency would probably bring a considerable sensitivity despite the small changes in dielectric properties from one glucose level to another [122]. These variations in dielectric constant and loss tangent were studied for the targeted concentrations across the centimeter-wave band 1 – 6 GHz using the first order Debye relaxation model for aqueous glucose solutions. A slight increase in ϵ_r' and, conversely, a tenuous decrease in $tan\delta$ were observed with an increased glucose concentration. In this tendency, the percent variation in $tan\delta$ is much higher than its corresponding on ϵ_r' (e.g., for a 10 mg/dL change at 2.4 GHz, the percent change in $tan\delta$ is about 0.4 % while the variance in ϵ_r' is approximately 0.005 %).

The sensor structure is primarily inspired from the metamaterial technology by incorporating four similar cells of hexagonal-shaped complementary split-ring resonators with localized elements in a novel configuration as shown in Fig. 3.46(a). The four CSRRs are engraved in a honey-cell pattern at depth 35 μm in the copper ground plane of an FR4 dielectric PCB of dielectric permittivity ϵ_r' = 4.4, loss tangent $tan\delta$ = 0.02, length L = 66 mm, width W = 20 mm, and thickness h = 0.8 mm. The four hexagonal cells are coupled through the substrate (~C_c) with a two-port microstrip-line (MTL) etched on the upper face of the substrate. The magnetic walls of the passive CSRRs are aligned perpendicularly to the MTL to guarantee an electric excitation for the resonance with time-varying electric field between the MTL strip and the ground plane. The dimensions of the feed line are optimized to 66×1.5 mm^2 in order to obtain a 50 Ω characteristic impedance that perfectly matches the SMA (SubMiniature version A) connectors of the driving power source.

Two topologies for the honey-cell configuration are realized, compact and dispersed. Accordingly, two hexagonal cells are placed horizontally along the axis of the MTL strip and detached with distance C_L = 7.6 mm (compact) and C_L = 12.6 mm (dispersed) between their corresponding geometric centres. The honey-cell design is completed by setting the other two hexagonal cells in a vertical placement with C_W = 12 mm between their corresponding centres. As sketched in Fig. 3.46(a), the unit-cell of each CSRR is composed of two concentric rings (outer and inner) of hexagonal shape nested within each other with a coupling-gap t = 0.4 mm in between. The loop of each ring has a dielectric slit of side-width s = 0.4 mm and ends in a metallic slot of width g = 0.4 mm. The diagonal length of the outer ring is a = 7.6 mm, while that of the inner one is set to b = 6.0 mm. The split gaps

for both rings are on diametrically opposite sides of each other. The overall geometry of the four cells in the honey-cell region corresponds to the average adult finger index to enable an effective BGL monitoring by finger placement.

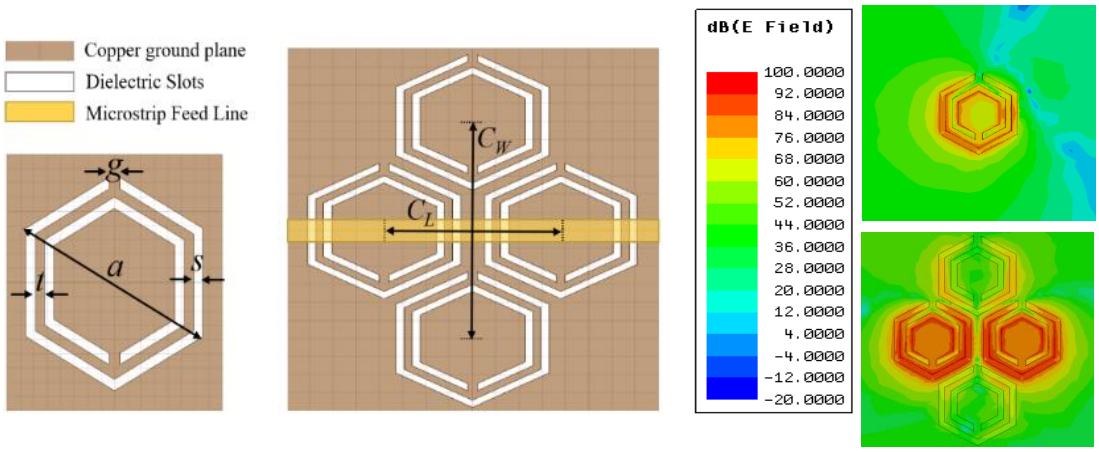

(a) (b)

Figure 3.46: (a) Configuration of the CSRRs sensing elements in the ground copper plane (top view). Topology of the hexagonal unit-cell with the geometrical parameters is also shown, (b) Electric field distribution on the CSRR surface at 3.0 GHz resonant frequency for the improved and conventional topologies.

As previously emphasized, for reliable blood glucose sensing it is required to maximize the resonance strength and to perfectly confine the resonating electromagnetic fields within the permittivity sensing region of the sensor. Therefore, the design and geometrical parameters of the planar transmission-line as well as the engraved CSRR cells were optimized to obtain a steep transmission resonance around f_o = 3.0 GHz for the unloaded sensor after studying the primary influence of each parameter using the HFSS FEM simulator as shown in Fig. 3.47. As mentioned earlier, the resonance characteristics of the proposed sensor are basically determined by the substrate dielectric specifications and geometries (i.e., width and height). In addition, the design parameters of each hexagonal unit-cell play a crucial role in defining the complete resonance profile for the sensor. These parameters include the diagonal length *a* and *b*, coupling-gap *t*, side-width *s*, split-gap *g*, and coupling-controllers (C_L and C_W) of the integrated honey-cell. In contrast, before engraving the hexagonal CSRRs, these resonance characteristics are solely determined by only the geometrical width and length of the dielectric patch.

The primary influence of each of these parameters on f_o was numerically investigated. First, since $a \propto L_R$, increasing *a* would reduce f_o as shown in Fig. 3.47(a) for *a* changing from 5.6 to 7.6 mm. Second, with $g \propto 1/C_R$ it is expected that f_o to shift towards higher frequencies (i.e., increasing) as the split gap *g* is increasing from 0.1 to 0.5 mm in Fig. 3.47(b). Similar functionality can be observed in Fig. 3.47(c) for the case of the slots-coupling distance *t*. Moreover, f_o also slightly increases with an increased side-width *s* as shown in Fig. 3.47(d). Both behaviors can be explained by the fact that the side width, slots-coupling distance, and split gap are all inversely proportional to the resonator capacitance C_R, thereby increasing these parameters would probably increase f_o. The effect of the

center-to-center separation distance is studied in Fig. 3.47(e) that shows a higher magnitude for the transmission response (i.e., insertion loss), and hence higher *Q*-factor, for larger distance C_L. This is expected since increasing C_L would reduce the effect of the mutual coupling between the adjacent hexagonal CSRRs.

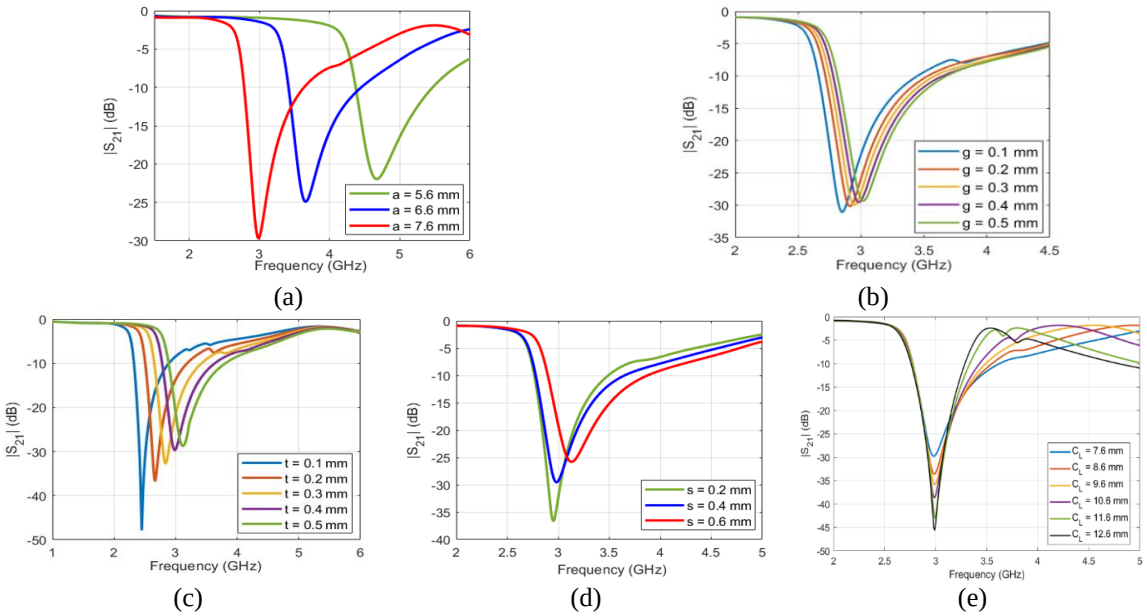

Figure 3.47: Simulated transmission coefficient S_{21} of the unloaded honey-cell CSRR at different (a) diagonal length of *a* (b) split gap *g* (c) side width *s* (d) slots-coupling distance *t*, and (e) center-to-center coupling distance C_L.

3.5.3 Numerical Analysis

Both topologies, compact and dispersed, were numerically analyzed using HFSS to test the functionality and quantify the resonant frequencies for three different cases: i) when unloaded, ii) loaded with an empty container, and iii) loaded with pure distilled-water (DI). A cylindrical glass container was designed to load the glucose samples onto the CSRRs surface (this is replaced later by a suitable fixture to place the fingertip) as shown in Fig. 3.48(a). The container has 8.9 mm outer diameter, 7.4 mm inner diameter, 1.5 mm wall thickness, and 10 mm height. In addition, a thin glass layer of h_g = 0.15 mm was introduced between the container and CSRRs in order to evade short-circuiting the dielectric slits of the CSRR cells when loaded with the glucose specimens of moist nature. The geometrical parameters of the integrated structure are presented in Table 3.12.

The intrinsic transmission resonant frequency prior-loading is 3.0 GHz for both topologies as shown in Fig. 3.48(b). Loading the sensors with the empty cylindrical container introduces a few MHz shifts in resonance as can be clearly seen in Fig. 3.48(b), where f_o for the compact and dispersed are tuned to 2.83 GHz and 2.75 GHz, respectively. The empty container response is set as a reference state when using the sensors for sensing the glucose concentrations of interest. Filling the container with the DI-water of volume 600 µL disturbs the electric field extended over the sensitive area of the dielectric substrate, thereby resulting into further shift in f_o due to the change in effective permittivity of the

media surrounding the resonators. A frequency shift of about 770 MHz (compact) and 710 MHz (dispersed) was noticed when the DI-water was simulated inside the container. Moreover, a damping effect was observed on these resonances with a significant drop in the resonance peaks due the lossy nature of the DI-water sample. Furthermore, an additional resonance is established around 1.56 GHz (compact) and 1.66 GHz (dispersed) as a result of this new configuration of the sensor structure that accommodates the DI-water sample.

Table 3.12: Geometrical parameters of the honey-cell sensor.

Parameter	***a***	***b***	***g***	***t***	***s***	C_W	C_L
Value (mm)	7.6	6.0	0.4	0.4	0.4	12	7.6 (compact) 12.6 (dispersed)
Parameter	***W***	***L***	W_{line}	L_{line}	***R***	***h***	h_g
Value (mm)	20	66	1.5	66	7.4	0.8	0.15

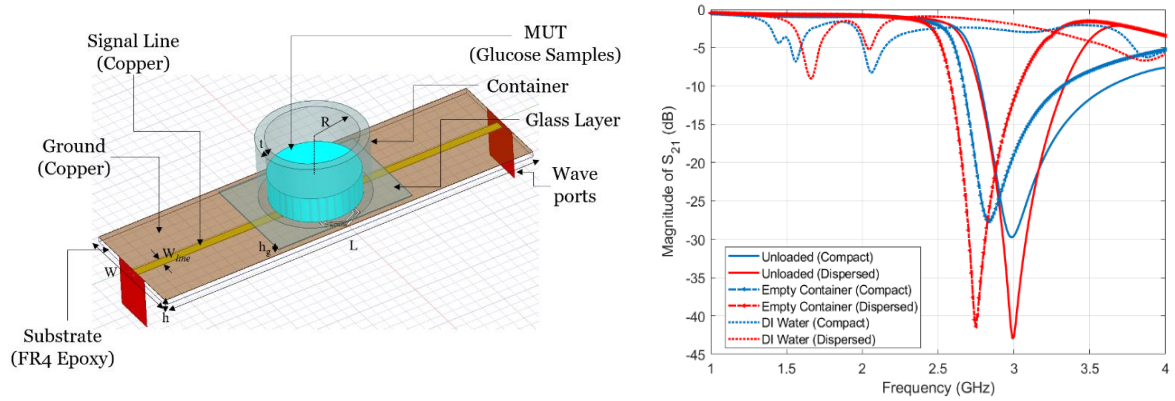

(a) (b)

Figure 3.48: (a) Geometrical model of the honey-cell CSRR integrated with the glass container used for loading the glucose samples, (b) simulated transmission response (S_{21}) of the sensor topologies (compact and dispersed) for three different states: unloaded, loaded with empty container, and filled with DI-water

Next, aqueous glucose samples of concentrations C_1 – C_{11} in the range 40 – 500 mg/dL were simulated on top of the sensing region inside the glass container. This range of concentrations covers the wide diabetes spectrum including hypoglycemia (< 70 mg/dL) and hyperglycemia (> 140 mg/dL). The single-pole Debye model (with the coefficients in Fig. 3.16(b)) was used to construct the numerical models for the dispersive EM properties of the glucose-water tissues at different concentrations. Figure 3.49 shows the simulated transmission responses for the different glucose samples C_1 – C_{11} loaded at volume 600 µL each (corresponds to 2 mm thickness inside the container). Four resonance frequencies were induced in the frequency range 1.5 – 5.0 GHz. All these resonances show variations in both frequency and amplitude for glucose level changes. However, the fourth harmonic resonance around 4.8 GHz is more responsive to the dielectric contrast of the glucose samples. This is reflected not only in the slight shift in resonance frequency, but also more distinctly in the significant change in resonance amplitude, implying that the loss property of the dissolved glucose contributes more to the system frequency response. The simulated response also demonstrates the sensor capability for detecting the hypoglycemia concentrations 40 – 60 mg/dL (C_1 – C_3, shown in blue), normal condition concentrations

70 – 140 mg/dL (C_4 – C_7, shown in red) and hyperglycemia concentrations 200 – 500 mg/dL (C_8 – C_{11}, shown in black).

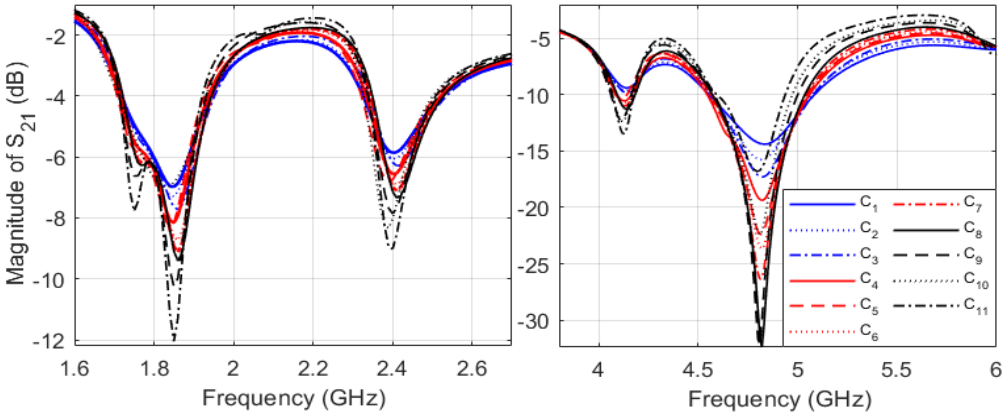

(a) (b)

Figure 3.49: Simulated transmission response of different glucose samples loaded on top of the compact sensor with no skin (a) 1.6 – 2.6 GHz, and (b) 4 – 6 GHz.

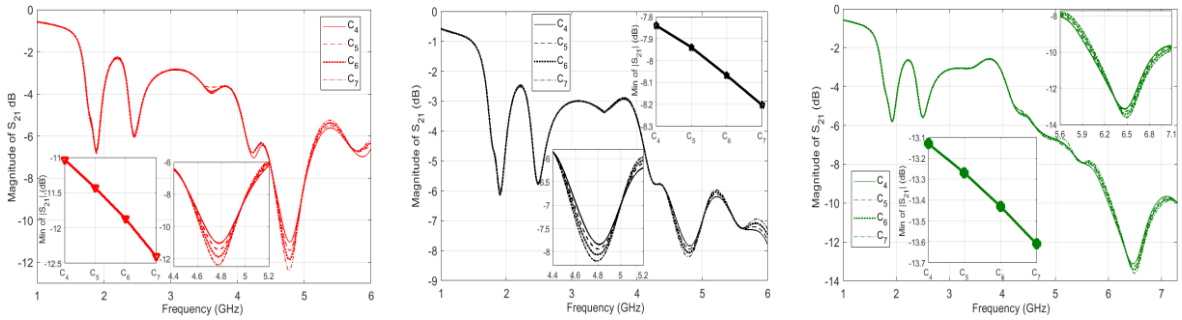

(a) (b) (c)

Figure 3.50: Simulated transmission response of different glucose samples loaded on top of the compact sensor with skin thickness of (a) 0.5, (b) 1.0, and (c) 1.5 mm, respectively.

To mimic the realistic scenario of placing a fingertip onto the sensing region, another simulation was performed where the glucose samples C_4 – C_7 of thickness 2 mm each were placed on top of a skin layer (ϵ_r' = 38.1 and $tan\delta$ = 0.28) [165], [183] of varying thicknesses 0.5, 1.0, and 1.5 mm (Fig. 3.51), and the corresponding transmission responses were analyzed over the frequency range 1 – 6 GHz as depicted in Fig. 3.50(a), 3.50(b), and 3.50(c), respectively. In fact, skin thickness is generally related to several factors such as body site, gender, skin type, age, pigmentation, etc., however, the simulated thicknesses are within the practical range of human fingertips [184]. It is observed that three distinct resonances were induced in these scattering responses around f = 1.9 – 1.95 GHz, f = 2.44 – 2.51GHz, and f = 4.77 – 6.5 GHz. The third resonance in each response conveys more information about the glucose concentrations of the simulated samples buried under the skin. This is demonstrated very clear in the larger amplitude variations compared to those existed at lower resonant frequencies as plotted in the

enclosed graphs. However, skin layers of larger thickness would damp the induced resonance strength due to their high permittivity, and therefore weaken the coupled electric field that interacts with the underneath glucose sample as shown in Fig. 3.51(a) – 3.51(d) that compare the electric field intensity coupled to the glucose tissue in the respective cases. Consequently, a lower sensitivity is reflected in the resonance readings with reduced amplitude resolution for sensing the glucose concentrations. For instance, by calculating the amplitude variation per unit change in ϵ_r' and $tan\delta$ for the two cases of 0.5- and 1.0-mm skin thickness, we got $\Delta|S_{21}|/\Delta|\epsilon_r'|$ of about 4 and 1, respectively. While that for $\Delta|S_{21}|/\Delta|tan\delta|$ is around 40 and 10, respectively.

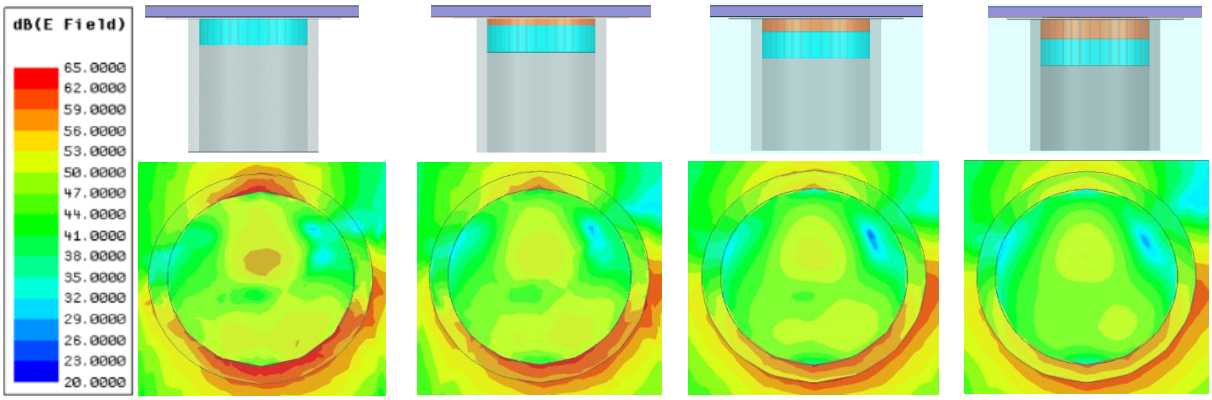

(a) (b) (c) (d)

Figure 3.51: Cross section of the electric field distribution across the glucose tissue in the respective cases (a) no skin, skin thickness of (b) 0.5, (c) 1.0, and (d) 1.5 mm, respectively.

3.5.4 In-vitro VNA Experiments

Various measurements were conducted to verify the performance of the honey-cell glucose sensor using a VNA setup. Aquatic glucose solutions were used in these experiments to imitate the blood behaviour at different glucose concentrations (70 – 120 mg/dL) of clinically relevant to Type-2 diabetes. First, the fabricated prototypes, compact (Fig. 3.52(a)) and dispersed (Fig. 3.52(b)), were experimentally tested using the VNA setup shown in Fig. 3.53 to record the intrinsic transmission responses before loading any glucose sample. Figure 3.54(a) presents the measured transmission coefficients as a function of frequency for the unloaded compact and dispersed sensors while comparing against the conventional single-hexagonal CSRR (shown in dotted green). Under unloading conditions, the three CSRR structures experience transmission resonances around f_o = 3.0 GHz with resonance minima of about -22.85 dB, -29.57 dB, and -43 dB, for the single-hexagonal, compact, and dispersed, respectively, as depicted in Fig. 3.54(a). Both compact and dispersed sensor have steeper resonance depth that would provide a better sensitivity for characterizing lossy glucose samples of high *tanδ* (i.e., detecting the tiny variations in the loss tangent for varying glucose concentrations). These measurement results show an excellent agreement with the previously predicted numerical simulations. Minor differences are due to typical tolerances in the fabrication process.

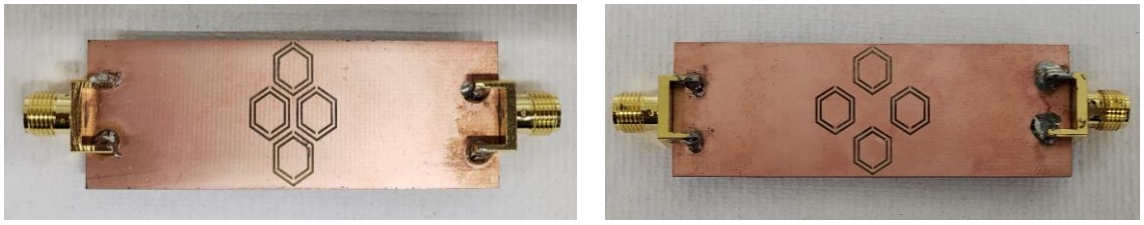

(a) (b)

Figure 3.52: Fabricated prototype of the (a) compact, and (b) dispersed honey-cell CSRR sensors.

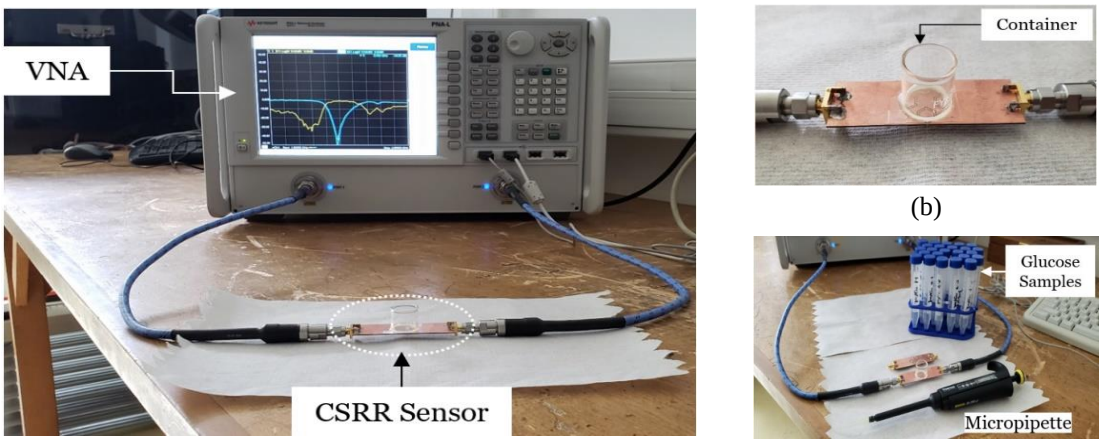

(a) (b) (c)

Figure 3.53: Glucose sensing experiments (a) VNA experimental setup, (b) sensor loaded with an empty container, and (c) micropipette and glucose aqueous solutions used in the experiments.

In order to measure the developed sensors for the glucose samples at the levels of interest, a cylindrical glass container was fabricated to hold the samples on top of the CSRRs surface. The empty cylindrical container was placed onto the honey-cell CSRR structure, as shown in Fig. 3.53(b). This would introduce a few MHz shifts from the reference resonance in S_{21} of the unloaded state. In each measurement trial, the micropipette device (Fig. 3.53(c)) was used to measure a precise volume of V = 600 µL from each concentration, load it inside the container and the change in the transmission resonance frequency response was recorded. This volume was adopted for testing various glucose samples to minimize the measurement errors due to uncertainty in the sample volume. In this regard, the sensor response was studied at different volumes of the tested sample as shown in Fig. 3.54(b). It is observed that the sensor shift in resonance frequency would converge to a lower frequency limit as the sample volume amounts to 600 – 700 µL whereby enabling a homogeneous distribution of the sample inside the container covering the entire the sensing region.

To test the sensor response for another concentration, a clean tissue paper was used to completely remove the previously tested glucose sample with attention to retrieve the exact reference resonance at S_{21} prior-loading the sample for a fair comparison. Figures 3.55(a) and 3.55(b) show the transmission response (magnitude and phase) of the compact sensor when the concentration of glucose is changing in 70, 90, and 110 mg/dL. Figures 3.55(c) and 3.55(d) capture the same responses when the dispersed

sensor was used for testing. In both responses, it is observed that the resonant frequencies at which the transmission is minimized are shifted towards lower frequencies as the glucose concentration increases. Additionally, trackable amplitude changes exhibit in some resonances due to the tiny variations in the loss tangent of the tested glucose samples. Notable variations are also observed in the transmission phase responses as shown in Fig. 3.55(b) and 3.55(d). Regions of significant changes were shown in the inset plots. Similar observations on the resonance frequency and amplitude were recorded when the compact sensor was tested for sensing higher glucose concentrations in the range 200 – 500 mg/dL that represent the hyperglycemia condition as shown in Fig. 3.56.

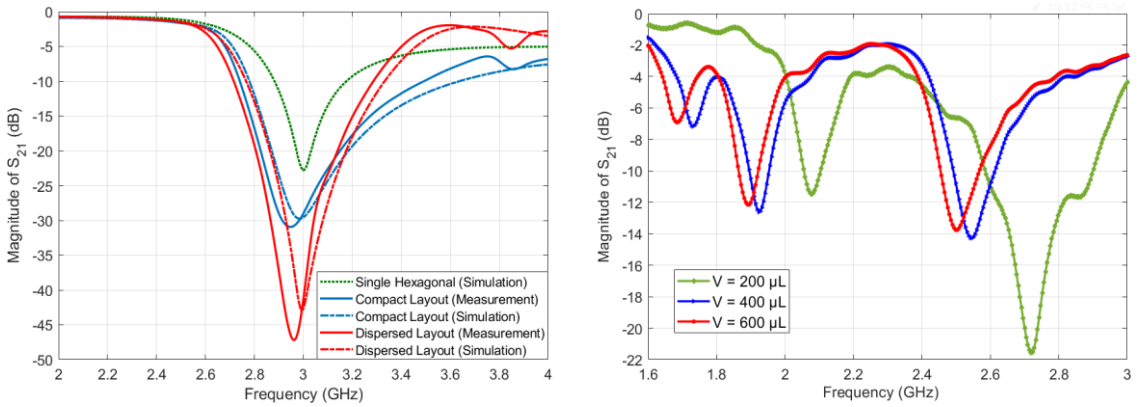

(a) (b)

Figure 3.54: (a) Measured and simulated transmission coefficients of the fabricated sensors before loading glucose samples (resonance around 3.0 GHz), and (b) measured transmission coefficient S_{21} when the compact sensor is experimented for the 70 mg/dL glucose sample at different volumes 200, 400, and 600 μL to compare the corresponding sensor behaviors.

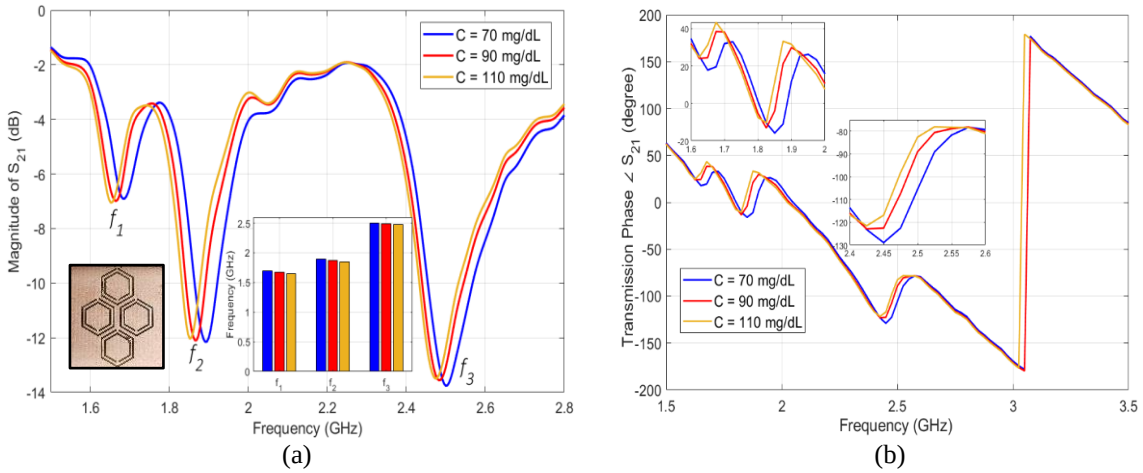

(a) (b)

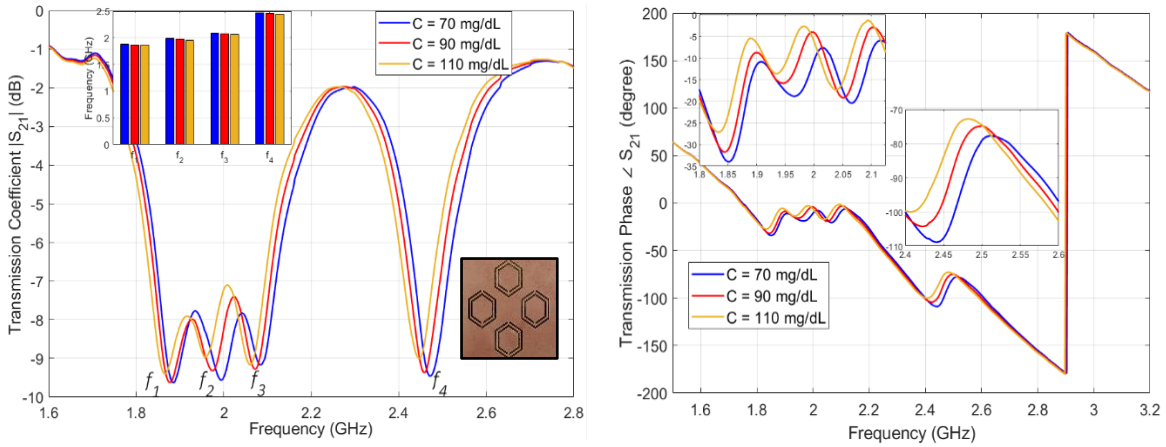

(c) (d)

Figure 3.55: Measured transmission response as function of frequency for tested glucose samples of various concentrations. The transmission coefficient and phase for the (a)-(b) compact and (c)-(d) dispersed sensors, respectively.

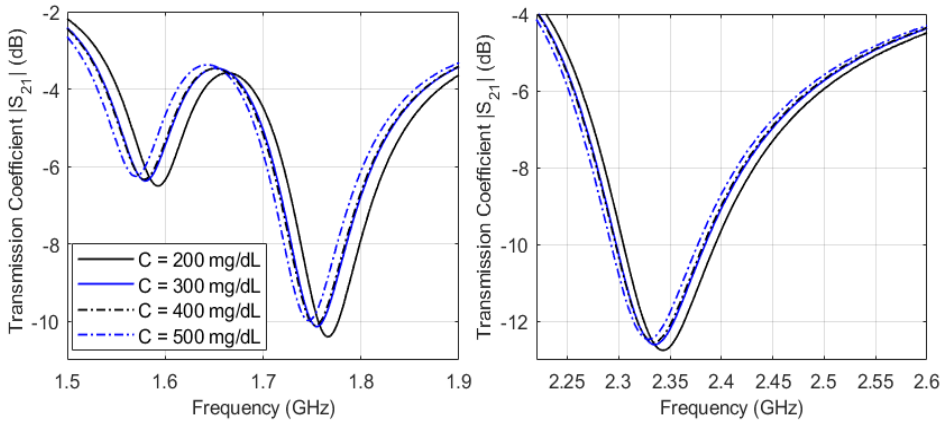

Figure 3.56: Measured transmission response as function of frequency for glucose samples of higher concentrations relevant to the hyperglycemia condition.

3.5.5 Sensitivity Analysis

The VNA measurements of the scattering-parameters of the glucose-loaded CSRR sensors show that the transmission responses (magnitudes and phases) are varying according to the glucose level changes in the loaded sample. Considerable shifts in the resonance frequencies of S_{21} were observed for varying between 70, 90, and 110 mg/dL, and therefore the frequency shifts were primarily considered for assessing the sensitivity range of the proposed sensors. As seen from Fig. 3.57(a) and 3.57(b), both sensors exhibit impressive frequency resolutions that would benefit distinguishing various glucose concentrations of relatively small contrast in dielectric properties. The resonance frequencies resultant from loading a specific glucose concentration can be estimated using the linear regression models derived for each sensor, compact and dispersed, as enclosed in Fig. 3.57(a) and 3.57(b), respectively. Conversely, the inverse models could be used to estimate the unknown glucose level of a tested sample. In these plots, it is observed that the respective resonant frequencies decrease with increased levels of glucose concentrations. However, the frequency resolutions for glucose level changes at the respective

resonances are not perfectly identical. The sensitivity of the compact sensor is estimated as -1.25 × 10^{-3} GHz/(mg/dL) representing the gradient of f_1 and f_2 linear models. However, the best sensitivity slope for the dispersed topology is -9.5 × 10^{-4} GHz/(mg/dL) at f_2 which is a bit lower than its compact counterpart.

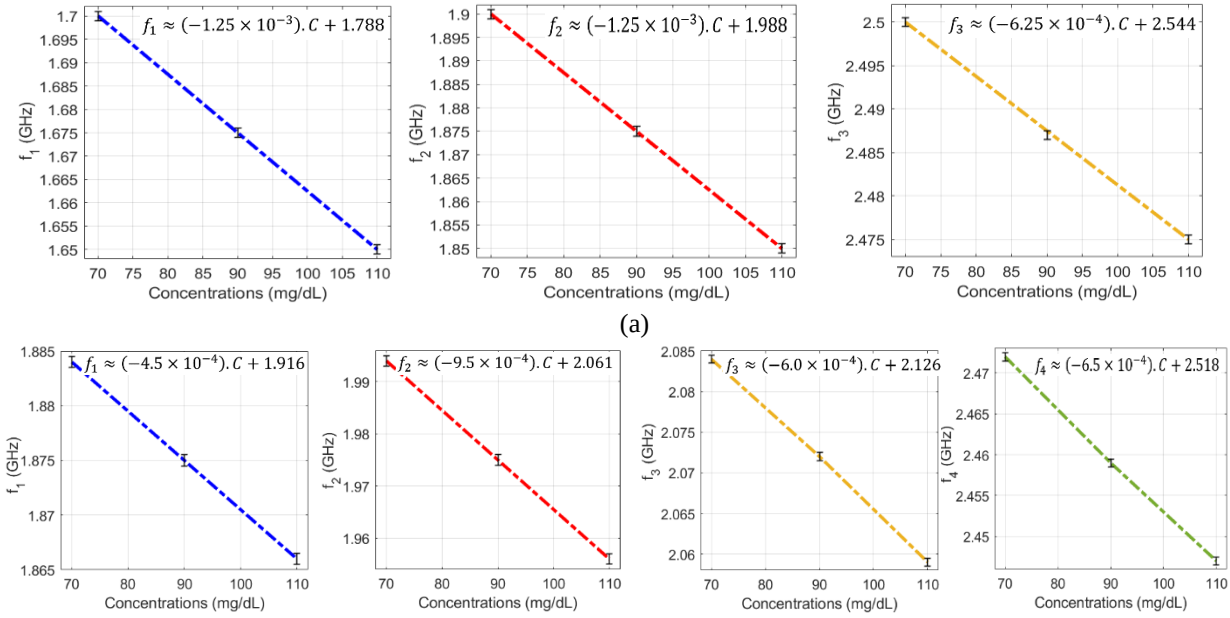

Figure 3.57: Linear correlation models for the resultant resonant frequencies of (a) compact and (b) dispersed sensors at different glucose concentrations. (a) For the compact sensor, three resonances, f_1, f_2, and f_3, are established in the frequency range 1.5 – 2.8 GHz. Sensing the glucose samples on (b) the dispersed sensor exhibits four distinct resonances f_1, f_2, f_3, and f_4 in the frequency range 1.6 – 2.8 GHz. A reduction in the resonant frequencies is observed with growing glucose concentrations.

The VNA microwave system was strictly calibrated to limit the transmission loss at 0.02 dB (back-to-back transmission) over the operating frequency range. This is important to acquire reproducible measurements that are more accurate. It is worthy to mention that all the glucose measurements were repeated three times and the average was reported for precision, repeatability, and reproducibility verifications. This averaging would help to eliminate random noise introduced by the source power (i.e., VNA) or any other uncorrelated noise and improve the SNR accordingly. In each repeatability trial, careful attention was paid towards retrieving the exact initial resonance response of the empty container-loaded sensor after removing the samples using a tissue paper. The robustness of the sensor could be seen from the stable and repeatable frequency responses that vary in a small range of ±0.5 MHz as indicated by the error bars enclosed in these visuals (Fig. 3.57). Given that the sensor frequency reading for 5 mg/dL is about 4.7 MHz (average sensitivity of 0.94 MHz/(mg/dL)), the glucose concentrations as small as 1 mg/dL could be identified using the proposed sensing platform with a reasonable accuracy.

Since the sensor scattering response is quite dependent on the sample EM properties which are temperature dependent, therefore, all the prepared glucose samples were stored in the same room

temperature regulated at 23±1°C. Additionally, the heat and temperature were controlled and monitored at 23±1°C during the glucose experiments to minimize the instrumental and environmental impact on the collected measurements. However, small fluctuations in temperature would not bring a significant effect on the resonance measurements of the CSRR sensors (±1 MHz shift in f_o). This is explained by the fact that, the far-field radiation of our small resonators of sub wavelengths could be effectively suppressed as depicted in Fig. 3.58 where the total electric field is quantified in the far-field region of the sensors with maximum magnitude of about 1 Volts/m. It is shown that most of the EM energy is concentrated in the honey cell area in the near-field region. Therefore, any unwanted environmental variations in the far-field region will not considerably impact the sensor measurements.

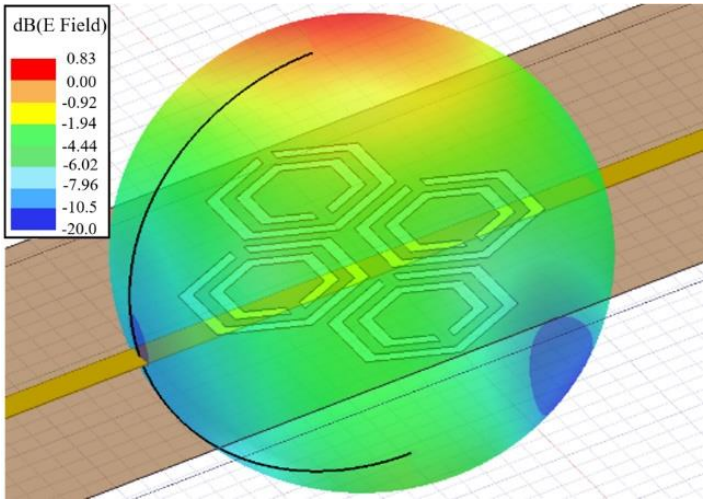

Figure 3.58: Far-field radiation of the honey-cell CSRR sensor

Lastly, in what follows the sensitivity performance of the proposed honey-cell CSRR sensors is compared to other microwave sensors in the recent literature. To this end, a comparative statement is presented in Table 3.13 where state-of-the-art glucose sensors are sorted in the order of increasing sensitivity along with their respective parameters. Herein, the sensitivity is defined as the frequency shift/variation Δf_o with respect to 1 mg/dL of glucose concentration change in SUT for a certain volume and specific test setup. Following this measure, the sensitivity achieved in earlier works based on diverse microwave sensing mechanism is found to be much lower than the least resolution captured by the honey-cell sensors. The sensors sensitivity is also superior to other techniques based on tracing the slight variations of S_{11} and S_{21} resonant magnitudes for which a measuring tool of high-precision is needed. The limited sensitivity in the literature is due to the confined EM fields coupled to the resonator surface that limit the interaction with the tested glucose sample. Because of this phenomenon, the substrate in traditional resonators has a more important role in defining the resonance frequency rather than the SUT of certain glucose content. However, the improved design of the CSRR elements in honey-cell fashion, expands the interaction over the sensing region and allows the frequency response of the sensor to be mainly defined by the SUT permittivity. The achieved sensitivity of this sensor, 0.94 MHz/[mg/dL] is far beyond the best results reported in literature regardless of shape and volume of

SUT. This would render the sensor response less susceptible to environmental and instrumental noises than its conventional counterparts. Therefore, it can be emphasized that the proposed sensor can in principle be used to detect normal blood sugar range quite conveniently as well as those for hypoglycemia and hyperglycemia.

Table 3.13: Comparison against other microwave glucose sensors

Ref	**Sensing technique**	**Operating frequency (GHz)**	**Test solution**	**Sample volume (μL)**	**Concentration (mg/dL)**	**Sensing parameter**	**S MHz/(mg/dL)**
[185]	Microstrip based series resonator	6.5	Aqueous solution	50	0 – 70000	$f_R (S_{21})$	3.13E-5
[186]	Active split ring resonator	1.156	Saline solution	10	18 – 540	$f_R (S_{21})$	7.30E-5
[60]	Spatially separated SRR	1.4	Aqueous solution	600	504 – 3531	$f_R (S_{21})$	1.83E-4
[79]	Dielectric resonator	1.68	Aqueous solution	5	5000 – 30000	$f_R (S_{11})$	2.00E-4
[159]	Rectangular waveguide cavity	1.9	Aqueous solution	43	0 – 2500	$f_R (S_{21})$	4.00E-4
[121]	Patch antenna	5.0	Saline-glucose solutions	36000	0 – 250	$f_R (S_{11})$	1.09E-3
[176]	Open split ring resonator	6.5	Aqueous solution	–	0 – 40000	$f_R (S_{21})$	1.88E-3
[154]	ENG unit-cell resonator	2.074	Aqueous solution	2	2000 – 10000	$f_R (S_{21})$	1.00E-2
[177]	Single-port resonator	4.8	Aqueous solution	125	100 – 1000	$f_R (S_{11})$	1.40E-2
[178]	Distributed MEMS transmission lines (DMTL)	16	Aqueous solution	–	0 – 34780	$f_R (S_{11})$	1.64E-2
[162]	Interdigitated capacitor (IDC) resonator-etched coplanar waveguide (CPW)	2.46	Aqueous solution	2	0 – 8000	$f_R (S_{21})$	2.00E-02
[179]	Complementary electric-LC (CELC) resonator	1.0 – 1.70	Aqueous solution	0.63	2000 – 10000	$f_R (S_{21})$	2.11E-02
[146]	Split ring resonator	4.18	Aqueous solution	–	0 – 5000	$f_R (S_{21})$	2.60E-02
[129]	Tag split ring resonator	4.0	Aqueous solution	200	90 – 720	$f_R (S_{21})$	6.80E-01
Honey -Cell CSRR	Complementary split ring resonator driven by an ISM Radar	2.45	Aqueous solution	600	40 – 140	$f_R (S_{21})$	4.5 – 9.50E-01 (dispersed) 6.3 – 12.5E-01 (compact)

3.5.6 PCA Post Processing

The sensors scattering responses collected from the VNA instrument were analyzed using the PCA unsupervised machine learning algorithm to clearly distinguish various glucose concentrations tested by the sensor. This is a vital add-on to the integrated microwave sensor that could further enhance its sensitivity for detecting the BGLs of interest that vary in a narrow range. It is shown in the previous experimental results that the sensor exhibits distinctive scattering responses in terms of the transmission

coefficient (magnitude and phase) when loaded by various glucose concentrations, however these responses recorded by the VNA (i.e., $|S_{21}|$ or $\angle S_{21}$) would exhibit small changes/shifts in f_o to reflect the varying glucose concentrations. For instance, the slight frequency shifts acquired by the VNA for the compact $|S_{21}|$ resonances that vary in a small resolution of 1.25 MHz/(mg/dL) as shown in Fig. 3.57(a). These changes would be tricky to trace using exclusively common sense and hence the difficulty of precise identification of various glucose levels.

The previous pseudocode in Algorithm 1 is applied to the VNA measurements in Fig. 3.55(a) and 3.55(b) where the transmission coefficient parameters (magnitude and phase) are considered the two feature vectors to be extracted from the frequency response of each tested glucose sample. Since these magnitude and phase responses were recorded at N = 201 frequency points spanning the range from 1.5 to 2.8 GHz, then each glucose sample is described by two feature vectors magnitude and phase with 201 length each. It is shown that samples of various concentrations have these magnitude and phase values varying at some of the respective frequency points especially at resonance frequencies. As described in Algorithm 1, the PCA algorithm could use either the magnitude ($|S_{21}|$) or phase ($\angle S_{21}$) vectors as input features to classify various glucose concentrations. Once the algorithm is provided with measured feature vector x_{C_m} for each glucose sample C_m, it processes the data using the steps in Algorithm 1 to extract the principal components $\mathcal{K}_{C_m}^{i}$ for all the glucose samples and cluster them accordingly based on their concentration-dependent principal components as shown in Fig. 3.59(a) and Fig. 3.59(b) where samples of different glucose concentrations are notably separated in a 2D space when the magnitude and phase feature vectors are used, respectively. It is also observed that both feature vectors (i.e., magnitude and phase) of the sensor are effective and efficient to bring higher discrimination or spatial separation between different glucose samples. This is considered as a training stage for the developed PCA model; therefore, any new tested sample could also be clustered accordingly following the same analytical recipe.

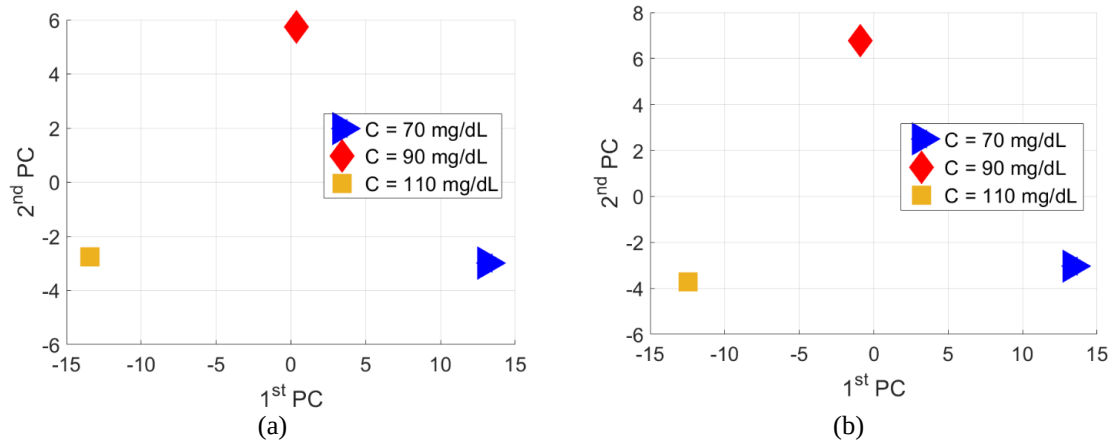

Figure 3.59: ML processing of the measured transmission responses of the compact sensor for various glucose concentrations, (a) Magnitude of S_{21} using PCA and (b) Phase of S_{21} using PCA

Chapter 4. Glucose Levels Monitoring at High Frequencies Using Whispering Gallery Mode Resonators

4.1 Why mm-Wave sensing?

Millimeter-wave (mm-wave) frequencies have been exploited for developing various biomedical appliances due to the enhanced security, available spectrum, reduced interference, and miniaturized sizing for the fabricated devices. In addition, the mm-wave region has shown to be promising for sensing the glucose-loaded solutions for many reasons: non-ionizing nature, good penetration depths inside the liquid tissues, and the good resolution feature for their relatively small wavelength compared to EM radiations at lower microwave frequencies. Additionally, higher sensitivity to the dielectric constant and loss tangents of glucose samples could be obtained as a result of the stronger interaction between the glucose molecules and EM waves in this spectrum. This is demonstrated by the wideband dielectric permittivity measurements performed in distinct frequency bands from 200 MHz to 67 GHz that show the mm-wave spectrum 50 – 67 GHz as a promising region for appreciable complex permittivity contrast between different glucose concentrations as previously discussed in Chapter 2.

Another motivational study that advocates the use of mm-wave regimes for glucose detection is the outcome of a recent clinical experiment where we analyzed clinical blood samples drawn from 7 distinct participants before and after consuming 75mg of glucose (i.e., 14 samples in total) using a VNA in the frequency range (50 – 67 GHz) [187]. In this investigative study, we used the 75g glucose consumption standard adopted by the diabetes check tests [188] to analyze the blood samples of the respective participants using the Keysight Technologies N5227A PNA-67GHz fitted with two V-band adapters connected to WR-15 waveguides. The blood samples were first tested using a standard glucometer device to use its readings as a reference for comparison. The glucometer measurements for all participants are shown in Fig. 4.1(a), pre and postprandial tests with a one-hour time gap. Various behavioural responses to glucose consumption (i.e., rising and dropping variations in glucose level) are attributed to the physiological differences amongst the participants. Next, blood samples of all subjects were tested in the VNA configuration setup by sweeping across the frequencies 50 – 67 GHz, and the corresponding transmission scattering coefficients (S_{21}) were measured as shown in Fig. 4.1(b)

The VNA transmission results were observed to be reliably consistent and aligned with the glucometer readings for BGL variations in certain frequency bands 55 – 57 GHz and 59 – 61 GHz that are highlighted in light green and red rectangles, respectively, as depicted in Fig. 4.1(b). For instance, the pre-prandial glucometer reading for subject 3 of about 0.99 mg/ml has descended to 0.90 mg/ml after consuming the glucose dosage. However, a totally different behaviour was observed in the glucose level variations of subject 6 whose pre-prandial measured glucometer reading of about 0.87 mg/ml jumped to 1.2 mg/ml post the glucose consumption. These trends in glucose levels variations for subjects 3 and 6 were plainly exhibited in the VNA transmission responses in the 55 – 57 GHz frequency

band as shown in Fig. 4.1(b). All the participants in this experiment gave their informed consent for inclusion before they participated in the study. The study was conducted in accordance with the Declaration of Helsinki, and the protocol was approved by the Clinical Research Ethics Committee of project number 31235 on 27 August 2018.

Subject	Pre-prandial reading (mg/ml)	Post-prandial reading (mg/ml)
#1	0.89	1.10
#2	0.80	0.69
#3	0.99	0.90
#4	0.71	1.10
#5	0.82	0.54
#6	0.87	1.20
#7	1.00	0.76

(a)

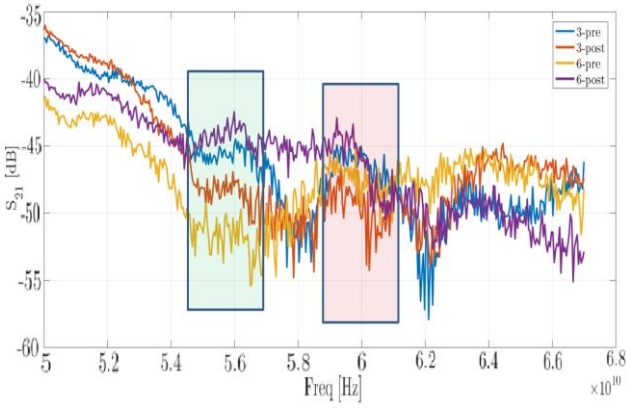

(b)

Figure 4.1: Comparative analysis for the clinical blood samples using VNA and glucometer: (a) Glucometer readings for the seven participants pre and post glucose consumption; (b) VNA measurements of the transmission coefficients for pre and post blood samples of two patients. Shaded windows show the frequency regions where both the PNA and glucometer patterns are consistent.

Microwave resonators are appealing structures for measuring the high complex permittivity of liquids in narrow bands across the electromagnetic spectrum while offering flexibility in design and low-cost fabrication. Circular shaped resonators have special types of higher order modes called "*Whispering Gallery Modes*" with unique properties which make them very suitable for sensing applications. Therefore, in this chapter and in view of the above experiments, several resonant structures supporting higher order WGMs in the mm-wave band were designed using different technologies, analyzed, and simulated for optimal sensing, fabricated, and practically tested in the lab for blood glucose monitoring.

4.2 WGM Sensing

The WGM concept was first introduced on the propagation of high frequency sound waves on concave surfaces by Lord Rayleigh in 1910 [189]. Since then, the idea has been used in a variety of applications in optics (e.g., spherical resonator for sensing [190]), microwave (e.g., antennas, power dividers, filters [191] [192]), and mm-wave electronic systems. Many researchers have studied WGM-based dielectric resonators [193], [194], [195]. WGM resonators feature higher sensitivity and selectivity capabilities as compared to the conventional resonators (of lower-order modes), and other electrochemical, reflectometry, and quasi-optical methods due to their high *Q*-factor resonances [191] [196]. Additionally, their development is more tolerant against dimensional errors in fabrication due to their relatively large size in terms of wavelength. Therefore, they are considered perfect candidates for sensing applications at mm-waves [197].

The principle of operation for those resonance structures can be explicated by the evanescent field concept of interaction. Particularly, when coupled to a wave-guiding structure, unique field distributions of higher-order modes are generated inside a dielectric disc/ring resonator (DDR/DRR) with more energy concentrated towards the cylindrical boundaries [198]. These higher order modes propagate azimuthally (with rapid circumferential variation) along the periphery of the DR with repeated total reflections from the outer edges. The interaction of the WGM evanescent fields with any nearby sample would instantly modify the resonance mode profile depending on the EM properties of the sample. Following the last point, the sensing method on such WGM resonators is based on the resonant perturbation of the excited WGM modes (i.e., perturbing the evanescent field distribution) and hence the modification of one or all its intrinsic resonance attributes, resonance frequency and/or *Q*-factor, in the presence of the sample under test, which are the glucose samples in our case.

There are mainly two types of WGMs possibly excited inside a resonator: travelling wave and standing wave WGMs. In the travelling wave WGM type, the peak locations of the electric field distribution continuously change over time, which is not the case for the standing wave WGMs. The resulting resonant modes triggered inside the DR are classified, depending on the spatial distribution and polarization of the EM fields, as WGE_{nml} of transverse electric-field (i.e., quasi-TE) or WGH_{nml} of an axial electric-field (i.e., quasi-TM) modes, where the integer subscripts *n*, *m*, and *l* represent the varying order or number of field cycles along the azimuthal, radial, and axial directions, respectively [199]. Among the various types of WG modes, we are more interested in WGE_{n00} (axial *H*-field is predominant) and WGH_{n00} (axial *E*-field is predominant) modes that offer highly confined, concentrated, and sensitive fields inside the resonator, and hence the great advantage for more effective sensing of glucose varying tissues. Higher-order WGMs exhibit less radiation loss as compared to lower-order modes. The type of the WGM inside the dielectric resonator is determined by its excitation type and the applied physical parameters.

WGM resonators are appealing because of their unique EM behavior and sensitivity. However, due to the various computational and theoretical challenges, not many WGM-based devices are implemented in the mm-wave range of frequencies. In [200] the maximum sensitivity was studied near critical coupling for specific gap distances between the DR and the coupling guiding structure. A WGM sensor was developed in [201] using a vacuum suction aspirator with a looped Goubau line. The sensor was tested on fixed cylindrical volume of glucose-water solutions of 100 – 500 mg/dL, where a near-linear correlation was observed around 56.2 GHz. In-vivo experiments were conducted on the surface of human arms over 1.8 – 5 GHz. However, beside the limited sensitivity, glucose changes were tracked using only the S_{21} resonant amplitude that is much influenced by the associated noise and other measurement uncertainties. A sapphire WGM resonator was used at $f = 35.5$ GHz to obtain the complex permittivity of biochemical liquids (including glucose aqueous solutions) loaded at sub-microliter volumes inside a microfluidic channel. However, the setup required a precisely stabilized temperature for reliable resonant frequency readings [202].

The concept of coupled WGM resonator can be effectively used for glucose sensing applications that require a confined field inside the resonator, while realizing a compact integrated device. In the next sections of this chapter, the aforesaid privileges of WGM are exploited to propose integrated WGM sensors operating at different mm-wave ranges to be used as sensing platforms for tracking the varying glucose concentrations in blood mimicking samples.

4.3 DIG-based WGM Sensor

A variety of wave guiding technologies has been used over the entire range of frequencies from microwave to optics such as TEM transmission lines (e.g., coaxial cables), TEM and quasi-TEM planar multi-layer metallic transmission lines (e.g., co-planar waveguide (CPW), microstrip, inverted microstrip, suspended strip-line), metallic waveguides, laminated waveguides, substrate integrated waveguides (SIWs), and more recently the dielectric waveguides. These guiding technologies are compared in Table 4.1.

Table 4.1: Comparisons of the wave guiding technologies in the microwave frequencies

Guiding Technology	**Examples**	**Pros**	**Cons**
TEM transmission lines	Coaxial cables	• Guide EM signals up to a few meters in the microwave range up to 110 GHz	• Loss and fabrication complexities
TEM and quasi-TEM planar multi-layer metallic transmission lines	Co-planar waveguide (CPW), microstrip, inverted microstrip, suspended strip-line, etc.	• Realizing planar devices in the microwave spectrum	• Ohmic loss and dispersion for off-chip configurations at mm-Waves and beyond
Metallic waveguides	Rectangular metallic waveguide	• Suitable for high power transmission at micro/mm-Wave • Low-insertion loss and simple design	• Large and bulky geometry • Integration difficulties At high frequencies: • Conductor loss • Dimensional inaccuracy • Complex interconnects of high performance
Substrate integrated waveguides (SIWs) [203]	Dielectric slab between two metal plates/sheets	• Reduced height waveguide • Dominantly support TM modes • Ease of fabrication • Integrable with planar circuit	• Higher losses than metallic waveguides • Challenging fabrication/manufacturing of hole arrays (> 150 GHz) [204]
Dielectric waveguides [205]	Rectangular dielectric waveguide (suspended), image guide, and insulated waveguide.	• Simple geometry • Efficient EM performance • Low-loss • Reasonable dimensions in the mm-Waves and beyond • High field confinement • Less radiation loss	NA

Featured dielectric waveguides emerge as a reasonable substitution to overcome the limitations of the traditional metallic waveguides in manufacturing inaccuracies and conductive losses at mm-wave

frequencies and beyond. They offer the combined advantages of low-cost, low-loss, light weight, and ease of fabrication and integration with planar circuits. Therefore, they are a promising candidate of guiding structure to achieve high confinement wave transmission inside the WGM resonators at mm-Wave range.

In what follows, it is presented a low-cost mm-wave integrated WGM bio-sensor that consists of a dielectric disc resonator (DDR) coupled to a dielectric image waveguide (DIG) where both combined inside a rectangular metallic waveguide. The DIG excites the WGM modes inside the DDR by linking the residual evanescent tail of the guided field to the neighboring resonator. The induced WGM waves propagate circularly (forward and backward) around the centre of the DDR towards its cylindrical boundaries. After *n* rotations they experience a $2\pi n$ phase shift. The induced travelling waves are confined inside the resonator by repeated total reflections from the internal/external edges of the DDR yielding high concentration of the field close to boundaries. The proposed sensor aims at monitoring the variations in blood glucose levels on a non-contact manner in the mm-wave regime. The tested glucose sample is placed inside a cylindrical container on top of the DDR surface whose rims are highly intensified with the WGM electric-fields. Therefore, intensive interaction is induced at the underlying mm-wave frequency between the lossy loaded sample and the coupled WGM evanescent fields. Consequently, the resulting changes in the WGM resonance characteristics are considered as a unique signature of the dielectric properties of the tested glucose sample that can be identified by carefully calibrating the sensing parameters for this WGM sensing structure. More insights into these sensing parameters are illustrated by studying the mathematical model of the WGM resonators in the next subsection.

4.3.1 Mathematical Coupling Model of Reaction-Mode WGM Resonators

The WGM sensor scheme of the dielectric resonator (DR) coupled to the dielectric image waveguide (DIG) (or microstrip-line MTL) can be approximated with a four-port coupler [191] as depicted in Fig. 4.1 where the power is transmitted from port 1 to port 2 (or vice versa). Ports 3 and 4 are virtual ports around the resonator to illustrate the coupled-wave behaviour that is travelling forward and backward around the DR (i.e., like a transmission line) following the relations as given by $V_3^- = e^{\gamma} V_4^+$ and $V_4^- = e^{\gamma} V_3^+$, where V_i^+ and V_i^- are the incident and reflected EM waves, respectively, $\gamma = \alpha + j\Phi$ is the complex propagation coefficient, α is the total attenuation of the travelling wave (or resonator attenuation), Φ is the total phase shift delay around the DR.

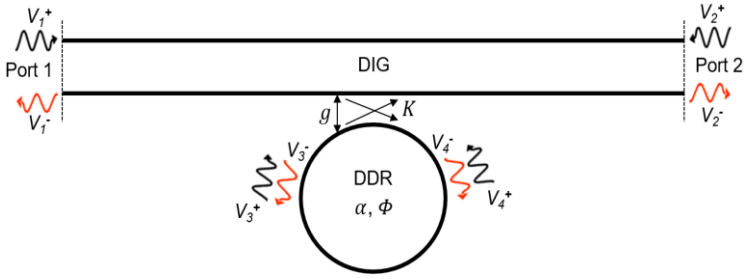

Figure 4.2: Approximated four-coupler model of the unloaded WGM sensor.

The two-ports transmission coefficient S_{21} (insertion loss) of the WGM resonator can be directly derived from the scattering matrix of the four-port coupler (given in Eq. (4.1)) while substituting the forward and backward relations for the waves presenting at ports 3 and 4, as given in Eq. (4.2) [191] [206]

$$S^{4p} = \begin{pmatrix} 0 & \sqrt{1-K^2} & jK & 0 \\ \sqrt{1-K^2} & 0 & 0 & jK \\ jK & 0 & 0 & \sqrt{1-K^2} \\ 0 & jK & \sqrt{1-K^2} & 0 \end{pmatrix} \tag{4.1}$$

$$\begin{pmatrix} V_3^- \\ V_4^- \end{pmatrix} = \begin{pmatrix} 0 & e^{\gamma} \\ e^{\gamma} & 0 \end{pmatrix} \begin{pmatrix} V_3^+ \\ V_4^+ \end{pmatrix} \tag{4.2}$$

And the resulting S_{21} is given in Eq. (4.3).

$$S_{21} = \frac{\sqrt{1-K^2} - e^{-j(\alpha+j\Phi)}}{1 - e^{-j(\alpha+j\Phi)}\sqrt{1-K^2}} \tag{4.3}$$

It could also be written as in Eq. (4.4) by considering $\xi = e^{-\alpha}$ as the loss factor of the DR representing the normalized amplitude of the WGM travelling-wave after one circular rotation around the resonator. It ranges from a minimum value of $\xi = 0$ (~ lossy resonator) up to the maximum of $\xi = 1$ (~ lossless resonator with zero attenuation). *K* is the coupling coefficient between the waveguide and resonator, and it has a similar range from 0 to 1, where *K = 0* represents the no coupling state with zero power transferred to the DR and *K = 1* indicates the critical-coupling state that will be explained next.

$$S_{21} = \frac{\sqrt{1-K^2} - \xi e^{-j\Phi}}{1 - \xi e^{-j\Phi}\sqrt{1-K^2}} \tag{4.4}$$

The DIG-to-DDR power transmission coefficient and phase will be

$$P_T = |S_{21}|^2 = \frac{(1-K^2) + \xi^2 - 2\xi\sqrt{1-K^2}cos\Phi}{1 + (1-K^2)\xi^2 - 2\xi\sqrt{1-K^2}cos\Phi}, \tag{4.5}$$

$$\Theta_T = \angle S_{21} = tan^{-1}\frac{\xi K^2 \sin\Phi}{\sqrt{1-K^2}(1+\xi^2) - \xi(2-K^2)cos\Phi}, \tag{4.6}$$

The loaded quality-factor (Q_L) of the WGM sensor is also dependent on the loss factor/attenuation and the coupling coefficient as given by [193]

$$Q_L = \frac{n\pi}{\xi\sqrt{1-K^2}}\sqrt{\frac{1+(1-K^2)\xi^2}{2}}, \tag{4.7}$$

Under critical coupling condition in the resonance condition ($\Phi = 2\pi n$), the WGM sensor exhibits band-stop filter characteristics where all the power fed from the input port is absorbed by the DDR yielding zero power to receive at the output port (i.e., $S_{21} = 0$) as long as the resonance is happening. By substituting these conditions of $S_{21} = 0$ and $\Phi = 2\pi n$ in Eq. (4.5) we derive the relation that defines the critical coupling state where the K and ξ are inversely related.

$$\xi = \sqrt{1-K^2}, \tag{4.8}$$

This critical-coupling state is an exceptional feature for the WGM travelling-wave sensors. It can be exploited to acquire an extremely high sensitivity in the transmission response when the sensor is perturbed at any of its parameters Φ, ξ, and K as demonstrated in Fig. 4.3(a) that shows the critical coupling resonances in the transmission response for different values of the coupling coefficients K = 0.2, 0.25, and 0.3 that meet the criteria in Eq. (4.8) when $\Phi = 2\pi n$. The dependency of the transmission resonant peak/notch on the ξ parameter of the DDR is illustrated in Fig. 4.3(b) that depicts the transmission coefficient response as a function of the phase shift per rotation inside the DDR for a specific coupling coefficient value at K = 0.2 and with different values for the loss factor ξ. For a relatively large value of ξ than the equality in Eq. (4.8), the resonant peak was about -22 dB and then it starts dipping down gradually with small perturbation in ξ. The critical coupling resonance of the deepest amplitude occurs when this ratio equals unity as shown with the dashed black curve. When ξ is getting smaller beyond this equality, the resonant peak starts decreasing to unlock the critical coupling state.

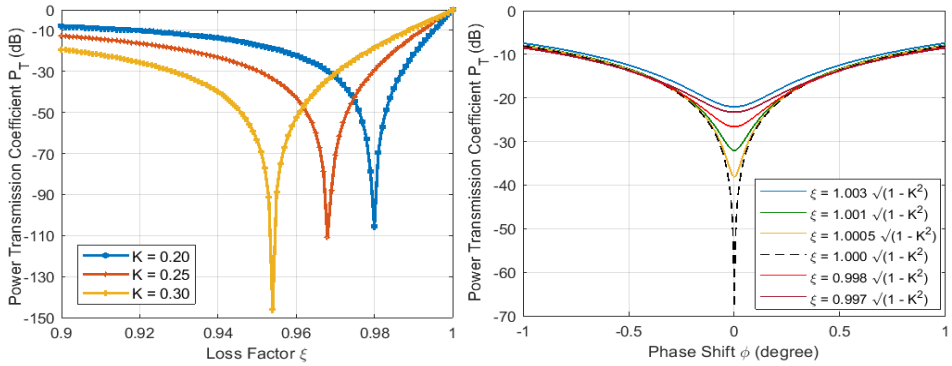

(a) (b)

Figure 4.3: Transmission coefficient variations at resonance as function of (a) loss factor of the DDR for different coupling coefficients, (b) phase delay per rotation inside the DDR for different loss factors.

4.3.2 Coupling Coefficient and Loss Factor Dependencies

Herein, we discuss the factors that affect the coupling coefficient K and the loss factor ξ for the WGM

sensor. First, the coupling coefficient K is considerably dependent upon the spacing distance g between the DIG and the DDR. This is illustrated very clear in Fig. 4.4 that depicts the simulated transmission responses (insertion loss) at different spacing distances for the WGH_{600}, WGH_{700}, and WGH_{800} excited modes. The transmission resonances are shifted in frequency and varied in Q-factor with g changing between 0.1 to 0.4 mm. The plot also implies a near critical coupling state for the WGH_{700} and WGH_{800} modes when the spacing is set around g = 0.3 mm, this would clearly emphasize that stronger coupling is not necessarily achievable by placing the DDR very close to the driving DIG. In fact, for a given amount of loss within the DDR, the strongest coupling occurs only at a specific distance between the DDR and the DIG, and if the resonator loss changes then the critical coupling will be defined for another gap distance. This statement also suggests that the coupling coefficient K is also a function of the amount of loss in the DDR as well as the loaded sample. This interesting phenomenon will be shown later when the lossy glucose samples are loaded on top of the DDR resulting into a new set of critical coupling conditions that differ from the one shown in Fig. 4.4 for the unloaded DDR for all the supported WGH modes.

The second important parameter for the WGM sensor is the loss factor ξ of the utilized DDR represented by the loss tangent $tan\delta$ property of its fabricated material. Generally, higher losses within the DDR will affect the transmission response by decreasing the transmitted power to the receiving port. It may also decrease the resonance peak of the WGM mode, however, the strongest WGM coupling might occur at a specific loss tangent for the DDR that is not necessarily the lowest in value. The aforesaid features would be advantageous for sensing the glucose level when the tested sample is integrated on top of the DDR. The S_{21} resonance characteristics (magnitude and phase) of the combined sensor become very sensitive to any small perturbation close to its boundary region making the sensor capable of differentiating various glucose concentrations with very small differences in EM properties.

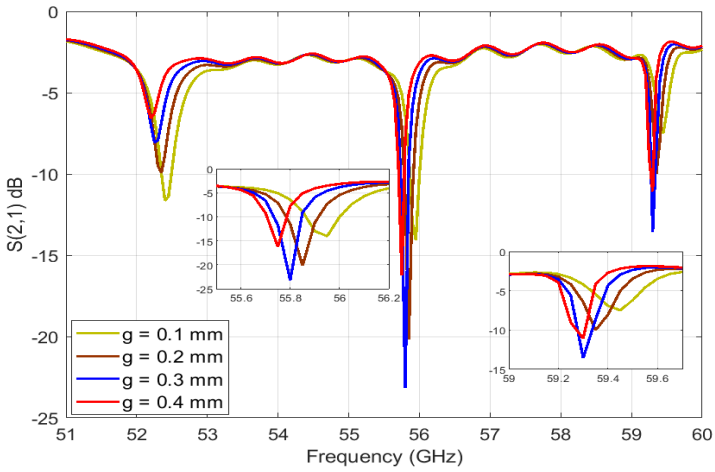

Figure 4.4: Simulated transmission coefficients for the unloaded DDR at different gap distances.

4.3.3 WGM Sensitivity Analysis for Glucose Dielectric Properties

In what follows we study the theoretical sensitivity of the WGM sensor to the variations in the dielectric properties (i.e., complex permittivity) of the glucose samples that are placed inside a cylindrical

container on top of the DDR. The glucose samples have complex relative permittivity of $\epsilon_{rg} = \epsilon'_{rg} - j\epsilon''_{rg}$ where both the real and imaginary parts have large values that vary based on the glucose concentrations dissolved in the sample as discussed earlier in Chapter 2. The DDR underneath the glucose sample has also a complex relative permittivity of $\epsilon_{rDR} = \epsilon'_{rDR} - j\epsilon''_{rDR}$ with small real and imaginary parts that are both fixed in value. The integrated structure of the DDR and the glucose sample are placed at a specific distance g from the exciting DIG. The interaction between the loaded glucose sample and the WGM evanescent field induced by the DDR is reflected in the measured transmission coefficient and phase of the entire structure as given by Eq. (4.5) and (4.6).

To account for the two varying properties of the tested glucose samples, the sensitivity of the sensing parameters P_T and Θ_T are defined for the real and imaginary parts of the glucose sample permittivity whose effects appear more dominantly in the phase delay per rotation inside the DDR and its loss factor, respectively. Therefore, the sensitivity expressions can be written as follows using the chain rule for partial derivatives.

$$S_{P_T}^{real} = \frac{\partial P_T}{\partial \epsilon'_{rg}} = \frac{\partial P_T}{\partial \Phi} \frac{\partial \Phi}{\partial \epsilon'_{rg}}, \tag{4.9}$$

$$S_{P_T}^{imag} = \frac{\partial P_T}{\partial \epsilon''_{rg}} = \frac{\partial P_T}{\partial \xi} \frac{\partial \xi}{\partial \epsilon''_{rg}}, \tag{4.10}$$

$$S_{\Theta_T}^{real} = \frac{\partial \Theta_T}{\partial \epsilon'_{rg}} = \frac{\partial \Theta_T}{\partial \Phi} \frac{\partial \Phi}{\partial \epsilon'_{rg}}, \tag{4.11}$$

$$S_{\Theta_T}^{imag} = \frac{\partial \Theta_T}{\partial \epsilon''_{rg}} = \frac{\partial \Theta_T}{\partial \xi} \frac{\partial \xi}{\partial \epsilon''_{rg}}, \tag{4.12}$$

The terms $\frac{\partial P_T}{\partial \Phi}$, $\frac{\partial P_T}{\partial \xi}$, $\frac{\partial \Theta_T}{\partial \Phi}$, and $\frac{\partial \Theta_T}{\partial \xi}$ are derived by differentiating Eq. (4.5) and (4.6) with respect to the corresponding parameters of Φ and ξ. When the critical-coupling condition for the integrated sensor is satisfied, these terms will be at their maximum values. This is very clearly illustrated in Fig. 4.3(a) and 4.3(b) that show the variation in P_T as function of the loss factor of the DDR and the phase shift per rotation, respectively. The variations in $\frac{\partial \Theta_T}{\partial \Phi}$, and $\frac{\partial \Theta_T}{\partial \xi}$ can be depicted using similar plots.

The term $\frac{\partial \Phi}{\partial \epsilon'_{rg}}$ in Eq. (4.9) and (4.11) can be calculated indirectly by relating the phase delay parameter Φ to the WGM resonant frequency f_r as given in Eq. (4.13) assuming that the axial propagation constant k_z is very small compared to the quantity $\sqrt{\epsilon'_{rDR}}\, k_o$, where ϵ'_{rDR} is the dielectric constant of the DDR and k_o is the free-space wave-number [207]

$$\frac{\partial \Phi}{\partial \epsilon'_{rg}} = 4\pi^2 R \frac{\sqrt{\epsilon'_{rDR}}}{C} \frac{\partial f_r}{\partial \epsilon'_{rg}}, \tag{4.13}$$

where R is the radius of the DDR, C is the speed of light in vacuum, and $\partial f_r / \partial \epsilon'_{rg}$ is the sensitivity of the resonant frequency with respect to the real permittivity of the glucose sample. The latter can be determined via numerical analysis for the shifts in f_r for a given WGH_{n00} mode due to the change in the

sample dielectric constant.

Similarly, the term $\frac{\partial \xi}{\partial \epsilon_{rg}''}$ in Eq. (4.10) and (4.12) is determined by formulating the loss factor of the DDR as a function of the unloaded *Q*-factor of the sensor structure approximately as given in Eq. (4.14) in the near resonance [193]. By differentiating this quantity with respect to the sample imaginary permittivity we obtain the relation in Eq. (4.15).

$$\xi = e^{\left(-\pi R k_o \sqrt{\epsilon_{rDR}'} {Q_U}^{-1}\right)}, \tag{4.14}$$

$$\frac{\partial \xi}{\partial \epsilon_{rg}''} = -\xi \ln(\xi)\, {Q_U}^{-1} \frac{\partial Q_U}{\partial \epsilon_{rg}''}, \tag{4.15}$$

where $\frac{\partial Q_U}{\partial \epsilon_{rg}''}$ is a figure of merit that defines the sensitivity of the *Q*-factor of the integrated sensor with respect to the glucose imaginary permittivity. It can be calculated as in Eq. (4.17) by the partial derivative of Eq. (4.16) [208]

$$\frac{1}{Q_U} = \mathrm{E}_{DR}\, tan\, \delta_{DR} + \mathrm{E}_g\, tan\, \delta_g + \frac{1}{Q_{con}} + \frac{1}{Q_{rad}}, \tag{4.16}$$

$$\frac{\partial \xi}{\partial \epsilon_{rg}''} = \xi_o \ln(\xi_o)\, Q_U \frac{\partial \mathrm{E}_g}{\partial \epsilon_{rg}'}, \tag{4.17}$$

By substituting Eq. (4.13) and (4.17) in the sensitivity expressions Eq. (4.9) – (4.12), we can clearly see that the sensitivity of a given WGM resonant mode with respect to the glucose real permittivity (dielectric constant) is determined by the resultant shifts in its resonant frequency. While the WGM sensitivity to changes in the imaginary permittivity (loss property) can be obtained by tracking the changes in the corresponding *Q*-factor. This sensitivity is also directly proportional to the *Q*-factor of the DDR, which means that higher sensitivity can be acquired by having DDR of larger *Q*-factor.

4.3.4 Design and Specifications

The WGM sensor structure consists of a Dielectric Image Guide (DIG) coupled to a dielectric disc resonator (DDR) with both installed on top of a planar metallic support structure. The DIG with the low-loss, easy-to-manufacture, and wide-band performance characteristics in the mm-wave band is designed in two different layouts, straight and curved. Both layouts of the DIG are linearly tapered at both ends to reduce the loss caused by the possible scattering and reflection at the discontinuities, and to enhance and strengthen its coupling to the rectangular metallic waveguide. Both DIG and DDR are integrated inside a rectangular metallic waveguide and excited via metallic wave ports/adaptors (WR-15) to support the dominant mode (E_z^{11}) operation in the mm-wave frequency band of interest, resulted into operating the DDR in WGH modes. However, exciting the structure by means of a metallic waveguide could possibly excite the E_x^{11} mode inside the DIG, therefore it should not be triggered.

The DIG is used for exciting the WGM modes with travelling-wave resonances inside the DDR by linking the evanescent tail of the guided field that is mostly confined inside the dielectric waveguide region to the neighboring dielectric resonator. The width parameter of the DIG is crucial in controlling the spread or the extent of the evanescent tail exploited for coupling the power into the DDR. In particular, the evanescent field with longer tail would be realized by fabricating the DIG with smaller width, and therefore making the DIG-to-DDR coupling less sensitive to their separating gap g. Following that, the exciting DIG is fabricated using Alumina of dielectric constant $\epsilon_r' = 9.2$ and loss tangent $tan\delta = 0.0005$, for its fairly low-loss, easy-to-fabricate, and low-cost. It has a cross section of 1×0.8 mm^2 (width $W = 0.8mm$, height $H = 1mm$) and a total length of 50 mm with linear tapers at both ends to reduce the insertion and return losses. The DDR was fabricated from a low-loss Silicon material of dielectric constant $\epsilon_r' = 11.6$ and loss tangent $tan\delta = 0.001$ using the Deep Reactive Ione Etching (DRIE). It is pivotal to consider the WGM mode number as a deigned parameter when designing the DDR for sensing applications. Low-order modes (n < 5) for example are radiating with low Q-factor while the relatively higher-order modes (n > 10) require a larger size of DDR for operating in the same desired range of frequency. Additionally, such higher-order modes are very confined around the DDR boundary with a very small evanescent field tail that is not adequate to sense any external perturbations outside of DDR.

With that being considered, the DDR is designed accordingly in a disk shape with axial height h = 0.5 mm and radius R = 3.42 mm such that the minimum mode number of WGM is larger than 5 over the desired range of frequency 50 – 70 GHz to enhance the mode confinement and minimize the radiation. All these design specifications and geometries were set after simulating the sensing structure using the 3D EM solver ANSYS HFSS as will be explained in the next subsection. Additionally, the sensitivity performance of the designed WGM sensors were analyzed when loaded with different glucose concentrations of interest via integrating their dielectric properties at the operating mode frequency using the single-pole Debye model extracted in Chapter 2.

4.3.5 Numerical Simulations

The proposed design of the sensor structure shown in Fig. 4.5(a) with a straight DIG was simulated with the previously specified parameters, before loading any glucose samples, using ANSYS HFSS. The gap between the DIG and DDR was set initially to g = 0.5 mm. The driven solution of the simulation model was set with the appropriate parameters of solution frequency, maximum number of passes, delta S for allowable variation between consecutive meshes, and minimum converged passes. The port and meshing sizes were chosen to achieve the convergence criteria accordingly. In another layout, the DIG is simulated with a curvature (R_c = 4 mm, θ_c = 45^o) in the area around the DDR to realize a more compact packaged system as shown in Fig. 4.5(b). It has a similar cross section of 1×0.8 mm^2 and a total length of 50 mm with linear tapers at both ends. The taper parts have a length of L_2 = 5 mm each. The simulated S_{21} transmission curves as function of the frequency for both layouts

straight and curved, are plotted in Fig. 4.6(a) and 4.6(b), respectively, in the entire mm-wave band 50 – 70 GHz when the DDR is unloaded (dashed green color). Five distinct WGH resonance modes are observed in this band as labelled accordingly in each plot, WGH_{600}, WGH_{700}, WGH_{800}, WGH_{900}, and WGH_{1000}. The few ripples shown are due to the imperfect coupling at g = 0.5 mm.

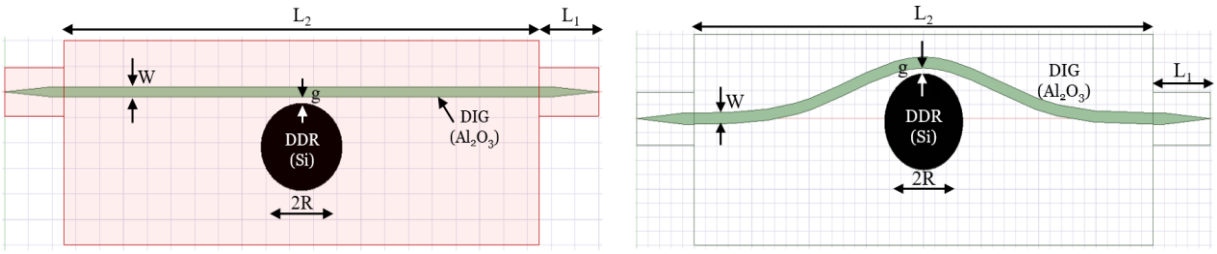

(a) (b)

Figure 4.5: The design geometries of the proposed WGM sensor structures with (a) straight DIG and (b) curved DIG, before loading glucose samples (top view)

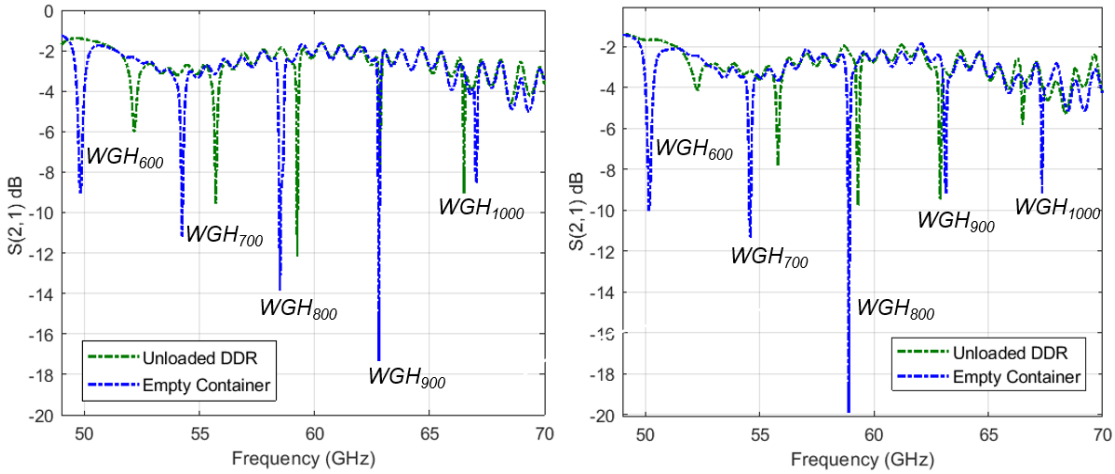

(a) (b)

Figure 4.6: Simulated transmission coefficients on 50 – 70 GHz mm-wave band for different DDR states and the corresponding WGM modes (a) straight DIG and (b) curved DIG

A plexiglass container of dielectric constant $\epsilon_r' = 3.4$ and loss tangent $tan\delta = 0.001$ was integrated on top of the DDR to hold the liquid samples of various glucose concentrations as shown in the final designs in Fig. 4.7. The parametric sweep function in HFSS was used to optimize the sensitivity performance of the integrated sensor when loaded with glucose samples inside the container. First, it was desired to achieve strong coupling between the DDR and glucose sample inside the container, and it was necessary to design the sample container properly to acquire the highest sensitivity at each WGM mode. Specifically, the bottom thickness t_2 of the container was observed to considerably affect the coupling between the DDR and the glucose sample inside the container when swept from 0 mm to 3 mm. The thickness of t_2 = 1.5 mm was resulted into better coupling as illustrated in Fig. 4.8(a) and 4.8(b), respectively, thereby it was used to design the integrated sample container. while the thickness for the side-wall t_1 brings no significant effect. Based on these observations, the container was designed

with height h_c = 7 mm, side and bottom thickness t_1 = 0.1 mm and t_2 = 1.5 mm, respectively. Loading the clear empty container on top of the DDR would result into small shifts in the resonant frequencies for each WGH mode as depicted in Fig. 4.6(a) and 4.6(b) for the straight and curved layouts, respectively. It is observed that the shift exhibited at each WGH mode is different from other modes.

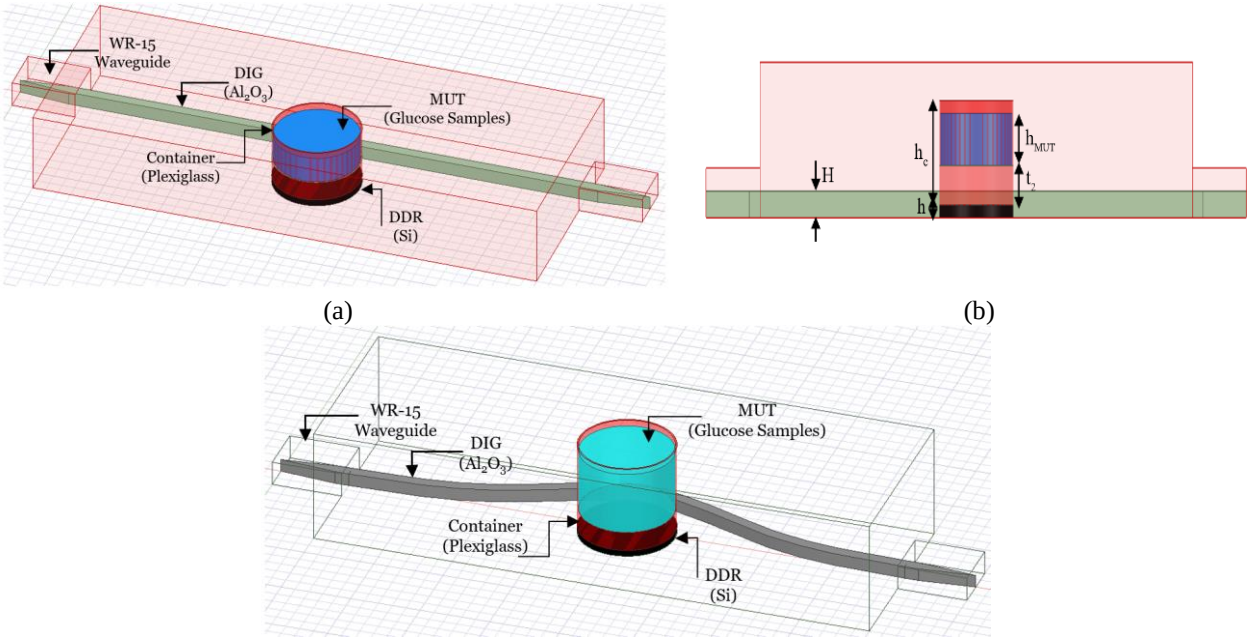

Figure 4.7: Final integration and geometrical parameters of the proposed WGM sensors with straight DIG (a) 3D view, (b) side view, and curved DIG (c) 3D view

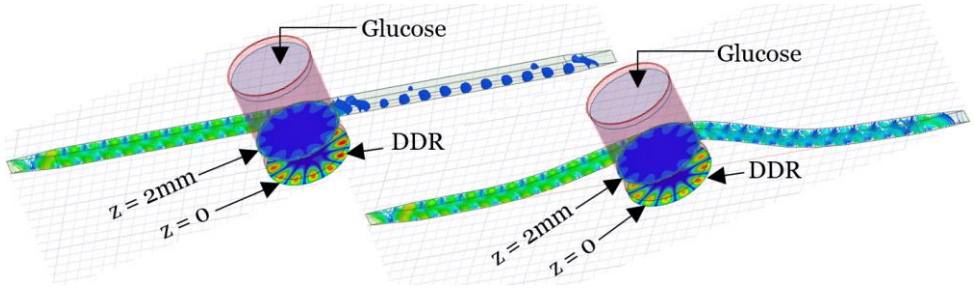

Figure 4.8: Electric-field distribution inside the dielectric waveguide, bottom surface of the DDR (z = 0), and inside the glucose sample (z = 2 mm) for (a) straight DIG and (b) curved DIG.

Second, we also aimed at creating a critical coupling between the loaded dielectric resonator and the dielectric waveguide at the different supported WGH modes in order to obtain the largest *Q*-factor with steepest resonant dips and depths for effective sensing. Such conditions were determined by sweeping the gap parameter g from 0.1 mm to 0.8 mm in steps of 0.1 mm when the structure was loaded with different glucose samples at each WGH resonance frequency. Interestingly, for a given WGH mode the resonator would have the same critical coupling gap when loaded with the different glucose samples. This is demonstrated in Fig. 4.9 that shows a critical coupling resonance at f = 54.1 GHz for the WGH_{700} mode when the spacing was set to g = 0.5 mm between the waveguide and the loaded resonator with

0.7, 0.9, and 1.1 mg/ml glucose samples. The variation in the amount of loss in these glucose concentrations is very small as shown earlier, therefore the resultant effective loss for the integrated resonator (DDR + glucose-varying sample) will hold the same critical coupling gap at various concentrations. However, this critical coupling condition is varying from one WGH mode to another as shown in Table 4.2.

To determine the critical coupling gap for each individual WGH mode, separate simulations were performed for the loaded DDR at the appropriate frequencies corresponding to each WGH mode while varying the gap parameter *g*. Table 4.2 presents the critical coupling gap for each WGH mode and for both sensor layouts, straight and curved. Finally, we studied the sensitivity behaviour of both WGM sensors under the critical coupling condition for each supported WGH mode for the glucose level variations in the loaded samples 0.7, 0.8, 0.9, 1.0, 1.1, and 1.2 mg/ml. Different glucose concentrations were simulated by integrating their dispersive EM properties, dielectric constant and loss tangent, in the HFSS simulator using the single-pole Debye model with the independent coefficients in Table 2.6 as extracted from the DAK-TL mm-wave measurements.

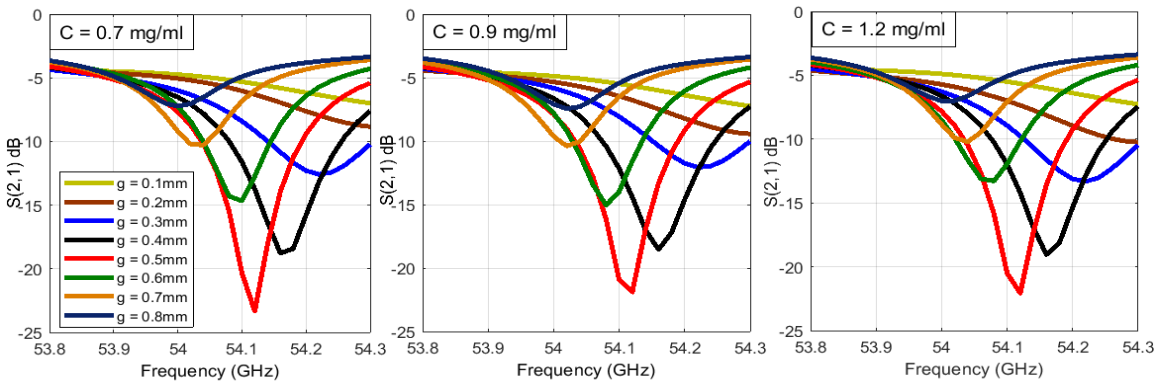

(a) (b) (c)

Figure 4.9: Transmission curves for WGH700 mode at different gaps between the DIG and DDR. The resonator has the same critical-coupling gap when loaded with glucose samples of concentrations 0.7, 0.9, and 1.1 mg/ml.

In these simulations, it is interesting to note that the first lower order modes WGH_{600} and WGH_{700} exhibit higher sensitivity for changes in glucose levels compared to the higher order modes WGH_{800}, WGH_{900}, and WGH_{1000} in the mm-wave range. For example, when the straight-DIG sensor operating at WGH_{600} and WGH_{700}, the $|S_{21}|$ varies by 0.31 dB and 0.25 dB, respectively, for 0.1 mg/ml increase in glucose concentration (e.g., from 0.7 to 0.8 mg/ml), while this variation in $|S_{21}|$ is shown to be around 0.04 dB and 0.03 dB in the higher modes WGH_{800} and WGH_{900}, respectively, for a similar change in glucose level.

Similar phenomena were noted when testing the glucose samples using the curved-DIG sensor. However, its sensitivity performance to variations in glucose levels is shown to be higher at the two lower-order WGH modes compared to that of the straight-DIG as demonstrated by the sensitivity computed for both using $\Delta S_{21}/\Delta C$ in dB/(mg/dL) and listed in Table 4.2 for each WGH mode. Fig. 4.10(a) and 4.10(b) show the transmission responses for the different glucose samples at WGH_{600} and

WGH$_{700}$, respectively, when tested using the straight-DIG sensor. Fig. 4.11(a) and 4.11(b) plot these transmission responses at *WGH*$_{600}$ and *WGH*$_{700}$, respectively, when the curved-DIG sensor was used. The amplitude resolution of the transmission coefficient for the glucose level changes at both modes *WGH*$_{600}$ and *WGH*$_{700}$ is plotted in Fig. 4.12(a) and 4.12(b), for the two WGM sensors.

The phase of S_{21} was also noticed to be sensitive to glucose level variations in the lower-order WGH modes. Fig. 4.13(a) and 4.13(b) depict the phase responses to glucose level changes when the *WGH*$_{600}$ mode was excited inside the sample using the straight-DIG and curved-DIG, respectively. For the straight-DIG case for example, the phase changes by 1.2^o and 0.7^o on average at f = 49.4 GHz and f = 49.48 GHz, respectively, for any 0.1 mg/ml change in glucose. However, the phase response of the curved-DIG sensor varies by 4^o at f = 49.9 GHz for a similar change in glucose level.

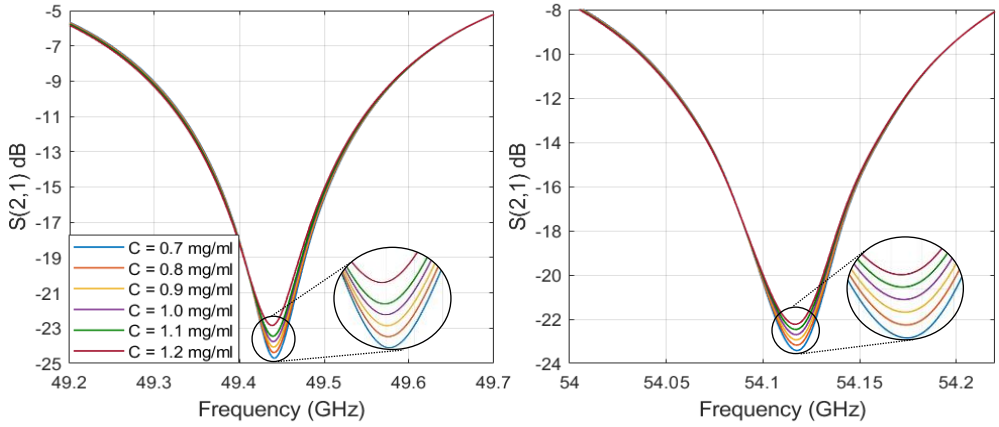

Figure 4.10: Simulated transmission coefficients for different glucose concentrations loaded on the straight WGM sensor at the WGH$_{600}$ and WGH$_{700}$ resonant modes

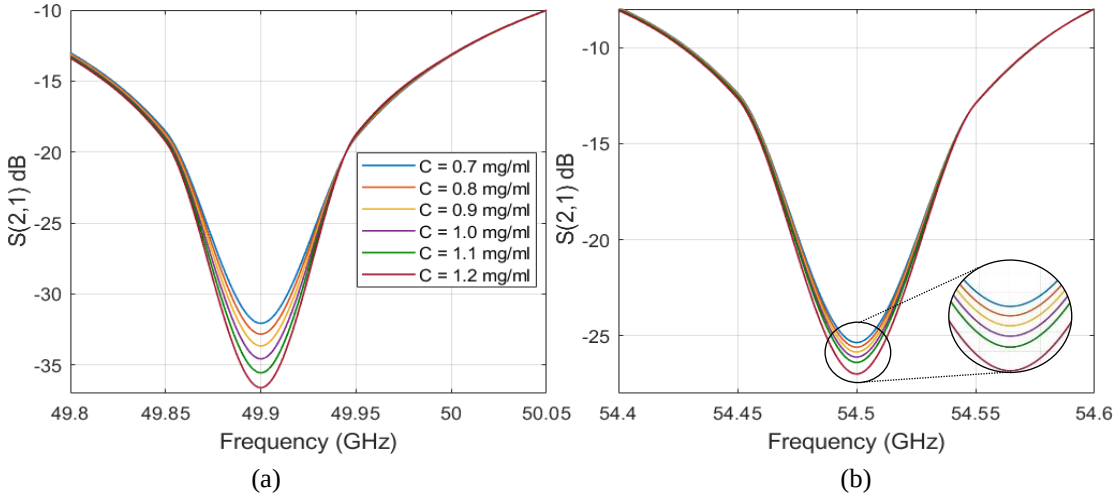

Figure 4.11: Simulated transmission coefficients for different glucose concentrations loaded on the curved WGM sensor at the WGH$_{600}$ and WGH$_{700}$ resonant modes

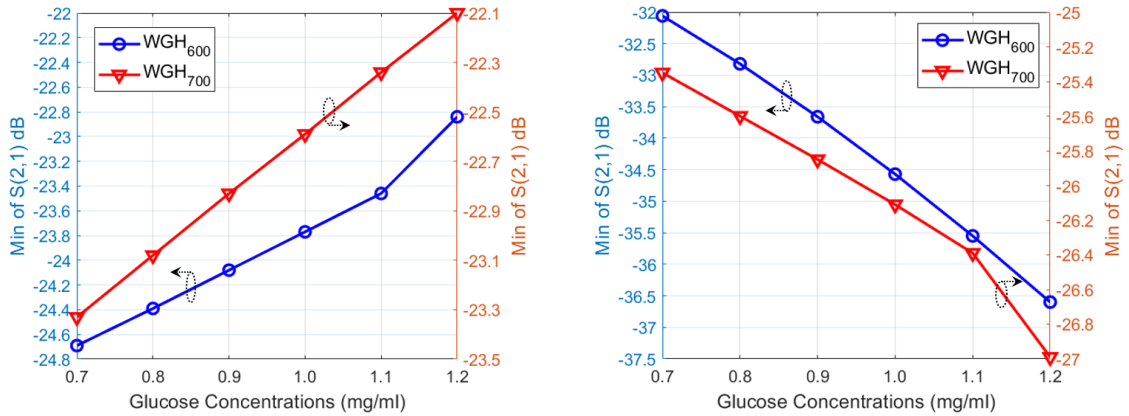

(a) (b)

Figure 4.12: Resolution of the resonant amplitude at WGH_{600} and WGH_{700} for the glucose level changes on the (a) straight and (b) curved WGM sensor

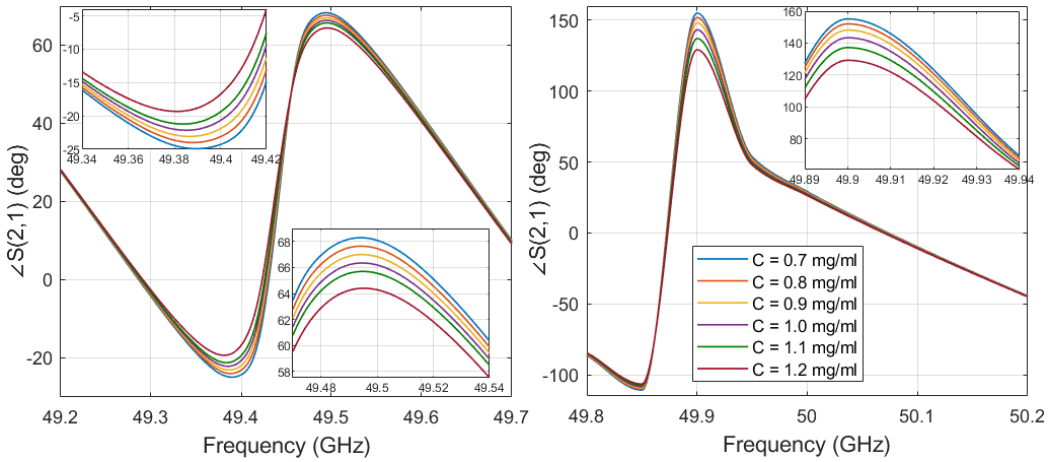

(a) (b)

Figure 4.13: Simulated transmission phases for different glucose concentrations loaded on the (a) straight and (b) curved WGM sensor at the WGH_{600} resonant mode

Table 4.2: Critical-coupling gap and sensitivity for each WGM mode for the straight and curved sensor

WGM Mode	Straight DIG		Curved DIG	
	Critical Coupling Gap g (mm)	Sensitivity (dB/[mg/ml])	Critical Coupling Gap g (mm)	Sensitivity (dB/[mg/ml])
WGH_{600}	0.50	3.10	0.42	7.70
WGH_{700}	0.50	2.50	0.45	2.50
WGH_{800}	0.30	0.40	0.45	1.04
WGH_{900}	0.50	0.30	0.40	0.30

This tendency in sensitivity could be interpreted by the nature of the interaction between the coupled WGM field and the glucose sample inside the container at each WGH mode as demonstrated in Fig. 4.14 that shows the electric-field distribution induced at each WGH resonance mode inside the DDR at the bottom surface $z = 0$ (first row) and inside the glucose at the sample floor $z = 2$ mm (second row). Particularly, it is clearly seen that the lossy glucose molecules have greater interactions with the

coupled evanescent fields at the lower-order modes WGH_{600} and WGH_{700} (Fig. 4.14(a) and 4.14(b)) compared to the higher-order modes WGH_{800} and WGH_{900} (Fig. 4.14(c) and 4.14(d)) that generate very small evanescent tails not adequate to sense the small external perturbations of the glucose dielectric constant and loss outside the DDR.

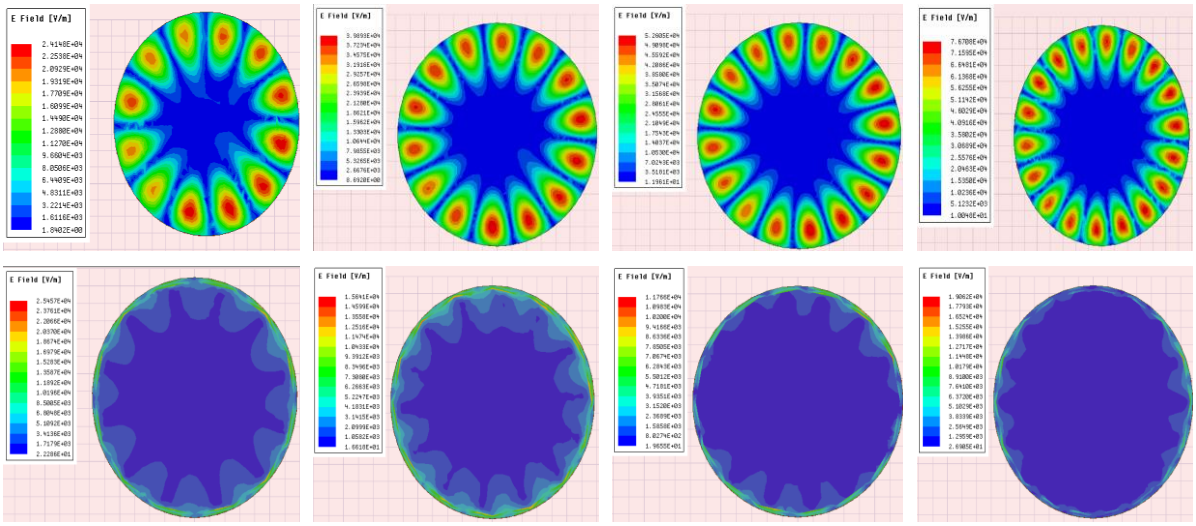

(a) (b) (c) (d)

Figure 4.14: Electric-field distribution at the bottom surface of the DDR z = 0 (top) and inside the glucose solution at z = 2mm (bottom) for different WGM resonances (a) WGH_{600} (b) WGH_{700} (c) WGH_{800} (d) WGH_{900}

4.3.6 Experimental Measurements

The fabricated DIG and DDR were combined and installed on top of a metallic support structure as shown in Fig. 4.15. The gap distance between the DDR and DIG was reasonably set to around 0.5 mm to maximize the sensitivity at different WGM resonances. Small drops of a low-loss epoxy glue were used to stabilize the position of the DIG and DDR over the metallic base. Fixing the DIG from both sides with a glue has a negligible increment in the loss and would not affect the field distribution of the desired mode inside the DIG which is nearly confined in the centre of the structure. The DDR was installed very carefully using an epoxy drop in the middle as the field coupled to the resonator is very sensitive to any small perturbations. The final sensor structure after integrating with the rectangular waveguides is shown in Fig. 4.15. A plexiglass cylindrical container was designed appropriately with the following dimensions (t_1 = 1 mm, t_2 = 1.5 mm, h_c = 10 mm*)* to fit on top of the DDR while holding a total volume of V_c = 0.37mL of liquid inside.

Two coaxial to WR-15 waveguide adapters were used to couple the power in and out of the DIG as shown in the complete experimental setup captured in Fig. 4.16 that consists of a Vector Network Analyzer (PNA), coaxial cables, and the integrated WGM sensor device. The preliminary prototype was tested when unloaded over the V-band to verify the overall functionality that exhibits five WGM resonances (WGH_{500}, WGH_{600}, WGH_{700}, WGH_{800}, and WGH_{900}) as depicted in Fig. 4.17 at frequencies f = 47.87, 51.98, 55.94, 60.05, and 64.21 GHz, respectively (black solid curves). Loading

the empty container on top of the DDR would result into shifting all the WGH resonances towards lower frequencies as depicted in Fig. 4.17 (green dotted curves).

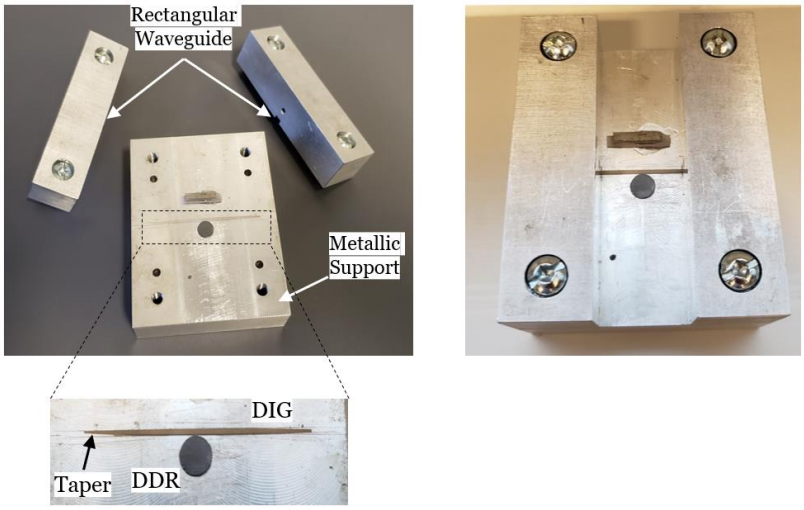

Figure 4.15: Fabricated prototype of the straight-DIG WGM sensor. Installing the DDR and DIG on top of a metallic support and integrating all the parts with the rectangular metallic waveguide (top view).

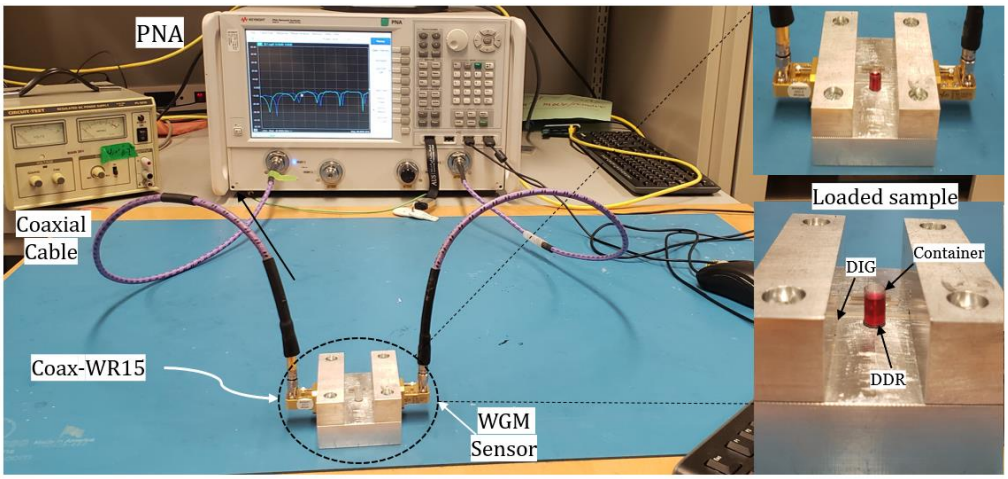

Figure 4.16: Experimental setup for WGM glucose measurements. Glucose sample loaded inside a container on top of a DDR is also shown.

To probe into the fabricated sensor capability and sensitivity for detecting the glucose concentrations, the combined DDR-container was loaded with three synthetic blood samples of varying concentrations 0.0, 0.7, and 1.0 mg/ml while monitoring the sensor response. In each trial, a precise 0.2 mL of each concentration was loaded into the container using a syringe (as depicted in Fig. 4.16), and the measurement was repeated three times for each glucose sample to confirm the repeatability. The average measured $|S_{21}|$ responses for the different glucose samples are plotted in Fig. 4.18 at the different WGM modes. Lower order modes (WGH_{600} and WGH_{700}) show higher sensitivity with larger amplitude resolutions comparing to other higher order modes.

The resolution of the resonant amplitude variations against the glucose concentrations is plotted in Fig. 4.19(a) and 4.19(b) for the WGH_{600} and WGH_{700}, respectively. Other WGH modes exhibit similar behavior in changing the resonance amplitudes yet with lower resolutions. The error bars are included

in the $|S_{21}|$ measurements in Fig. 4.19 to indicate a repeatability error of about ±0.2 – 0.25 dB for the WGH_{600} readings and ±0.15 – 0.25 dB for the WGH_{700}

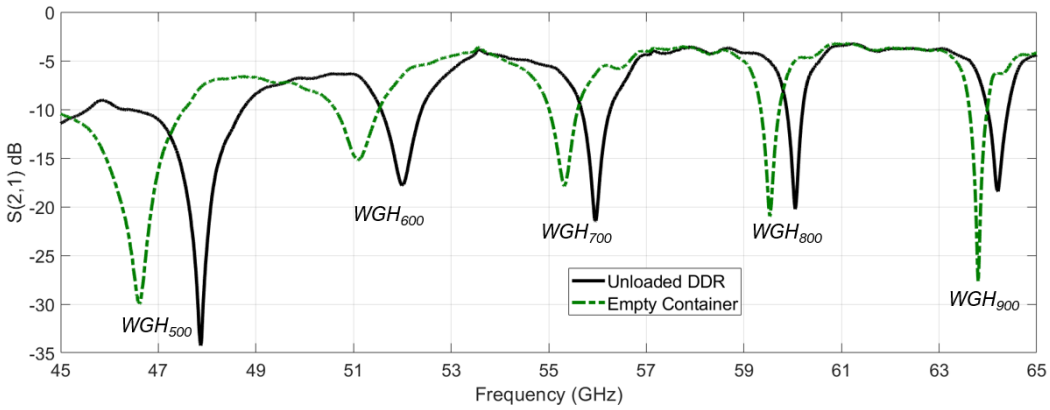

Figure 4.17: Measured transmission response of the WGM sensor in the mm-wave range when unloaded and loaded with empty container.

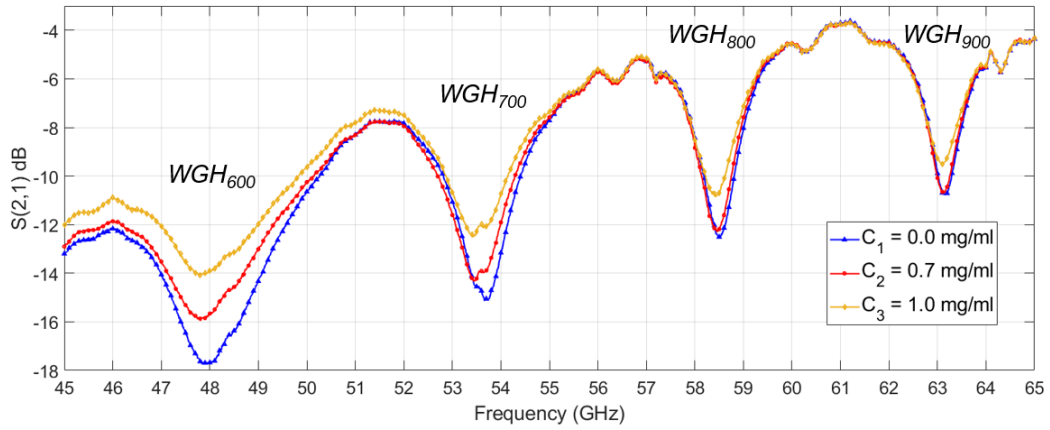

Figure 4.18: Measured transmission response of the WGM sensor when loaded with various glucose concentrations

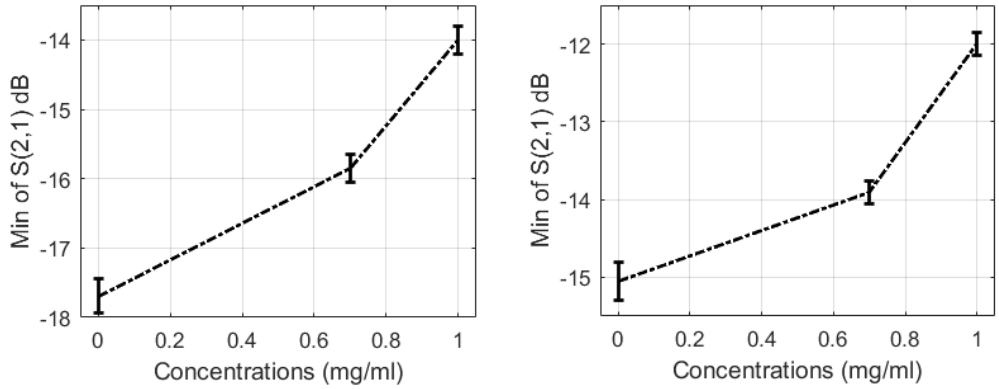

(a) (b)

Figure 4.19: Resonant amplitude variations at different glucose concentrations when (a) WGH_{600} and (b) WGH_{700} are excited

In another round of measurements, we first added one drop of volume ($V_1 \approx 0.1$ mL) of glucose-water solution of concentration C_1 = 1.2 mg/ml and noticed the change in the Q-factors for all the WGH

modes including WGH_{700} and WGH_{700}. The second tested concentration C_2 was formed by adding a drop of similar volume ($V_2 \approx 0.1$ mL) of 0.7 mg/ml to that of 1.2 mg/ml inside the container resulting into a new diluted glucose of concentration $C_2 = 0.95$ mg/ml. Following the same recipe, the last concentration C_3 was composed by adding a third drop of volume ($V_3 \approx 0.1$ mL) of distilled water of 0 mg/ml resulting into 0.3 mL glucose sample inside the container with a new concentration of $C_3 = 0.63$ mg/ml. In each trial, measurements were recorded for amplitude changes at the WGH_{700} resonance mode at $f = 53.7$ GHz. Other WGH modes exhibit similar behavior in changing the resonance amplitudes but with lower resolutions.

These perturbations observed in the last experiments were considerably dominant by the amount of loss that varies from one glucose concentration to another. To prove this experimentally, another test was performed by adding one drop of $V \approx 0.1$ mL and $C = 1.2$ mg/ml inside the container and recorded a reading of approximately -11.30 dB for the transmission coefficient at $f = 53.63$ GHz resonant frequency of WGH_{700}. Another drop of the same volume and concentration was added inside the container, and no significant change was noticed in the recorded reading. The test was repeated using a sample of different concentration C = 1.1 mg/ml which was added twice inside the container with no change in the recorded $|S_{21}|$ of about −13.8 dB at $f = 53.7$ GHz. However, a considerable jump in $|S_{21}|$ was noticed in the third trial when two droplets of different concentrations C = 0 and 1.2 mg/ml were added respectively inside the container causing the $|S_{21}|$ to jump from −18.2 dB to −17.4 dB at $f =$ 50.13 GHz of the WGH_{600} mode.

To achieve accurate producible measurements, we ensured that our mm-wave regime was calibrated precisely to limit the measurement error due to transmission loss. Moreover, all the glucose sensing experiments were held in an environment of controlled and monitored temperature to reduce the environmental impact on the collected scattering data. Particularly, the temperature in the experimentation room was regulated at 22±1°C. However, the resonance characteristics of the integrated sensor would not be considerably affected by such small fluctuation in temperature (less than ±2 MHz shift in the resonance frequency) as both alumina and silicon have low thermal expansion coefficients. In addition, given the strong dependency of the sensor transmitted mm-waves on the dielectric properties of the tested glucose samples, where those properties are known to be functions of the sample temperature; therefore, all the glucose samples were stored in the same temperature condition of 22±1°C. All the measurements were repeated three times for repeatability verifications while making sure to exactly retrieve the initial resonance response of the unloaded DDR when the sample container is taken off for cleaning for a new repeatability trial.

4.3.7 Sensitivity Analysis

The WGM sensor was designed to work in the mm-wave frequency range 45 – 70 GHz aiming at the accurate detection of the glucose levels resembling the normal diabetes condition. The proposed bio-sensor achieved higher levels of sensitivity when the lower order modes WGH_{600} and WGH_{700} were

excited inside the resonator. This is explained by their longer evanescent field tails that enable the spread of the coupled electric-field at higher magnitudes inside the glucose samples compared to those of WGH_{800} and WGH_{900} where the fields are more concentrated towards the boundary. These higher order modes might prove a leverage for a different sample allocation, for example placing small droplets in the boundary of the DDR, which is impractical for continuous glucose monitoring purpose.

In this study, we adopted one measure of the sensitivity as calculated from the variations in the transmission resonant amplitudes at each WGH mode. However, from theoretical perspectives the variations on the glucose levels could also be tracked on the transmission phases near resonances as demonstrated by the numerical simulations in a previous discussion. These variations in the transmission phase responses were also observed in the practical measurements using the preliminary sensor prototype but they did not change significantly from one concentration to another. This is because the fabricated sensor was not optimized for the highest sensitivity in terms of the critical coupling gap. However, the level of sensitivity recorded experimentally at WGH_{600} and WGH_{700} has shown to be much higher compared to other glucose sensors operating at different frequency bands and recently reported in the literature as shown in Table 4.3.

For instance, the Microstrip line (MLIN)-based glucose sensor proposed in [171] achieved an average sensitivity of 0.18 dB/(mg/ml) in terms of the reflection coefficient when working in the frequency band 1.4 – 1.9 GHz. The sensor exploits the interaction between the main field and the SUT in the substrate region of an MLIN terminated with a load. The fluidic glucose sensor proposed in [172] used a CSRR in the frequency band 2.4 – 2.9 GHz was able to detect 0.03 dB variation in $|S_{21}|$ when the glucose level changed from 0 to 4 mg/ml (i.e., sensitivity of 0.0075 dB/(mg/ml)). The work in [209] used a setup of a VNA connected to two horn antennas to sense glucose samples inside a plastic liquid container in the mm-wave range 60 – 80 GHz. Collected measurements recorded 0.7 dB as the largest change in the transmission magnitude for the variation from 0 to 3 mg/ml at some frequency points (i.e., sensitivity of 0.23 dB/(mg/ml)). However, our WGM sensor measures a minimum of 1.62 dB/(mg/ml) sensitivity when operating at the WGH_{700} mode. This was demonstrated by measuring the transmission responses for the WGH_{700} to glucose changes under non-critical coupling condition. The WGH_{600} (below 50 GHz) achieves a higher measure as evidenced by the numerical simulations and practical tests (~2.6 dB/(mg/ml)). In addition, the sensor can be optimized in terms of the DIG-to-DDR gap to trigger the critical coupling state for these lower order modes and thereby acquire higher sensitivity similar to those calculated from the optimized simulations 2.5 – 7.7 dB/(mg/ml). Furthermore, the WGM sensor with the curved DIG is also expected to score higher in this field as evidenced by the finite element simulations.

Table 4.3: Comparison against other state-of-art sensors for glucose level detection

Ref	Sample volume (μL)	Concentration (mg/ml)	Operating frequency (GHz)	Sensing parameter	S (dB per mg/ml)
[171]	7500	0.78 – 50	1.4 – 1.9	$\|S_{11}\|$	0.18
[172]	-	0 – 4	2.4 – 2.9	$\|S_{21}\|$	0.0075
[209]	-	0 – 3	60 – 80	$\|S_{21}\|$	0.23
[173]	-	0.3 – 80	7.5	$\|S_{21}\|$	0.008
[159]	170	5 – 25	1.91	$\|S_{21}\|$	0.025
[174]	20	40 – 200	2.5 – 6	$\|S_{21}\|$	0.01
[69]	-	5 – 50	14 – 16	Phase	0.02°
[152]	20	200 – 1000	3.02	$\|S_{21}\|$	0.007
[175]	1000	0 – 300	2.0 – 2.5	$\|S_{11}\|$	0.003
This sensor	50 – 370	0.7 – 1.2	45 – 65 GHz (WGM modes)	$\|S_{21}\|$	1.62 – 2.6 (Measurement) 2.5 – 7.7 (Simulation)

Lastly, in the search for better sensitivity we investigated different ways for loading the glucose samples onto the sensor. However, all the considered setups resulted into relatively lower level of sensitivity compared to that of a low-loss container on top of the DDR. For instance, all WGH resonance modes have shown low sensitivity to changes in concentrations when the ring resonator is tamped with glucose samples in the middle of the setup shown in Fig. 4.18(a). We have also tried developing a virtual DDR shown in Fig. 4.18(b) by coupling the glucose sample in container directly to the DIG while removing the DDR, but that would heavily attenuate the fields coupled to the virtual lossy DDR whereby all the transmission resonances are defaced resulting into slight variations in the reflection coefficients that are not enough to trace the variations in glucose levels. Additionally, we tried to excite the WGM modes inside the glucose sample by coupling the combined resonator into two branches of dielectric waveguides using the structure shown in Fig. 4.18(c). However, this would result into exciting higher order WGH modes (e.g., WGH_{1000}, WGH_{1200}, etc.) as well as triggering other undesired modes that are not benefiting an effective glucose sensing in the mm-wave band of interest.

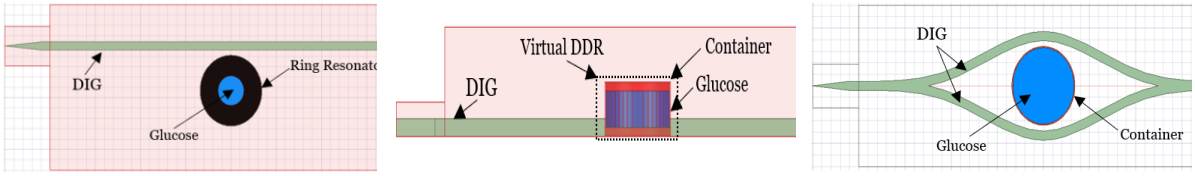

(a) (b) (c)

Figure 4.20: Other investigated WGM sensing structures (a) virtual DDR, (b) dielectric ring resonator, and (c) eye structure of double-branched DIG (top view)

4.4 Near-infrared WGM Sensor

In the previous WGM sensor, we have seen that the maximum sensitivity and selectivity is obtained under near-critical or critical coupling condition between a DR and a guiding structure which excites the DR. However, such a critical coupling occurs only at an exact distance between the DR and the guiding structure. Therefore, practically, it is difficult to provide such condition by adjusting this gap distance especially at millimeter wave and optical range of frequencies, where high level of accuracy is needed. In [210], by employing highly accurate nanofabrication process, a silicon image waveguide and

a high-resistivity silicon (HRS) disk have been etched on a silicon-on-insulator (SOI) substrate. By using this technique, it is guaranteed that the specific distance between the guiding structure and the DR, which is obtained through optimization analysis in simulation, is realized for critical coupling condition with high accuracy. Nevertheless, the distance value obtained by numerical simulation does not necessarily provide critical coupling condition in experimental measurements possibly due to the inaccuracy in modeling. Besides, temperature, aging, and other physical parameters will affect the critical coupling condition.

Herein, the coupling level between the guiding structure and the HRS disk is controlled by illuminating HRS disk by a near-infrared (NIR) light source. Principally, the light intensity results into the formation of a thin plasma layer (depth determined by the light intensity and wavelength) at the surface of the HRS disk. This plasma layer appreciably changes the conductivity (or the loss) of the intrinsic silicon. Therefore, by applying an appropriate optical source (e.g., LED) the behaviour of the HRS resonator (~*Q*-factor) could be changed and controlled as required from the exposure of the illuminated radiation. In [211], this technique has been used for fabricating tunable passive devices like power dividers and couplers. By changing the conductivity of the HRS disk, the coupling level between the guiding structure and the HRS disk can be controlled precisely, and therefore, the requirement for high-precision positioning of the DR with respect to the guiding structure is relaxed. On the other hand, by using this technique, a novel method of non-invasive sensing is realized, which exploits the transparency of the sample-under-test to the NIR radiation. In contrast to other resonance perturbation methods which consider the shift in the resonance frequency of the resonator as the sensing parameter, this proposed method of sensing monitors the strength of coupling level of the guiding structure to the resonator. One of the main advantages of this method is that the resonance frequency of the resonator remains fixed during the interaction.

4.4.1 Design, Specifications, and Simulations

The WGM resonator was implemented by placing an HRS disk in the proximity of a microstrip-line that was used as the guiding structure as depicted in Fig. 4.19(a). The HRS disk has a relative permittivity of ε_r = 11.6 and resistivity of ρ = 10 kΩ.cm. Rogers 4003 with dielectric constant = 3.55, loss tangent tanδ = 0.003, and thickness H = 8 mils was used for fabricating the dielectric substrate. All the geometrical parameters of the resonating structure are presented in Table. 4.4. To demonstrate the abovementioned theory, the WGM resonator was first simulated using ANSYS HFSS where the loss factor (α) of the HRS disk was controlled by tuning its value of the loss tangent using the parametric sweep function. Fig. 4.19(b) shows that by tuning the value of the loss tangent from 0.006 to 0.009, there is an optimum value (~ 0.0075) in which the critical coupling occurs.

Table 4.4: Design parameters of the structure (mm)

Parameter	**Hs**	**Ds**	**D**	**W**	**T**	**H**	**L**
Value	1.7	7.7	6.95	0.28	0.018	0.2	35

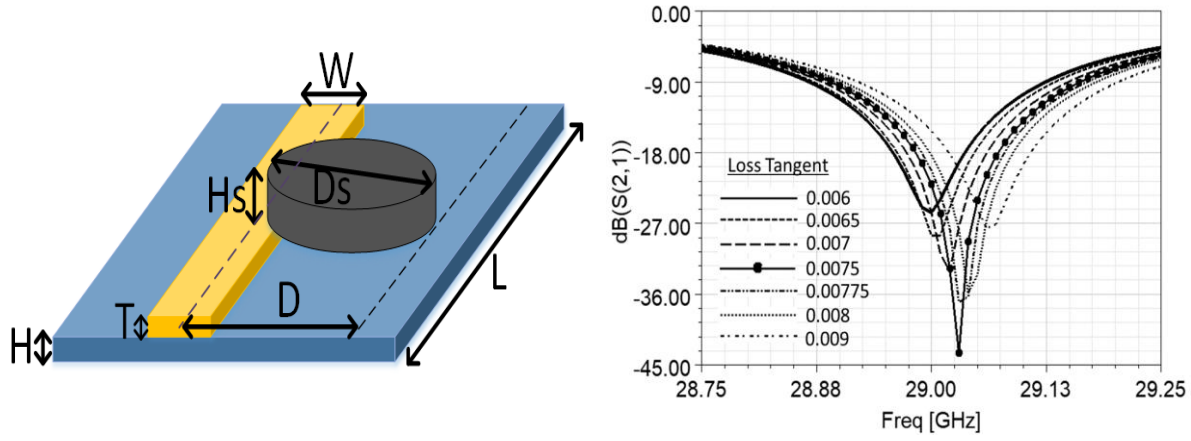

(a) (b)

Figure 4.21: (a) Structure of the WGM resonator, and (b) coupling level with respect to the loss tangent of HRS (Simulation)

4.4.2 Experiments on a Prototype (Concept Validation)

A prototype was connected in the setup shown in Fig. 4.20(a) to practically demonstrate the behaviour of the HRS resonator when exposed to NIR radiation. In the experiment, the loss factor (α) of the HRS was tuned by illuminating the HRS disk by NIR-LED of wavelength 860 nm. Accordingly, it is expected that the conductivity of the intrinsic silicon will change as well as its loss tangent property. The intensity of the NIR radiation is controlled by the applied DC current from external source. Figure. 4.20(b) shows the tunability of the coupling level with respect to the DC current. As depicted in Fig. 4.20(b), at a certain DC current level (or NIR radiation intensity), there is a peak in the graph that captures the critical coupling condition with the maximum insertion loss. Figure. 4.20(c) shows the frequency response of the WGM resonator before and after tuning the NIR LED. It is clearly observed that, the critical coupling condition is easy captured with minimum effort by tuning the radiation intensity of the NIR-LED around 100 mA. Varying the NIR intensity would greatly affect the WGM resonance mode. It is worth mentioning that there is a good agreement between simulation and measurement on the resulting resonance frequency (less than 70 MHz difference) which shows the accuracy of the parameters used in the previous simulation study.

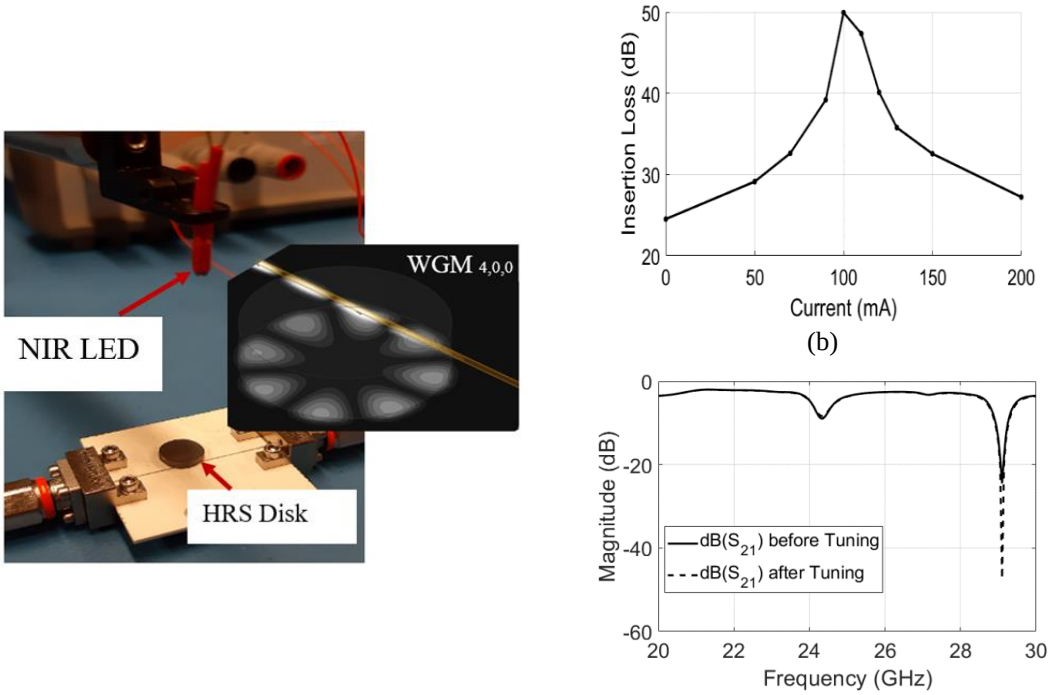

Figure 4.22: (a) Prototype of the WGM resonator, (b) Tunability of the coupling level in WGM resonator with respect to the dc current (the intensity of illumination is controlled by dc current), and (c) Insertion Loss of the WGM resonator before and after tuning by NIR LED (measurement).

4.4.3 Experimental Glucose Sensing Approach

An appropriate sensing method was implemented based on the transparency of the sample-under-test to a consistent NIR radiation from the LED. By placing the sample between the HRS disk and the NIR LED as shown in Fig. 4.21, the level of NIR radiation intensity illuminating the HRS disk is affected. As a result, the loss factor (α) (or tanδ) of the HRS disk is altered, and the coupling level is changed. By measuring the coupling levels, the insertion loss (or S_{21}) of the tested sample at that specific NIR is determined. In what follows, the sensitivity and selectivity capabilities of the developed NIR-WGM sensor for detecting aqueous glucose solutions are practically tested. To do so, a rectangular container was placed in the region between the NIR-LED and the resonator as shown in Fig. 4.21, that captures the complete setup for the VNA and other sensor connections. The container has a cross section of 26 × 39 mm^2, height of 6 mm, and a thickness of about 0.9 mm for the bottom layer.

The WGM sensor was tested for glucose level detection by placing precise volumes inside the container and measuring the transmission response of the sensor by the VNA. Measured transmission response exhibits variations in the resonant depth at frequency of 29.08 GHz when the sensor was loaded with aqueous samples of varying glucose concentrations as plotted in Fig. 4.22. To elaborate, in this experiment, first the rectangular container was loaded with distilled water C_1 = 0 mg/ml of specific volume of V ≈ 2.76 mL (half-filled) and the resulting response of about −47.03 dB was recorded (solid red). Then, three droplets of precise volume V = 0.2 mL of glucose solution of C = 10 mg/ml were added by a controllable syringe to the water inside the container. The resulting S_{21} magnitude for the

consequent glucose concentration of C_2 = 0.68 mg/ml was recorded at −45.93 dB (dotted blue). Finally, three more droplets from the 10 mg/ml standard glucose solution were added to the mixture inside the container modulating the concentration to C_3 = 1.27 mg/ml that shifted the amplitude response to −45.48 dB (dash-dot green). Measured data were quadratically fitted as depicted in Fig. 4.22(c). Given these amplitude variations, the sensitivity was calculated in terms of the change in the sensing parameter (magnitude of S_{21}) due to the change in glucose concentration in dB/(mg/ml). The NIR-WGM glucose sensor can measure up to 3060 uL of a sample at excellent sensitivity of about 0.76 – 1.62 dB/(mg/ml).

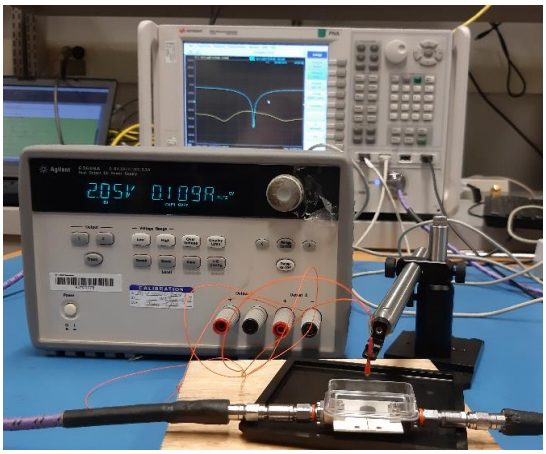

Figure 4.23: Measurement setup for glucose sensing.

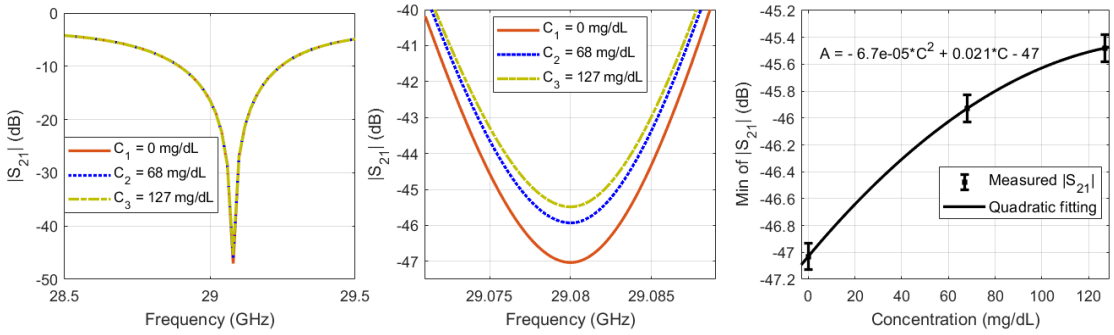

(a) (b) (c)

Figure 4.24: Scattering transmission response of the sensor when loaded with aqueous glucose solutions of various concentrations, (a) full range 28.5 – 29.5 GHz, (b) zoom-in window in 29.07 – 29.09 GHz, and (c) resonant amplitudes at varying glucose with quadratic fitting incorporated for in-between concentrations (maximum repeatability error of ±0.15 dB)

4.5 Ferrite-based WGM Sensor

Another simple, inexpensive, and miniaturized microwave sensing system is developed for BGL monitoring using the WGM technology. Given the physiological blood glucose behaviour that varies within limited range 50 – 500 mg/dL for all humans, the proposed device is ought to be highly sensitive to detect the small permittivity changes in that range. The interference imposed by the ambient environment also requires the developed sensor to perform the glucose sensing at multiple frequency points to mitigate any uncertainties. The corresponding sensing data would thereby be more stable, repeatable, and reliable. Therefore, we chose to implement this sensor using the WGM technology in the sub-centimeter wavelength range 22 – 32 GHz to further enhance its sensitivity and distinctly

observe the dependency between the varying concentration and permittivity at multiple WGM resonance frequencies. This is multi-frequency is also helpful when adapting the sensor as a portable gadget for glucose monitoring by allowing wider range of penetration depths (at different frequencies) suitable for different users' physiological needs (e.g., age and gender).

The proposed structure couples the input power into a dielectric ring resonator via a microstrip-line that secures a low-cost, low-loss, and high confinement wave transmission. The ring resonator is fabricated using a ferromagnetic material, of high electrical resistivity and significant magnetic anisotropy at microwave frequencies, to acquire WGM resonances of high *Q*-factors over the operating frequency range. A permanent magnet is incorporated in the bottom layer of the microstrip substrate to trigger the anisotropy of the ferrite ring, and thereby achieve the nonreciprocal operation where more sensing data on the varying concentrations could be collected from the multiple resonances of the excited WGM modes in both S_{21} and S_{12} frequency signals. Moreover, and in contrast to many conventional microwave glucose sensors in the literature that mostly explored the varying amplitude of the reflection and transmission responses, herein we exploit the spectral information provisioned in two distinguishing features of the excited WGM mode, its resonant frequency accompanied by the phase reversal in the vicinity of the resonance. The noise immunity of both frequency and phase sensing will provide more accuracy and reliability for the extracted glucose sensing data, while considerably reducing the impact of the external environment including the uncontrolled errors inherent in the attached instruments.

Figure. 4.23(a) depicts the practical implementation of the integrated sensor for glucose detection when applied a few millimetres underneath the glucose sample. The interaction of the resonant mode fields with the bulky dielectric properties of the glucose sample placed in the sensing zone, allows for detecting its EM fingerprint. The latter is translated as changes in the resonance phase, amplitude, and frequency of the induced WGM modes as observed in the minimum peaks of the S_{12} and S_{21} responses on the VNA. The raw data could be further analysed on a processing machine, or in the cloud, to correlate the sensing data to their corresponding glucose concentrations using Artificial Intelligence (AI) algorithms.

The proposed WGM sensor is endowed with favourable advantages of low-power consumption, high sensitivity, and miniaturized sizing (~6 cm^2 cross section), making its development as a mobile gadget for affordable non-invasive BGL monitoring from the person's fingertip very promising as shown in Fig. 4.23(b). Next sections will detail the structure of the WGM ferrite sensor, its sensing mechanism, numerical analysis, and EM simulations for the reciprocal and non-reciprocal modalities. The practical in-lab testing of the prototyped sensor for glucose monitoring is presented alongside the sensitivity comparison against state-of-the-art glucose biosensors.

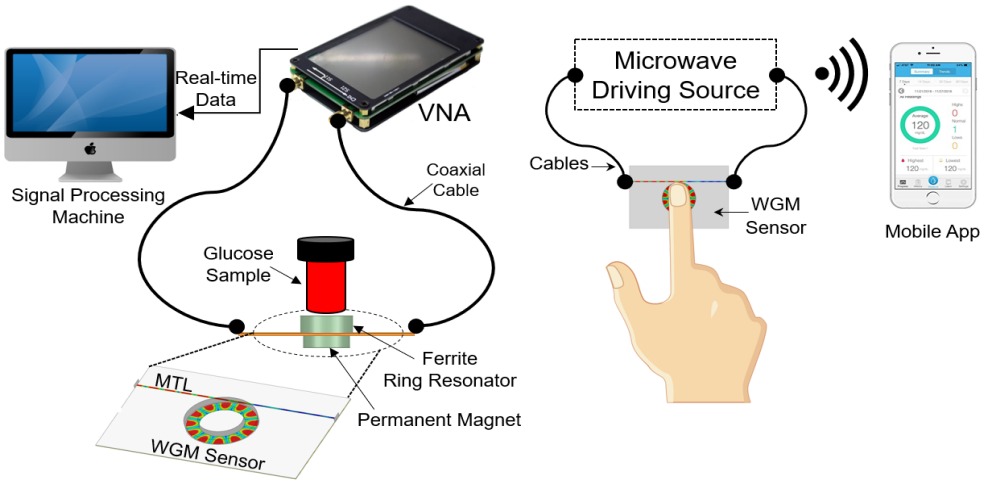

(a) (b)

Figure 4.25: (a) Schematic diagram of the proposed ferrite WGM sensor, and its application for non-invasive blood glucose monitoring, (b) Adapting the WGM sensor as portable to measure glucose from the fingertip.

4.5.1 Design and Specifications

The reciprocal (i.e., demagnetized) version of the WGM sensor comprises a ferrite ring resonator (FRR) coupled to a microstrip-line (MTL) guiding structure as shown in Fig. 4.24. The MTL is patterned on top of a dielectric substrate to excite the WGM modes inside the FRR, which is installed in the middle of the structure at distance g from the MTL. When the tails of the MTL propagating modal field are coupled to the neighbouring FRR, the coupled waves will start propagating circularly forward and backward around the FRR boundaries. After n rotations they experience a $2\pi n$ phase shift. The induced travelling waves are confined inside the ring by repeated total reflections from the internal/external boundaries of the FRR yielding high concentration of the field close to boundaries.

To enhance the sensitivity and acquire more sensitive instants of high Q-factor WGM resonances, a compact permanent magnet is attached beneath the ground plane of the dielectric substrate to bias the FRR with strong DC magnetic field H_{dc} in the z direction as illustrated in Fig. 4.25(a). This turns the FRR into non-reciprocal device whose S_{21} and S_{12} have different resonance characteristics. Particularly, the WGM transmission (S_{12}, S_{21}) resonances of similar WGM modes become different. For instance, as will be shown later, the WGM_{600} S_{12} resonance occurs around f = 27.95 GHz, and S_{21} resonance is around f = 28.28 GHz. This phenomenon is due to the nonreciprocal behaviour of the FRR when it is magnetized by a bias magnetic field under which the magnetic permeability of the ferrite becomes a non-symmetrical matrix as given in Eq. (4.18) for the case of z-oriented bias, where $\pm j\kappa$ represent the induced anisotropy of the medium under the external magnetic field. This matrix governs the local interaction between B and H in the FRR [212]

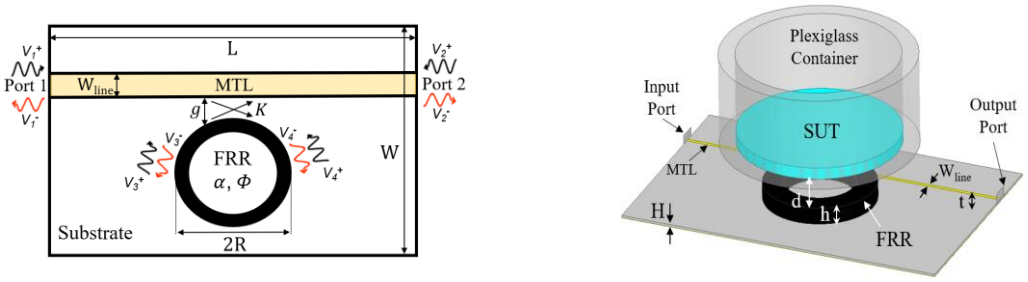

(a) (b)

Figure 4.26: (a) Sensor schematic showing the coupled FRR-MTL integrated on a dielectric substrate, (b) Geometrical configuration with the glucose SUT loaded onto the FRR.

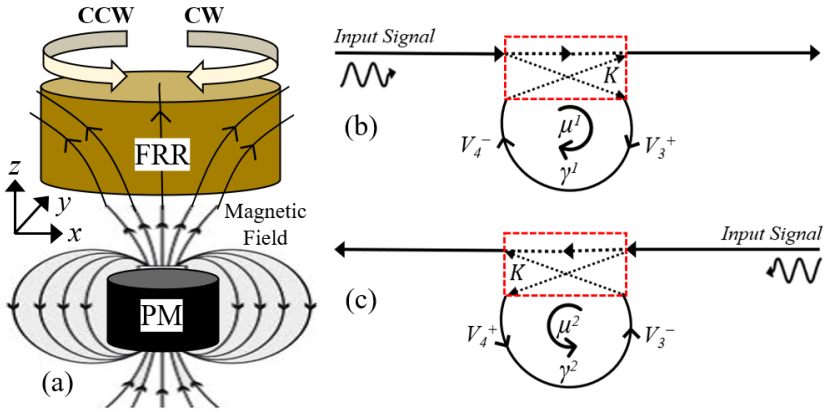

Figure 4.27: (a) Illustration of non-reciprocal wave propagations when a magnetic bias is applied, (b) CW and (c) CCW modes travelling around the FRR at different propagation directions due to the magnetic anisotropy of the FRR.

$$[\mu] = \begin{bmatrix} \mu & j\kappa & 0 \\ -j\kappa & \mu & 0 \\ 0 & 0 & \mu_o \end{bmatrix} \quad (z\ bias), \tag{4.18}$$

This non-symmetrical magnetic property causes the nonreciprocal nature of the EM wave propagation in the ferrite resonator. Essentially, for plane waves propagating along the DC magnetic field, a right hand circularly polarized (RHCP) wave will experience a magnetic permeability of (μ + κ), whereas a left hand circularly polarized (LHCP) plane wave sees a permeability of (μ – κ). In a similar sense, clockwise (CW) and counter-clockwise (CCW) azimuthal modes of an excited WGM would experience different effective permeabilities μ^1 and μ^2, respectively, based on the precession direction of the induced magnetic dipoles by the biasing magnetic field. Therefore, WGM waves travelling around the FRR would have two different azimuthal propagation constants γ^1 and γ^2, and hence $V_4^- = e^{-\gamma^1} V_3^+$ and $V_3^- = e^{-\gamma^2} V_4^+$ for the CW and CCW rotations, respectively, depending on the MTL coupling signal from the two ports, as illustrated in Fig. 4.25(b) and 4.25(c). To this end, the corresponding WGM modes would exist with the same azimuthal '*n*', radial '*m*', and axial '*l*' variations but at distinct resonant frequencies in S_{21} and S_{12} for the CW and CCW propagations, respectively, as will be demonstrated later by the EM simulations and measurements.

4.5.2` EM Numerical Analysis of the Reciprocal FRR

In this subsection, we investigated the core design of the sensor before applying any biasing magnetic field to trigger the nonreciprocal behaviour. The sensor structure was primarily designed, using the 3D full-wave ANSYS HFSS, to operate in the frequency range 22 – 32 GHz. In the structure shown in Fig. 4.24, the 50Ω MTL has a width of W_{line} = 0.28 mm and a thickness of t = 0.017 mm on top of a Rogers 4360G2 dielectric substrate of length L = 30 mm, width W = 20 mm, thickness H = 0.2 mm, dielectric constant = 6.15, and loss tangent = 0.0038 [213]. The FRR of radius R = 5.13 mm, height h = 1.44 mm, was implemented with a low-loss (tanδ = 0.0004) nickel ferrite spinel of relative permittivity = 13.2 [214]. With these geometrical dimensions and specifications, the EM simulator reveals four WGM modes in the spectrum 22 – 32 GHz as shown in Fig. 4.26(a): WGM_{400} (~22.86 GHz), WGM_{500} (~25.57 GHz), WGM_{600} (~28.36 GHz), and WGM_{700} (~31.1 GHz), respectively. Figure. 4.26(b), 4.26(c), 4.26(d), and 4.26(e) depict the intensity (magnitude) of the modal field distributions induced across the x-y plane of the FRR surface (at z = 0 ~ bottom surface) when each mode WGM_{400}, WGM_{500}, WGM_{600}, and WGM_{700} is excited, respectively. As it is shown, the induced electric fields are mostly concentrated in small regions along the FRR periphery between the outer boundary and inner radius. These fields are more intensified with higher magnitudes in WGM_{500} and WGM_{600} compared to the other two modes. Therefore, they are expected to show more sensitivity to the EM perturbations of glucose changes in the loaded SUT.

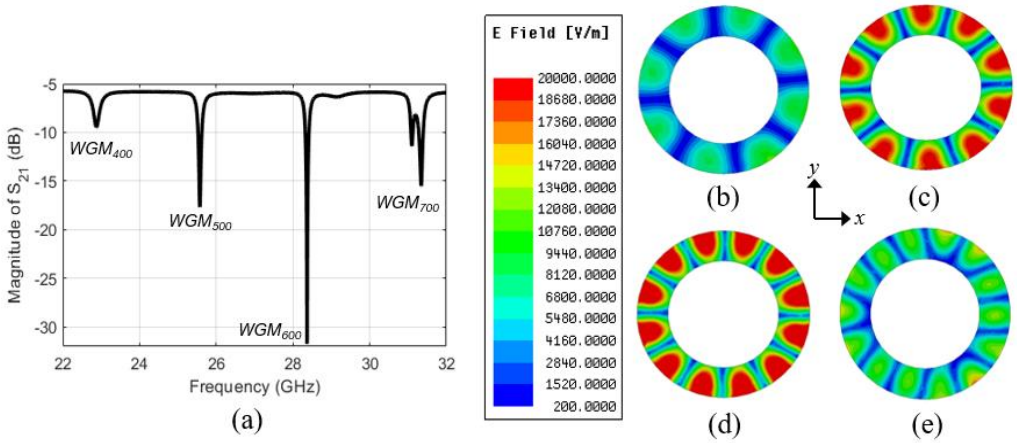

Figure 4.28: (a) Simulated transmission coefficients S21 at different WGM modes (reciprocal operation). Intensity of the electric field distributions at the respective resonances of (b) WGM_{400}, (c) WGM_{500}, (d) WGM_{600}, and (e) WGM_{700}.

The MTL-FRR coupling gap g was optimized by numerically analyzing the transmission response (S_{21}) of the FRR at varying gaps between 0 and 0.8 mm in increments of 0.1 mm. Figure 4.27 depicts the resulting resonant frequency, depth, and phase of the WGM_{600} at varying g. As g increases in Fig. 4.27(a), the mode resonant frequency shifts downwards, and the Q-factor is observed to vary significantly. A stronger coupling of -38.62 dB (≈ near critical coupling) is acquired when g = 0.1 mm.

The sensor also exhibits an abrupt change with double reversal in the phase slope near critical coupling as clearly seen in Fig. 4.27(b). Measured results of the reciprocal sensor also confirm the simulated behaviour with strong coupling performance at g = 0.1 mm for both WGM_{600} and WGM_{700} as depicted in Fig. 4.28(a) and 4.28(b), respectively. To demonstrate the effect of the loss variation on the S_{21} response, the FRR is simulated at different tanδ between 0.0005 to 0.005 at $5x10^{-4}$ steps. Figure 4.29(a) shows the gradual upshift in the resonant frequency with increased tanδ. A critical coupling is shown to occur at specific tanδ ($\approx$ 0.002) that is not necessarily the lowest value. These loss variations could also be monitored in the corresponding phase signals (Fig. 4.29(b)) that change significantly over the dispersed bandwidth near the WGM resonance.

Considering the purposed application in which the glucose samples of interest have complex permittivity $\epsilon_{rG} = \epsilon'_{rG} - j\epsilon''_{rG}$ where both ϵ'_{rG} and ϵ''_{rG} have relatively large dispersion (values vary between 23 – 33 and 32 – 36, respectively, in the operating spectrum), and both change very little from one glucose concentration to another. The permittivity $\epsilon_{rRR} = \epsilon'_{rRR} - j\epsilon''_{rRR}$ of the FRR underneath the SUT has rather small, fixed values for the two components. Loaded glucose samples on top of the resonator (Fig. 4.24(b)) would endure an intensive interaction with the WGM field and the intrinsic FRR loss ξ is perturbed as a result. The critical coupling would therefore be defined for another loss configuration, and the entire S_{21} profile of the excited WGM mode will change in accordance with the new effective permittivity and loss of the integrated sensing structure as controlled by the varying concentrations.

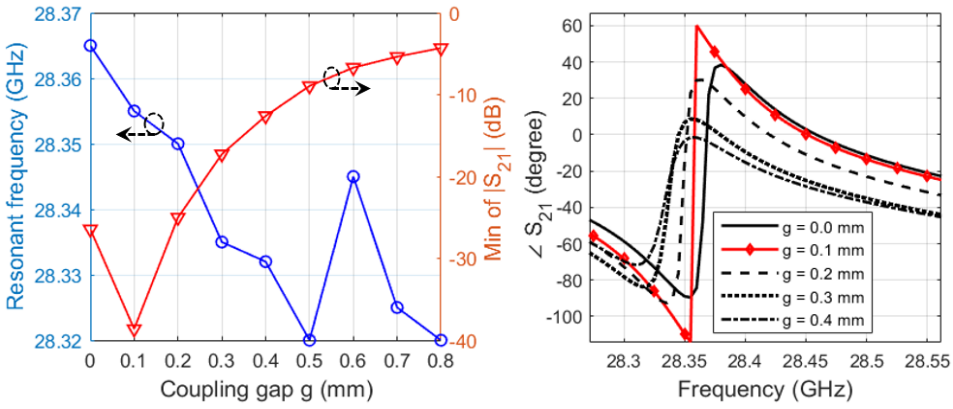

(a) (b)

Figure 4.29: Simulated transmission responses (a) resonant frequency and amplitude and (b) phase for the bare FRR at varying gaps g (WGM_{600})

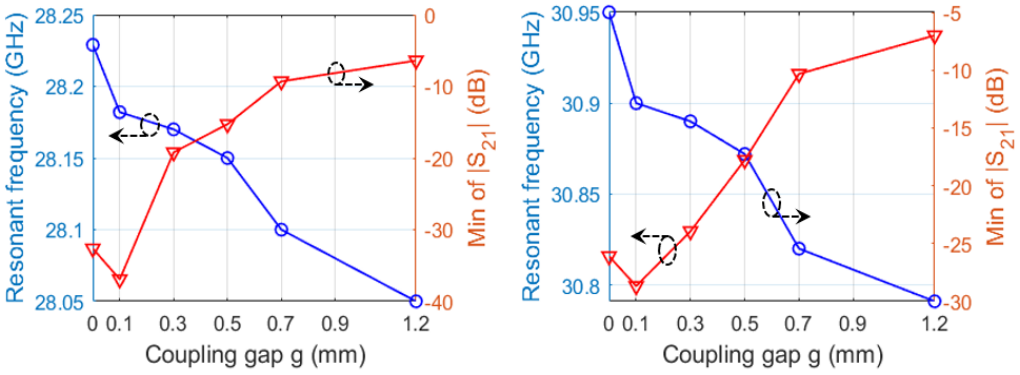

(a) (b)

Figure 4.30: Measured resonant frequency and amplitude for the bare FRR at varying gaps g (a) WGM_{600}, (b) WGM_{700}.

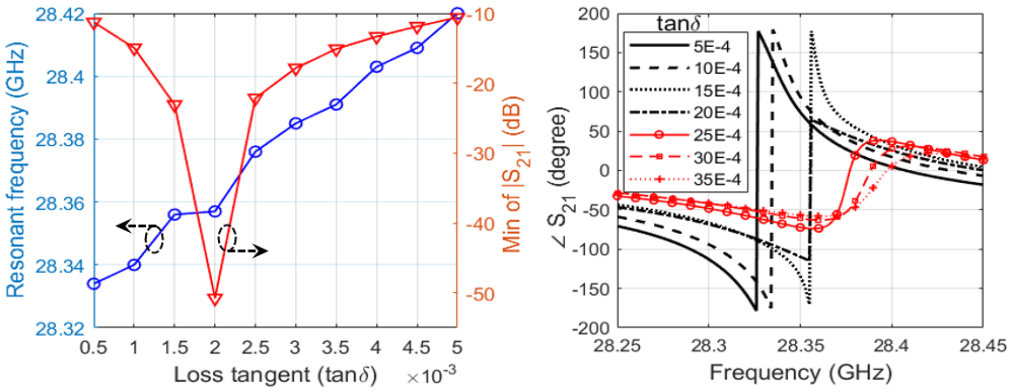

(a) (b)

Figure 4.31: Effect of the loss variation on the coupling level of the FRR at g = 0.1 mm (a) Resonant frequency and depth (b) Transmission phase (WGM_{600}).

4.5.3 Magneto-static Analysis of the Non-reciprocal FRR

A magneto-static analysis is performed using Maxwell 3D to find the internal biasing fields and the resulting magnetization inside the FRR when the permanent magnet is introduced as shown in Fig. 4.25(a). The permeability tensor components μ and κ are then calculated using the Generalized Polder (GP) model in Eq. (4.18) considering the spatial variation of the internal magnetic fields along the z direction. The complex components of the GP are integrated thereafter in HFSS to compute the non-reciprocal scattering parameters of the sensor using the frequency domain solver. In the magneto-static simulations, we consider the case of a 1.44 mm thick hollow cylindrical shaped ferrite material uniformly magnetized by the permanent magnet along the longitudinal direction (z-axis, see Fig. 4.30(a)). The FRR is of outer diameter 5.13 mm, inner diameter 3.2 mm, saturation magnetization $4\pi M_s$ = 4750 Gauss. The FRR is placed at 0.2 mm distance on top of the compact magnet of 5 mm diameter and 3 mm thickness as shown in Fig. 4.30(a). In order to describe the evolution of the FRR magnetization with magnitude and direction of the applied DC magnetic field, the FRR is defined, from a static point of view, as anisotropic material with the diagonal matrix resulting from Eq. (4.18) when $\kappa = 0$ and $\mu = 1 + M_s/H_o$, where H_o is the internal biasing field.

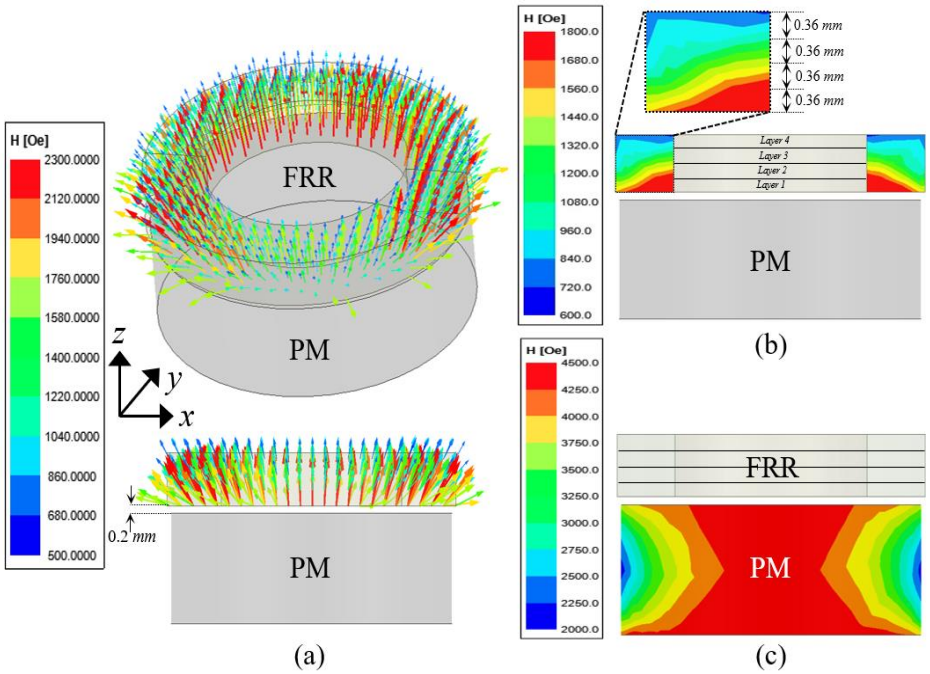

Figure 4.32: Maxwell-3D simulations, (a) Magnetization of the FRR by the permanent magnet, (b) Magnitude of the internal biasing fields inside the FRR along the z axis, (c) Intrinsic magnetic fields in the permanent magnet.

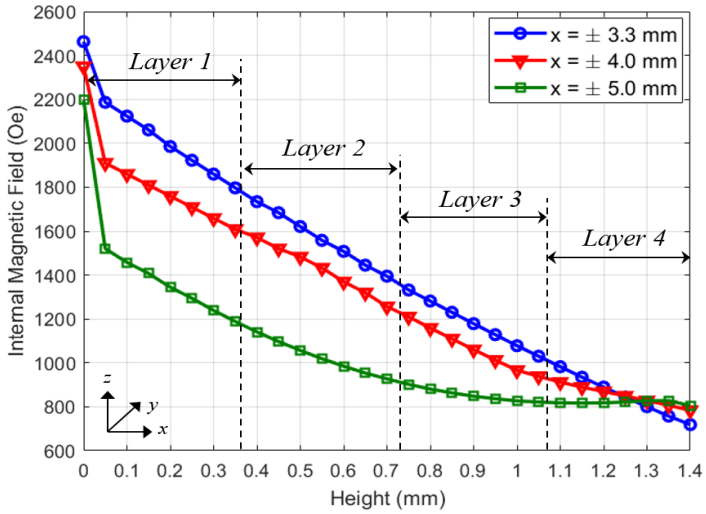

Figure 4.33: Spatial variation of the DC biasing field inside the FRR at the four defined layers.

Figure 4.30(a) depicts the magnetization of the FRR as calculated using Maxwell 3D. The spatial variations of the resulting magnetic fields in both the FRR and PM along the magnetization direction are shown in Fig. 4.30(b) and 4.30(c), respectively. The intrinsic magnetization of the PM is shown to be homogenous in modulus and direction, yet it slightly decreases towards the outer sides. As can be seen in Fig. 4.30(b), the intensity of the internal biasing field H_o is non-uniform in modulus and direction from the bottom of the ferrite to the top. Particularly, H_o is observed to be relatively weaker in some upper regions, while it has higher magnitudes at the bottom and middle parts of the FRR. The internal fields have shown insignificant variation along the 'phi' or 'y' direction. Therefore, and due to the strength of the DC field that is above the saturation level, the ferrite sample is reasonably assumed

to be saturated with M_s applied in most of the regions. To better model this field variations, the magnitude of H_o is averaged in four longitudinal layers of thickness 0.36 mm each as depicted in Fig. 4.30(b). Figure 4.31 plots the decaying magnitude of H_o across the four layers (in the z axis) of the FRR at six different locations in the x axis, ± 3.3, ± 4.0, and ± 5.0 mm. The average field in each layer is computed and used for defining the components of the GP model in HFSS.

4.5.4 Integration of GP Model with HFSS

The anisotropic nature of FRR is modeled in HFSS by defining the permeability tensor components in Eq. (4.18). In order to calculate the permeability tensor of the bulk FRR considering the nonuniform (or inhomogeneous) magnetic field distribution, the ferrite sample is divided into multiple layers in the longitudinal direction where the internal DC field is considered to be uniform in each of the four layers. These layers are then defined as different materials or simply as computational regions in which the ferrite material is the same but with different internal DC biasing fields and thus different permeability tensors. For each computational region, real and imaginary parts of the permeability tensor components are defined as frequency dependent polynomial functions and computed from the corresponding GP formulations in Eq. (4.19) and (4.20) at any frequency value in the operating frequency range 22 – 32 GHz using the inbuilt piecewise linear interpolation function of HFSS. S-parameters are then calculated using the frequency domain solver in HFSS

$$\mu = \mu' - j\mu'' = \mu_o \left(1 + \frac{\omega_m(\omega_o + j\alpha\omega)}{(\omega_o + j\alpha\omega)^2 - \omega^2}\right), \tag{4.19}$$

$$\kappa = \kappa' - j\kappa'' = \mu_o \left(\frac{\omega_m \omega}{(\omega_o + j\alpha\omega)^2 - \omega^2}\right), \tag{4.20}$$

where $\omega_o = \gamma H_o$ is the Larmor or precession frequency, γ is the gyromagnetic ratio (2.8 MHz/Oe), H_o is the magnitude of the internal magnetic field in Oersted (Oe), $\omega_m = \gamma(4\pi M_s)$ is the frequency proportional to saturation magnetization M_s of the ferrite material, α is the damping factor that describes the dissipative effects and other magnetic losses in the ferrite sample, and $\omega = 2\pi f$ is the angular wave frequency [212].

Each of μ and κ has a double dependence with respect to the wave frequency f and the internal magnetic field H_o. In our analysis, the saturation magnetization $4\pi M_s$ = 4750 Gauss is used to describe the magnetization inside the anisotropic FRR where all the magnetic moments are aligned in the direction of the applied DC field. Additionally, the internal biasing fields are found to be non-uniform with spatial variations along the z axis. Therefore, the resulting magneto-static quantities are averaged to approximate the biasing field in each layer. The magnetic losses of the FRR are represented by a damping factor α of 0.0002. For simplicity, our model neglects the macroscopic demagnetizing field effects that are strongly dependent on the ferrite sample shape. However, the internal static field seen by the magnetic moments would be slightly decreased by the demagnetizing fields present in the sample. Figure 4.32(a) presents the simulated non-reciprocal transmission coefficients S_{21} and S_{12} in the

entire frequency range 22 – 32 GHz, where the S_{21} and S_{12} resonances of similar WGM modes are shown with different characteristics in amplitude and frequency. For instance, in Fig. 4.32(b), the WGM_{600} S_{21} resonance occurs around f = 27.97 GHz with -9.8 dB, and S_{12} resonance is around f = 28.16 GHz with higher coupling of about -15 dB. The frequency gap Δf between the two resonances is around 200 MHz. The resulting S_{21} and S_{12} resonance frequencies are observed to be directly proportional to the internal field present in the sample $f_r \propto H_o$. The effect of the damping factor α on the coupling level of both S_{21} and S_{12} resonances is studied for the WGM_{600} operation. As shown in Fig. 4.32(c) and 4.32(d), increasing α from 0 to 0.001 at steps of 0.0002, will decrease the resonance depth at S_{21}, and in contrary, increase the S_{12} resonance amplitude, respectively.

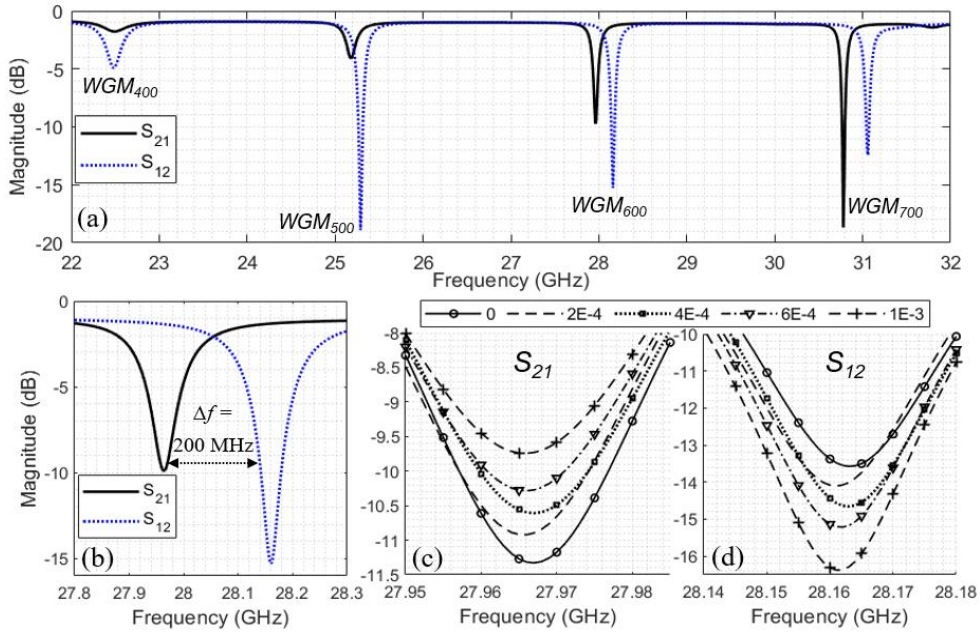

Figure 4.34: Simulated non-reciprocal coefficients S_{21} and S_{12} (a) in the entire operating frequency range for different WGM modes, (b) at WGM_{600}. Effect of the damping factor on the coupling level at both (c) S_{21} and (d) S_{12} of WGM_{600}.

4.5.5 Experimental Measurements

A prototype of the WGM sensor was fabricated following the design specifications in Table 4.5 on Rogers 4360G2 dielectric substrate as shown in Fig. 4.33. A pair of end-launch connectors were attached to both ends of the MTL to facilitate the coaxial connections at the input and output ports when feeding the microwave signal from VNA. The FRR was distanced 0.1 mm off the MTL and appropriately fixed by attaching the permanent magnet disc on the other side of the substrate (i.e., ground plane) as shown in Fig. 4.33. The developed prototype was used to test synthetic blood samples of clinical concentrations related to the diabetes conditions (normal, hypoglycemia, and hyperglycemia), using the Keysight Technologies VNA N5227A at a controlled room temperature of 22±1°C.

Table 4.5: Design parameters of the FRR sensing structure

Parameter	***L***	***W***	***H***	W_{line}	***t***	***R***	***h***
Values (mm)	30	20	0.2	0.28	0.017	5.13	1.44

First, the reflection S_{11} and transmission S_{21} responses of the bare sensor were measured without the ring resonator and the magnetic disc as depicted in Fig. 4.34(a). A transmission loss of about 3.5 dB is shown due to the connectors and MTL losses over this range of frequency. When the FRR is introduced at close proximity (g = 0.1 mm) to the MTL, the power is coupled onto the resonator and higher order WGM modes are excited. Figure 4.34(b) plots the measured S_{21} spectra of the unloaded FRR (without magnetic bias) where four WGM resonances are observed in the spectrum 22 – 32 GHz as listed in Table 4.6. Good agreement is observed between the collected measurements and EM simulations of the reciprocal sensor shown previously in Fig. 4.26(a). The resonance frequency and *Q*-factor for the WGM resonances are highest when there is no SUT introduced in the sensing area. Table 4.6 compares the four WGM modes in terms of the loaded *Q*-factor by considering the 3-dB bandwidth at resonance. Among the four WGM resonances, we chose to perform the glucose measurements using the WGM_{600} mode of higher *Q*-factor. WGM_{700} could also be used for sensitive glucose measurements.

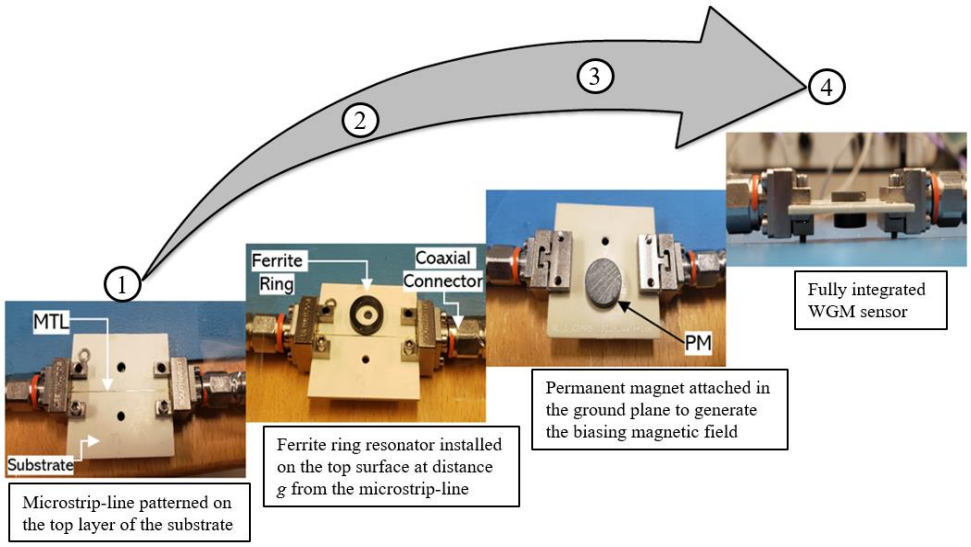

Figure 4.35: Fabricated prototype of the FRR sensor and the integration of different parts.

Table 4.6: Performance comparison between reciprocal WGM modes

Mode	**WGM_{400}**	**WGM_{500}**	**WGM_{600}**	**WGM_{700}**
Resonance Frequency	22.86 GHz	25.57 GHz	28.36 GHz	31.33 GHz
Loaded Q-factor	176	1346	2462	2005

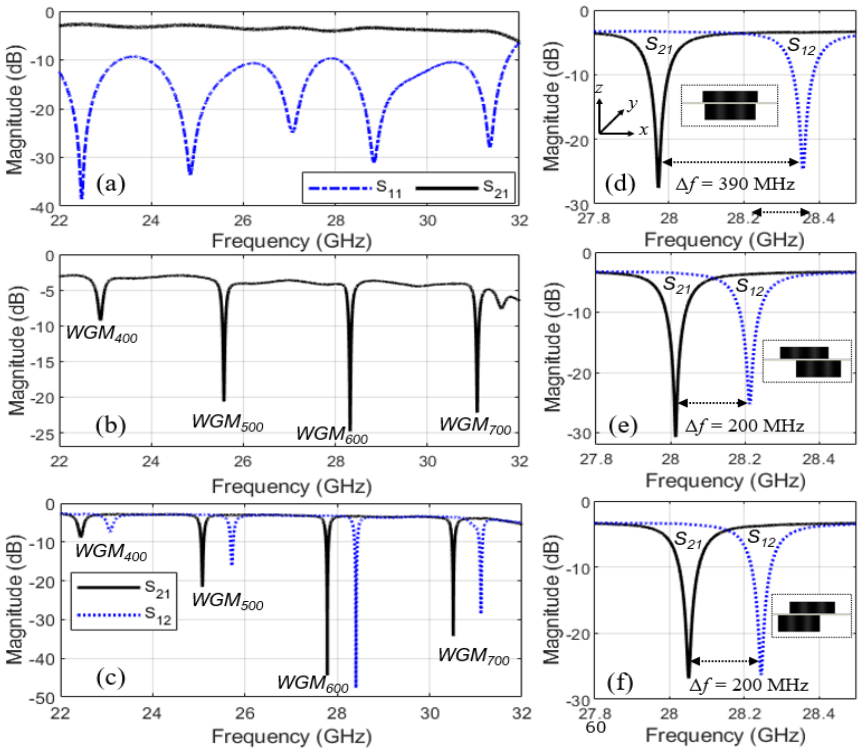

Figure 4.36: (a) Non-resonance behaviour with no FRR installed. Measured transmission coefficients at different WGM modes (b) before magnetic biasing (reciprocal operation) and (c) after biasing (non-reciprocal mode). Measured S_{12} and S_{21} at WGM_{600} when the magnet is attached with (d) full alignment, (e – f) partial alignment in the +x and –x direction, respectively.

Under the action of DC magnetic field, the FRR is magnetized, becomes anisotropic, and thereby exhibits a non-reciprocal behaviour when the permanent magnet disc is attached beneath the MTL substrate (Fig. 4.33). The S_{12} response has changed with significant frequency shift from that of S_{21} as shown in Fig. 4.34(c). WGM resonances of similar modes are set to different frequencies over a narrow bandwidth. The measured nonreciprocal response also validates the HFSS-Maxwell simulations in Fig. 4.32(a). Both simulation and measurement results demonstrate the split in S_{21}/S_{12} resonant frequencies where observed a travelling wave behaviour that fits the approximating transmission line model in Fig. 4.25(b) and 4.25(c) for the CW/CCW modes. The frequency gap between the two resonances of a specific WGM mode in S_{12} and S_{21} is shown to be impacted by the alignment of both the FRR and PM, and the resulting magnetic field intensity. For instance, the frequency gap Δf is largest (~390 GHz) with the maximum bias when both components are co-centered or fully aligned (Fig. 4.34(d)). However, Δf gradually decreases to 200 MHz due to the weaker bias resulting from the partial alignment in the +x and -x directions as depicted in Fig. 4.34(e) and 4.34(f), respectively. It is also observed that other resonance attributes (e.g., amplitude and *Q*-factor) will be slightly influenced by every alignment setting. Next subsections discuss the experimental validation of the ferrite sensor in different setups to ensure its capability in detecting the small changes of glucose EM properties. To imitate the practical application for diabetes while avoiding the intricacies associated with using

authentic blood at this time, a set of synthetic blood samples (hemoglobin-based) of glucose concentrations 50 – 350 mg/dL were used.

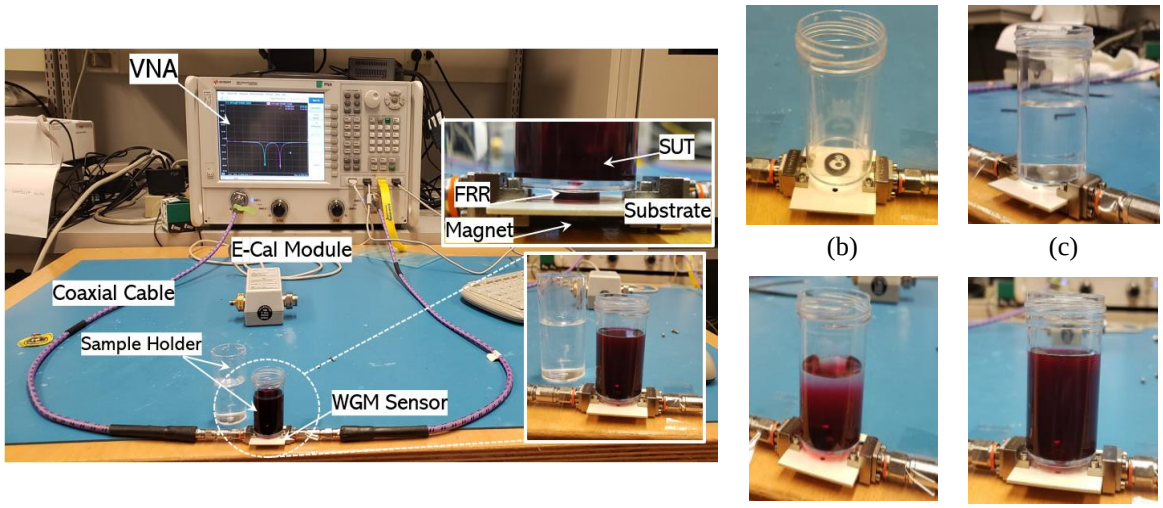

Figure 4.37: (a) Experimental setup for glucose sensing inside plexiglass containers with detailed view for the sensor parts, (b) loading an empty container, (c) distilled water, (d)-(e) some resulting glucose concentrations.

The detection sensitivity of the developed WGM system was first experimented by monitoring the change in glucose levels of a loaded blood sample using the setup in Fig. 4.35(a). To do so, an empty plexiglass container of cylindrical shape was first introduced at d = 1 mm on top of the resonator as depicted in Fig. 4.35(b). This 1 mm gap would allow for greater interactions of the glucose sample with the WGM fields while not decimating the resonances. The container was filled with V = 10 mL of distilled water (C = 0 mg/dL), and the resulting response was recorded. Next, small droplets of blood glucose were added, at four intermittent stages with precise volumes, using a controllable syringe to the distilled water inside the container. The sensor response was recorded accordingly in every stage. Each added droplet of glucose changes the concentration of the loaded mixture as appeared on Fig. 4.35(c) and 4.35(d). Particularly, the consequent glucose concentrations were 16.7, 31.8, 51.0, and 82.0 mg/dL. The S_{12} and S_{21} spectra corresponding to those concentrations are plotted in Fig. 4.36(a) and 4.36(b), respectively. As observed, increasing the glucose concentrations on the loaded blood sample would shift the S_{12} and S_{21} resonance frequencies of WGM_{600} towards lower bands. Larger shift of about 3 MHz was observed for the concentration change from 51 mg/dL to 82 mg/dL. The resolutions for other concentration changes (of very close increments) were in the range 0.7 – 1 MHz. The change resolution of both $f_{S_{12}}$ and $f_{S_{21}}$ resonances is nearly similar. Another interesting feature when sensing with this non-reciprocal resonator is the contrary pattern of the S_{12} and S_{21} depths with each concentration (i.e., S_{12} amplitude decreases and that of S_{21} increases, and vice versa for another concentration).

The resulting perturbations are solely driven by the change in glucose concentration of the mixture in each measurement trial. This was demonstrated very clear in a supplemental experiment on the

reciprocal sensor where distilled water was added consecutively at volume increments of 0.5 mL before loading any glucose content. As shown in Fig. 4.37, increasing V would induce slight downward shifts in the S_{21} resonant frequencies of the WGM mode. However, this shift converges around f = 28.076 GHz (at WGM_{600}) and f = 30.788 GHz (at WGM_{700}) for volumes beyond 3.0 mL. Therefore, to carefully mitigate the sensor's cross-sensitivity to SUT volume (i.e., dependency of resonance characteristics on SUT volume), glucose samples should be tested at V >3 mL.

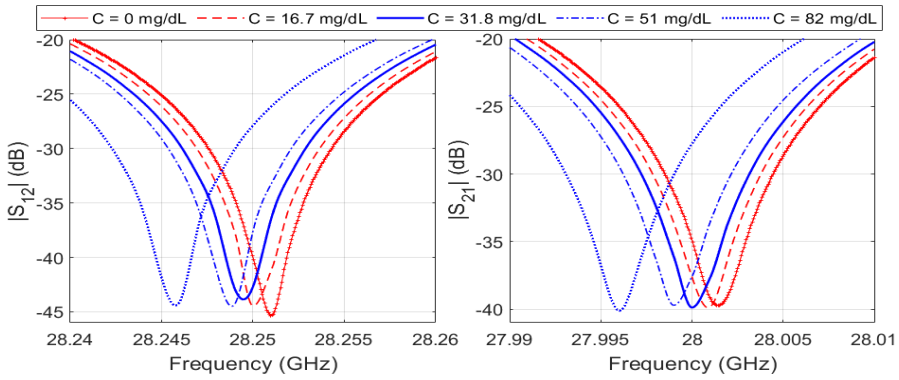

(a) (b)

Figure 4.38: Modulus of the measured (a) S_{12} and (b) S_{21} for varying glucose levels in the loaded sample when operating in WGM_{600} mode.

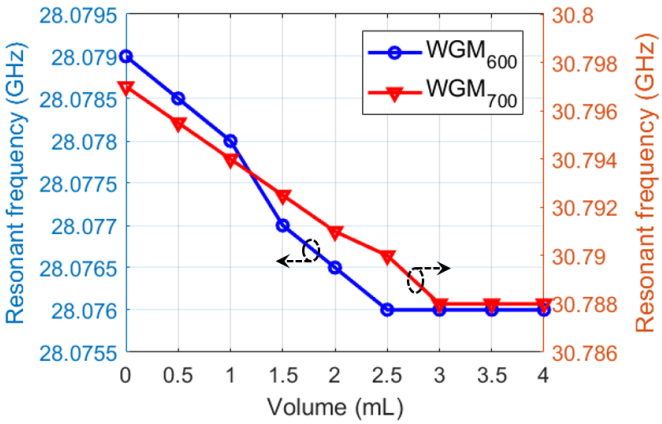

Figure 4.39: Convergence of the S_{21} resonant frequency of WGM_{600} and WGM_{700} beyond a certain volume of distilled water.

In the second experiment, six synthetic blood samples of glucose concentrations 70, 100, 150, 200, 250, and 300 mg/dL were prepared at consistent volume V = 2 mL inside glass containers of identical geometries of height 5.6 cm, diameter 2.5 cm, and bottom thickness of 1 mm as shown in Fig. 4.38. This was done to confirm the consistency in the measured data, clear any uncertainty related to volume and/or container shape, and to capture only dependence on the EM characteristics of the tested glucose samples.

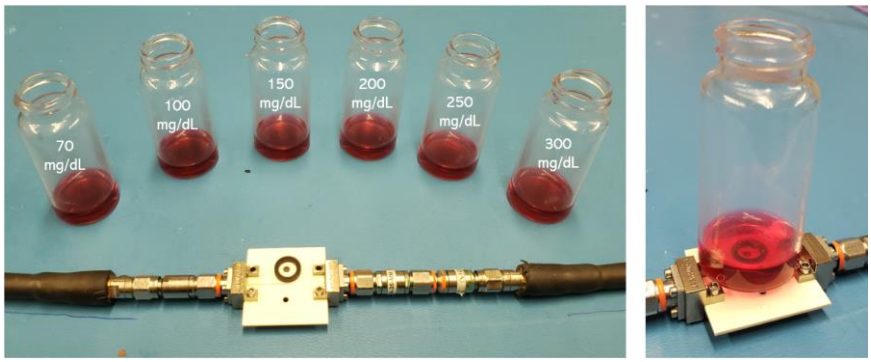

(a) (b)

Figure 4.40: (a) Measuring blood glucose samples in vials, (b) placing a sample on top of the sensor.

In each measurement trial, a specific glucose vial was tested onto the WGM sensor as captured in Fig. 4.38(b). The scattering response of the bare sensor (~baseline) was exactly retrieved after testing each glucose sample to guarantee robust and accurate measurements among all samples. Four scattering responses $|S_{12}|$, $|S_{21}|$, $\angle S_{12}$, and $\angle S_{21}$ were measured (and averaged over 3 repeatable trials) for the six glucose samples at WGM_{600} in 27.7 – 28.4 GHz as plotted in Fig. 4.39(a), 4.39(b), 4.40(a), and 4.40(b), respectively. As shown, the various glucose concentrations (having slightly different EM properties) disturb the evanescent E-fields each in a unique manner. Therefore, varying shifts in resonance frequency and depth were noticed in the $|S_{21}|$ and $|S_{12}|$ where each glucose specimen maintains a specific resonance signature. These shifts are nearly consistent; however, they might occur at a higher resolution in one response compared to other. For instance, 5 MHz shift was observed between the $|S_{12}|$ responses of C = 200 mg/dL and C = 300 mg/dL. However, the corresponding change in $|S_{21}|$ was only 4 MHz. This demonstrates the benefit of simultaneously sensing the glucose samples at multiple resonance frequencies of the operating WGM mode. Moreover, the WGM phases of both S_{21} and S_{12} append the sensing information to enable precise identification of the tested concentrations. The glucose samples are shown to have phase spectra that change nearly linearly from -70° to 10° (in S_{12}) and from 10° to 100° (in S_{21}) over the operating spectrum as plotted in Fig. 4.40(a) and 4.40(b), respectively. For 200 to 300 mg/dL change, the phase at f = 28.28 GHz in S_{12} shifts by 16.25° (from -53.45° to -37.2°), while that at f = 27.82 GHz in S_{21} shifts by 18.15° (from 35.68° to 53.83°). Significant shifts were also observed for other glucose variations in the magnified ranges 27.815 – 27.825 GHz (in S_{21}) and 28.275 – 28.285 GHz (in S_{12}). Measured glucose data was repeated three times at error bounds of ±0.2 MHz, ±0.05 dB, and ±0.5° in frequency, amplitude, and phase, respectively.

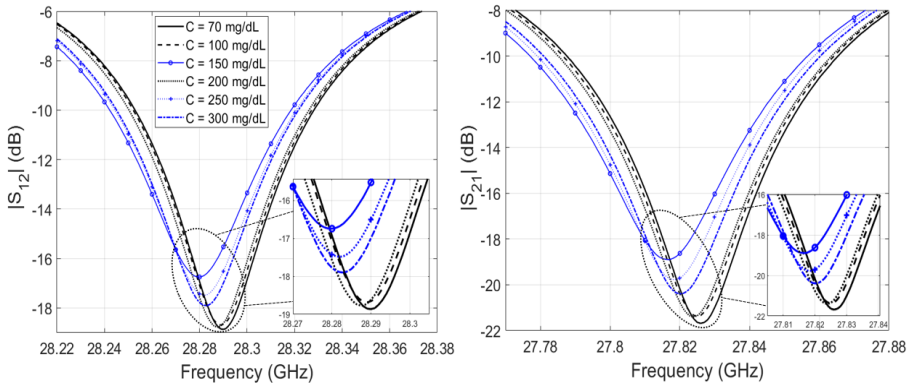

(a) (b)

Figure 4.41: Magnitudes of (a) S_{12} and (b) S_{21} for the measured glucose concentrations when operating in the WGM_{600} mode.

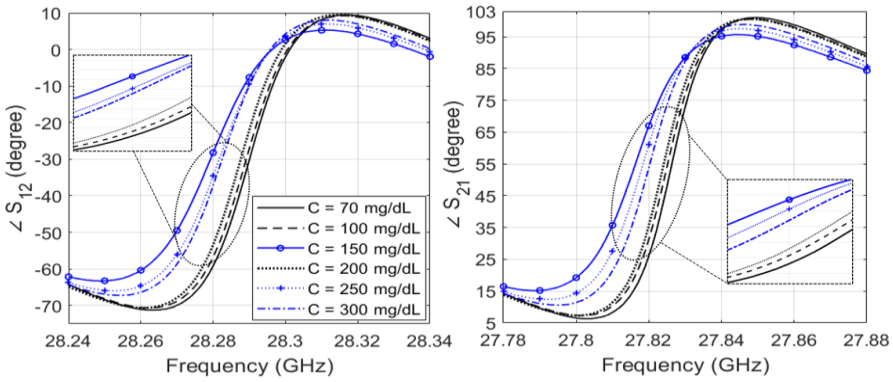

(a) (b)

Figure 4.42: Phases of (a) S_{12} and (b) S_{21} for the measured glucose concentrations when operating in the WGM_{600} mode. Zoom-in windows focus the range 28.275 – 28.285 GHz for S12 and 27.815 – 27.825 GHz for S_{21}.

Lastly, the ferrite sensor was tested for detecting the glucose concentrations 50, 200, and 350 mg/dL of synthetic blood samples prepared inside clinical test tubes using the setup in Fig. 4.41(a). Those tubes have identical geometrical diameters very close to that of the FRR, and hence a proper perpendicular alignment would be achieved for the SUT above the sensing spot as shown in Fig. 4.41(b). Therefore, greater interactions are expected for the glucose sample with the WGM fields localized along the FRR periphery. To facilitate such alignment, a fixture arm was designed appropriately to retain the sample tube position at consistent distance d = 1 mm relative to the FRR, while mitigating any placement errors during the measurement. Figure 4.42(a) plots the sensor response before plugging in any blood sample. The measured $|S_{12}|$ and $|S_{21}|$ spectra for glucose samples are depicted in Fig. 4.42(b) and 4.42(c), respectively. A non-monotonic trend was observed with higher frequency resolutions in S_{21} data compared to S_{12}. For 200 – 350 mg/dL change, S_{21} shifts by 12 MHz while S_{12} shifts by 11 MHz. Each glucose sample was tested three times to prove the repeatability of the sensor as shown in Fig. 4.43(a), 4.43(b), and 4.43(c), for 50, 200, and 350 mg/dL, respectively. The interaction of the blood sample with

the modal fields was greatly expanded in the new fixture setup with test tubes of slim thickness. As a result, the sensitivity and repeatability for glucose monitoring were evidently improved.

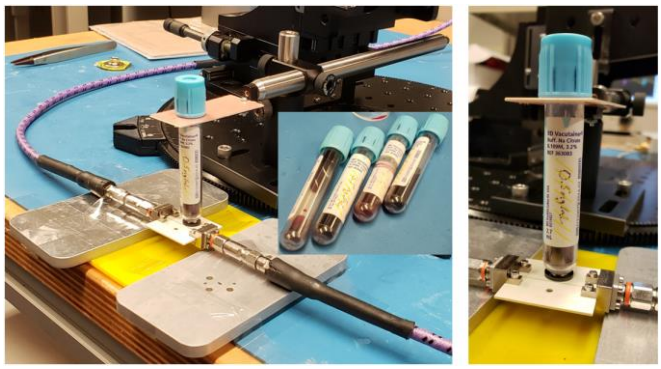

(a) (b)

Figure 4.43: (a) Lab setup for experiment III, (b) Sample tube under test.

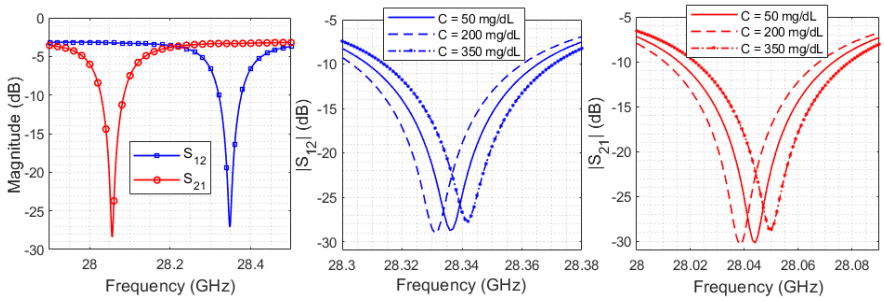

(a) (b) (c)

Figure 4.44: Measured scattering response (a) prior loading, and (b)-(c) post loading.

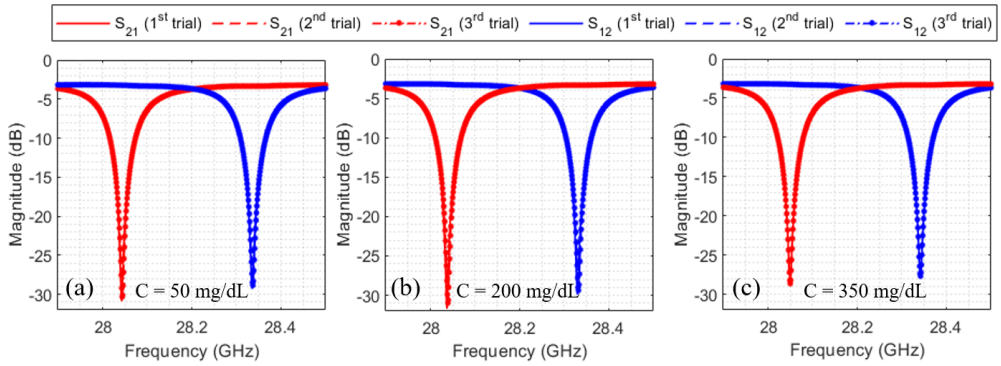

(a) (b) (c)

Figure 4.45: Repeatability tests for blood samples of (a) C = 50 mg/dL, (b) 200 mg/dL, and (c) 350 mg/dL

4.5.6 Sensitivity Analysis

The foregoing VNA measurements, from the three experiments, have revealed considerable variations in S_{12} and S_{21} resonances of the excited WGM_{600} in response to the varying glucose-levels. More sensing data could be acquired from the sensitive WGM_{700} to associate each glucose concentration with unique dataset of resonant frequencies, phases, amplitudes in the induced modes. Frequency and phase shifts were adopted as more robust and reliable sensing parameters for measurements. Other sensing

parameters such as peak amplitudes could also be used for detection. In terms of the absolute change in the resonance frequency of S_{12}/S_{21} (in MHz) corresponding to concentration change (in mg/dL), the calculated sensitivities from the three experiments are 0.06, 0.03, and 0.07 MHz/(mg/dL). The phase sensitivity is about 0.17°/(mg/dL) on average. Samples were loaded in different manners using different setups, and thereby such variances in the sensitivity metric are expected. The minimum recorded sensitivity (0.03 MHz/(mg/dL)) is yet superior to other state-of-art microwave glucose sensors as presented in Table 4.7.

Table 4.7: Comparison against state-of-the-art microwave glucose sensors

Ref	**Concentration (mg/dL)**	**Operating frequency (GHz)**	**Sensing parameter**	**S (MHz per mg/dL)**
[69]	50 – 40000	14 – 16	Phase	0.024°/[mg/dL]
[125]	504 – 3531	1.4	$f_r\ (S_{21})$	1.83E-04
[202]	500 – 20000	35.5	$f_r\ (S_{21})$	4.00E-05
[159]	500 – 2500	1.91	$f_r\ (S_{21})$	4.00E-04
[79]	5000 – 30000	1.68	$f_r\ (S_{11})$	2.00E-04
[154]	2000 – 10000	2.074	$f_r\ (S_{21})$	1.00E-02
[177]	100 – 1000	4.8	$f_r\ (S_{11})$	1.40E-02
[178]	0 – 34780	16	$f_r\ (S_{11})$	1.64E-02
[146]	0 – 5000	4.18	$f_r\ (S_{21})$	2.60E-02
Ferrite WGM Sensor	50 – 350	22 – 32	$f_r\ (S_{12}/\ S_{21})$ $\Phi\ (S_{12}/\ S_{21})$	7.00E-2 0.17°/[mg/dL]

Chapter 5. Glucose Sensing System Integration Using Radars

5.1 Radar Sensing

Radar systems have been increasingly used over the recent years for a variety of applications. For instance, radars for automotive, ground and weather applications are commonly employed at different scales with variable lighting, peripheral, and environmental conditions. The low-cost hardware items of small-size modules have recently become available and have been allowed for some introductory explorations in [215], [216], [217], [218]. Human Computer Interface (HCI) has also shown to be a potential area for radars to detect the human's hand gesture at a micro scale (finger motion recognition) [219], [220], enhance reality interactions [221], activity discernment [222], liquid identification [223] and to distinguish between various materials and objects by analyzing the characteristics of the reflected radio waves [224]. Smart lighting products that detect incoming motions for automatic lighting have recently replaced the conventional passive infrared sensors (PIR) with radar systems that are cost-effective, highly sensitive, and of better sensing resolution with a wider range. Radars have also demonstrated success in the health scope for a variety of applications such as sleep monitoring [225], sensing the respiratory and heart/pulse rates [226], emotion tracking [227], gas detection [228], and many other aspects of radar capabilities are still under exploration.

Motivated by the results of our prior study [187] that succeeded in differentiating the amount of sugar in three different drinks (coke, diet coke, and zero coke) using the reflection data from a multi-channel radar sensor as confirmed by the reflected scattering signals from one channel of a 4-port Keysight Technologies N5227A PNA-67GHz; in this chapter, radar sensing and signal processing were both employed for the purpose of identifying the glucose levels in synthetic blood samples of varying glucose concentrations typical to the diabetes condition. First, a compact low-cost multi-channel radar system was practically experimented to demonstrate the efficacy for non-invasive BGL monitoring when testing the small glucose concentrations present in the blood mimicking samples. Next, portable sensor prototypes/devices were realized by interconnecting the previously developed glucose sensors in low- and high-bands with appropriate radar boards as driving sources instead of the bulky and expensive VNA instrument.

5.2 mm-Wave Radar Sensor (57 – 64 GHz)

An integrated mm-wave radar system is used as a sensing platform for tracking different glucose concentrations in blood samples (Fig. 5.1(a)). In this system, a two-transmitters (Tx) and four-receivers (Rx) high resolution radar working in the 57 – 64 GHz frequency range (bandwidth of 7 GHz and centre frequency of 60 GHz) [219], was utilized to experiment the detection of glucose levels in blood-mimicking samples [169] by analyzing the raw data of the reflected radio waves. To do so, synthetic

"fake blood" samples were first prepared at assorted glucose concentrations from 0.5 to 3.5 mg/ml at 0.5 mg/ml increments. The prepared blood samples were loaded at a specific volume inside clinical test tubes, then placed onto a 3D-printed fixture device that was particularly developed to retain the sample tube position at a consistent distance relative to the radar sensor. The blood samples under test were illuminated with frequency-modulated continuous electromagnetic waves at very high frequencies and the raw data of reflected mm-waves were collected simultaneously from the four channels of the radar. The collected raw data was then analyzed using signal processing techniques to identify the corresponding glucose concentrations in blood.

5.2.1 Working Principle of the Proposed Radar System

In radar systems, a transmitting antenna sends an electromagnetic-wave signal towards a target of certain properties. Parts of the transmitted signal are absorbed, scattered, and reflected back towards the radar receiver, which receives a tiny portion of the transmitted signal for further analysis and estimation of target location, speed, as well as other properties. Among the different kinds of radars such as Doppler, impulse, etc., the Frequency-Modulated Continuous-Wave (FMCW) type has shown to be promising for materials and objects recognition and characterization [224]. In FMCW radars, the signal is transmitted continuously. This signal, called "chirp", has a frequency which varies linearly from a minimum up to a maximum frequency over the duration of one chirp. These chirps are continuously transmitted. The received signal is then amplified, filtered to reduce noise, and then correlated with the transmitted signal to generate what is called a beat signal that contains all necessary information about the target. The time delay between the transmitted and received chirps results in a frequency difference between the two signals. The resultant beat signal can be spectrally analyzed to extract the range and velocity of the target. Generally, the range resolution for FMCW radars is given by $c/2BW$, where c is the speed of light and BW is the transmitted signal bandwidth.

In view of the abovementioned information, the proposed sensing system in this chapter utilizes a mono-static, multi-channel FMCW radar chip operating in the 57 – 64 GHz frequency range (center frequency of 60 GHz) [216], [219]. The radar has two transmitters and four receivers (2-Tx/4-Rx) enclosed in a compact (8 × 11 mm) hardware chip as shown in Fig. 5.1(a) – 5.1(b). The four receivers are arranged in a 2 × 2 matrix pattern as depicted in Fig. 5.1(c). This multi-channel configuration will enable greater capabilities for sensing minute changes in the target attributes, for example detection of movement changes in gesture recognition applications [219] [220]. The transceiver chip is co-developed by Infineon using a Silicon-Germanium (SiGe) process technology that realizes a high level of physical miniaturization by direct placement of patch array antenna into package (AiP). More details about the hardware architecture of the radar chip can be found in [229].

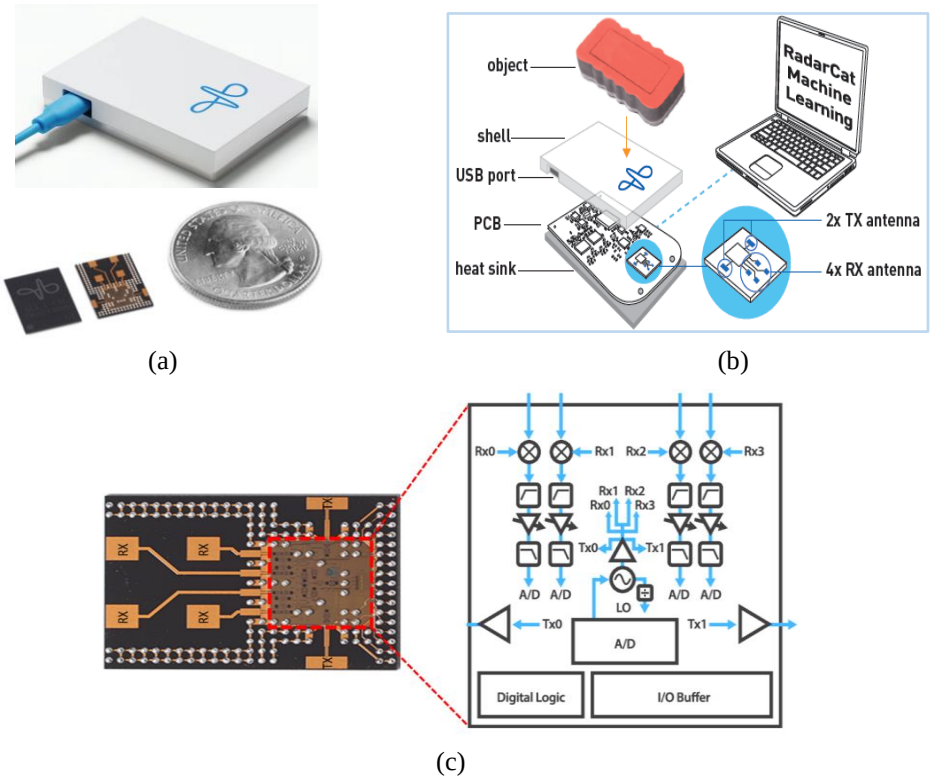

Figure 5.1: Soli FMCW radar system: (a) Radar integrated system in package and 8 mm × 10 mm radar transceiver chip, (b) Soli connection with PC for simple experimental setup for object identification, (c) Radar chip with antennas-in-chip, Tx/Rx positions and hardware architecture (adapted from [219]).

One interesting property of this mm-wave radar is the high-resolution capability that enables resolving the illuminated target, of relatively greater thickness than the radar range resolution, into more than a single range bin at a frequency peak. Consequently, the resultant beat signal becomes quite sensitive to any tiny changes in the characteristics of detected target such as physical state, thickness, height, material properties, radar cross section, etc. Such enriched information in the beat signal can be used as remarkable signatures to recognize and classify the surrounding objects and materials, whereas here in this study this feature is exploited to enable novel glucose levels detection.

The framework of the mm-wave radar employed in this study uses a high temporal resolution rather than the conventional high spatial resolution adopted by classical radars. In this technique, the radar measures the target responses to the FMCW signals radiated periodically at extremely high frame rates. Particularly, a synthesizer generates a modulated electromagnetic wave S_{Tx}, as defined in Eq. (5.1), whose frequency sweeps linearly from 57 to 64 GHz. This FMCW chirp is radiated periodically at a high frequency denoted as RRF (radar repetition frequency) that varies between (1 – 10 KHz) toward a target of certain properties

$$S_{Tx}(t,T) = u(t-T)e^{-j2\pi(f_{min}+kt/2)\,t}, \qquad T = 0, RRI, 2RRI, \ldots \tag{5.1}$$

where f_{min} is the start frequency, k is the chirp slope, $u(t)$ is the complex envelope over one period of the modulation scheme, and RRI is the radar repetition interval that defines the chirp duration between the

starting point of each modulated waveform to the next. With part of the transmitted energy being scattered by the target, a reflected signal S_{Rx}, defined in Eq. (5.2), is received by the radar receiving antennas during each *RRI* at frequency *RRF = 1/RRI*, then filtered and sampled using a 12-bit analog-to-digital converter (ADC) at 1.79 Msamples/s [219].

$$S_{Rx}(t,T) = u(t-\tau-T)\sigma e^{-j2\pi(f_{min}+\,kt/2)\,(t-\tau)}, \qquad T = 0, RRI, 2RRI, \ldots \tag{5.2}$$

where σ represents the combined effects of radar cross section and propagation loss, τ is the round-trip time for the transmitted EM signal ($\tau = 2D/c$), where D is the distance to the target, and c is the speed of light in vacuum (3×10^8 m/s).

These reflected responses are analyzed to extract fine variations in the temporal signal that are attributed to the target adaptive status such as orientation, motion, composition, etc. In this regard, two distinct time scales are used to analyze the reflected mm-wave signals, one is the slow time $T_{slow} = t$ defined by the repetition interval of the radar (i.e., chirp duration) and used to collect the reflected signals at the corresponding radar repetition frequency *RRF* that varies in the range 1 to 10 KHz as mentioned earlier. The second time scale is the fast time $T_{fast} = T$ by which the transmitted signal is varying over one RRI or modulation period, and that will be used for sampling the corresponding received signal at the ADC. Given the considerably high radar repetition frequency *RRF*, the properties of a moving target can be assumed to be constant over one RRI. Therefore, the reflected signals collected every T_{slow} would represent the instantaneous features of the target such as range, orientation, and reflectivity, that can be elicited by processing $S_{Rx}(t,T)$ as function of the fast time *t*. However, the dynamic features of the target (e.g., velocity, change in physical state, or geometry) can be extracted by looking into the collection of the reflected signals over multiple RRIs and analyzing $S_{Rx}(t,T)$ as function of the slow time *T*.

5.2.2 Radar Experimental Approach for Glucose Detection

The glucose detection approach investigated herein exploits the SOLI radar sensor capabilities whereby the characteristics of the object(s) placed in the vicinity of the sensor, right on top or at a definite distance, can be explored by looking into the reflected signals as collected by the radar receiving antennas. These signals represent a rich store of information that describe various attributes (e.g., thickness, volume, range, density, surface properties, internal synthesis, etc.) respecting the object(s) on target of the radar transmitted EM waves. In the case under study, there are liquid samples of the homogenous composition of synthetic blood but with different amounts of dissolved glucose. In other words, all the samples have a similar shape, volume, placement, and almost the same composition except for the concentrations of the dissolved glucose that have tiny variations from one sample to another. This variation in glucose levels modifies the dielectric properties of the sample in place, thereby making it possible for the radar signals to capture the unique signature of each blood sample of respective glucose concentration. By recording the multi-channel raw radar signals that are unique to

various glucose samples, and analyzing them using signal processing algorithms we were able to differentiate between the blood samples of 0.5, 1.0, 1.5, 2.0, 2.5, 3.0, and 3.5 mg/ml. No feature extraction or machine learning module is applied in this analysis, however, the supervised learning approach inherent in SOLI could also be used to train, classify, and accurately correlate the collected raw signals to their respective level of glucose concentrations.

A set of seven samples of synthetic blood at different glucose concentrations 0.5, 1.0, 1.5, 2.0, 2.5, 3.0, and 3.5 mg/ml, were prepared in the test tubes and labelled accordingly. This was done by mixing the synthetic blood samples with different proportions of the glucose standard solution (CAROLINA) of 10 mg/ml as determined by the dilution equation while using a micropipette device for harvesting the exact volume precisely. All the prepared blood glucose samples were measured using a commercial glucometer device to ensure the accuracy of the prepared glucose concentrations as shown in Table. 5.1.

Table 5.1: Concentration verification of the prepared synthetic blood samples using a Glucometer device.

Targeted concentration for the prepared sample (mg/ml)	0.5	1.0	1.5	2.0	2.5	3.0	3.5
Measured concentration using Glucometer (mg/ml)	0.5	1.06	1.63	2.16	2.79	3.15	3.32

The experimental setup for testing the blood glucose samples is shown in Fig. 5.2 where the Soli radar and tested sample tube were placed at their respective locations in the designed fixture that would help to mitigate any placement error in the sample tube position during the experiment. The fixture would also enable the sample tube to be in perpendicular alignment with the incoming mm-wave, thereby avoiding any complex bending of the mm-wave signal due to oblique incidence. Note that in this setup, all the transmitting and receiving antennas (2-Tx and 4-Rx) were placed on one side facing the blood sample under test as shown in Fig. 5.2(b). A metallic plate was used to improve the quality of the collected measurements by excluding the noisy reflections from the surrounding environment. The radar system was connected to the PC interface whereby the radiation operation was controlled for starting and ending each measurement trial, and further to gather and process the raw data reflected by the blood glucose sample under test. In each trial, the radar shined an mm-wave signal from one side in the designed fixture towards a blood sample and received the reflected backscattered signal. A signal processing module was applied in the connected PC to analyze the characteristics of the received signals to identify the glucose level of concentration in the specific blood sample on target.

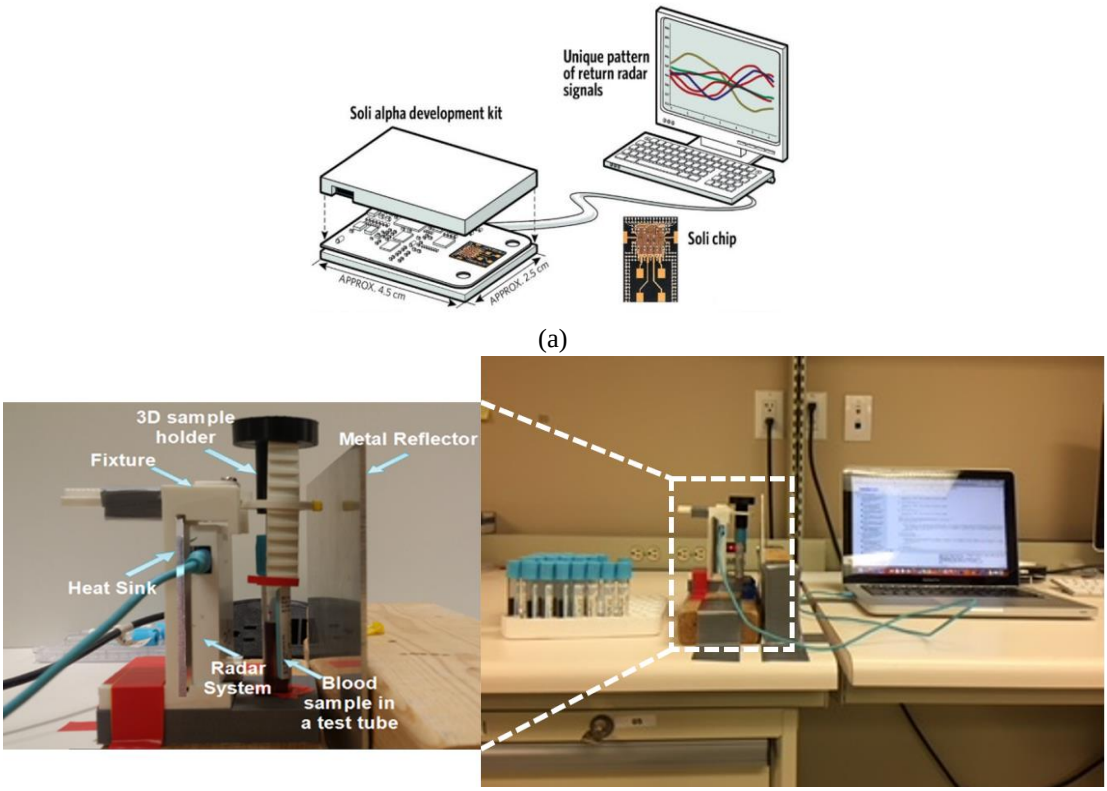

Figure 5.2: Radar experimental setup for glucose detection in blood test tubes: (a) Soli connection to PC, (b) Experiments setup showing the integrated system that employed mm-wave radar to detect changes in dielectric properties of samples with different glucose levels. PC interface where the collected raw data were monitored and processed using DSP algorithms for accurate identification.

5.2.3 Results, Analysis, and Signal Processing

As mentioned earlier, the glucose-loaded blood samples in test tubes were tested in the 3D-printed fixture setup that was developed to mitigate any placement errors. Each blood sample of a specific concentration was tested three times in order to prove the repeatability of the radar measurements. In this repeatability routine, all the measurements were completed once for all different concentrations 0.5 – 3.5 mg/ml in one round then repeated twice following the same course. This was done to compensate for the uncertainty which occurs due to the position change in test tubes when they were replaced in the consecutive measurements for each glucose concentration. This position change becomes quite sensitive in such an mm-wave regime, and therefore, we needed to ensure that only the glucose concentrations have a substantial impact and dependency on the millimeter-wavelength of the radar. In each trial of this repeatability routine, the raw data of the reflected signals were collected and measured by the radar antennas on all four receiving channels. Each channel has a total of 64 samples (bins) of the raw data of the reflected signal amplitudes that would be analyzed and processed to extract the glucose concentration in each tested blood sample.

It is worth mentioning that the phase responses in this radar sensing experiment were not directly useful due to wrapping multiple times (around 2π) inside the blood sample, thereby the measured values carry no unique information about the blood sample under test. A glucometer device was used as a reference to ensure the accuracy of the collected measurements, and the magnitudes of the radar reflected signals were shown to have a similar tendency to the reference glucometer readings. Figure 5.3 shows the raw measured data for each glucose concentration sample as collected in channel 1. The same measurements are plotted in Fig. 5.4 when channel 2 was used. These visuals clearly confirm the very good repeatability of all concentration measurements tested on channels 1 and 2 as demonstrated by the three repetitive trials. Repeatability measurements of relatively higher variations in comparison, e.g., 2.5 mg/ml in channel 1 and 3.5 mg/ml in channel 2, might be attributed to minor shifts in positioning the test tubes inside the 3D-printed sample holder. In addition, the labels of the test tubes might also contribute to these variations when these labels were directly facing the radar mm-wave radiations of very fine resolution.

Next, averages of the absolute reflected magnitudes were calculated for each glucose sample in each of the three trials collected in channels 1 and 2. Figure 5.5 depicts the variations in the averages of the absolute reflected magnitudes of each of the three repeated tests and the corresponding error in each concentration readings. The reflected signals in channel 1 were of relatively higher magnitudes than their peers collected in channel 2 especially for the smaller concentrations 0.5, 1.0, and 1.5 mg/ml. The repeatability error in each glucose readings was in the range of ±1.18 unit/sample point max. A reasonable level of repeatability was also achieved on the readings of the other two channels (channels 3 and 4).

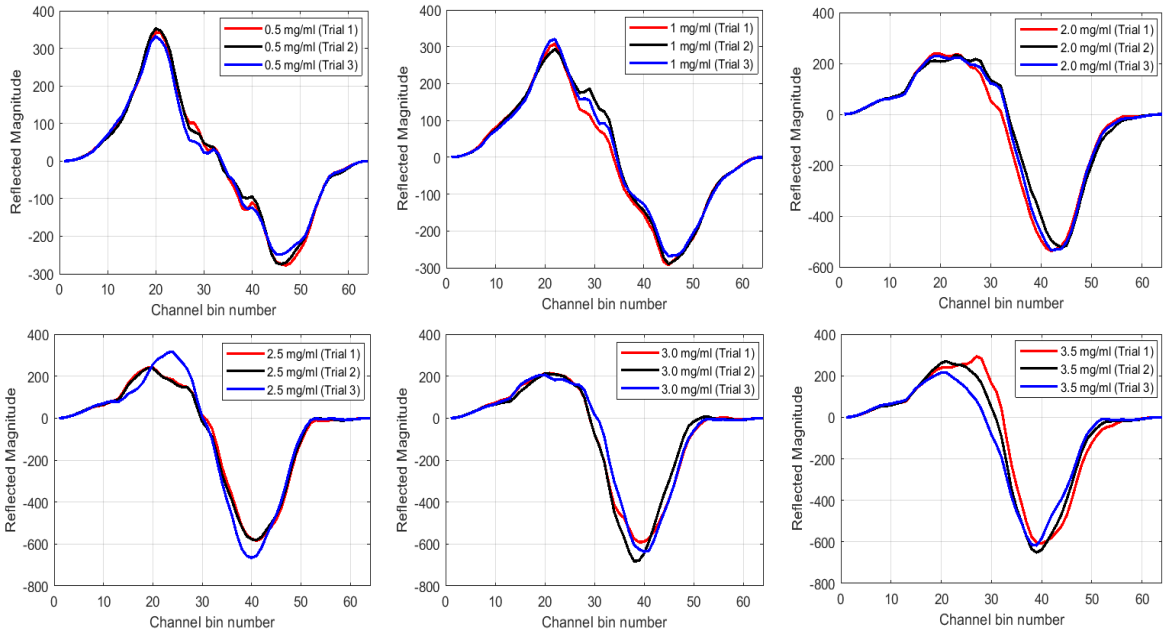

Figure 5.3: Raw data collected via radar channel 1 for glucose concentrations 0.5 – 3.5 mg/ml. Each subfigure shows the three measurement trials for each blood glucose concentration sample.

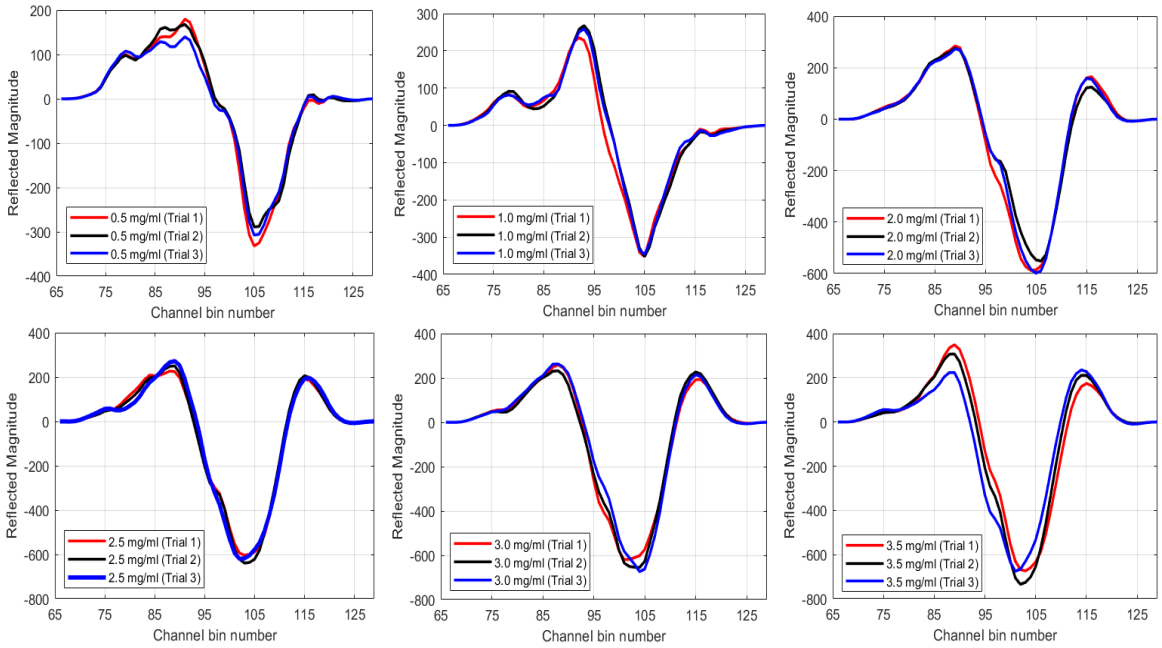

Figure 5.4: Raw data collected via radar channel 2 for glucose concentrations 0.5 – 3.5 mg/ml. Each subfigure shows the three measurement trials for each blood glucose concentration sample.

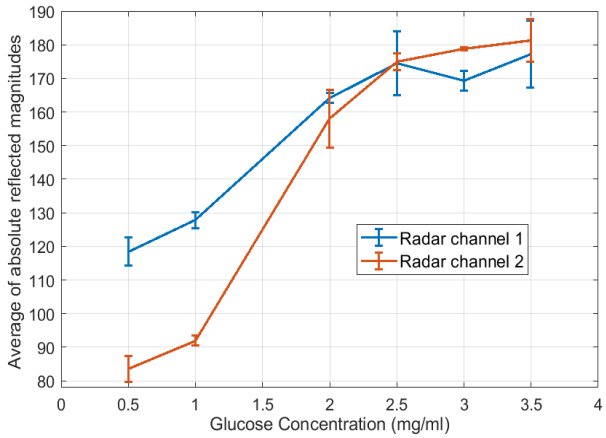

Figure 5.5: Averages of absolute magnitudes in the three trials and corresponding errors.

In what follows, the raw data collected for each tested blood sample of a specific concentration is analyzed. In this analysis, we only relied on the data collected by channel 1 and 2 which were shown to be more stable in terms of the data repeatability and glucose sample distinguishability. For each channel, the average of the three repeatability data sets of each glucose sample was calculated using

$$s_{avg}^{C} = \frac{1}{N}\sum_{n=1}^{N} s_{n}^{C} \tag{5.3}$$

where s_{avg}^{C} is the averaged scattering signal for a given blood sample of concentration C, s_{n}^{C} is the raw data collected for blood sample of concentration C at trial n, and N is the total number of trial repetitions that were fixed to three trials in this experimental study. Next, to process the average data of a given

channel we applied the sample gating signal processing [230] to extract the data points of the respective channel using

$$s_{ch}^{C} = s_{avg}^{C} \times H(s), \tag{5.4}$$

where s_{ch}^{C} is the sample gated signal for channel ch, $H(s)$ is the applied gated window of unit values in the sample range of interest, and zeros otherwise. In this case, $H(s)$ is applied in the range of $1 \leq s \leq 64$ and $65 \leq s \leq 128$, for processing the data from channel 1 and 2, respectively. The sample gated signals s_1^C and s_2^C for the average measured data for each tested concentration C = 0.5, 1.0, 2.0, 2.5, 2.5, 3.0, and 3.5 mg/ml are plotted in Fig. 5.6(a) and 5.6(b), respectively.

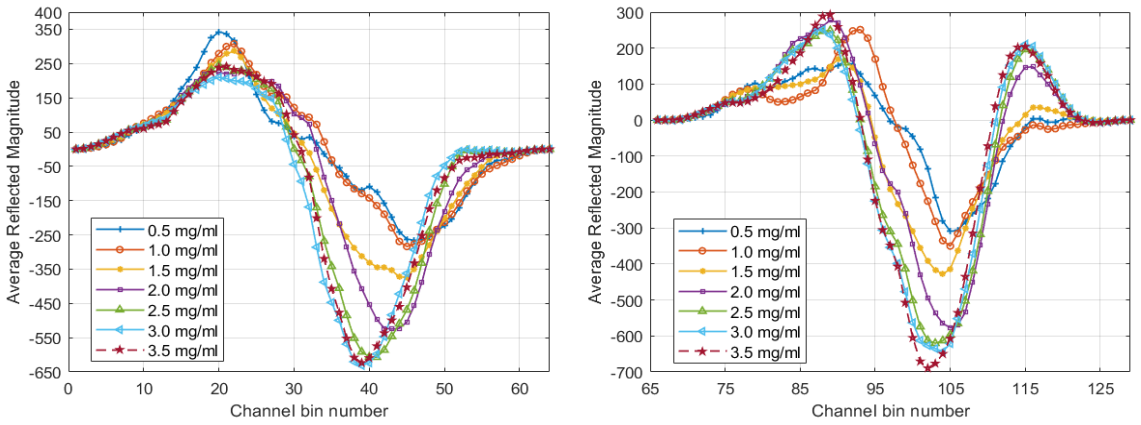

Figure 5.6: Average raw data in the three trials for each concentration across each radar channel: (a) channel 1; (b) channel 2.

In what follows, signal processing algorithms were applied to analyze the radar measured raw data in channels 1 and 2. This will allow for identifying the different glucose concentrations and correlate them to the reflected mm-wave readings. In this regard, the Fourier transform was applied to reveal the interaction between the amplitudes of the backscattered signals and the glucose concentrations in the tested blood samples. Specifically, the discrete Fourier transform (DFT) algorithm was applied to each gated signal s_{ch}^{C} of 64-radar bin points for ch = 1 and 2, C = 0.5, 1.0, 2.0, 2.5, 2.5, 3.0, and 3.5 mg/ml as given by Eq. (5.5). Each gated signal of limited data points (i.e., 64) was zero-padded to increase the length of the gated signal to N = 256 and therefore an improved quality was acquired for the processed DFT data in the transformed frequency-domain.

$$S_{ch}^{C}(k) = \sum_{n=1}^{N} s_{ch}^{C}[n]\, e^{\left(-\frac{j2\pi(n-1)(k-1)}{N}\right)}, 1 \leq k \leq N \tag{5.5}$$

where N is the total number of points for the processed gated signal $s_{ch}^{C}[n]$ applied to compute the DFT using Fast Fourier Transform (FFT) algorithm. The resulted spectrums shown in Fig. 5.7(a) and 5.7(b) are symmetric since the input signals $s_{ch}^{C}[n]$ are real-valued. The double-sided Fourier transform was rearranged by shifting the zero-frequency component to the center of the spectrum as depicted in the small

plot windows enclosed in Fig. 5.7(a) and 5.7(b) for channels 1 and 2, respectively. It is observed that the magnitudes of the Fourier transform of the backscattering signals of the blood glucose samples are directly proportional to the glucose concentrations dissolved in the respective specimens. In other words, blood samples of higher glucose concentrations would have a modulus of larger magnitudes compared to lower levels of glucose concentrations. This is also evidenced by the average power spectral density (PSD) that is estimated for each gated signal vector of a particular glucose concentration using the periodogram figure of merit as given in Eq. (5.6)

$$P(w) = \frac{1}{2\pi N}\left|\sum_{n=1}^{N} s_{ch}^{C}[n]e^{-jwn}\right|^{2}, -\pi \le w \le \pi \tag{5.6}$$

where w is the normalized frequencies in the range $-\pi < w < \pi$ for a DC-centered PSD estimate. The units of the PSD estimate are in squared magnitude units of the time series data per unit frequency. A rectangular window was used to estimate the PSD in decibels for each real-valued $s_{ch}^{C}[n]$. Fig. 5.7(c) and 5.7(d) show the centered two-sided PSD estimate for each real-valued gated signal that corresponds to each glucose sample. The PSD has a length of $N = 256$ and is computed over the interval $(-\pi, \pi]$ rad/sample, which is related to the operational frequency f_s as $(-\pi f_s, \pi f_s]$.

Lastly, all glucose concentrations in channels 1 and 2 are compared in Fig. 5.7(e) and 5.7(f), respectively, in terms of the energy density that is noticed to be increasing as the glucose concentration levels increase. In this regard, the finite energy for each glucose-specific gated signal s_{ch}^{C} is calculated as in Eq. (5.7) by accumulating over all the N sample points, where $S_{ch}^{C}[k]$ is the sampled energy density spectrum for the gated signal $s_{ch}^{C}[n]$. The raw data collected in channel 2 has shown to be more stable compared to those of channel 1. Therefore, the energy densities computed for channel 1 data are noticed to be nearly saturated towards the higher glucose concentrations with $(4.046, 4.075, 4.094) \times 10^{6}$ Volts^2 for the 2.5, 3.0, and 3.5 mg/ml, respectively. This would yield a non-linear correlation relation between the glucose concentration and the resulted energy density. However, the glucose concentrations tend to be more distinguishable when the radar raw data from channel 1 is processed using the DFT as depicted from the transform magnitudes in Fig. 5.7(a). Given the three repeatable radar measurements for each blood glucose sample, the energy density metric was computed for the reflected signals in channel 1 and 2 for each of the three trials as E_1, E_2, and E_3, as shown in Table. 5.2. The variance of the energy density from the three measurement trials was also computed and indicated as error bars in Fig. 5.7(e) and 5.7(f).

Table 5.2: Computation of the energy density in the three measurement trials for each blood glucose sample and the corresponding variance

Metrics	**0.5 mg/ml**		**1.0 mg/ml**		**2.0 mg/ml**		**2.5 mg/ml**		**3.0 mg/ml**		**3.5 mg/ml**	
(× 10^6)	**Ch1**	**Ch2**	**Ch1**	**Ch2**	**Ch1**	**Ch2**	**Ch1**	**Ch2**	**Ch1**	**Ch2**	**Ch1**	**Ch2**
E_1	1.64	1.04	1.60	1.11	3.42	3.70	3.87	3.97	4.03	4.34	4.43	4.65
E_2	1.62	0.91	1.65	1.17	3.08	3.01	3.84	4.21	4.36	4.47	4.46	5.08
E3	1.45	0.86	1.57	1.11	3.31	3.44	4.86	4.22	4.01	4.39	3.72	4.37
Mean	1.57	0.94	1.61	1.13	3.27	3.38	4.19	4.13	4.13	4.40	4.20	4.70
Variance	73E-4	58E-4	11E-4	8E-4	2E-2	81E-3	224E-3	133E-4	25E-3	28E-4	117E-3	85E-3

$$\varepsilon_s = \sum_{n=1}^{N} \left| s_{ch}^{C}[n] \right|^2 = \frac{1}{N} \sum_{k=0}^{N-1} \left| S_{ch}^{C}[k] \right|^2 \tag{5.7}$$

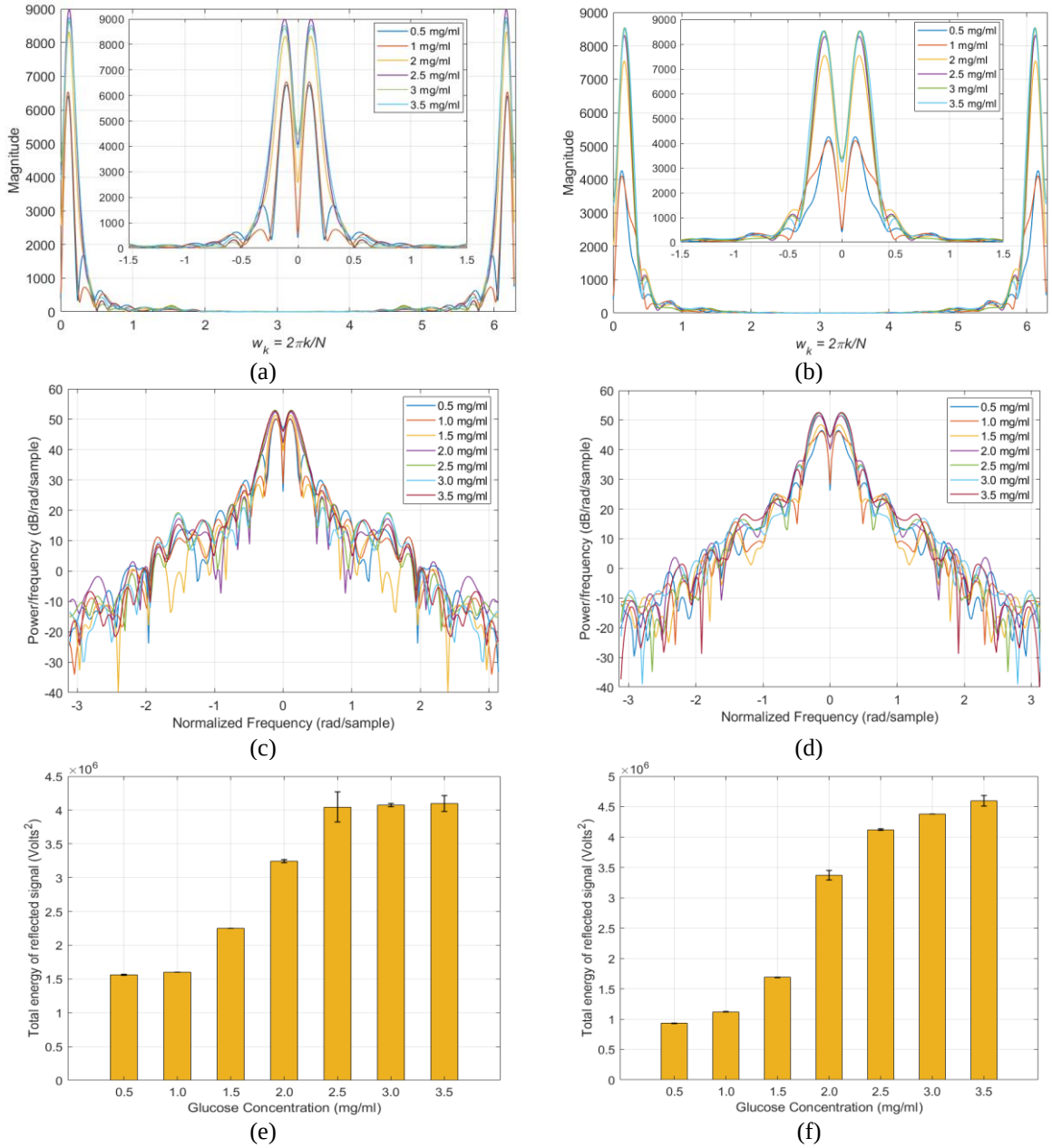

Figure 5.7: Raw data analysis (a) DFT result for data in channel 1 (enclosed plot is for the spectrum when shifted to the center), (b) DFT result for data in channel 2 (enclosed plot is for the spectrum when shifted to the center), (c) power spectral density estimation for data in channel 1, (d) power spectral density estimation for

data in channel 2, (e) resultant energy for glucose concentrations in channel 1, (f) resultant energy for glucose concentrations in channel 2.

5.2.4 Discussion

In view of the DAK-TL findings in Chapter 2, we decided to use a millimeter-wave system operating in the frequency range 57 – 64 GHz for the goal of reliably detecting BGLs relevant to the diabetes condition. Since the mm-wave sensor relies on the reflection data from the blood sample in target, then a small penetration depth of few millimeters would be sufficient to capture the variations in the dielectric properties of the dissolved blood glucose [142]. This was demonstrated by the radar measurements that show a correlation between the IF signal amplitude and the loss property of the blood glucose sample. The theory behind the correlation of the minute changes in the complex permittivity and the amplitude of the IF signal for material and subject identification were explained in [187], [142], [231]. These research papers detail the methodology for understanding the correlation between the average amplitude of the output IF signal and the dielectric parameters of the MUT.

The radar experiments have also shown that by adding a 3D printed fixture device, we can greatly expand the interaction between the lossy glucose samples and the electromagnetic wave which, consequently, improves the glucose sensing accuracy and repeatability. Additionally, the influences of the instrumental and environmental factors were minimized by holding the glucose-sensing experimentation in a controlled environment where both the heat and temperature were controlled and monitored. Since the reflected magnitudes of the mm-waves are enormously dependent on the dielectric properties of the tested glucose samples, and those properties are known to be a function of the sample temperature, therefore, all the blood samples were stored in the same temperature condition of 22±1^{o}C. All the radar experiments were performed in the same room environment of 22±1^{o}C regulated temperature. A metal sheet was also installed behind the radar to serve as a heat sink to dissipate any overheating might occur for the radar device.

The effectiveness of these applied solutions is reflected in the strong repeatability of the collected raw data from the radar sensor. In the analysis of the radar raw data, averaging was used for processing the data sets of the three measurement trials collected for each blood glucose sample. This would help to increase the strength of the reflected mm-wave signals relative to all sources of noise in the experiment environment including the minor displacements of the test tubes. Additionally, the gating was employed to extract the raw data collected in specific radar channels that are shown to be more stable than others (e.g., channel 1 and 2). Each channel occupies a total of 64 data points, hence channel 1 spans from 1 to 64, and channel 2 spans from 65 to 128.

The radar results have shown to be essentially consistent with the dielectric spectroscopy collected via the DAK-TL system. It is noticed that in the experimented radar setup, where a high reflecting surface was employed behind the blood samples, the mm-wave signals were reflected with greater energy for blood samples of higher glucose concentrations, a phenomenon that can be explained by the fact that

incident mm-wave signals encountered less absorption and attenuation inside higher-concentrated samples compared to the those of lower glucose content. This is also evidenced by the previous DAK-TL dielectric measurements in the mm-wave range (50 – 67 GHz) that showed a decrease in the loss tangent when the amount of glucose dissolved in the aqueous solution is increased.

5.3 Portable Low-Band Glucose Sensor

A portable prototype of an improved microwave sensor integrated with a low-cost 2.45 GHz ISM band radar is developed for measuring the glucose level non-invasively in the blood tissue as illustrated in Fig. 5.8. The compact honey-cell CSRR sensor is interconnected to a small low-cost and -power radar module as a driving source instead of the bulky VNA instrument. In particular, the open-source QM-RDKIT that supports the frequency modulated continuous wave (FMCW) functionality, was utilized to couple the CSRR sensor at the ISM frequency range (2.4 – 2.5 GHz) [182]. To do so, the transmitting "Tx" and receiving "Rx" ports of the radar board were connected to the feeding ports of the CSRR sensor using the SMA-RF coaxial cables as shown in Fig. 5.9(a).

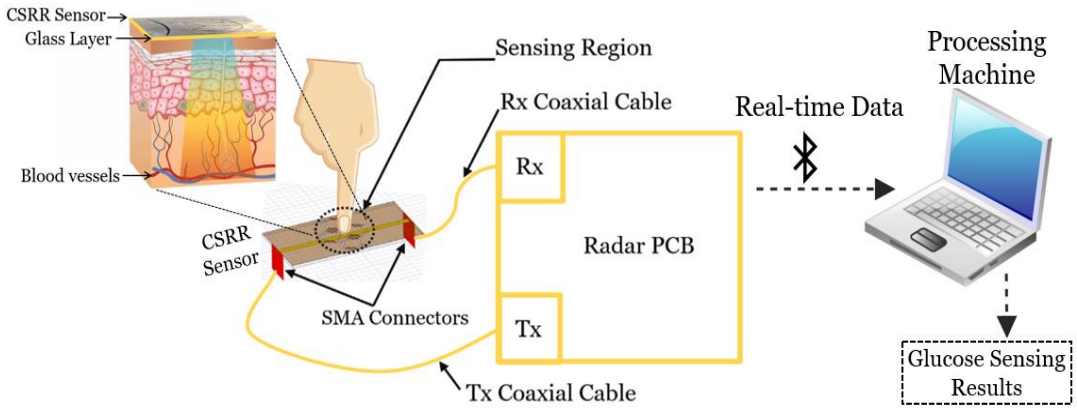

Figure 5.8: General conceptual illustration of the portable radar-driven sensor for measuring the glucose level non-invasively from the fingertip by sending electromagnetic waves of small wavelength into the blood vessels.

The major sections of the radar board are shown in Fig. 5.9(b). It has an RF section to generate and output the transmitted signal and to down-convert the received signal to a frequency range that can be easily digitized using the onboard Analog-to-Digital converter (ADC). Specifically, the onboard Voltage Controlled Oscillator (VCO) and Phase Lock Loop (PLL) are used to generate the transmitted signal of defined frequency. The PLL serves to frequency lock the output of the VCO using the onboard reference to provide a stable and repeatable output frequency. The output of the VCO is amplified before being passed to the input port of the interconnected sensor. The corresponding signal from the sensor output port is first mixed with a sample of the transmitted signal to produce a frequency offset (beat frequency), then it is filtered to remove any unwanted signals developed from the mixing process. Afterwards, the signal is passed to the ADC for digitization, and either stored in memory or streamed over the USB/Bluetooth connection. In addition to the ADC, the digital section also contains the PIC

microcontroller, USB, and power interfaces. The PIC microcontroller coordinates all functions of the radar board, responds to all control commands and data requests received through the USB/Bluetooth connections. As shown in Table 5.3, the radar board operates at 2.45 GHz, 5 Volts and 0.5 Amp with an output power of about 1 Watt. Given an input port of 1 Watt into the CSRR sensor, about 0.5 Watt will be coupled via the MTL to the resonating cells, other small amounts are counted for radiation, dielectric, and conductive losses. The output power at the Rx port will always be percentage of the total input power of 1-Watt limit, therefore no excessive power would damage the receiving end.

Table 5.3: Radar operating specifications

Specification	Frequency Range	Centre Frequency	Max Bandwidth	ADC	ADC Sampling Rate	Output Power	Operating Voltage	Operating Current
Value	2.4 – 2.5 GHz	2.45 GHz	100 MHz	16 bits	20,000 Hz	1 Watt (sweeping) 0.125 Watt (CW mode)	5 Volts	0.5 Amp

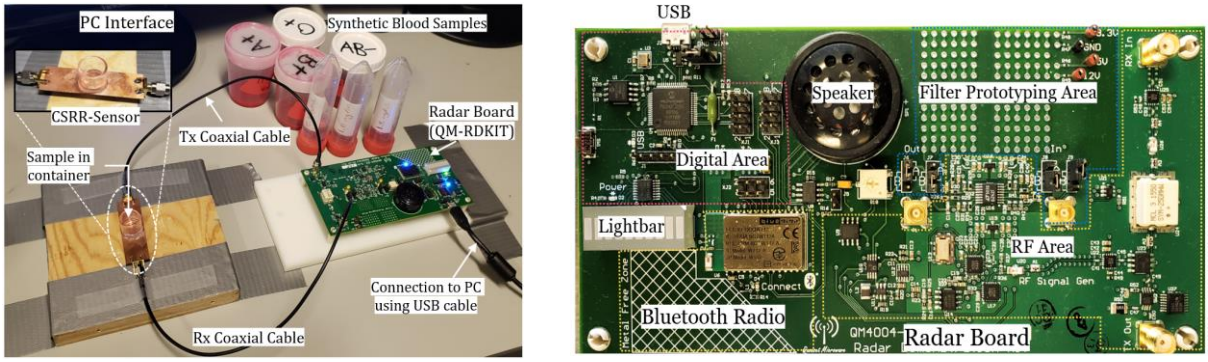

(a) (b)

Figure 5.9: (a) Glucose sensing experiments in the portable sensor setup, (b) Major sections inside the radar board: digital, Bluetooth radio, RF, filter prototyping, and lightbar for audiovisual feedback.

5.3.1 In-Vitro Experiments

A micropipette was used to measure a precise volume of V = 600 µL from each blood sample 70, 90, and 110 mg/dL and transfer it into the cylindrical container on top of the sensor. Once the glucose sample is fully loaded, the RF power button is triggered from the PC interface to transmit a radar signal of one-way single-sweep mode into the CSRR sensor. For repeatability verifications, each measurement trial for a glucose sample was repeated three times with a repeatability error of about ±0.02 Volts. The corresponding raw data was collected accordingly and sent to the host PC over a USB connection. The data could also be sent wirelessly from the radar module via a Bluetooth connection. The average of M = 3 repeatable voltage signals $A_C(n) = \frac{1}{M}\sum_{i=1}^{M} x_C^i(n)$ for each glucose sample C is plotted in Fig. 5.10(a). The average signals $A_C(n)$, C = 70, 90, and 110 mg/dL, were further processed to reveal the energy density corresponding to each glucose sample. Particularly, the finite energy for each average

signal $A_C(n)$ of a tested glucose sample was evaluated using $\varepsilon_s = \sum_{n=1}^{N} |A_C(n)|^2$, where N = 600 is the total number of time samples in each average signal. The dielectric contrast of the tested glucose samples was distinctly captured by the sensor and demonstrated in the varying energy density 1604, 1382, and 1153 Volts^2 for the 70, 90, and 110 mg/dL, respectively, as depicted in Fig. 5.10(b). The radar measured data was also processed using the PCA classification algorithm that clusters the corresponding glucose samples based on their extracted principal components as depicted in Fig. 5.10(c).

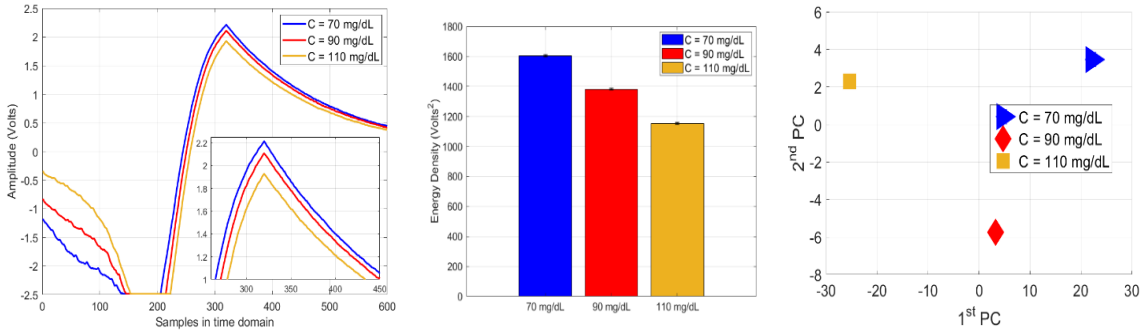

(a) (b) (c)

Figure 5.10: Glucose level detection using the radar setup (a) Raw data for tested glucose samples as collected on the receiving channel, (b) Comparison of energy density, and (c) PCA processed results.

5.3.2 In-Vivo Experiments

In light of previous positive results, the integrated portable sensing system was further tested for a simple in-vivo experiment as a proof-of-concept for this technology when revised for intermittent or continuous BGLs monitoring. For this purpose, the CSRR compact sensor was attached to a fixture structure suitable for finger placement as shown in Fig. 5.11(a). The geometrical dimensions of the fixture are shown in Fig. 5.11(b). The body of the fixture was made of acrylic, also known as "Poly Methyl Methacrylate". The thicknesses of the material used to construct the overall body were 9 mm and 6 mm. The base of the fixture consists of 6 mm acrylic, which was cut using Epilog Fusion 40, a 75W carbon laser cutter. The design and the thickness of the base plate allows the device to be stable when in use. The upper part of the body consists of 9 mm acrylic, designed to provide stability to the user's fingertip when using the device (Fig. 5.11(c)). The thickness is particularly useful for allowing the users to precisely place their finger onto the sensor for accurate measurements. To precisely combine the upper part of the fixture with the lower part, there were a multitude of methods used. The first was the cut holes, that allow both parts to be screwed together. Another key aspect to aid the placement of the parts was engraving the base of the acrylic about 2 mm deep so that the sensor could be accurately placed in between the acrylic plates. Overall, the design and the material used were professionally chosen to allow for both portability and precision for preliminary tests on the sensor. The glass layer on top of the CSRR sensing region was used to avoid the possibility of short-circuiting the dielectric slits of the sensing cells when the fingertip is placed inside the fixture. The new prototype was integrated

with the radar board (QM-RDKIT) as captured in Fig. 5.12(a) for the entire system setup. The radar system was interconnected to a laptop where the radar operation was controlled through a GUI.

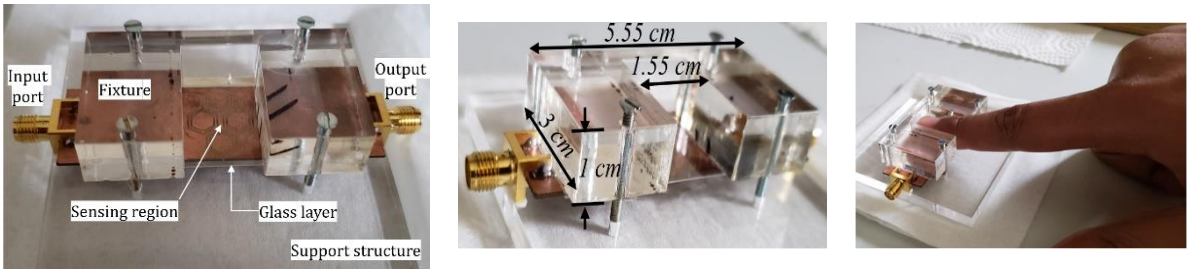

(a) (b) (c)

Figure 5.11: (a) Fabricated fixture for fingertip placement, (b) geometrical dimensions of the fixture, and (c) fingertip placement inside the fixture.

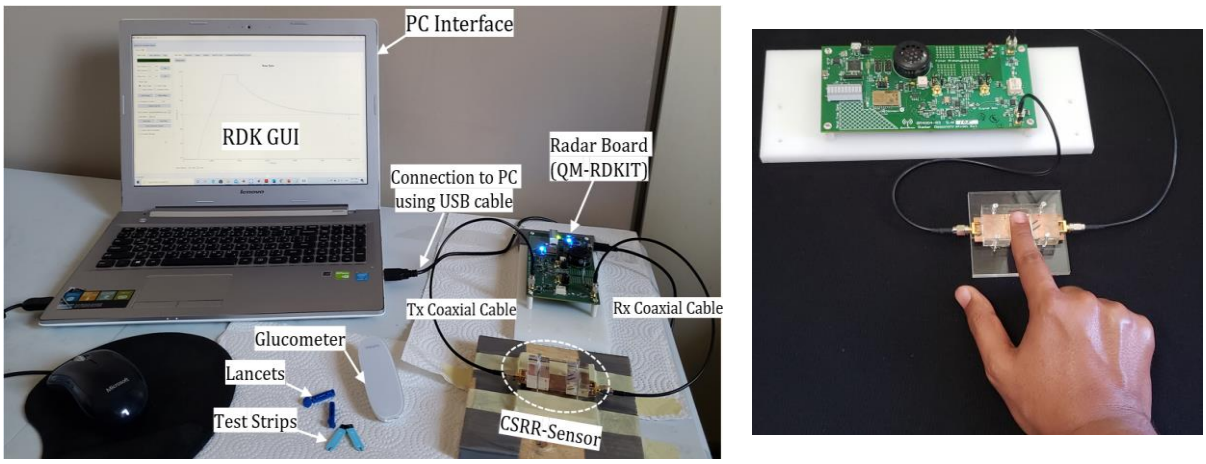

(a) (b)

Figure 5.12: (a) Complete setup for the in-vivo experiment, and (b) Testing the BGL from an individual's fingertip.

Preliminary tests were performed on a healthy male volunteer at age 29 before and after having the lunch meal while comparing the non-invasive measurements against a standard glucometer used as a reference for comparison. This testing recipe was guided by the fact that, in healthy non-diabetic people, the BGL should measure between 72 – 99 mg/dL before a meal and should be less than 140 mg/dL two hours after a meal. Therefore, a pre-prandial test was first performed for the tested subject by placing his fingertip suitably in the sensing region inside the fixture as shown in Fig. 5.12(b). The finger should be in contact with the sensing region (firmly attached to the fixture) to perturb the electromagnetic fields and induce noticeable changes in the sensor transmission response. The sensing process from the fingertip would take a short time of about one-minute max during which no changes in the temperature status of the subject finger is expected. The corresponding raw data in response of a one-way single-sweep transmission was collected from the radar receiving channel using the featured GUI. The same test was repeated three times for repeatability verification and the average of the three readings (with ±0.03 Volts error max) is plotted in Fig. 5.13(a) (black curve). Afterwards, the individual's BGL was measured using the commercial invasive glucometer to get the actual pre-prandial BGL of about 4.4 mmol/L (≈ 80 mg/dL). Similarly, a second test was performed for the tested

subject two hours after having a lunch meal for normal diet. The test on the non-invasive sensor was repeated for three consecutive times and the average voltage signal is plotted in Fig. 5.13(a) (blue curve). The post-prandial BGL was measured at 6.9 mmol/L (≈124 mg/dL) on the glucometer.

Following these measurements, the transmission results of the CSRR sensor were observed to be reliably consistent and aligned with the glucometer readings for the individual BGL variations before and after the meal. Particularly, the sensor transmitted signal exhibits a change in amplitude and a shift in time domain in response to the varying BGL of the tested subject. The black curve is corresponding to 80 mg/dL BGL while the blue one is representing the 124 mg/dL reading that leveled up two hours after the meal intake.

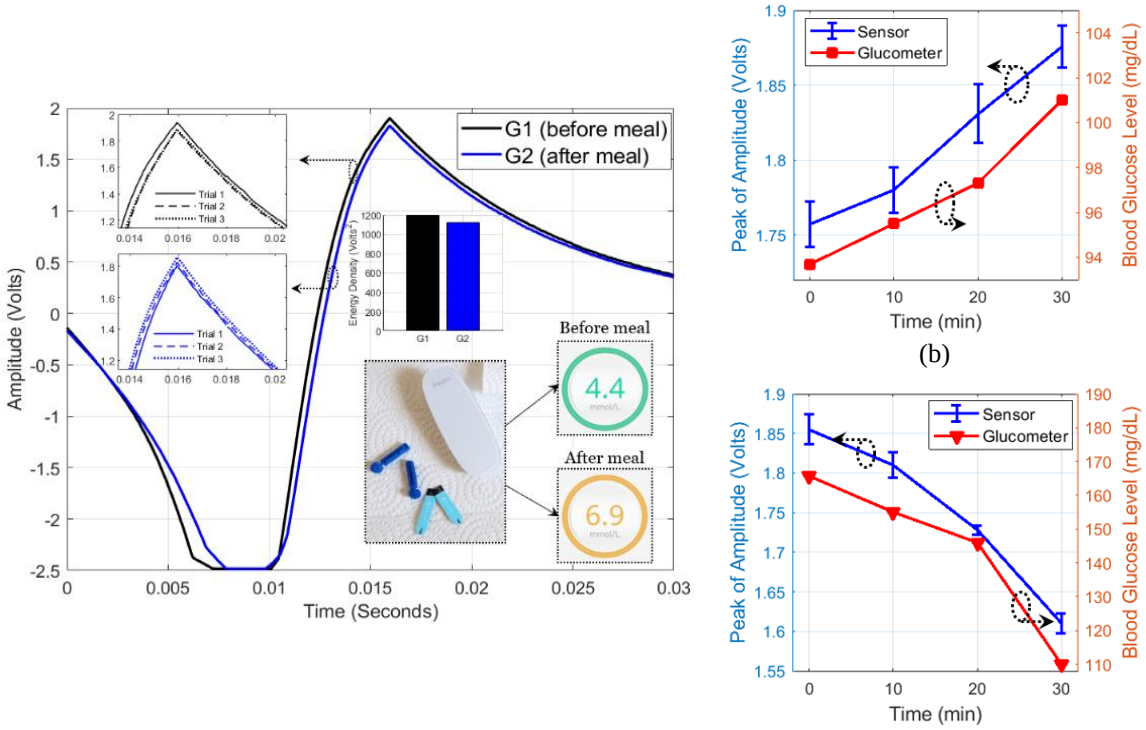

Figure 5.13: (a) Analysis of the BGL discrete readings from the CSRR sensor and glucometer. Continuous BGL monitoring over a course of 30 mins for (b) pre-prandial, and (c) post-prandial testing. The peak amplitude of the sensor response versus time (blue curve). The invasive measurements for BGL variations over time (red curve).

To better understand the BGL detection, the measured sensor data was further analyzed and processed using the DFT algorithm. The consequent energy density has shown to be varying for the two processed data corresponding to the two different BGL readings, 80 and 124 mg/dL, as depicted in the enclosed plot in Fig. 5.13(a), that shows an energy density of about 1207 and 1122 Volts^2, respectively. This would also imply that the sensitivity to glucose variation is slightly reduced when compared to that of the samples in glassy container. In fact, the coupled electric field in the sensing region has less interaction with the glucose molecules in this case given the lossy nature of the fingertip biological structure including the cornified skin layer. This is seen very clearly when a skin layer model was introduced in the numerical simulations showing the field intensity with decaying magnitudes halfway

through the glucose-contained layer. However, the sensitivity could be enhanced by modifying the design specifications through incorporating a flexible substrate of smaller loss tangent or utilizing a more powerful driving circuit (> 1Watt output power) instead of the RDKIT used in this preliminary prototype as a proof-of-concept.

To confirm the correlation of the sensor readings to that of the actual BGL in real-time setting, another experiment was performed while continuously monitor a volunteer's BGL over a course of 30 minutes before and after a meal. First, the pre-prandial test was conducted, and the corresponding sensor data were collected every 10 minutes resulting into four distinct readings. At each trial instant, the measurement was repeated for three times while placing the fingertip and the average of was plotted in Fig. 5.13(b) in terms of peak amplitudes (blue curve). The invasive readings were collected accordingly using the Glucometer and plotted in Fig. 5.13(b) (red curve). The sensor measurements follow the trend of the reference BGL that increases slightly in the range 93.7 – 101 mg/dL. In this narrow range of BGL variation, the sensor readings exhibited a repeatability error of about ±0.0198 Volts max.

The post-prandial test was performed similarly right after the meal (~10 mins) by collecting four distinct readings over a period of 30 minutes. The average of three repeatable sensing trials was plotted in Fig. 5.13(c) in terms of the peak amplitudes with a repeatability error of about ±0.019 Volts. The invasive measurements revealed a significant jump to 165.7 mg/dL 10 mins after the meal intake, then dropped slightly to 155, 146, then 110 mg/dL by the fourth check performed 40 mins after the meal. The sensor readings follow this descending pattern as depicted in Fig. 5.13(c). The sensor results for both pre- and post-prandial measurements shows no delay compared to the reference BGL, thus indicating the direct BGL monitoring from blood. The in-vivo measurements attained in this study have not investigated the effect of physical activities or the physiological differences between different subjects on the sensor responses; and that will be further explored in future studies on many patients with different diabetes conditions.

5.3.3 Discussion

As previously emphasized, the sensor scattering response is crucially dependent on the EM properties of the tissue part (i.e., glucose solution or fingertip) placed in the sensing region. These EM properties could change slightly if the tissue temperature changes, and further impact the sensor response. The ambient temperature also impacts the air permittivity in the near-field region of the sensor. Therefore, both the in-vitro and in-vivo experiments were conducted in an environment of controlled temperature 22±1^{o}C to guarantee that the resulting sensor response is exclusive to glucose changes in the respective glucose solution or fingertip. The sensor response might be affected by the temperature condition (of both the subject finger and the surrounding environment) if the measurements are taking relatively long time for processing, during which the sensor is exposed to temperature changes of the surrounding

environment. The sensing process from the fingertip is normally done in a short time of about one-minute maximum during which no significant changes are expected in the temperature status of the body part or the controlled environment.

Some studies have investigated the temperature effect for testing glucose in environments of relatively low and high temperature than normal room conditions [172] [170]. However, in our study we are interested in monitoring the varying-levels glucose samples in indoor environments with stable room temperature where most of these microwave setups are installed. It is also a reasonable premise for the sensor deployment in many biomedical applications where the temperature is controlled and monitored. When adapting the sensor as a wearable device for daily usage by diabetics a temperature sensor could be integrated with the microwave sensor to compensate the response deviations by reporting the real-time temperature. Furthermore, a machine learning model could be trained with the appropriate input features at different temperature conditions, then used to derive a temperature compensation function that accurately predicts the glucose level.

The performance of the sensor is stable and repeatable, and only slight variations were observed in the repeatability trials (±0.03 Volts) that are attributed to trivial finger motion inside the fixture. Once the finger is placed and stabilized onto the sensor with low exerted pressure, the measurement could be recorded within 30 – 60 seconds to ensure stable placement and temperature equilibrium. Placing the finger at a distance from the device will not affect the sensor response, and hence no signature for the BGL could be generated.

Applying higher pressure while placing the fingertip is expected to affect the sensor reading by decreasing the resonance magnitude and slightly shifting its frequency. This could be since the skin tissue is relatively thinner while compressed that would also affect the number of capillary blood vessels in the tissue appear nearer to the sensitive region of the sensor. The uncertainty in the BGL measurements due to the stability (i.e., movement, exerted pressure, etc.) of the finger over the sensing region could be further alleviated by integrating a tiny pressure sensor to continuously report the pressure exerted onto the sensing zone. This way the tested subject could be instructed to conveniently place his/her finger when a pressure threshold is crossed with a warning indicated on the user interface. Alternatively, the pressure readings could be used to build and train a machine learning model that helps correcting the BGL readings accordingly. Ultimately, an enclosed clip that fits into the finger (like the Oximeter) could be designed appropriately to help mitigating any placement or pressure errors.

The CSRR microwave sensor is compliant to the green form of technology that features the non-invasive measurements in non-destructive fashion using non-ionizing radiation of electromagnetic waves penetrating inside the skin tissue. The sensor has been used in two different setups; when integrated with the VNA, the coupled power into the sensor is about 10 dBm. However, when the radar board is used as a driving source in the portable prototype, the input power at the feeding port of the CSRR sensor is about 30 dBm (1 W), and the power coupled to the sensing region where the fingertip is placed is about 0.42 W. These values lie well below the IEEE safety radiation exposure limit for these

frequencies found in [232]. While the input power should be within specific range that guarantees the safe integration with the human body, it is also an important factor to enhance the sensitivity of the sensor while minimizing the radiation losses. Particularly, as previously discussed, the sensing principle of the sensor device is based on the electric field localization in the sensing region. The larger the energy concentration in the sensing region, less radiation loss would be incurred, and higher sensitivity is acquired for detecting various glucose levels.

5.4 Portable High-Band Glucose Sensor

Recent advances in the 60 GHz RF design, Complementary Metal-Oxide Semiconductor (CMOS) and packaging have led to a plethora of antenna-on-chip and radar-on-chip systems. A portable high-band glucose sensor was developed by interconnecting the mm-wave WGM sensor with a radar board operating in 60 – 64 GHz. Particularly, the TI radar board (IWR6843ISK) that supports the FMCW functionality in the mm-wave range was modified to couple the developed WGM sensor at the input and output ports as illustrated in Fig. 5.14. The IWR6843ISK board is generally used to evaluate the IWR6843 radar chip, enable access to point-cloud data and power over USB interface.

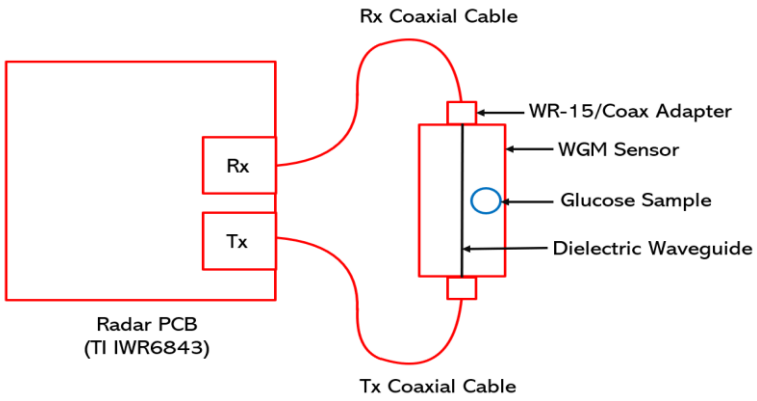

Figure 5.14: General illustration of the portable high-band glucose sensor prototype that interconnects IWR6843ISK and the WGM sensor.

The commercially available evaluation board IWR6843ISK that incorporates the IWR6843 radar chip of 3-transmit (Tx) and 4-receive (Rx) antennas with 120° azimuth field of view (FoV) and 30° elevation FoV (shown in Fig. 5.15) was modified to remove the 3×4 array of patch antennas while supporting only one transmitting channel and one receiving channel to be coupled with the input and output ports of the WGM sensor, respectively, via end launch connectors and coaxial cables.

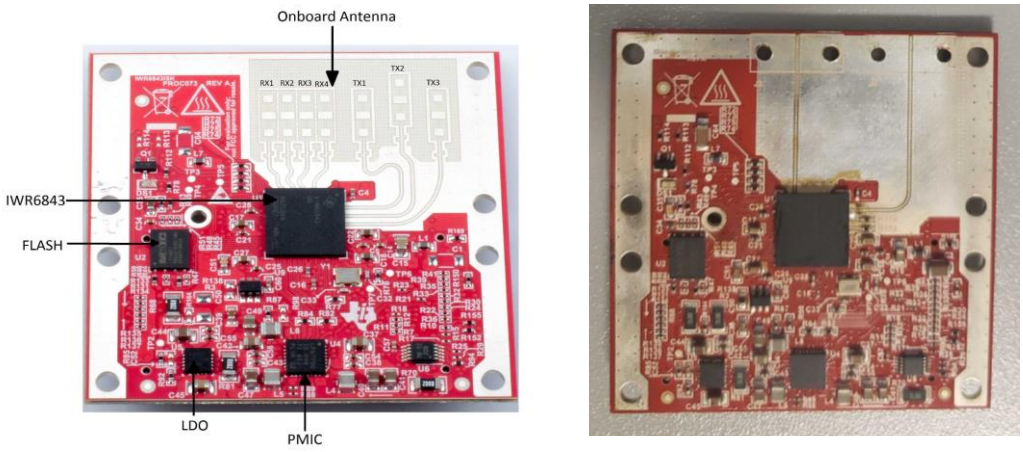

Figure 5.15: Original radar board IWR6843 provided by Texas Instruments (left) and modified 1-Tx and 1-Rx radar board (right).

Five copies of the radar board were assembled and fabricated by "AngusTech" manufacturing company (based in China). The fabricated boards were tested accordingly to verify their functionality when connected to the full system that involves the mmWaveICBoost (enabling software development and trace capabilities) and DCA1000 EVM (captures ADC raw data and transfer over the Universal Asynchronous Receiver Transmitter (UART) interface to a PC). Fig. 5.16 shows the modified IWR6843ISK radar board (small red board) connected on top of the mmWaveICBoost system (wide red board) and the DCA1000 EVM (green board in the back). The consequent debugging tests performed on the mmWave Studio platform have shown a major deficiency in the functionality of the radar boards as detailed in Appendix III.

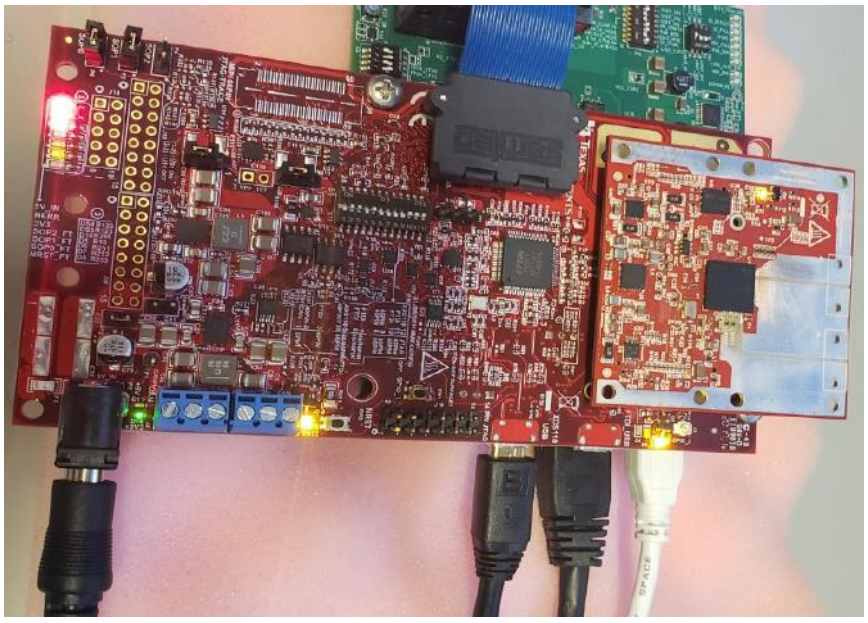

Figure 5.16: Full integration of the fabricated radar board.

Chapter 6. Conclusion and Future Works

6.1 Conclusions and Contributions

Towards the purpose of developing an affordable pain-free glucose monitoring gadget for diabetics, in this thesis, different RF/microwave sensing structures were developed for monitoring the glucose concentration levels of diabetes conditions at different frequency bands. The proposed sensors were designed, numerically analysed, and optimized for the desired performance using 3D full-wave electromagnetic computer simulations. Additionally, proof-of-concept prototypes were fabricated and practically tested for glucose levels detection using convenient setups in the microwave lab. Blood mimicking materials (e.g., aqueous glucose solutions and synthetic blood) were used in these feasibility experiments to approximate the behaviour of authentic bloods and to assure the repeatability of the collected measurements. The sensitivity of the proposed EM sensors was studied for detecting narrow range of glucose concentrations related to the practical diabetes conditions (e.g., normal, hyperglycemia, and hypoglycemia). The excellent sensitivity to glucose detection along with the advantages of being non-destructive, low-cost, and simply fabricated in electrically small size, lay the foundation for realizing the next generation of portable/wearable wireless devices for non-invasively monitoring blood glucose levels in diabetics, including detection of hyperglycemia and hypoglycemia conditions. The sensors could also be used as a warning tool to diabetic patients when attempting to consume energy drinks and fruit juices which have inherently high glucose concentrations. The developed EM sensors could also be used in other vital applications to identify the loaded liquid and monitor the change in its physical quantity and quality.

With appropriate AI-powered signal processing and a one-time personalized invasive calibration, the proposed devices promote the potentiality of personalized, fast, accurate, and non-invasive monitoring of the blood glucose level for diabetes control and prevention. Additionally, the sensors miniature scale offers a great advantage for realizing a wearable technology (e.g., smart watch, ring, earring) for continuous blood glucose monitoring similar to those of other vital signs (e.g., blood pressure, breathing and heart rates). Such a microwave wearable system, that to our knowledge has not yet existed, will allow real-time glucose-level monitoring, thereby leading to better management of diabetes and earlier warning of adverse health events such as strokes, diabetic coma, and heart attacks. The system is also beneficial for critical care situations where the patient's data can be analyzed remotely in real-time on the cloud, and thus provide the physicians greater insights to aid in clinical assessments and instant diagnosis that are more accurate. Results of this study, as summarized next, could be considered as a paradigm shift in microwave sensors for personalized biomedical-specific applications like diabetes monitoring and pave the way towards their commercialization.

In Chapter 2, the dielectric properties of binary glucose-water samples of small concentrations like blood sugar levels of diabetics were explored through measurements using a commercial coaxial-probe kit in the broad band 200 MHz – 67 GHz. The mm-wave range 50 – 67 GHz has shown to be promising for differentiating between the glucose-loaded samples as demonstrated by the noticeable trend among various concentrations, and the amount of change in dielectric constant and loss tangent due to varying glucose level. However, loss parameters of the glucose samples at this mm-wave band are relatively larger to those seen in lower frequency bands (e.g., 0.5 – 10 GHz). The effect of the sample volume on the accuracy of the DAK-TL measurements was also explored as part of this study using two petri-dishes of different dimensions and capacity. Different volumes of the tested glucose liquid samples were used to probe the DAK-TL accuracy in measurements, and hence conclude the lowest volume of liquid that can be used for stable accurate measurement at different frequency bands. Such a knowledge would certainly help on the decision to use such a measuring tool for testing authentic biological tissues (e.g., tears) that are very expensive in large volume concoction.

More in-depth dielectric measurements were performed using DAK-TL to address how ABO-Rh blood types and other medical conditions may impact the blood EM properties at different frequency bands. Both synthetic and authentic bloods of different types and medications were characterized across the microwave spectrum 500 MHz to 67 GHz using the DAK-TL coaxial probe. Measured results have indicated an appreciable contrast in the dielectric properties of various blood types across the spectrum especially at the mm-wave range 50 – 67 GHz where the differences are quite visible. A similar behaviour was observed for blood samples exposed to medications. Such variances in the blood dielectric properties would advocate the suggestion of calibrating any proposed microwave blood glucose monitors on individual basis to respect the physiological differences among the diabetic patients. The DAK spectroscopy results were further confirmed by the resonance measurements in CSRRs that show strong potential for development as alternative in-vitro non-destructive tools for identifying the ABO-Rh blood group.

In Chapter 3, the low frequency band 1 – 6 GHz (of centimeter wavelengths) was explored for glucose detection by developing planar sensing structures that utilize complementary spit ring resonators (CSRRs) of novel configurations and improved sensitivity performance. The proposed CSRRs exploit the inter-resonator coupling between adjacent cells to enlarge the sensing zone for more intensive interaction with the glucose tissue. The introduced metamaterial-inspired CSRRs could be simply fabricated with low cost and miniaturized size, thus offering a great potential for integration with other microwave components in embedded sensors and systems-on-chip to realize a low-power wearable/portable non-invasive device for glycemia level monitoring in real-time.

- First, a TP-CSRR structure was designed using three-coupled CSRRs each of a circular shape. The CSRR sensing elements are coupled to a planar microstrip-line in the same structure to allow for a compact structure. The three cascaded CSRR cells are mutually coupled to enlarge the sensing region

and intensify the induced fields interacting with the glucose samples. The sensor capability for glucose detection was practically demonstrated by testing the glucose samples inside a vein-resembling rectangular channel integrated on top of the CSRRs surface. The sensor has shown to be highly sensitive to glucose level changes with a sensitivity performance of about 6.2 dB/(mg/mL) in $|S_{21}|$.

- The multiple-cell CSRR sensor has numerically shown an appreciably higher sensitivity for detecting MUT changes in dielectric constant and loss tangent as compared to the single-cell CSRR. Additionally, the single-loop design of the sensor cells has shown more sensitivity to permittivity variations as compared to the double-loop configuration.
- Second, an advanced prototype of the TP-CSRR was realized by integrating a microfluidic PDMS channel onto the sensing area to maximize the sensitivity required for detecting small dielectric contrasts of the flowing glucose/liquids of lossy nature. The desired performance of the integrated sensor was practically validated for different liquid samples: distilled water, bacteriostatic water, saline (0.9% NaCl), and methanol. Distinctive resonant feature dataset was extracted for each liquid sample to allow for its unique identification. Synthetic bloods of targeted glucose concentrations were also tested inside the channel mimicking the blood flow into biological veins to demonstrate the sensor capability for monitoring the varying glucose levels with high sensitivity of about 33.4 MHz/(mg/ml) and 2.1 dB/(mg/ml) that outperforms other EM sensors in the literature.
- Third, a wearable format of the TP-CSRR was developed in the tag/reader configuration for non-invasive blood glucose monitoring. This design configuration offered a sensing distance between the communicating reader and tag suitable for adapting the device as wearable. The passive tag structure was efficiently designed using three-coupled CSRRs engraved in a groundless dielectric PCB. The CSRR sensing elements are electrically coupled to a remote antenna to allow for distant sensing from the tag when attached to the finger. Numerical analysis in HFSS has shown a good sensitivity for the integrated sensor for detecting the glucose levels of interest by tracking the reflected power of the antenna.
- Fourth, a microstrip CSRR structure was developed with a honey-cell fashion of four hexagonal sensing cells. Two preliminary prototypes were numerically modelled, fabricated, and experimented for monitoring the targeted glucose levels. The honey-cell CSRR sensor has shown a superior detection sensitivity for the glucose-level variations as demonstrated by the VNA measurements. The compact topology of the sensor has shown distinguishable frequency shifts of about 94 MHz/(mg/ml) resolution at several transmission resonances in response to the varying-level glucose samples.
- Fifth, to further enhance the detection sensitivity of the CSRR sensors, and mitigate any issues with repeatability and placement, a principal component analysis (PCA) unsupervised machine learning algorithm was proposed to extract important features inherent in the resonance scattering data and

map them into a low-dimensional space with a distinctive spatial separation that helps identifying the correlated glucose concentrations with higher resolution.

In Chapter 4, integrated WGM sensing structures were proposed as sensitive platforms for glucose level detection in higher mm-wave frequencies. Implementing the WGM technology in the sub-centimetre and mm-wave wavelengths would further enhance the sensitivity and distinctly observe the dependency between the varying concentration and permittivity at multiple WGM resonance frequencies. This multi-frequency operation is also helpful when adapting the sensors as portable gadget for glucose monitoring by allowing wider range of penetration depths (at different frequencies) suitable for different users' physiological needs (e.g., age and gender). A machine learning model could potentially be driven by the rich sensitive dataset produced at the multiple WGM resonances.

- The *first WGM structure* couples an HRS disc resonator to a dielectric image guide in the mm-wave range 50 – 70 GHz. It is shown theoretically, numerically, and experimentally that WGM travelling waves at millimeter wavelengths are quite sensitive to perturbations in the loss property of the integrated structure when the glucose level is changing. Two layouts of DIG, straight- and curved-DIG, were compared to strongly couple the input power into the resonator. The curved-DIG has shown a superiority performance as demonstrated by numerical simulations in the mm-wave band. The sensor was used to practically monitor small glucose concentrations in aquatic solutions with higher sensitivities observed at the WGH_{600} (~49 GHz) and WGH_{700} (~54 GHz). The concentration difference as small as 0.1 mg/ml can be easily resolved using a preliminary prototype that employs a straight-DIG as evidenced by the in-lab measurements. However, exciting the DIG by an appropriate waveguide was not the only challenge but also testing considerable volumes of glucose samples on top of the disc resonator of small diameter (~ 7 mm), and therefore the difficulty to demonstrate the repeatability.
- In the *second WGM structure*, a new methodology of tuning the coupling level in the WGM resonator has been introduced. The method is based on changing the conductivity of the underlying resonator using the interaction of the controlled near-infrared illumination with the high resistivity silicon. Accordingly, a novel non-invasive sensing method that exploits the transparency of the glucose samples to the NIR radiation has been implemented and experimentally verified.
- The *third WGM structure* was implemented using a ferromagnetic material to induce nonreciprocal WGM waves on the ring resonator. A permanent magnet was incorporated in the bottom layer of the microstrip substrate to inject the magnetic bias field necessary to trigger the anisotropy of the ferrite ring, and thereby achieve the nonreciprocal operation where more sensing data on the varying concentrations could be collected from the multiple high Q resonances of the excited WGM modes in both S_{21} and S_{12} frequency signals. By considering the inhomogeneity of the internal DC biasing fields, the dynamic EM behaviour of the FRR was modelled more accurately as compared to the practical measurements of a fabricated prototype. The detection functionality of the sensor to small

changes in dielectric properties of glucose-varying samples was demonstrated practically in three sets of experimental measurements with frequency and phase shifts (7 MHz and 17° per 1 mg/ml, respectively) of the measured S_{21} and S_{12} at the WGM_{600} mode with repeatability error of about ±0.2 MHz and ±0.5°. The sensor proves its leverage for monitoring the glucose levels inside a closed capillary without a direct contact with the sample, thus rendering the technique more feasible for continuous non-invasive glucose monitoring.

In Chapter 5, radar sensing and signal processing were both employed for non-invasive glucose level detection. First, using the DAK-TL findings, a low-cost, mm-wave, multi-channel radar was proposed as a sensing platform for monitoring the blood sugar levels related to patients with diabetes. The suitability of using mm-wave radars for glucose detection was practically validated by testing synthetic blood samples of varying glucose concentrations in clinical tubes placed in a 3D-printed fixture. The mm-wave radar has exhibited a sensitive detection capability with high sensitivity to the small disparities in blood glucose concentrations as demonstrated by the scattered raw data collected via the radar receiving channels. Signal processing of the radar raw data has shown that blood samples of higher glucose concentrations resulted into reflected signals of greater energy, which allows for the identification of various blood glucose concentrations via the correlation with the reflected mm-wave readings. Next, portable sensor prototypes operating in the low- and high-bands were developed by interconnecting the previously developed EM sensors (CSRR and WGM) with appropriate radar boards as driving sources instead of the bulky and expensive VNA instrument. Additionally, the preliminary in-vivo experiments performed on the low-band portable prototype have demonstrated the efficacy of tracking the glucose varying patterns from the fingertip when tested pre- and post-prandial.

6.2 Future Works

The works in this thesis are primary developing steps towards the ultimate goal of continuously monitoring blood glucose in diabetics using a wearable microwave sensing device. The reported results and scientific findings are essentially pivotal and pave the way for direct sensing of blood inside the human body using EM waves. The following are suggested as possible directions for future research work:

- **Performing blood glucose sensing at higher range of frequencies (e.g., THz spectrum)**
  The proposed EM sensing technologies were employed for blood glucose sensing in the microwave frequencies up to 70 GHz. Exploring and studying the THz spectrum for glucose sensing is needed to understand the EM behaviour of glucose molecules at much higher frequencies, and the possible limiting factors.

- **Design and implementation of more advanced, powerful, and practical CSRRs**

  In Chapter 3, different configurations of CSRRs were designed and realized. More advanced CSRRs can be developed in flexible substrate of low loss property and with further optimization on the geometry of the sensing cells that could possibly be excited off the microstrip structure. For instance, the four CSRR cells in the honey-cell design could be reconfigured as shown in Fig. 6.1 where each resonating cell is composed of three concentric slits of rhombus shapes nested within each other. The two vertical cells have their edges overlapped with the microstrip-line for stronger mutual coupling performance that boosts for higher glucose sensitivity. To alleviate the uncertainty of glucose measurements in the portable prototype, a fixture device was integrated appropriately with the CSRR sensor to allow for stable placement of the fingertip over the sensing region. This would enable acquiring more accurate and stable measurements from the fingertip with normal exerted pressure. For more cautious usage of the CSRRs for BGL monitoring from the subject's finger, a robust pressure sensor could be integrated in the device substrate to provide continuous feedback on the pressure applied onto the sensor. Such feedback is then considered in the AI processing algorithm to properly calibrate the system for more accurate glucose results or possibly by instructing the user to place the finger more conveniently as required. An enclosed clip could also be used to ensure the stability of the measurements.

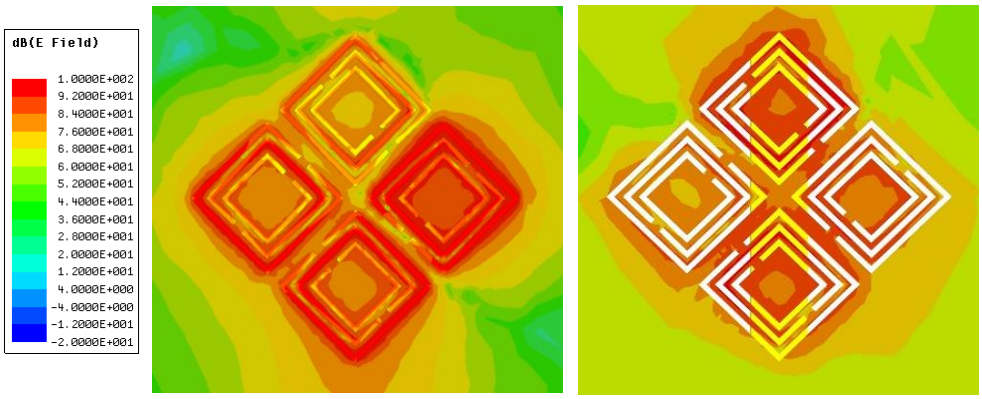

Figure 6.1: Improved honey-cell CSRR configuration for sensitive BGL monitoring

- **Design and implementation of an in-package glucose sensing device**

  A low-cost non-invasive fully integrated wearable/portable system is a dream for the diabetes community. Packaging and integration are major challenges in realization of a commercial micro/mm-wave systems. As mentioned in the introduction chapter, the miniature sizes of the developed sensing structures empower the compact integration with other microwave components in one chip. Most of the EM sensors developed in this thesis were tested using VNA setups that are less convenient for on-body glucose sensing. Replacing the bulky and expensive VNA measuring instrument in the measurement setups with small radar boards of low-cost and -power is among the main future research activities. In fact, as presented in

Chapter 5, the Radar Demonstration Kit (QM-RDKIT) was interconnected to drive the developed CSRR sensors at low band (2.4 – 2.5 GHz). We also aimed at integrating the mm-wave sensors with the Texas Instrument radar board TI IWR6843ISK in one compact portable device operating in the (60 – 64 GHz) frequency range, yet some technical defects were detected on the fabricated boards. Careful development of more compatible radar boards would be considered in future studies.

- **Advanced analysis for glucose data using machine learning**

  Recent advances in machine learning and artificial intelligence could be used to analyze the raw data of the RF/microwave measurements from the developed glucose sensors in order to identify trends in the scattered signals corresponding to varying glucose concentrations. For instance, as proposed in Chapter 3, the resulting scattering responses to glucose variations were projected into a low-dimensional space using the principal component analysis (PCA) algorithm to epitomize the data variances near resonance in fewer variables with a higher spatial resolution.

  Extracted features from the sensing parameters could be used to train and optimize a robust classification model (e.g., random forest, support vector machine, complex value neural network, etc.) capable of correlating testing samples to their accurate blood glucose concentrations. This would also help reducing the ambient noise and improve the robustness of the integrated sensing system. MI/AI powerful tools could effectively address issues of identifying glucose samples outside of the training data sets, along with scalability among various people with different physiological features and skin variations that might impact the sensor data. Additionally, among the many challenges to address is the fact that scattered electromagnetic energy through skin and blood stream is shown to change with naturally varying physiological parameters such as moisture levels, sweat, and temperature. Such variations could significantly affect the accuracy of the glucose detection system, and therefore attempts to minimize their impacts using advanced ML/AI tools are also part of the future research campaign. For instance, a temperature-adapted feature could be enabled in the microwave sensors by training a classification model with the raw data at the possible range of temperatures to accurately predict the glucose concentration when the system and/or the subject is operating at a given temperature condition.

  The raw data is now sent to computers for analysis and processing by DSP and ML algorithms, yet the ultimate aim is to realize a working prototype of the glucose sensor as a self-contained technology for continuous monitoring like the topology of smart watches or finger pulse oximeters that monitor heart and breathing rates.

6.3 Research Publications

The contributions and results presented in this thesis were published in the following conference and journal papers:

6.3.1 Conference Papers

1. **A. E. Omer**, G. Shaker, S. Safavi-Naeini and R. M. Shubair, "Low-Cost MoM-Solution of Blood Tube Scattering," *2019 IEEE International Symposium on Antennas and Propagation and USNC-URSI Radio Science Meeting (APS/URSI)*, Atlanta, GA, USA, Jul. 2019, pp. 1859-1860

2. **A. E. Omer**, G. Shaker, S. Safavi-Naeini and R. M. Shubair, "EM Measurements of Glucose-Aqueous Solutions," *2019 IEEE International Symposium on Antennas and Propagation and USNC-URSI Radio Science Meeting (APS/URSI)*, Atlanta, GA, USA, Jul. 2019, pp. 103-104

3. **A. E. Omer**, G. Shaker, S. Safavi-Naeini, H. Kokabi, G. Alquié and F. Deshours, "Compact Honey-Cell CSRR-based Microwave Biosensor for Monitoring Glucose Levels," *2020 14th European Conference on Antennas and Propagation (EuCAP)*, Copenhagen, Denmark, Mar. 2020, pp. 1-5

4. **A. E. Omer**, G. Shaker, S. Safavi-Naeini, H. Kokabi, G. Alquié and F. Deshours, "Multiple-Pole CSRR-based Microwave Sensor for Glucose Levels Detection," *2020 14th European Conference on Antennas and Propagation (EuCAP)*, Copenhagen, Denmark, Mar. 2020, pp. 1-5

5. **A. E. Omer**, G. Shaker, and S. Safavi-Naeini, "Wearable CSRR-based Sensor for Monitoring Glycemic Levels for Diabetics," *20th IEEE International Conference on BioInformatics And BioEngineering (BIBE)*, Cincinnati, OH, USA, Oct. 2020, pp. 922-928

6. **A. E. Omer**, G. Shaker, R. Hughson, and S. Safavi-Naeini, "Microwave-based Nondestructive Sensing Approach for Blood Types Identification," *20th IEEE International Conference on BioInformatics And BioEngineering (BIBE)*, Cincinnati, OH, USA, Oct. 2020, pp. 504-508

7. **A. E. Omer**, S. Safavi-Naeini, R.M. Shubair, H. Kohabi, and G. Shaker "Microwave Sensor of Integrated CSRR Cells for Typing Detection in Synthetic Blood," *2020 IEEE International Symposium on Antennas and Propagation and USNC-URSI Radio Science Meeting (APS/URSI)*, Montreal, QC, Canada, Jul. 2020, pp. 1221-1222

8. **A. E. Omer**, A. Hojjati-Firoozabad, S. Gigoyan, G. Shaker, and S. Safavi-Naeini "Compact Ferromagnetic WGM Resonator for Sensing Applications at Sub-Centimeter Wavelengths," *2021 IEEE International Symposium on Antennas and Propagation and USNC-URSI Radio Science Meeting (APS/URSI)*, Marina Bay Sands, Singapore, Dec. 2021, pp. 631-632.

9. **A. E. Omer** and G. Shaker, "Non-Invasive Blood Glucose Monitoring Using Electromagnetic Sensors – A Tribute to the memory of Professor Safieddin Safavi-Naeini," *2022 IEEE*

International Symposium on Antennas and Propagation and USNC-URSI Radio Science Meeting (APS/URSI), Denver, Colorado, USA, Jul. 2022

6.3.2 Journal Papers

1. **A. E. Omer**, G. Shaker, S. Safavi-Naeini, K. Murray and R. Hughson, "Glucose Levels Detection using mm-Wave Radar", in *IEEE Sensors Letters*, vol. 2, no. 3, pp. 1-4, Sep. 2018.

2. **A. E. Omer**, S. Safavi-Naeini, R. Hughson, and G. Shaker, "Blood Glucose Level Monitoring Using an FMCW Millimeter-Wave Radar Sensor," in *MDPI Remote Sensing Journal*, vol. 12, no. 3, pp. 385-409, Jan. 2020

3. **A. E. Omer**, S. Gigoyan, G. Shaker and S. Safavi-Naeini, "WGM-Based Sensing of Characterized Glucose- Aqueous Solutions at mm-Waves," in *IEEE Access*, vol. 8, pp. 38809-38825, Feb. 2020

4. A. Raeesi, **A. E. Omer**, A. Hojjati-Firoozabadi, A. Taeb, S. Gigoyan and S. Safavi-Naeini, "Near Infrared-Controlled Whispering Gallery Mode Resonator Sensor," in *IEEE Sensors Letters*, vol. 4, no. 7, pp. 1-4, Jul. 2020

5. **A. E. Omer**, G. Shaker and S. Safavi-Naeini, "Portable Radar-Driven Microwave Sensor for Intermittent Glucose Levels Monitoring," in *IEEE Sensors Letters*, vol. 4, no. 5, pp. 1-4, May. 2020

6. **A. E. Omer**, G. Shaker, S. Safavi-Naeini, H. Kokabi, G. Alquié, F. Deshours and R. M. Shubair, "Low-Cost Portable Microwave Sensor for Non-Invasive Monitoring of Blood Glucose Level: Novel Design Utilizing a Four-Cell CSRR Hexagonal Configuration," in *Nature Scientific Reports*, vol. 10, Sep. 2020

7. **A. E. Omer**, G. Shaker, S. Safavi-Naeini, G. Alquié, F. Deshours, H. Kokabi, and R. M. Shubair, "Non-Invasive Real-Time Monitoring of Glucose Level Using Novel Microwave Biosensor Based on Triple-Pole CSRR," in *IEEE Transactions on Biomedical Circuits and Systems*, vol. 14, no. 6, pp. 1407 – 1420, Dec. 2020

8. **A. E. Omer**, G. Shaker, S. Safavi-Naeini, K. Ngo, R. M. Shubair, G. Alquié, F. Deshours, and H. Kokabi "Multiple-Cell Microfluidic Dielectric Resonator for Liquid Sensing Applications," in *IEEE Sensors Journal*, vol. 21, no. 5, pp. 6094-6104, Mar. 2021.

9. **A. E. Omer**, S. Gigoyan, G. Shaker, and S. Safavi-Naeini, "Whispering-Gallery-Mode Microwave Sensing Platform for Oil Quality Control Applications," in *IEEE Internet of Things Journal*, vol. 9, no. 6, pp. 4065 – 4075, Aug. 2021.

10. **A. E. Omer**, G. Shaker, and S. Safavi-Naeini, "PCA-Assisted Blood Glucose Monitoring Using Metamaterial-Inspired Sensor," in *IEEE Sensors Letters*, vol. 5, no. 9, pp. 1-4, Sep. 2021

11. **A. E. Omer**, A. Hojjati-Firoozabad, S. Gigoyan, S. Safavi-Naeini, and G. Shaker, "Non-Reciprocal Whispering-Gallery-Mode Resonator for Sensitive Blood Glucose Monitoring," in *IEEE Transactions on Instrumentation & Measurement*, vol. 71, pp. 1-12, Feb. 2022.

References

[1] W. Gao *et al*., "Fully integrated wearable sensor arrays for multiplexed in situ perspiration analysis," *Nature*, vol. 529, no. 7587, pp. 509 – 514, Jan. 2016

[2] D. Whiting *et al*., "Diabetes Atlas: Global estimates of the prevalence of diabetes for 2011 and 2030," *Diabetes Res. Clin. Pract*. vol. 94, no. 3, pp. 311 – 321, Dec. 2011

[3] WHO, "WHO_World Health Day 2016_WHO calls for global action to halt rise in and improve care for people with diabetes.pdf," World Health Org., Geneva, Switzerland, *Tech. Rep.*, 2016.

[4] American Diabetes Association, "Diagnosis and classification of diabetes mellitus," *Diabetes Care*, vol. 37, pp. S81 – S90, Jan. 2014.

[5] N. Bansal, "Prediabetes diagnosis and treatment: A review," *World Journal of Diabetes*, vol. 6, no. 2, pp. 296 – 303, Mar. 2015

[6] R. Holt, C. Cockram, A. Flyvbjerg and B. Goldstein, Textbook of Diabetes, New York, NY: John Wiley & Sons, 2011.

[7] Diabetes Canada, "Managing your blood sugar," [Online]. Available at https://www.diabetes.ca/managing-my-diabetes/tools---resources/managing-your-blood-sugar. [Accessed 30 June 2020].

[8] American Diabetes Association, "Glycemic targets: standards of medical care in diabetes–2019," *Diabetes Care*, vol. 42, supplement. 1, S61 – S70, Jan. 2019

[9] D. Bruen, C. Delaney, L. Florea, D. Diamond, "Glucose Sensing for Diabetes Monitoring: Recent Developments," *Sensors*, vol. 17, no. 8, pp. 1866 – 1886, Aug. 2017

[10] L. C. Clark Jr, C. Lyons, "Electrode systems for continuous monitoring in cardiovascular surgery," *Ann. N. Y. Acad. Sci*., vol. 102, no. 1, pp. 29 – 45, 1962.

[11] E-H. Yoo, S-Y. Lee, "Glucose Biosensors: An Overview of Use in Clinical Practice," *Sensors*, vol. 10, no. 5, pp. 4558 – 4576, May. 2010

[12] L. C. Clark Jr, "Monitor and control of blood and tissue oxygen tensions," *Trans. Am. Soc. Artif. Intern. Organs*, vol. 2, no. 1, pp. 41 – 48, Apr. 1956

[13] P. Hilditch, M. Green, "Disposable electrochemical biosensors," *Analyst*, vol. 116, no. 12, pp. 1217 – 1220, 1991.

[14] A. Philis-Tsimikas, A. Chang, L. Miller, "Precision, accuracy and user acceptance of the OneTouch SelectSimple blood glucose monitoring system," *J. Diabetes Sci Technol.*, vol. 5, no. 6, pp. 1602 – 1609, Nov. 2011

[15] ISO 15197:2013, "In Vitro Diagnostic Test Systems—Requirements for Blood-Glucose Monitoring Systems for Self-Testing in Managing Diabetes Mellitus,"

[Online]. Available: https://www.iso.org/standard/54976.html. [Accessed 23 November 2019]

[16] M.G. Burt, G.W. Roberts, N.R. Aguilar-Loza, S.N. Stranks, "Brief report: comparison of continuous glucose monitoring and finger-prick blood glucose levels in hospitalized patients administered basal-bolus insulin," *Diabetes Technology & Therapeutics*, vol. 15, no. 3, pp. 241 – 245, Mar. 2013.

[17] W.V. Gonzales, A.T. Mobashsher, A. Abbosh, "The Progress of Glucose Monitoring—A Review of Invasive to Minimally and Non-Invasive Techniques, Devices and Sensors," *Sensors*, vol. 19, no. 4, pp. 800 – 845, Feb. 2019

[18] A. E. Omer, G. Shaker, S. Safavi-Naeini, "Wearable CSRR-based Sensor for Monitoring Glycemic Levels for Diabetics," IEEE 20th International Conference on Bioinformatics and Bioengineering (BIBE), Oct. 2020, pp. 922 – 928.

[19] T. Lin, A. Gal, Y. Mayzel, K. Horman, K. Bahartan, "Non-invasive glucose monitoring: a review of challenges and recent advances," *Current Trends in Biomedical Engineering and Biosciences*, vol. 6, no. 5, pp. 1 – 8, Jul. 2017.

[20] N. Spegazzini *et al*., "Spectroscopic approach for dynamic bioanalyte tracking with minimal concentration information," *Scientific Reports*, vol. 4, Article no. 7013, Nov. 2014

[21] M. Kuroda *et al*., "Effects of daily glucose fluctuations on the healing response to everolimus-eluting stent implantation as assessed using continuous glucose monitoring and optical coherence tomography," *Cardiovascular Diabetology*, vol. 15, no. 1, Article no. 79, May. 2016.

[22] J.Y. Sim, C-G. Ahn, E-J. Jeong, B.K. Kim, "In vivo microscopic photoacoustic spectroscopy for non-invasive glucose monitoring invulnerable to skin secretion products," *Scientific Reports*, vol. 8, no. 1, Article no. 1059, Jan. 2018.

[23] M. Goodarzi, W. Saeys, "Selection of the most informative near infrared spectroscopy wavebands for continuous glucose monitoring in human serum," *Talanta*, vol. 146, pp. 155 – 165, Jan. 2016

[24] J. Yadav, A. Rani, V. Singh, B.M. Murari, "Prospects and limitations of non-invasive blood glucose monitoring using near-infrared spectroscopy," *Biomedical Signal Processing and Control*, vol. 18, pp. 214 – 227, Apr. 2015

[25] S.K. Vashist, "Non-invasive glucose monitoring technology in diabetes management: A review," *Analytica Chimica Acta*, vol. 750, pp. 16 – 27, Oct. 2012

[26] J.R. Sempionatto *et al*., "Eyeglasses-based tear biosensing system: Non-invasive detection of alcohol, vitamins and glucose," *Biosensors and Bioelectronics*, vol. 137, pp. 161 – 170, Jul. 2019.

[27] L. Chen *et al*., "Cellular Wireless Energy Harvesting for Smart Contact Lens Applications [Education Corner]," in *IEEE Antennas and Propagation Magazine*, vol. 60, no. 5, pp. 108 – 124, Oct. 2018

[28] J. Zhang *et al*., "Noninvasive Diagnostic Devices for Diabetes through Measuring Tear Glucose," *Journal of Diabetes Science and Technology*, vol. 5, no. 1, pp. 166 – 172, Jan. 2011

[29] L.F. De Castro *et al*., "Salivary diagnostics on paper microfluidic devices and their use as wearable sensors for glucose monitoring," *Analytical and Bioanalytical Chemistry*, vol. 411, no. 19, pp. 4919 – 4928, Apr. 2019.

[30] E.V. Karpova *et al*., "Noninvasive diabetes monitoring through continuous analysis of sweat using flow-through glucose biosensor," *Analytical Chemistry*, vol. 91, no. 6, pp. 3778 – 3783, Feb. 2019

[31] M. Bariya *et al*., "Wearable sweat sensors," *Nature Electronics*, vol. 1, no. 3, pp. 160 – 171, Mar. 2018.

[32] A.A. Karyakin *et al*., "Non-invasive monitoring of diabetes through analysis of the exhaled breath condensate (aerosol)," *Electrochemistry Communications*, vol. 83, pp. 81 – 84, Oct. 2017.

[33] L. Lipani *et al*., "Non-invasive, transdermal, path-selective and specific glucose monitoring via a graphene-based platform," Nature Nanotechnology, vol. 13, no. 6, pp. 504 – 511, Apr. 2018

[34] J. Kim *et al*., "Wearable non-invasive epidermal glucose sensors: A review," *Talanta*, vol. 177, pp. 163 – 170, Jan. 2018.

[35] A. Orna *et al.*, "Continuous Noninvasive Glucose Monitoring Technology Based on "Occlusion Spectroscopy"," *Journal of Diabetes Science and Technology*, vol. 1, no. 4, pp. 463 – 469, Jul. 2007.

[36] Noviosense, "Noviosense," [Online]. Available: http://noviosense.com/. [Accessed 30 January 2019].

[37] Novartis, "Novartis," [Online]. Available: http://www.novartis.com/newsroom/mediareleases/en/2014/1824836.shtml. [Accessed 30 January 2019]

[38] QuickLLC, "QuickLLC," [Online]. Available: http://www.iquickitsalivaanalyzer.com/. [Accessed 30 January 2019].

[39] C. Medical, "Cnoga Medical," [Online]. Available: http://cnogacare.co/portfolioitem/combo-glucometer/. [Accessed 30 January 2019].

[40] Y. Segman, "Device and Method for Noninvasive Glucose Assessment," *Journal of Diabetes Science and Technology*, vol. 12, no. 6, pp. 1159 – 1168, Mar. 2018

[41] Glucosense Diagnostic Ltd, “Glucosense,” [Online]. Available: http://www.glucosense.net/. [Accessed 30 January 2019].

[42] Grove Instruments, “Grove Instruments,” [Online]. Available: http://www.groveinstruments.com/. [Accessed 30 January 2019].

[43] World Global Network, “Helo Extense,” [Online]. Available: https://website.worldgn.com/heloextense/. [Accessed 15 June 2020]

[44] I. Harman-Boehm *et al*., “Noninvasive glucose monitoring: Increasing accuracy by combination of multi-technology and multi-sensors,” *Journal of Diabetes Science and Technology*, vol. 4, no. 3, pp. 583 – 595, May. 2010

[45] I. Gouzouasis *et al*., “Detection of varying glucose concentrations in water solutions using a prototype biomedical device for millimeter-wave non-invasive glucose sensing,” in 10th European Conference on Antennas and Propagation (EuCAP), Davos, Switzerland, Apr. 2016, pp. 1 – 4

[46] Glucowise, “Glucowise,” [Online]. Available: http://www.gluco-wise.com/. [Accessed 30 January 2019]

[47] Nemaura Medical, “Nemaura Announces Positive Results for Its SugarBEAT® European Clinical Program,” [Online]. Available: http://nemauramedical.com/nemaura-announces-positive-results-sugarbeat-europeanclinical-program/. [Accessed 15 June 2020].

[48] E. Hadar *et al*., “Noninvasive, continuous, real-time glucose measurements compared to reference laboratory venous plasma glucose values,” *Journal of Maternal-Fetal & Neonatal Medicine*, vol. 32, no. 20, pp. 3393 – 3400, Apr. 2018

[49] T. Karacolak *et al*., “Cole-Cole model for glucose-dependent dielectric properties of blood plasma for continuous glucose monitoring,” *Microwave and Optical Technology Letters*, vol. 55, no.5, pp. 1160 – 1164, May. 2013

[50] R. Dobson *et al*., “Blood glucose monitoring using microwave cavity perturbation,” *Electronics Letters*, vol. 48, no. 15, pp. 905 – 906, 2012.

[51] S. Wiwatwithaya *et al*., “Real-time monitoring glucose by used microwave antenna apply to biosensor,” The 4th 2011 Biomedical Engineering International Conference, Chiang Mai, Mar. 2012, pp. 135 – 137.

[52] M. Hofmann *et al*., “A novel approach to non-invasive blood glucose measurement based on RF transmission,” MeMeA 2011 IEEE International Symposium on Medical Measurements and Applications, Bari, 2011, pp. 39 – 42.

[53] M. Hofmann *et al*., “Non-invasive glucose monitoring using open electromagnetic waveguides,” in 42nd European Microwave Conference, Amsterdam, Nov. 2012, pp. 546 – 549.

[54] A. E. Omer, R. Hughson, S. Safavi-Naeini, G. Shaker, “Blood Glucose Level Monitoring Using an FMCW Millimeter-Wave Radar Sensor,” *Remote Sensing Journal*, vol. 12, no. 3, pp. 385 – 409, Jan. 2020

[55] S. Saha *et al*., “A glucose sensing system based on transmission measurements at millimetre waves using micro strip patch antennas,” *Scientific Reports*, vol. 7, Article no. 6855, Jul. 2017

[56] M. A. H. Ansari, A. K. Jha, M. J. Akhtar, “Design and Application of the CSRR-Based Planar Sensor for Noninvasive Measurement of Complex Permittivity,” in *IEEE Sensors Journal*, vol. 15, no. 12, pp. 7181 – 7189, Dec. 2015

[57] A. Raj *et al*., “Metamaterial-inspired microwave sensor for measurement of complex permittivity of materials,” *Microwave and Optical Technology Letters*, vol. 58, no. 11, pp. 2577 – 2581, Nov. 2016

[58] A. Ebrahimi, J. Scott, K. Ghorbani, “Differential Sensors Using Microstrip Lines Loaded With Two Split-Ring Resonators,” in *IEEE Sensors Journal*, vol. 18, no. 14, pp. 5786 – 5793, Jul. 2018.

[59] A. Ebrahimi, J. Scott, K. Ghorbani, “Transmission Lines Terminated With LC Resonators for Differential Permittivity Sensing,” in *IEEE Microwave and Wireless Components Letters*, vol. 28, no. 12, pp. 1149 – 1151, Dec. 2018

[60] H. Choi *et al*., “Design and In Vitro Interference Test of Microwave Noninvasive Blood Glucose Monitoring Sensor,” in *IEEE Transactions on Microwave Theory and Techniques*, vol.63, no.10, pp. 3016 – 3025, Oct. 2015.

[61] M. Islam *et al*., “Left-handed metamaterial-inspired unit cell for s-band glucose sensing application,” *Sensors*, vol. 19, no. 1, pp. 169 – 181, Jan. 2019.

[62] A. Kandwal *et al*., “Highly Sensitive Closed Loop Enclosed Split Ring Biosensor With High Field Confinement for Aqueous and Blood-Glucose Measurements,” *Scientific Reports*, vol. 10, no. 4081, Mar. 2020

[63] C.G. Juan *et al*., “Concentration Measurement of Microliter-Volume Water–Glucose Solutions Using Q Factor of Microwave Sensors,” in *IEEE Transactions on Instrumentation and Measurement*, vol. 68, no. 7, pp. 2621 – 2634, Jul. 2019

[64] T. Yilmaz *et al*., “Broadband tissue mimicking phantoms and a patch resonator for evaluating noninvasive monitoring of blood glucose levels,” in *IEEE Transactions on Antennas and Propagation*, vol. 62, no. 6, p. 3064 – 3075, Jun. 2014

[65] S. Gabriel *et al*., “The dielectric properties of biological tissues: III. Parametric models for the dielectric spectrum of tissues,” *Phys. Med. Biol*., vol. 41, no. 11, pp. 2271 – 2293, 1996

[66] C. Lee, C. Yang, “Complementary Split-Ring Resonators for Measuring Dielectric Constants and Loss Tangents,” *in IEEE Microwave and Wireless Components Letters*, vol. 24, no. 8, pp. 563 – 565, Aug. 2014.

[67] A. E. Omer *et al*., "Whispering-Gallery-Mode Microwave Sensing Platform for Oil Quality Control Applications," in *IEEE Internet of Things Journal* (early-access), Aug. 2021.

[68] P. Mehrotra, B. Chatterjee, & S. Sen, "EM-Wave Biosensors: A Review of RF, Microwave, mm-Wave and Optical Sensing," *Sensors*, vol. 19, no. 5, pp. 1013, Feb. 2019

[69] M. Hofmann *et al*., "Microwave-Based Noninvasive Concentration Measurements for Biomedical Applications," in *IEEE Transactions on Microwave Theory and Techniques*, vol. 61, no. 5, pp. 2195 – 2204, May. 2013.

[70] J. Baker-Jarvis, M.D. Janezic, P.D. Domich, and R. Geyer, "Analysis of an Open-Ended Coaxial Probe with Lift-Off for Non-destructive Testing," in *IEEE Transactions on Instrumentation and Measurement*, vol. 43, no. 5, pp. 711 – 718, Oct. 1994

[71] S. Bakhtiari, S. I. Ganchev and R. Zoughi, "Analysis of radiation from an open-ended coaxial line into stratified dielectrics," *in IEEE Transactions on Microwave Theory and Techniques*, vol. 42, no. 7, pp. 1261 – 1267, Jul. 1994.

[72] P.M. Meaney, A.P. Gregory, J. Seppälä, and T. Lahtinen, "Open-Ended Coaxial Dielectric Probe Effective Penetration Depth Determination," in *IEEE Transactions on Microwave Theory and Techniques*, vol. 64, pp. 915 – 923, Mar. 2016

[73] A.E. Omer, G. Shaker, S. Safavi-Naeini, R.M. Shubair, "EM Measurements of Glucose-Aqueous Solutions," IEEE International Symposium on Antennas and Propagation and USNC-URSI Radio Science Meeting, Atlanta, GA, USA, 2019, pp. 103 – 104.

[74] F. Costa, M. Borgese, M. Degiorgi, A. Monorchio, "Electromagnetic Characterisation of Materials by Using Transmission/Reflection (T/R) Devices," *Electronics*, vol. 6, no. 4, pp. 95, Nov. 2017

[75] J. Kerouedan *et al*., "Detection of micro-cracks on metal surfaces using nearfield microwave dual-behavior resonator filters," Measurement Science and Technology, vol. 19, no. 10, Aug. 2008

[76] D. Shimin, "A New Method for Measuring Dielectric Constant Using the Resonant Frequency of a Patch Antenna," in *IEEE Transactions on Microwave Theory and Techniques*, vol. 34, no. 9, pp. 923 – 931, Sep. 1986.

[77] P.A. Bernard and J.M. Gautray, "Measurement of dielectric constant using a microstrip ring resonator," *in IEEE Transactions on Microwave Theory and Techniques*, vol. 39, no. 3, pp. 592 – 595, Mar. 1991.

[78] V. Turgul and I. Kale, "On the accuracy of complex permittivity model of glucose/water solutions for non-invasive microwave blood glucose sensing," *E-Health and Bioengineering Conference (EHB)*, Iasi, 2015, pp. 1 – 4.

[79] J. Kim *et al*., "Microwave dielectric resonator biosensor for aqueous glucose solution," *Review of Scientific Instruments*, vol. 79, no. 8, pp. 086107 – 086109, Aug. 2008.

[80] H. Cano-Garcia *et al*., "Reflection and transmission measurements using 60 GHz patch antennas in the presence of animal tissue for non-invasive glucose sensing," 2016 10th European Conference on Antennas and Propagation (EuCAP), Davos, Switzerland, Apr. 2016, pp. 1 – 3.

[81] P. H. Siegel, Y. Lee, V. Pikov, "Millimeter-wave non-invasive monitoring of glucose in anesthetized rats," 2014 39th International Conference on Infrared, Millimeter, and Terahertz waves (IRMMW-THz), Tucson, AZ, USA, Sep. 2014, pp. 1 – 2.

[82] S. Amrane, N. Azami and Y. Elboulqe, "Optimized algorithm of dermis detection for glucose blood monitoring based on optical coherence tomography," in 10th International Conference on Intelligent Systems: Theories and Applications (SITA), Rabat, Morocco, Oct. 2015, pp. 1 – 5.

[83] N. Wadamori, "Behavior of long-period measurements using a small-sized photoacoustic cell for aqueous glucose monitoring," in 37th Annual International Conference of the IEEE Engineering in Medicine and Biology Society (EMBC), Milan, Italy, Aug. 2015, pp. 1267 – 1270

[84] S. Ramasahayam, L. Arora, S. Chowdhury, M. Anumukonda, "FPGA based system for blood glucose sensing using photoplethysmography and online motion artifact correction using Adaline," in 9th International Conference on Sensing Technology (ICST), Auckland, New Zealand, Dec. 2015, pp. 22-27

[85] A. Asaduzzaman, S. Samadarsinee, K.K. Chidella, "Simulating multi sensor noninvasive blood glucose monitoring systems," SoutheastCon 2016, Norfolk, VA, USA, Apr. 2016, pp. 1 – 7.

[86] P.P. Pai, P.K. Sanki, A. De, S. Banerjee, "Nir photoacoustic spectroscopy for non-invasive glucose measurement," 37th Annual International Conference of the IEEE Engineering in Medicine and Biology Society (EMBC), Milan, Italy, Aug. 2015, pp. 7978 – 7981.

[87] X. Li, C. Li, "Research on non-invasive glucose concentration measurement by NIR transmission," IEEE International Conference on Computer and Communications (ICCC), Chengdu, China, Oct. 2015, pp. 223 – 228.

[88] S. Ling, P. San, H. Nguyen, "Non-invasive hypoglycemia monitoring system using extreme learning machine for type 1 diabetes," *ISA Transactions*, vol. 64, pp. 440 – 446, Sep. 2016

[89] J. Shao, F. Yang, F. Xia, Q. Zhang, Y. Chen, "A novel miniature spiral sensor for non-invasive blood glucose monitoring," in 10th European Conference on Antennas and Propagation (EuCAP), Davos, Switzerland, Apr. 2016, pp. 1 – 2.

[90] A. Adhyapak, M. Sidley, J. Venkataraman, “Analytical model for real time, noninvasive estimation of blood glucose level,” in 36th Annual International Conference of the IEEE Engineering in Medicine and Biology Society, Chicago, IL, USA, Aug. 2014, pp. 5020 – 5023.

[91] R. Baghbani, M. Rad, A. Pourziad, “Microwave sensor for noninvasive glucose measurements design and implementation of a novel linear,” *IET Wireless Sensor Systems*, vol. 5, pp. 51 – 57, Apr. 2015

[92] V. Deshmukh, R. Ghongade, “Measurement of dielectric properties of aqueous glucose using planar ring resonator,” in International Conference on Microelectronics, Computing and Communications (MicroCom), Durgapur, India, Jan. 2016, pp. 1 – 5

[93] C.-L. Yang *et al*., “Noncontact measurement of complex permittivity and thickness by using planar resonators,” in *IEEE Transactions on Microwave Theory and Techniques*, vol. 64, no. 1, p. 247 – 257, Jan. 2016

[94] A. E. Omer *et al*., “Multiple-Cell Microfluidic Dielectric Resonator for Liquid Sensing Applications,” in *IEEE Sensors Journal*, vol. 21, no. 5, pp. 6094 – 6104, Mar. 2021.

[95] H.-J. Lee *et al*., “A planar split-ring resonator-based microwave biosensor for label-free detection of biomolecules,” *Sens. Actuators B, Chem*, vol. 169, pp. 26 – 31, Jul. 2012.

[96] R. Vyas *et al*., “Inkjet Printed, Self Powered, Wireless Sensors for Environmental, Gas, and Authentication-Based Sensing,” in *IEEE Sensors Journal*, vol. 11, no. 12, pp. 3139 – 3152, Dec. 2011

[97] S. Trabelsi, S. O. Nelson, “Microwave sensing of quality attributes of agricultural and food products,” in *IEEE Instrumentation & Measurement Magazine*, vol. 19, no. 1, pp. 36 – 41, Feb. 2016.

[98] H. L. Gan *et al*, “Characterization of vegetable oils by surface acoustic wave sensing electronic nose*,” Food Chem*., vol. 89, no. 4, pp. 507 – 518, Mar. 2005

[99] M. Rashvand *et al*, “Adulteration detection in olive oil using dielectric technique and data mining,” *Sens. Bio-Sens. Res*., vol. 11, no. 1, pp. 33 – 36, Dec. 2016

[100] V. Kostik, S. Memeti, B. Bauer, “Fatty acid composition of edible oils and fats,” *J. Hyg. Eng. Des.*, vol. 4, pp. 112 – 116, 2013

[101] C. A. Nunes, “Vibrational spectroscopy and chemometrics to assess authenticity, adulteration, and intrinsic quality parameters of edible oils and fats,” Food Res. Int., vol. 60, pp. 255 – 261, Jun. 2014.

[102] A. E. Omer *et al*., “Non-Invasive Real-Time Monitoring of Glucose Level Using Novel Microwave Biosensor Based on Triple-Pole CSRR,” in *IEEE Trans. Biomed. Circuits Syst*., vol. 14, no. 6, pp. 1407 – 1420, Dec. 2020.

[103] Food and Agriculture Organization of the United Nations, “Dairy Market Review,” FAO, Apr. 2021 [Online]. Available: https://www.fao.org/3/cb4230en/cb4230en.pdf

[104] D. Wang, J. Fritsch, and C.I. Moraru, “Shelf life and quality of skim milk processed by cold microfiltration with a 1.4-μm pore size membrane, with or without heat treatment,” Journal of Dairy Science, vol. 102, no. 10, pp. 8798–8806, Oct. 2019

[105] T. Yilmaz *et al*., “Radio-frequency and microwave techniques for non-invasive measurement of blood glucose levels,” *Diagnostics*, vol. 9, no. 1, pp. 6 – 39, Jan. 2019

[106] A. E. Omer, S. Gigoyan, G. Shaker, S. Safavi-Naeini, “WGM-Based Sensing of Characterized Glucose-Aqueous Solutions at mm-Waves,” in *IEEE Access*, vol. 8, pp. 38809 – 38825, Feb. 2020

[107] A. E. Omer, G. Shaker, S. Safavi-Naeini, “Portable radar-driven microwave sensor for intermittent glucose levels monitoring,” in *IEEE Sens. Lett*., vol. 4, no. 5, pp. 1 – 4, May. 2020

[108] A. Brady, C. McCabe, M. McCann, “Fundamentals of Medical-Surgical Nursing,” John Wiley & Sons, Jan. 2013

[109] E. Topsakal, T. Karacolak, E. C. Moreland, “Glucose-dependent dielectric properties of blood plasma,” in *XXXth URSI General Assembly and Scientific Symposium*, Istanbul, Turkey, Oct. 2011, pp. 1 – 4

[110] K.S. Cole, R.H. Cole, “Dispersion and Absorption in Dielectrics I. Alteranting Current Characteristics,” *The Journal of Chemical Physics*, vol. 9, no. 4, pp. 341 – 351, Feb. 1941

[111] Y. Feldman, A. Puzenko, and Y. Ryabov, Dielectric Relaxation Phenomena in Complex Materials, John Wiley & Sons, Inc., 2005

[112] K. Yaws, D. Mixon, and W. Roach, “Electromagnetic properties of tissue in the optical region,” in *Optical Interactions with Tissue and Cells XVIII*, San Jose, California, United States, Feb. 2007

[113] V. Komarov, S. Wang, J. Tang, Permittivity and Measurements. Hoboken, NJ, USA: Wiley, 2005. [Online]. Available: http://dx.doi.org/10.1002/0471654507.eme308. [Accessed 12 February 2019]

[114] Y. Fan, X. Deng, Q. Wang, W. Wang, “Testing glucose concentration in aqueous solution based on microwave cavity perturbation technique,” 2010 3rd International Conference on Biomedical Engineering and Informatics, Yantai, 2010, pp. 1046 – 1049.

[115] J. Venkataraman and B. Freer, “Feasibility of non-invasive blood glucose monitoring: In-vitro measurements and phantom models,” in IEEE International Symposium on Antennas and Propagation (APSURSI), Spokane, WA, USA, 2011, pp. 603 – 606

[116] B. Freer and J. Venkataraman, “Feasibility study for non-invasive blood glucose monitoring,” in *IEEE Antennas and Propagation Society International Symposium*, Toronto, Ontario, Canada, 2010, pp. 1 – 4.

[117] M. Sidley and J. Venkataraman, “Feasibility of blood glucose estimation from real time monitoring,” in IEEE Antennas and Propagation Society International Symposium (APSURSI), Orlando, FL, USA, 2013, pp. 2055 – 2056

[118] X. Xiao and Q. Li, “A Noninvasive Measurement of Blood Glucose Concentration by UWB Microwave Spectrum,” in *IEEE Antennas and Wireless Propagation Letters*, vol. 16, pp. 1040 – 1043, Oct. 2016

[119] T. Yilmaz, R. Foster, Y. Hao, “Patch resonator for non-invasive detection of dielectric property changes in biological tissues,” Proceedings of the 2012 IEEE International Symposium on Antennas and Propagation, Chicago, IL, USA, 2012, pp. 1 – 2.

[120] T. Yilmaz, T. Ozturk, Saul Joof, “A Comparative Study for Development of Microwave Glucose Sensors,” in 32nd URSI GASS, Montreal, QC, Canada, 2017.

[121] J. Vrba, J. Karch, D. Vrba, “Phantoms for development of microwave sensors for noninvasive blood glucose monitoring,” *International Journal of Antennas and Propagation*, vol. 2015, no. 570870, Mar. 2015.

[122] V. Turgul, I. Kale, “Permittivity extraction of glucose solutions through artificial neural networks and non-invasive microwave glucose sensing,” *Sensors and Actuators A: Physical*, vol. 277, pp. 65 – 72, Jul. 2018.

[123] A.S. Zapasnoy *et al*., “Application of Broadband Microwave Near-Field Sensors for Glucose Monitoring in Biological Media,” *Applied Science*, vol. 11, no. 4, pp. 1470 – 1478, Feb. 2021.

[124] J. Hanna *et al*., “Noninvasive, wearable, and tunable electromagnetic multisensing system for continuous glucose monitoring, mimicking vasculature anatomy,” *Science Advances*, vol. 6, no. 24, Jun. 2020.

[125] H. Choi, S. Luzio, J. Beutler and A. Porch, “Microwave noninvasive blood glucose monitoring sensor: Human clinical trial results,” IEEE MTT-S International Microwave Symposium (IMS), Honololu, HI, USA, Oct. 2017, pp. 876 – 879

[126] R. J. Buford, E. C. Green and M. J. McClung, “A microwave frequency sensor for non-invasive blood-glucose measurement,” IEEE Sensors Applications Symposium, Atlanta, GA, USA, Mar. 2008, pp. 4 – 7

[127] N-Y. Kim *et al*., “Rapid, Sensitive and Reusable Detection of Glucose by a Robust Radiofrequency Integrated Passive Device Biosensor Chip,” *Scientific Reports*, vol. 5, article no. 7807, Jan. 2015.

[128] K.K. Adhikari, N. Kim, “Ultrahigh-Sensitivity Mediator-Free Biosensor Based on a Microfabricated Microwave Resonator for the Detection of Micromolar Glucose Concentrations,” in *IEEE Transactions on Microwave Theory and Techniques*, vol. 64, no. 1, pp. 319 – 327, Jan. 2016

[129] M. Baghelani *et al*., "Non-invasive continuous-time glucose monitoring system using a chipless printable sensor based on split ring microwave resonators," *Scientific Reports*, vol. 10, article no. 12980, Jul. 2020.

[130] T. Yilmaz, R. Foster, Y. Hao, "Towards Accurate Dielectric Property Retrieval of Biological Tissues for Blood Glucose Monitoring," in *IEEE Transactions on Microwave Theory and Techniques*, vol. 62, no. 12, pp. 3193 – 3204, Dec. 2014

[131] M. Hofmann, F. Trenz, R. Weigel, G. Fischer, D. Kissinger, "A microwave sensing system for aqueous concentration measurements based on a microwave reflectometer," IEEE/MTT-S International Microwave Symposium Digest, Montreal, QC, Aug. 2012, pp. 1 – 3

[132] H. Cano-Garcia *et al*., "Detection of glucose variability in saline solutions from transmission and reflection measurements using V-band waveguides," *Measurement Science and Technology*, vol. 26, no. 12, pp. 125701 – 125710, Dec. 2015.

[133] P. H. Siegel *et al*., "First millimeter-wave animal in vivo measurements of L-Glucose and D-Glucose: Further steps towards a non-invasive glucometer," 41st International Conference on Infrared, Millimeter, and Terahertz waves (IRMMW-THz), Copenhagen, Denmark, Dec. 2016, pp. 1 – 3.

[134] P. H. Siegel *et al*., "Noninvasive in vivo millimeter-wave measurements of glucose: First results in human subjects," in 42nd International Conference on Infrared, Millimeter, and Terahertz Waves (IRMMW-THz), Cancun, Mexico, Oct. 2017, pp. 1 – 2

[135] P.F.M. Smulders *et al*., "Dielectric Properties of Glucose Solutions in the 0.5 – 67 GHz Range," *Microwave and Optical Technology Letters*, vol. 55, no. 8, pp. 1916 – 1917, Aug. 2013.

[136] V.V. Meriakri *et al*., "Dielectric Properties of Water Solutions with Small Content of Glucose in the Millimeter-Wave Band and the Determination of Glucose in Blood," in International Kharkov Symposium Physics and Engrg. of Millimeter and Sub-Millimeter Waves (MSMW), Kharkov, Ukraine, Aug. 2007, pp. 873 – 875

[137] V. V. Meriakri *et al*., "Dielectric properties of glucose solutions in the millimetre-wave range and control of glucose content in blood," *Measurement science and technology*, vol. 18, no. 4, p. 977 – 982, Feb. 2007.

[138] M. Zhadobov et al., "Complex permittivity of representative biological solutions in the 2–67 GHz range," *Bioelectromagnetics*, vol. 33, no. 4, pp. 346 – 355, May. 2012.

[139] Y. Nikawa, D. Someya, "Application of millimeter waves to measure blood sugar level," in Asia-Pacific Microwave Conference (APMC), Taipei, Taiwan, Dec. 2001, pp. 1303 – 1306

[140] H-J. Lee, H.H. Choi, “Microwave transmission properties of D-(+)-glucose solution with concentration variations,” *J. Phys. D: Appl. Phys*., vol. 52, no. 38, pp. 385401, Jul. 2019

[141] O.P. Gandhi, A. Riazi, “Absorption of Millimeter Waves by Human Beings and its Biological Implications,” in *IEEE Transactions on Microwave Theory and Techniques,* vol. 34, no. 2, pp. 228 – 235, Feb. 1986

[142] K. Diederichs, A. Qiu, G. Shaker, “Wireless Biometric Individual Identification Utilizing Millimeter Waves,” in *IEEE Sensors Letters,* vol. 1, no. 1, pp. 1 – 4, Feb. 2017

[143] C. Lee, C. Yang, “Single-Compound Complementary Split-Ring Resonator for Simultaneously Measuring the Permittivity and Thickness of Dual-Layer Dielectric Materials,” in *IEEE Transactions on Microwave Theory and Techniques*, vol. 63, no. 6, pp. 2010 – 2023, Jun. 2015

[144] H. Torun *et al*., “An antenna coupled split-ring resonator for biosensing,” *J. Appl. Phys*., vol. 116, no. 12, pp. 124701, Sep. 2014.

[145] H. Caglayan *et al*., “Ultrafast and sensitive bioassay using split ring resonator structures and microwave heating,” *Appl. Phys. Lett*., vol. 97, no. 9, Aug. 2010.

[146] G. Govind, M.J. Akhtar, “Metamaterial-Inspired Microwave Microfluidic Sensor for Glucose Monitoring in Aqueous Solutions,” in *IEEE Sensors Journal,* vol. 19, no. 24, pp. 11900 – 11907, Sep. 2019

[147] A. Ebrahimi *et al*., “High-sensitivity metamaterial-inspired sensor for microfluidic dielectric characterization,”in *IEEE Sensors Journal,* vol. 14, no. 5, p. 1345 – 1351, May. 2014.

[148] J. B. Pendry, A. J. Holden, D. J. Robbins and W. J. Stewart, “Magnetism from conductors and enhanced nonlinear phenomena,” in *IEEE Transactions on Microwave Theory and Techniques*, vol. 47, no. 11, pp. 2075 – 2084, Nov. 1999,

[149] M.S. Boybay, O.M. Ramahi, “Material Characterization Using Complementary Split-Ring Resonators,” in *IEEE Transactions on Instrumentation and Measurement*, vol. 61, no. 11, pp. 3039 – 3046, Nov. 2012

[150] F. Deshours *et al*., “Improved microwave biosensor for non-invasive dielectric characterization of biological tissues,” *Microelectronics Journal*, vol. 88, pp. 137 – 144, Jun. 2019.

[151] F. Deshours *et al*., “Microwave Resonant Sensor for Non-invasive Characterization of Biological Tissues,” *IRBM journal*, vol. 39, no. 6, pp. 445 – 450, Dec. 2018.

[152] S. Harnsoongnoen, A. Wanthong, “Coplanar waveguides loaded with a split ring resonator-based microwave sensor for aqueous sucrose solutions,” *Measurement Science & Technology,* vol. 27, no. 1, Dec. 2015.

[153] S. Hardinata *et al*., "Complementary Split-Ring Resonators for Non-Invasive Characterization of Biological Tissues," 18th International Symposium on Antenna Technology and Applied Electromagnetics (ANTEM), Waterloo, Canada, 2018, pp. 1 – 2

[154] R. Kumari *et al*., "An ENG resonator-based microwave sensor for the characterization of aqueous glucose," *J. Phys. D: Appl. Phys*., vol. 51, no. 7, Jan. 2018.

[155] J. Naqui *et al*., "Transmission Lines Loaded With Pairs of Stepped Impedance Resonators: Modeling and Application to Differential Permittivity Measurements," in *IEEE Transactions on Microwave Theory and Techniques*, vol. 64, no. 11, pp. 3864 – 3877, Nov. 2016

[156] L. Su, J. Naqui, J. Mata-Contreras, F. Martín, " Modeling and Applications of Metamaterial Transmission Lines Loaded With Pairs of Coupled Complementary Split-Ring Resonators (CSRRs)," in *IEEE Antennas and Wireless Propagation Letters*, vol. 15, pp. 154 – 157, Feb. 2016

[157] M. Abdolrazzaghi, M. H. Zarifi, M. Daneshmand, "Sensitivity enhancement of split ring resonator based liquid sensors," in *IEEE Sensors*, Orlando, FL, USA, Nov. 2016, pp. 1 – 3

[158] L. Su, J. Mata-Contreras, P. Vélez, F. Martín, "Splitter/Combiner Microstrip Sections Loaded With Pairs of Complementary Split Ring Resonators (CSRRs): Modeling and Optimization for Differential Sensing Applications," in *IEEE Transactions on Microwave Theory and Techniques*, vol. 64, no. 12, pp. 4362 – 4370, Dec. 2016

[159] G. Gennarelli, S. Romeo, M. R. Scarfì, F. Soldovieri, "A Microwave Resonant Sensor for Concentration Measurements of Liquid Solutions," in *IEEE Sensors Journal*, vol. 13, no. 5, pp. 1857 – 1864, May. 2013

[160] E. Silavwe, N. Somjit, I.D. Robertson, "A Microfluidic-Integrated SIW Lab-on-Substrate Sensor for Microliter Liquid Characterization," in *IEEE Sensors Journal*, vol. 16, no. 21, pp. 7628 – 7635, Sep. 2016

[161] C.-F. Liu *et al*., "Microfluidics-based hairpin resonator biosensor for biological cell detection," *Sensors and Actuators B: Chemical*, vol. 263, pp. 129 – 136, Jun. 2018.

[162] N.K. Tiwari *et al*., "Flexible biomedical RF sensors to quantify the purity of medical grade glycerol and glucose concentrations," *International Journal of Microwave and Wireless Technologies*, vol. 12, no. 2, pp. 120 – 130, Mar. 2020.

[163] J.D. Baena *et al*., "Equivalent-circuit models for split-ring resonators and complementary split-ring resonators coupled to planar transmission lines," in *IEEE Transactions on Microwave Theory and Techniques*, vol. 53, no. 4, pp. 1451 – 1461, Apr. 2005.

[164] A. Ebrahimi *et al*., "Dual-mode behavior of the complementary electric-LC resonators loaded on transmission line: Analysis and applications," *Journal of Applied Physics*, vol. 116, no. 8, pp. 083705 – 083712, Aug. 2014.

[165] Institute of Applied Physics, "Dielectric properties of human tissues," [Online]. Available: http://niremf.ifac.cnr.it/tissprop/.

[166] A.E. Omer *et al*., "Facial recognition using principal component analysis based dimensionality reduction," in International Conference on Computing, Control, Networking, Electronics and Embedded Systems Engineering (ICCNEEE), Khartoum, Sudan, Sep. 2015, pp. 434 – 439

[167] H. Abdi, L.J. Williams, "Principal component analysis," *Wiley Interdiscip. Rev. Comput. Stat*., vol. 2, no. 4, pp. 433 – 459, 2010.

[168] M. Ur-Rehman *et al*., "A Low Profile Antenna for Millimeter-Wave Body-Centric Applications," in *IEEE Transactions on Antennas and Propagation*, vol. 65, no. 12, pp. 6329 – 6337, Dec. 2017

[169] S. American, "Fake Blood Made Scientific," [Online]. Available: https://www.scientificamerican.com/article/fake-blood-made-scientific. [Accessed 19 January 2018].

[170] C. Jang *et al*., "Non-Invasive Fluidic Glucose Detection Based on Dual Microwave Complementary Split Ring Resonators With a Switching Circuit for Environmental Effect Elimination," in *IEEE Sensors Journal*, vol. 20, no. 15, pp. 8520 – 8527, Apr. 2020

[171] S.Y. Huang *et al*., "Microstrip Line-Based Glucose Sensor for Noninvasive Continuous Monitoring Using the Main Field for Sensing and Multivariable Crosschecking," in *IEEE Sensors Journal*, vol. 19, no. 2, pp. 535 – 547, Oct. 2018

[172] C. Jang *et al*., "Temperature-corrected fluidic glucose sensor based on microwave resonator," *Sensors*, vol. 18, no. 11, pp. 3850 – 3862, Nov. 2018.

[173] T. Chretiennot *et al*., "Microwave-based microfluidic sensor for non-destructive and quantitative glucose monitoring in aqueous solution," *Sensors*, vol. 16, no. 10, pp. 1733 – 1739, Oct. 2016.

[174] S. Harnsoongnoen, A. Wanthong, "Coplanar waveguide transmission line loaded with electric-LC resonator for determination of glucose concentration sensing," in *IEEE Sensors Journals*, vol. 17, no. 6, pp. 1635 – 1640, Mar. 2017.

[175] S. Kim *et al*., "Noncontact characterization of glucose by a waveguide microwave probe," *Current Applied Physics*, vol. 9, no. 4, pp. 856 – 860, Jul. 2009.

[176] J. A. Byford *et al*., "Metamaterial inspired periodic structure used for microfluidic sensing," in IEEE 65th Electronic Components and Technology Conference (ECTC), San Diego, CA, Jul. 2015, pp. 1997 – 2002

[177] V. Turgul *et al*., “Simulating the effects of skin thickness and fingerprints to highlight problems with non-invasive RF blood glucose sensing from fingertips,” in *IEEE Sensors Journal*, vol. 17, no. 22, pp. 7553 – 7560, Sep. 2017.

[178] L. Li & D. Uttamchandani, “A Microwave Dielectric Biosensor Based on Suspended Distributed MEMS Transmission Lines,” in *IEEE Sensors Journal*, vol. 9, no. 12, pp. 1825 – 1830, Oct. 2009

[179] A. Ebrahimi *et al*., “Microwave microfluidic sensor for determination of glucose concentration in water,” in IEEE 15th Mediterranean Microwave Symposium (MMS), Lecce, Italy, Dec. 2015, pp. 1 – 3

[180] Omkar, W. Yu & S. Y. Huang, “T-Shaped Patterned Microstrip Line for Noninvasive Continuous Glucose Sensing,” in *IEEE Microwave and Wireless Components Letters*, vol. 28, no. 10, pp. 942 – 944, Oct. 2018

[181] F. Aezinia & B. Bahreyni, “An interface circuit with wide dynamic range for diferential capacitive sensing applications,” in *IEEE Transactions on Circuits and Systems II: Express Briefs*, vol. 60, no. 11, pp. 766 – 770, Sep. 2013.

[182] J. Carroll, G. Paparisto & D. Vye, “The \"Coffee-Can\" Radar Redesigned as an Inexpensive RF PCB [Application Notes],” in *IEEE Microwave Magazine*, vol. 17, no. 10, pp. 62 – 74, Oct. 2016

[183] The Foundation for Research on Information Technologies in Society (IT'IS)., “Dielectric properties of human tissues,” [Online]. Available: http://itis.swiss/virtual-population/tissue-properties/database/dielectric-properties.

[184] R. Lundström et al., “Vibrotactile and thermal perception and its relation to finger skin thickness,” *Clinical Neurophysiology Practice*, vol. 3, pp. 33 – 39, 2018.

[185] A.K. Jha *et al*., “Broadband wireless sensing system for non-invasive testing of biological samples,” in *IEEE Journal on Emerging and Selected Topics in Circuits and Systems*, vol. 8, no. 2, pp. 251 – 259, Jun. 2018.

[186] M. Abdolrazzaghi *et al*., “Noninvasive Glucose Sensing in Aqueous Solutions Using an Active Split-Ring Resonator,” in *IEEE Sensors Journal*, vol. 21, no. 17, pp. 18742 – 18755, Sep. 2021

[187] G. Shaker *et al*., “Non-Invasive Monitoring of Glucose Level Changes Utilizing a mm-Wave Radar System,” *International Journal of Mobile Human Computer Interaction (IJMHCI)*, vol. 10, pp. 10 – 29, Jul. 2018.

[188] J-M. Ekoé *et al*., “Screening for Type1 and Type2 Diabetes,” *Canadian Journal of Diabetes*, vol. 37, no. 1, pp. S12 – S15, Apr. 2013.

[189] L. Rayleigh, “The problem of the whispering gallery,” *Philosophical Magazine*, vol. 20, no. 120, pp. 1001 – 1004, 1910.

[190] F. Vollmer & S. Arnold, “Whispering gallery mode biosensing: label free detection down to single molecules,” *Nature Methods*, vol. 5, pp. 591 – 596, 2008.

[191] D. Cros & P. Guillon, “Whispering gallery dielectric resonator modes for W-band devices,” in *IEEE Transactions on Microwave Theory and Techniques*, vol. 38, no. 11, pp. 1667 – 1674, Nov. 1990

[192] L.K. Hady, A.A. Kishk & D. Kajfez, “Power Dividers Based on Dielectric Resonator Whispering-Gallery Modes Fed by Probe or Slot Type of Coupling,” in *IEEE Transactions on Microwave Theory and Techniques*, vol. 57, no. 12, pp. 3404 – 3409, Dec. 2009

[193] X.H. Jiao, P. Guillon, L.A. Bermudez & P. Auxemery, “Whispering-Gallery Modes of Dielectric Structures: Applications to Millimeter-Wave Bandstop Filters,” in *IEEE Transactions on Microwave Theory and Techniques*, vol. 35, no. 12, pp. 1169 – 1175, Dec. 1987

[194] N. Chen & Z.L. Sun, “Theoritical analysis of whispering gallery mode dielectric resonator in mm-wave,” *Infrared and Millimeter waves*, vol. 14, no. 1, pp. 1801 – 1812, Jul. 1993.

[195] C. Vedrenne & J. Arnaud, “Whispering gallery modes of dielectric resonators,” *IEE Proceedings Microwaves, Optics and Antennas*, vol. 129, no. 4, pp. 183 – 187, 1982.

[196] H. Yoshikawa & A. Nakayama, “Measurements of Complex Permittivity at Millimeter-Wave Frequencies With an End-Loaded Cavity Resonator,” in *IEEE Transactions on Microwave Theory and Techniques*, vol. 56, no. 8, pp. 2001 – 2007, Aug. 2008

[197] D. L. Creedon *et al*., “High Q-factor sapphire whispering gallery mode microwave resonator at single photon energies and millikelvin temperature,” *Applied Physics Letters*, vol. 98, no. 22, pp. 222903 – 222906, 2011.

[198] G. Annino, M. Cassettari, I. Longo & M. Martinelli, “Whispering gallery modes in a dielectric resonator: characterization at millimeter wavelength,” in *IEEE Transactions on Microwave Theory and Techniques*, vol. 45, no. 11, pp. 2025 – 2034, Nov. 1997

[199] J. R. Wait, “Electromagnetic whispering gallery modes in a dielectric rod,” Radio Science, vol. 2, no. 9, pp. 1005 – 1017, 1967.

[200] A. Yariv, “Universal relations for coupling of optical power between micro resonators and dielectric waveguides,” *Electronics Letters*, vol. 36, no. 4, pp. 321 – 322, Feb. 2000.

[201] L.W.Y. Liu *et al*., “In-Vivo and Ex-Vivo Measurements of Blood Glucose Using Whispering Gallery Modes,” *Sensors*, vol. 20, no. 3, pp. 830 – 840, Feb. 2020.

[202] A.I. Gubin *et al*., “Whispering-Gallery-Mode Resonator Technique With Microfluidic Channel for Permittivity Measurement of Liquids,” in *IEEE Transactions on Microwave Theory and Techniques*, vol. 63, no. 6, pp. 2003 – 2009, Jan. 2015.

[203] D. Deslandes & K. Wu, “Integrated transition of coplanar to rectangular waveguides,” in IEEE MTT-S International Microwave Sympsoium Digest (Cat. No.01CH37157), May. 2001, pp. 619 – 622.

[204] S.W. Wong, K. Wang, Z.N. Chen, Q.X. Chu, “Electric Coupling Structure of Substrate Integrated Waveguide (SIW) for the Application of 140-GHz Bandpass Filter on LTCC,” in *IEEE Transactions on Components Packaging and Manufacturing Technology*, vol. 4, no. 2, pp. 316 – 322, Feb. 2014.

[205] A. Malekabadi, S.A. Charlebois, D. Deslandes & F. Boone, “High-Resistivity Silicon Dielectric Ribbon Waveguide for Single-Mode Low-Loss Propagation at F/G-Bands,” in *IEEE Transactions on Terahertz Science and Technology*, vol. 4, no. 4, pp. 447 – 453, Jul. 2014

[206] M.S. Kheir, H.F. Hammad & A. Omar, “Graphical Representation and Evaluation of Attenuation and Coupling Parameters of Whispering-Gallery-Mode Resonators,” in *IEEE Transactions on Instrumentation and Measurement*, vol. 60, no. 8, pp. 2942 – 2950, Aug. 2011

[207] G. Annino, M. Cassettari & M. Martinelli, “Study on planar whispering gallery dielectric resonators. I. General properties,” *International Journal of Infrared and Millimeter Waves*, vol. 23, no. 4, pp. 597 – 615, 2002.

[208] M. Neshat *et al*., “Whispering-gallery-mode resonance sensor for dielectric sensing of drug tablets,” *Measurement Science and Technology*, vol. 21, no. 1, p. 015202 – 015212, Nov. 2009.

[209] S. Hu, S. Nagae & A. Hirose, “Millimeter-wave adaptive glucose concentration estimation with complex-valued neural networks,” in *IEEE Transactions on Biomedical Engineering*, vol. 66, no. 7, p. 2065 – 2071, Jul. 2019.

[210] M. Basha *et al*., “Low-cost, monolithic and integrated whispering gallery mode ring resonator for sensing applications,” in 41st European Microwave Conference, Manchester, UK, Oct. 2011, pp. 515 – 518

[211] S. Lin, S. Gigoyan, J. Wilson, A. E. Fathy, “Novel Ka-band IR Controlled Dielectric Image Guide Components,” in IEEE MTT-S International Microwave Symposium Digest, San Francisco, CA, USA, Jun. 2006, pp. 1389 – 1392

[212] V. VK Thalakkatukalathil *et al*., “Electromagnetic modeling of anisotropic ferrites—Application to microstrip Y-junction circulator design,” *J. Appl. Phys.*, vol. 123, no. 23, pp. 234503 – 234513, Jun. 2018.

[213] “RO4360G2 Datasheet,” Rogers, [Online]. Available: https://www.rogerscorp.com/. [Accessed 10 June 2021].

[214] “Ferrite Domen Datasheet,” [Online]. Available: https://www.domen.ru/files/upload/2020-12-24_15:45:46_a87f8931b921eab9.pdf. [Accessed 10 June 2021].

[215] “XeThru: Single-chip radar sensors with sub-mm resolution,” [Online]. Available: https://www.xethru.com. [Accessed 23 September 2019].

[216] “Project Soli - Google ATAP,” [Online]. Available: https://atap.google.com/soli. [Accessed 23 September 2019].

[217] “Walabot Sensor | Radio Frequency technology for Advanced Detection,” [Online]. Available: https://walabot.com. [Accessed 23 September 2019].

[218] H-S. Yeo & A. Quigley, “Radar Sensing in Human-computer Interaction,” *Interactions,* vol. 25, pp. 70 – 73, Dec. 2017.

[219] J. Lien *et al*., “Soli: Ubiquitous Gesture Sensing with Millimeter Wave Radar,” *ACM Transactions on Graphics (TOG),* vol. 35, pp. 142 – 161, Jul. 2016.

[220] S. Wang *et al*., “Interacting with Soli: Exploring Fine-Grained Dynamic Gesture Recognition in the Radio-Frequency Spectrum,” in the 29th Annual Symposium on User Interface Software and Technology (UIST ’16), Tokyo, Japan, Oct. 2016, pp. 851 – 860

[221] B. Ens *et al*., “Exploring Mixed-Scale Gesture Interaction,” In Proceedings of the SIGGRAPH Asia 2017 Posters (SA ’17), Bangkok, Thailand, Nov. 2017.

[222] D. Avrahami *et al*., “Below the Surface: Unobtrusive Activity Recognition for Work Surfaces Using RF-radar Sensing,” In Proceedings of the 23rd International Conference on Intelligent User Interfaces (IUI ’18), Tokyo, Japan, Mar. 2018, pp. 439 – 451.

[223] A. Dhekne *et al*., “LiquID: A Wireless Liquid IDentifier,” In Proceedings of the 16th Annual International Conference on Mobile Systems, Applications, and Services (MobiSys ’18, Munich, Germany, Jun. 2018, pp. 442 – 454

[224] H.-S. Yeo *et al*., “RadarCat: Radar Categorization for Input & Interaction,” In Proceedings of the 29th Annual Symposium on User Interface Software and Technology (UIST ’16), Tokyo, Japan, Oct. 2016, pp. 833 – 841

[225] T. Rahman *et al*., “DoppleSleep: A Contactless Unobtrusive Sleep Sensing System Using Short-Range Doppler Radar,” In Proceedings of the 2015 ACM International Joint Conference on Pervasive and Ubiquitous Computing (UbiComp ’15), Osaka, Japan, Sep. 2015, pp. 39 – 50

[226] F. Adib *et al*., “Smart Homes That Monitor Breathing and Heart Rate,” In Proceedings of the 33rd Annual ACM Conference on Human Factors in Computing Systems (CHI ’15), Seoul, Republic of Korea, Apr. 2015, pp. 837 – 846.

[227] M. Zhao *et al*., “Through-Wall Human Pose Estimation Using Radio Signals,” In Proceedings of the 2018 IEEE/CVF Conference on Computer Vision and Pattern Recognition (CVPR), Salt Lake City, UT, USA, Jun. 2018, pp. 7356 – 7365.

[228] S. Liu *et al*., “Low-cost Gas Sensors Utilizing Mm-Wave Radars,” In Proceedings of the 2017 IEEE International Symposium on Antennas and Propagation & USNC/URSI National Radio Science Meeting, San Diego, CA, USA, Jul. 2017, pp. 1853 – 1854.

[229] I. Nasr *et al*., "A Highly Integrated 60 GHz 6-Channel Transceiver with Antenna in Package for Smart Sensing and Short-Range Communications," in *IEEE Journal of Solid-State Circuits*, vol. 51, pp. 2066 – 2076, Sep. 2016.

[230] G. Heinzel, A. Rüdiger & R. Schilling, "Spectrum and spectral density estimation by the Discrete Fourier transform (DFT), including a comprehensive list of window functions and some new at-top windows," *Tech. Rep*. 2002, 12.

[231] H.-S. Yeo *et al*., "Exploring Tangible Interactions with Radar Sensing," *In Proceedings of the ACM on Interactive, Mobile, Wearable and Ubiquitous Technologies*, vol. 2, no. 4, pp. 1 – 25, Dec. 2018.

[232] "IEEE Standard for Safety Levels with Respect to Human Exposure to Radio Frequency Electromagnetic Fields, 3 kHz to 300 GHz," IEEE Std C95.1, pp. 1 – 83, 1999.

[233] S. Sarkar, "Artificial blood," *Indian journal of critical care medicine: peer-reviewed*, official publication of Indian Society of Critical Care Medicine, vol. 12, no. 3, pp. 140 – 144, 2008.

[234] D.R. Branch, "Anti-A and anti-B: what are they and where do they come from?," *Transfusion*, vol. 55, no. S2, p. S74 – S79, 2015.

[235] L. Marks, "Monoclonal antibodies and the transformation of blood typing," *MAbs*, vol. 6, no. 6, p. 1362 – 1367, 2014.

[236] M. Li, W.L. Then, L. Li & W. Shen, "Paper-based device for rapid typing of secondary human blood groups," *Analytical and bioanalytical chemistry*, vol. 406, no. 3, pp. 669 – 677, 2014

[237] J. Noiphung *et al*., "A novel paper-based assay for the simultaneous determination of Rh typing and forward and reverse ABO blood groups," *Biosensors and Bioelectronics*, vol. 67, pp. 485 – 489, 2015.

[238] A. Chung, P. Birch & K. Ilagan, "A microplate system for ABO and Rh(D) blood grouping," *Transfusion*, vol. 33, no. 5, pp. 384 – 388, 1993.

[239] Y. Lapierre *et al*., "The gel test: A new way to detect red cell antigen-antibody reactions," *Transfusion*, vol. 30, no. 2, pp. 109 – 113, 1990.

[240] T. Xu *et al*., "Quantitative and multiplexed detection for blood typing based on quantum dot–magnetic bead assay," *International journal of nanomedicine*, vol. 12, p. 3347 – 3356, 2017.

[241] H. Zhang *et al*., "A dye-assisted paper-based point-of-care assay for fast and reliable blood grouping," *Science translational medicine*, vol. 9, no. 381, 2017.

Appendix I. DAK-TL System Calibration

The first step in the operation of the DAK-TL is to define the 0 mm value by setting the thickness measurement to zero. To do so, the sample platform under the probe beam must be clean and empty, then the transparent covers are appropriately replaced on the probe beam to enable the movement of the sample platform up until it touches the cylindrical probe mounted in the probe beam. Measurements of liquid samples or biological tissues are performed using metal dishes of appropriate size as shown in Fig. 2.3. The sample must be backed by metal; therefore, non-metallic dishes cannot be used. A clean and dry petri-dish is used for containing the SUT then placed onto the platform.

To achieve precise reproducible measurements, DAK-TL system is calibrated by means of a port extension using the standard Open-Short-Load method (single port calibration with three standards) to normalize the magnitude and phase changes of the probe and coaxial cable so that the reflection coefficient measured by the VNA is normalized to the reference plane at the interface of the probe with the MUT. Distilled water is used as a reference liquid for calibration at the room temperature of about 20°C. Liquid calibration should be handled carefully as it is sensitive to cable movement and temperature where the dielectric parameters of liquids can vary up to 2% per 1°C temperature change. Therefore, SUT temperature is measured and entered into the software, then a precise volume is poured on the metallic petri-dish and placed on the sample platform which brings it in touch with the probe for measurement. The platform is set to move to a pre-defined distance that is sufficient for the sample-probe contact. Specifically, the probe is perfectly immersed inside the SUT at a depth of 2 – 4 mm to have a good contact with no bubble underneath.

To achieve precise producible measurements, the next procedural steps are followed to ensure an accurate calibration for the system setup:

- First, a clean and dry petri-dish is put onto the sample platform and the measurement mode is changed to solid with a force level of 400 N.
- *Open circuit* calibration is performed by pressing the open button in the base system controller to move the platform to the fully open position (i.e., leaving the probe in the air), then open calibration button is pressed in the interface to store the open circuit measurement and apply calibration factors. The trace on the Smith chart will be stabilized close to the open circuit position (as depicted in Fig. 7.1(a)) to indicate a true open circuit at the probe interface (i.e., $\bar{R} < \infty$, $\bar{X} < 0$) that differs from the ideal case of ($\bar{R} = \infty$, $\bar{X} = 0$) that appears at the rightmost point due to the radiations of the fields from the probe into air.
- *Short circuit* calibration is performed by removing the petri-dish while placing the copper shorting strip on the sample platform. Before that the short tape is scrubbed with a fine sandpaper and cleaned with methyl alcohol. The close button is then pressed to bring the probe in contact with the short tape and the short calibration button is clicked once the trace is stabilized towards the short

circuit position in the Smith chart as shown in Fig. 7.1(b). This short calibration is repeated while twisting the tape till a high-quality short is achieved with a trace that is very close to the leftmost point on the circle, representing $\bar{R} = 0$, $\bar{X} = 0$. The quality of the short calibration is critical for accurate probe calibration.

- *Mechanical zeroing* is performed by placing the empty dry petri-dish again and changing the measurement mode to liquids with a low force level of about 3 N. The zeroing button is pressed to bring the petri-dish in contact with the probe at this low force.
- The petri-dish is half-filled (i.e., 10 mL volume) with a distilled water of a measured temperature of 20^{o}C and placed on the sample platform. The probe is adjusted to go to distance of 3 mm that can better immerse the probe into the water. When the trace on Smith chart is stabilized (Fig. 7.1(c)), the load calibration button is pressed.
- After the three measurements (open, short, and load) are performed, the Apply button is clicked to save the calibration and calculate the calibration factors.

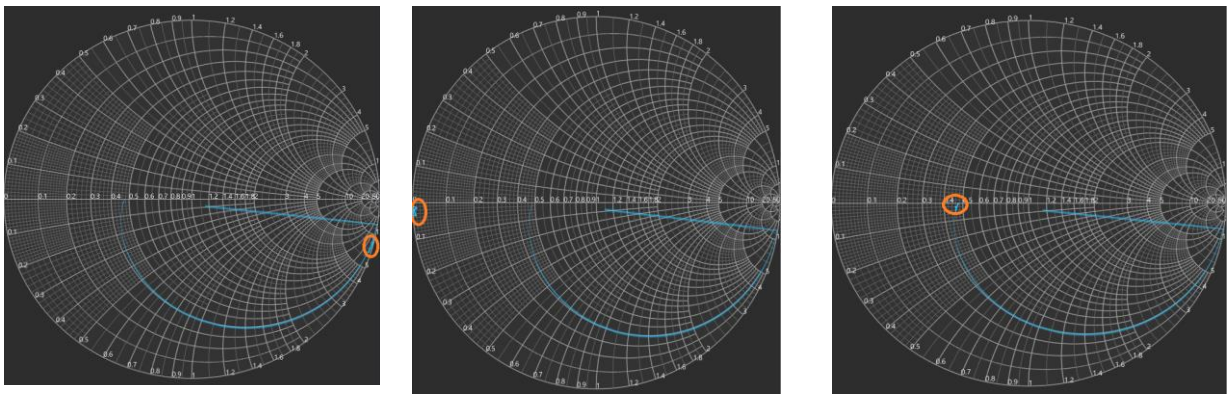

(a) (b) (c)

Figure 7.1: Results of (a) open, (b) short, and (c) load (using distilled water) calibrations steps on the Smith chart.

Appendix II. Blood Typing and Medication Effect in EM Properties of Blood

8.1 ABO-Rh Blood Typing

A variety of vital functions inside the human's body are served by the blood biological tissue and its cellular components of the white cells, red cells, platelets, and the plasma fluid [233]. In particular, the platelets help in transporting the metabolic products, beside serving along with the plasma in blood clotting. The white cells reinforce the immunity response, while the red blood cells (RBCs) are accountable for transporting the oxygen and carbon dioxide throughout the body. Additionally, they exhibit the "typing" phenomenon by the body-specific proteins "antigens" found in their membranes, thus allowing only blood of compatible types to be accepted by the body. Accurate and reliable typing (ABO-type and Rh-D status) becomes particularly important for the blood group of the donor and recipient to guarantee safe transfusions and thereby avert any serious health risks in reaction such as kidney failure, trauma, circulatory collapse, or possibly sudden death caused by the triggered immunity and clotting systems [234]. To avoid a transfusion reaction, donated blood must be compatible with the blood of the recipient patient. Particularly, the donated RBCs must lack the same ABO and Rh-D antigens that the patient's RBCs lack.

Different methods are used for screening the ABO blood groups that are commonly identified by detecting the antigen on the surface of RBCs [235], [236], [237]. For instance, the slide (Fig. 5.1) and tube (Fig. 5.2) tests are regarded as conventional methods that assess the presence of A and B antigens in RBCs by agglutination reactions with antibodies. There are also the assays based on the microplate [238] and gel column [239]. These conventional approaches are limited by their long turnaround time (10 to 20 minutes), training skills requirements for lab technicians, exhaustive operational and overhead costs that encumber the health care system. Therefore, developing a simple, quick, and economical approach for fast blood grouping would expedite the accessibility for this tool in emergencies and resource-limited areas. A recent study in [240] proposed a simple, quantitative, and multiplexed detection method for blood grouping using quantum dots (QDs) and magnetic beads. A reliable paper-based assay was proposed in [241] for blood grouping using immobilized antibodies and bromocresol green dye, where the dye-assisted colour changes in accordance with distinct blood components resulting into a visual readout.

Continuing to these efforts, we chose to exploit the benefits of using microwave sensing to extract the primary features and frequency patterns of various blood samples, and hence developing it as a simple and cost-effective blood-type identification tool. To do so, we first aimed at understanding the dielectric behaviour of the blood samples of various ABO-Rh types as reflected by their dielectric spectroscopy measurements across the microwave spectrum from centimeter(cm) to millimeter(mm)-

wave bands (500 MHz – 67 GHz). That would help to design any proposed microwave biosensor at specific frequency band that exhibits noticeable permittivity contrast between various blood types, and hence their identification with higher sensitivity. Additionally, within the framework of non-invasive blood glucose monitoring, we are interested in exploring and addressing how factors such as the patient's blood type, pre-existing medical conditions, or other illnesses, may impact the sensor accuracy and sensitivity.

In this appendix, the blood typing and medication effect on the dielectric properties of blood was discussed. Synthetic and authentic blood samples of different ABO-Rh types were characterized over the frequency spectrum 2 – 67 GHz using the coaxial probe kit (DAK-TL). The extracted permittivity measurements were analyzed in different bands and some promising regions of appreciably dielectric contrast between various blood types were identified. The blood samples were also tested on the low-frequency resonant sensors to confirm their differences. Lastly, the medication effect in the EM behaviour of blood was studied by measuring healthy and medicated blood samples of varying types and concentrations.

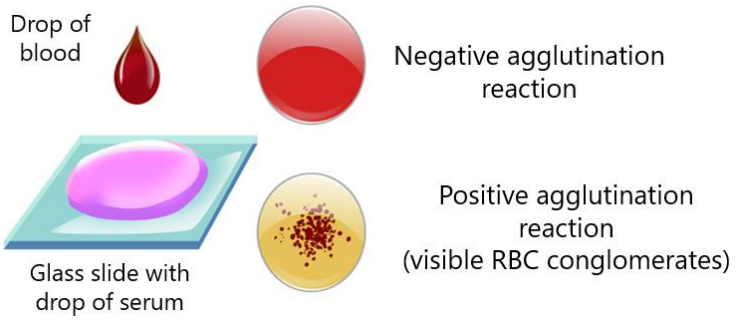

Figure 8.1: Slide method for blood typing.

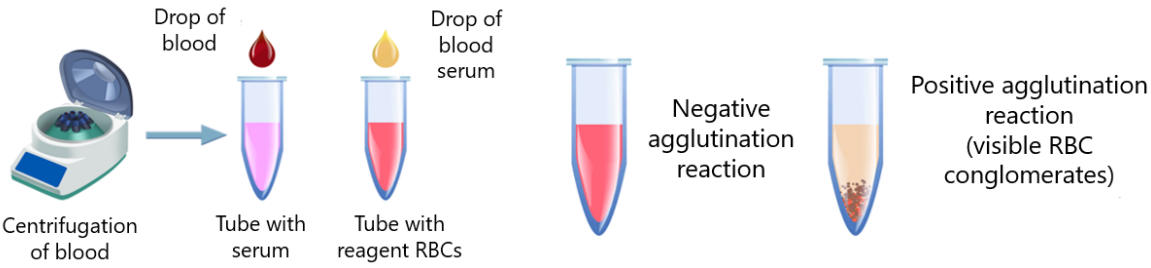

Figure 8.2: Tube method for blood typing.

8.2 Authentic and Synthetic Blood Samples

In what follows, DAK-TL was used to measure the EM dielectric properties of synthetic "artificial" as well as authentic "human" blood samples of different types (Fig. 8.3). Natural or authentic blood is a complex biological tissue that serves many different functions inside the human body as discussed earlier. However, the artificial or synthetic blood is a product made to act as a substitute for RBCs. It is

designed for the sole purpose of transporting oxygen and carbon dioxide throughout the body. Artificial bloods carry several advantages over real donated blood including larger supply, lower risk of blood-borne pathogen transmission, no risk of immune incompatibility, and extended survival of stored RBCs. Artificial blood also has the very realistic typing behaviour as real blood, and hence they could be used effectively for typing-related studies.

Figure 8.3: Authentic and synthetic blood samples.

8.3 Spectroscopy Dielectric Measurements of ABO-Rh Types

The blood tissue is classified as a dispersive medium where the EM properties are frequency dependent [49]. In what follows, the differences between various blood types were investigated by characterizing the dielectric properties of synthetic blood of types A+, B+, AB–, and O+, across the microwave spectrum 500 MHz – 67 GHz in distinct intervals using the DAK-TL characterization system. A similar investigative study was performed for authentic clinical blood samples collected from healthy participants in adult ages to validate the behaviour of the synthetic blood samples.

8.3.1 Experimental Setup of DAK-TL Measurements

The system setup interconnects the DAK-TL, PNA and computer (PC) as shown in Fig. 8.4. To speed up the measurements and reduce the associated noise, the PNA settings were tuned to 100 Hz IF bandwidth and 0 dBm output source power for both probes DAK 3.5/1.2E-TL. The noise filter was activated to minimize the error of the collected measurements, and the averaging reset was set for 5 PNA traces. The standard Open-Short-Load method was used to calibrate the DAK-TL system in the selected frequency band using distilled water at 20°C. All the measurement trials in different frequency bands used a stable volume of 10 mL from each blood sample in a petri dish to minimize the measurement errors due to uncertainty in the sample volume and therefore assure the reproducibility of the measurements.

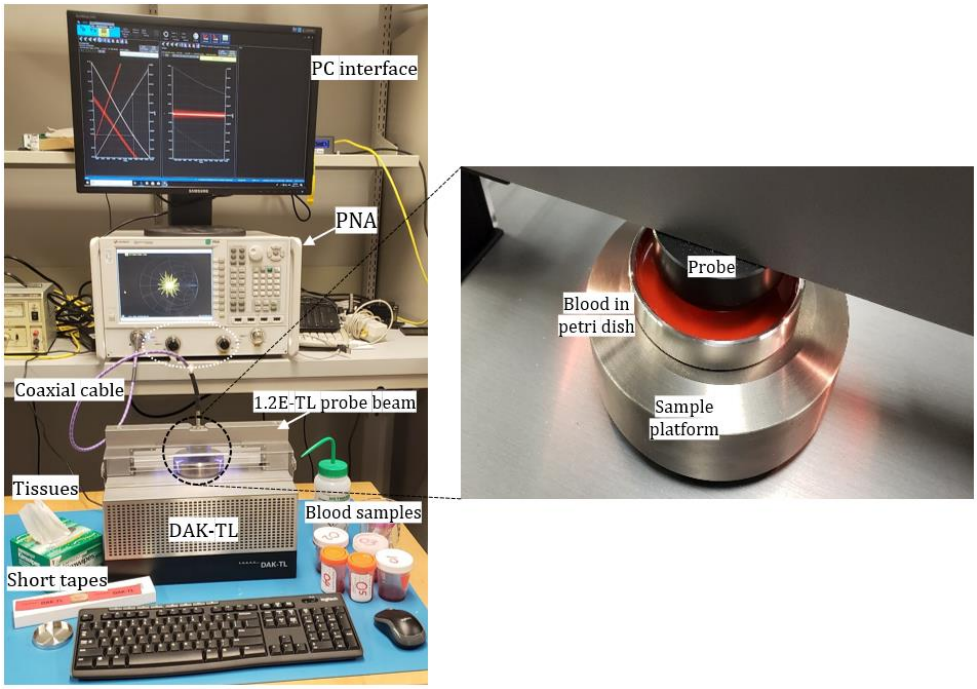

Figure 8.4: DAK-TL system setup for dielectric measurements of blood samples.

8.3.2 Measurements and Results

The dielectric measurements of four types A+, B+, AB–, and O+ of Carolina's synthetic blood samples were performed on five distinct frequency intervals: 500 MHz – 4 GHz using DAK 3.5-TL probe at 50 MHz resolution while DAK 1.2E-TL was used for measurements at the higher frequency intervals 4 – 10 GHz, 10 – 20 GHz, 20 – 50 GHz, and 50 – 67 GHz, all at 200 MHz resolution. The measurements for every blood sample were repeated five times in each frequency band. The dielectric constant and loss tangent extracted from the reflection measurements were plotted in Fig. 8.5.

In these plots, beside the clearly observed trend of decreasing ϵ' and increasing $tan\delta$ with the increasing frequency, some interesting phenomena are perceived. First, the increasing/decreasing variations of the properties are not entirely linear in some frequency bands, such as the dielectric constants in the low-band 500 MHz – 4 GHz and the loss tangent variations in 500 MHz – 2.5 GHz, 4 – 10 GHz and 50 – 67 GHz, depicted in Fig. 8.5(a), Fig. 8.5(b), 8.5(d), and 8.5(j), respectively. Second, different blood types exhibit a noticeable contrast that appears more dominantly in their loss property compared to the dielectric constants that change in relatively smaller units from one type to another. This variance, however, is maximized at the mm-wave band 50 – 67 GHz where different types could be clearly distinguished as shown in Fig. 8.5(j). The low frequency band 500 MHz – 4 GHz is also favourable for identifying various blood types as evidenced by the relatively large variations in both ϵ' and $tan\delta$ depicted in the corresponding band in Fig. 8.5(a) and 8.5(b), respectively.

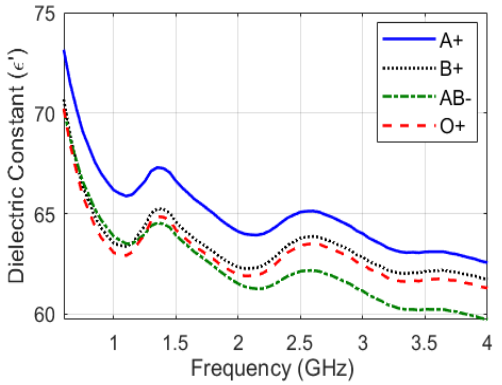
Dielectric Constant (ϵ')
Frequency (GHz)
A+
B+
AB-
O+

(a)

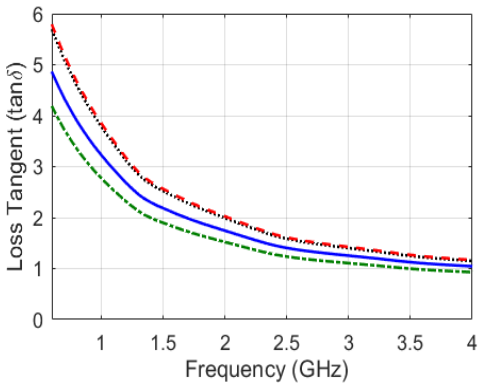
Loss Tangent (tanδ)
Frequency (GHz)

(b)

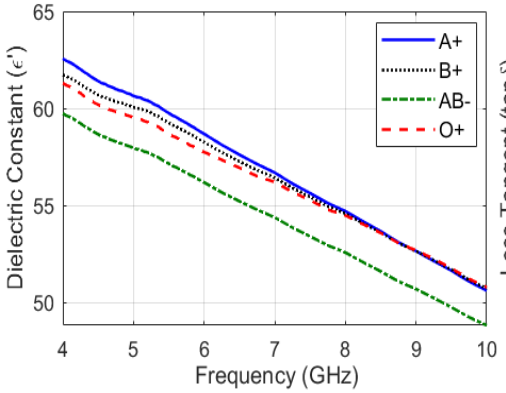
Dielectric Constant (ϵ')
Frequency (GHz)
A+
B+
AB-
O+

(c)

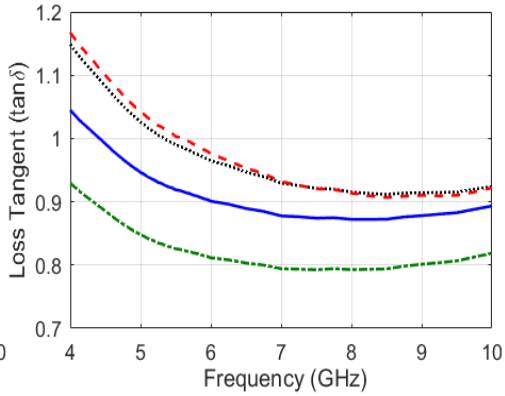
Loss Tangent (tanδ)
Frequency (GHz)

(d)

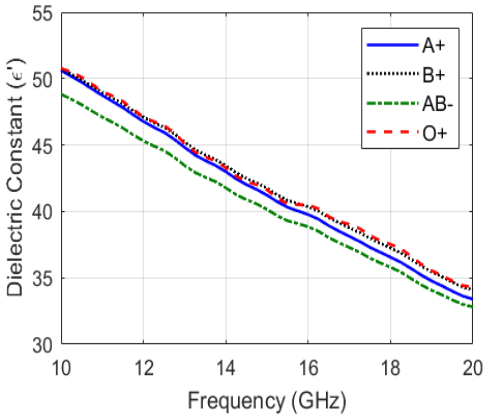
Dielectric Constant (ϵ')
Frequency (GHz)
A+
B+
AB-
O+

(e)

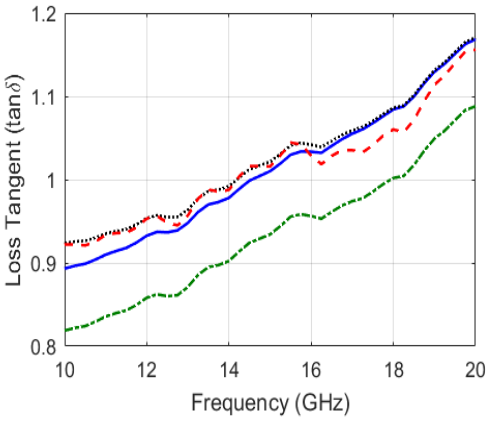
Loss Tangent (tanδ)
Frequency (GHz)

(f)

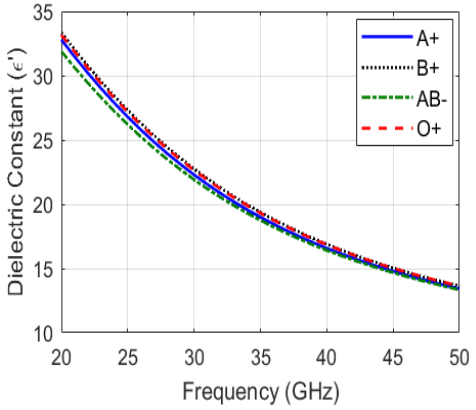
Dielectric Constant (ϵ')
Frequency (GHz)
A+
B+
AB-
O+

(g)

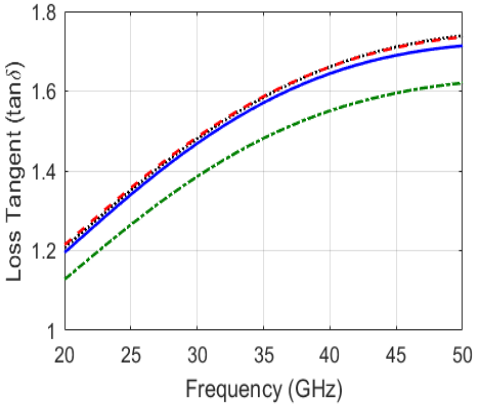
Loss Tangent (tanδ)
Frequency (GHz)

(h)

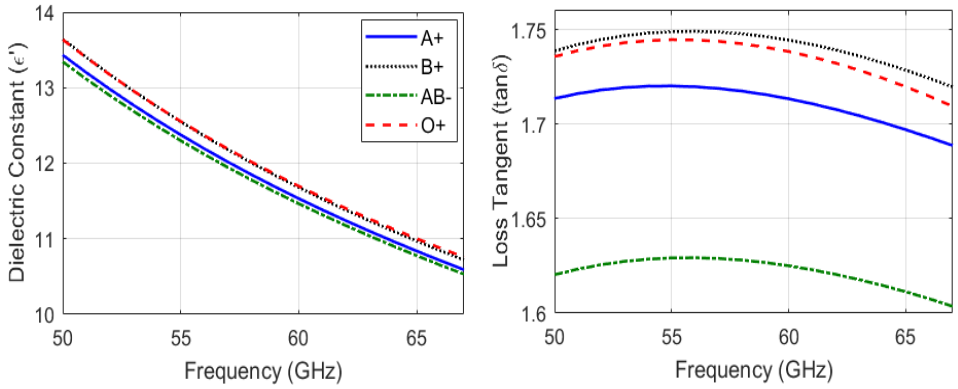

(i) (j)

Figure 8.5: The dielectric measurements of synthetic blood types at different frequency bands, (a) ϵ' in 0.6 – 4 GHz, (b) *tanδ* in 0.6 – 4 GHz, (c) ϵ' in 4 – 10 GHz, (d) *tanδ* in 4 – 10 GHz, (e) ϵ' in 10 – 20 GHz, (f) *tanδ* in 10 – 20 GHz, (g) ϵ' in 20 – 50 GHz, (h) *tanδ* in 20 – 50 GHz, (i) ϵ' in 50 – 67 GHz, (j) *tanδ* in 50 – 67 GHz.

The dielectric behaviour exhibited by the synthetic blood types in the previous experiment, was verified in another investigative study that characterized the dielectric properties of five authentic blood samples of various types using the same DAK-TL setup. Healthy blood samples were collected from five male volunteers in 27 – 40 ages. Three blood samples (S1 – S3) were of O+ types while the other two samples (S4 and S5) were of B+ and AB+ types, respectively. All the reported measurements were conducted in a short period at the same day after collection to avoid any substantial change in their biological nature due to environmental factors. The dielectric properties of the five collected samples were characterized and studied in two distinct spectrums: 5 – 20 GHz and 50 – 67 GHz. The measurements for each blood sample in each frequency band were repeated 5 times and the average is plotted in Fig. 8.6.

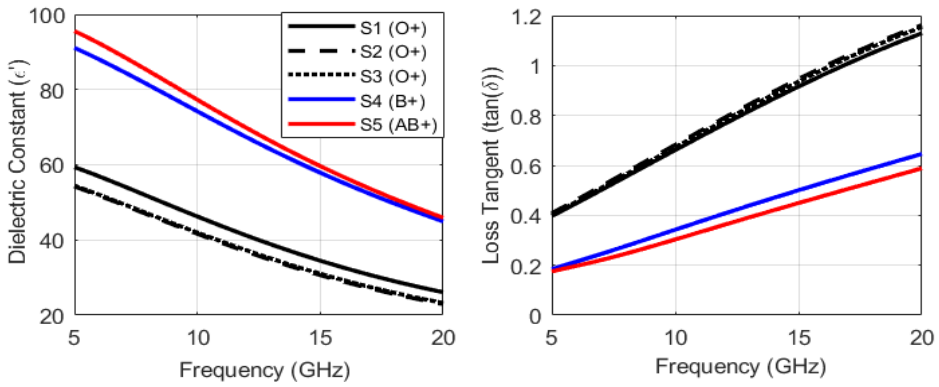

(a) (b)

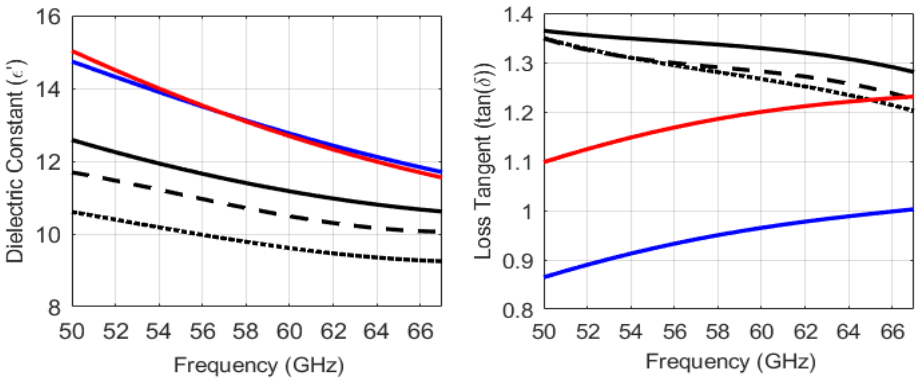

(c) (d)

Figure 8.6: EM measurements of human blood samples of various ABO-Rh types at two frequency bands, (a)-(b) 5 – 20 GHz (top row) and (c)-(d) 50 – 67 GHz (bottom row)

8.4 Medication Effect in Blood's Dielectric Measurements

To investigate the medication effect on the dielectric properties of blood, an additional experiment was performed where Advil tablets were added to some blood samples. Particularly, a solid Advil tablet containing 200 mg ibuprofen and 38 mg diphenhydramine citrate was added to an O+ blood sample of 8 mL volume as shown in Fig. 8.7. The sample was left for about 15 mins to homogenize then measured onto the DAK-TL petri-dish in the mm-wave spectrum 50 – 67 GHz. Another healthy (without medication) O+ blood sample was measured at the same volume. Another liquid-filled Advil capsules with 200 mg ibuprofen and 25 mg diphenhydramine hydrochloride was mixed with a 7.1 mL hemoglobin glucose sample of 150 mg/dL concentration as depicted in Fig. 8.7. The resulting sample was similarly measured in the mm-wave spectrum and compared to that of the Advil-free hemoglobin sample. The visual analysis shows how the Advil medication has mutated the dielectric constant (Fig. 8.8) and loss tangent (Fig. 8.9) of both blood samples across the spectrum. Each sample measurement was repeated three times and the average is reported in these figures.

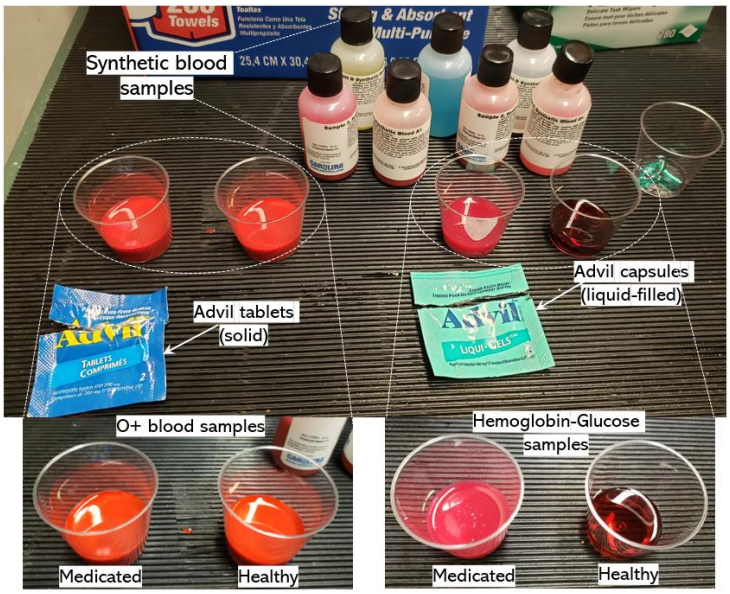

Figure 8.7: Mixing blood samples with different medications

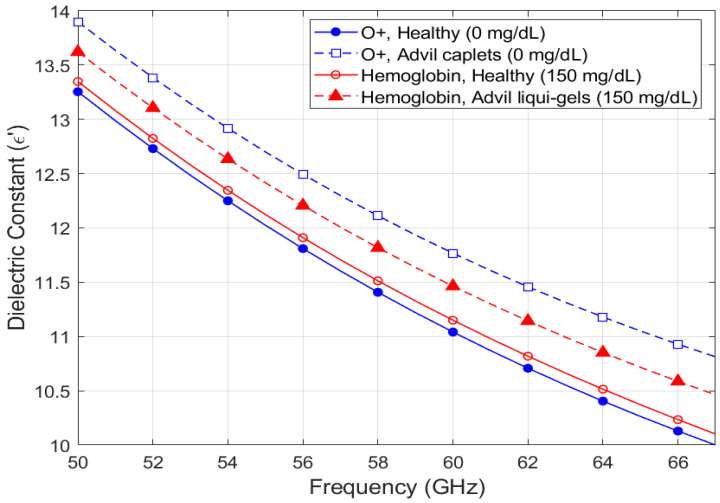

Figure 8.8: Dielectric constant measurements for the healthy and medicated blood samples

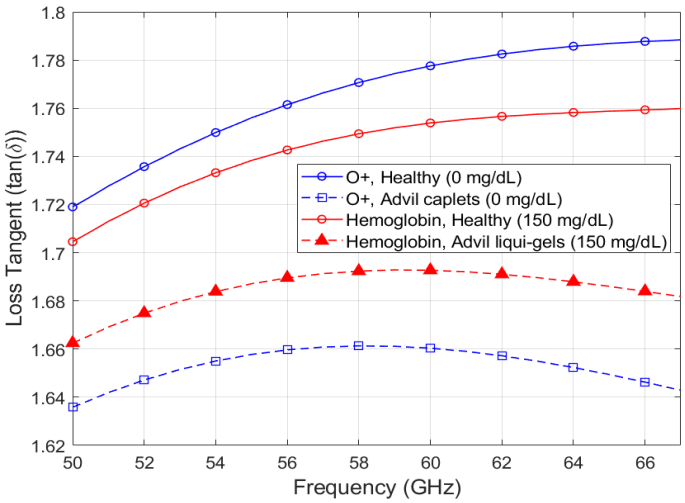

Figure 8.9: Loss tangent measurements for the healthy and medicated blood samples

8.5 Resonance Measurements of ABO-Rh Types

8.5.1 Measurements on TP-CSRR

The four different types A+, B+, AB–, and O+ of Carolina's synthetic blood samples – of realistic blood-typing behaviour – were experimentally tested on the TP-CSRR prototype when connected to the Keysight Technologies VNA N5227A as shown in Fig. 8.10. The VNA was calibrated using the N4694A E-Cal module, then used to measure the reflection and transmission responses by sweeping across 1 – 6 GHz in a 6 MHz resolution at a room temperature of 22°C. A syringe was used to load a precise volume of V = 600 µL from each blood sample inside the rectangular channel and the change in the S_{11} and S_{21} resonance responses was measured.

The scattering response of the TP-CSRR sensor when loaded with an empty channel was considered as a reference for all measurements of blood samples. A clean tissue paper was used to completely remove the previously experimented blood sample while being careful to retrieve the exact reference responses at S_{11}/S_{21} prior-loading the blood sample. The scattering coefficients corresponding to various tested blood types were measured to record the resonance frequencies as well as their minimal amplitudes in both modes of reflection and transmission as shown in Fig. 8.11(a) and 8.11(b), respectively. These microwave responses demonstrate the sensor capability to identify the differences between various blood types by tracking the changes in resonant amplitude and frequency at some intervals in S_{11} (e.g., 0.8 – 1.2 & 5.0 – 5.2 GHz) and S_{21} (e.g., 1.3 – 1.6 GHz & 5.0 – 5.2 GHz). For instance, in the transmission response shown in Fig. 8.11(b), the sensor resonates around 1.473 GHz with -9.778 dB peak amplitude when loaded with the A+ blood sample. However, the sensor metrics for other blood samples were measured as (1.461 GHz, -9.304 dB), (1.449 GHz, -8.973 dB), and (1.444 GHz, -8.742 dB), for the AB–, O+, and B+ types, respectively. All the measurements were repeated three times for repeatability verifications with about ±0.05 dB max.

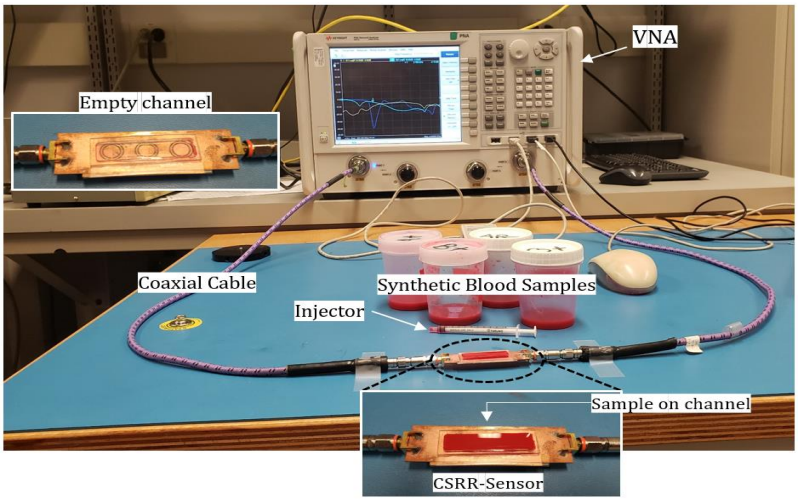

Figure 8.10: Experimental setup for blood typing identification using the TP-CSRR sensor.

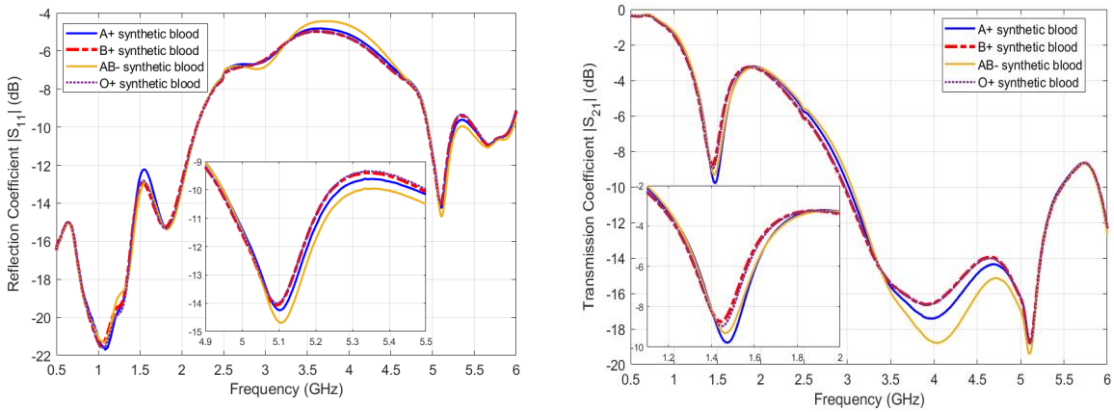

(a) (b)

Figure 8.11: Measured (a) reflection response of various types (enclosed window zooms in 4.9 – 5.5 GHz band), (b) transmission response of various types (enclosed window zooms in 1.2 – 1.8 GHz band).

8.5.2 Measurements on Honey-Cell CSRR

The four synthetic blood types (A+, B+, AB–, and O+) were tested again on the honey-cell CSRR prototype when connected to the Keysight Technologies PNA N5227A as shown in Fig. 8.12(a). A syringe was used to load a precise volume of 600 µL from each blood type inside the cylindrical container integrated on top of the sensing region of the sensor. Subsequently, changes in S_{11} and S_{21} resonance responses were measured as depicted in Fig. 8.13(a) and 8.13(b), respectively. Various blood types could be distinctly identified by tracking the changes in resonant amplitude and frequency in these microwave signals at the corresponding intervals in S_{11} (1.5 – 1.55 GHz) and S_{21} (2.3 – 2.4 GHz). To test the sensor response for another blood type, a clean tissue paper was used to entirely remove the previously loaded sample while retrieving the exact reference resonances at S_{11} and S_{21} prior loading the sample for a fair comparison as shown in Fig. 8.12(b) and 8.12(c), respectively. All the measurements were repeated three times for repeatability verifications with about ±0.05 dB error max.

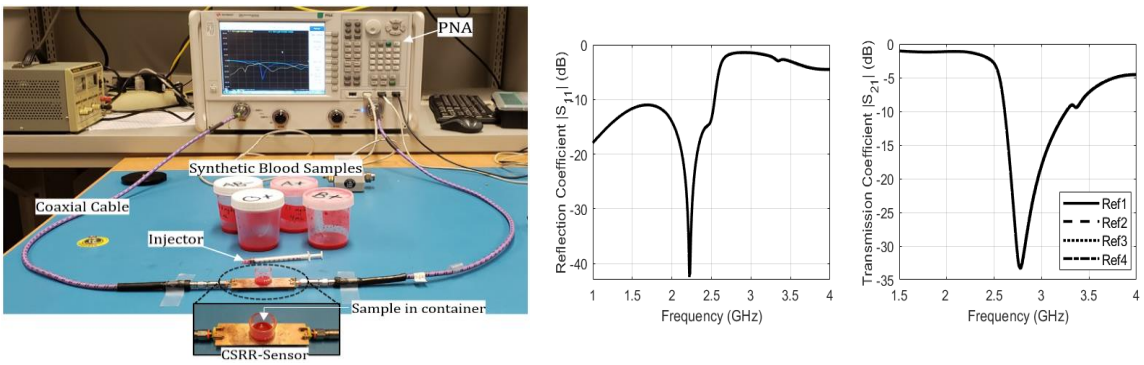

(a) (b) (c)

Figure 8.12: (a) PNA experimental setup for blood typing using the honey-cell CSRR. Referenced scattering responses of the sensor when loaded with empty container (b) reflection coefficient $|S_{11}|$, and (c) transmission coefficient $|S_{21}|$

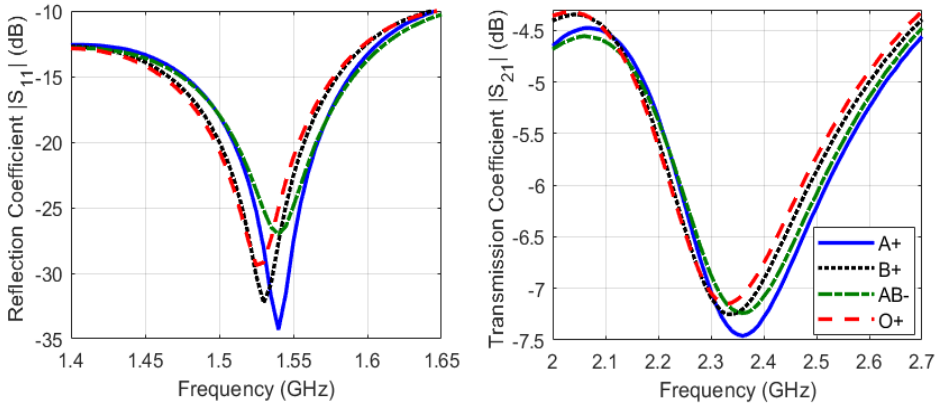

(a) (b)

Figure 8.13: Scattering responses of the sensor when loaded with blood samples of various types, (a) reflection coefficient $|S_{11}|$, (b) transmission coefficient $|S_{21}|$

Appendix III. Debugging Tests of the High-Band Radar Boards

A few technical tests were performed to verify the functionality of the fabricated 60 – 64 GHz TI radar boards. First, the original TI radar board was tested in the mm-wave setup shown in Fig. 8.1. The test has shown the full functionality of the connected system when configured and evaluated on the mmWave Studio as shown in Fig. 9.2.

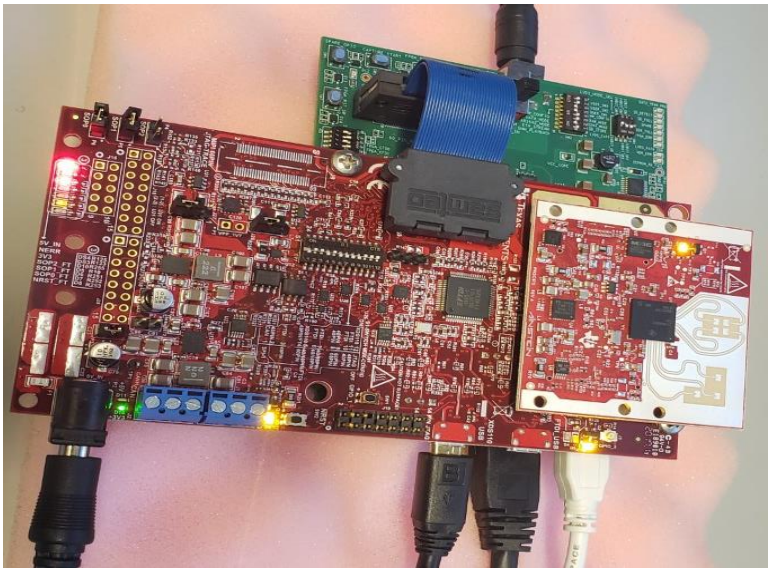

Figure 9.1: Original TI radar board integrated into the mm-wave system.

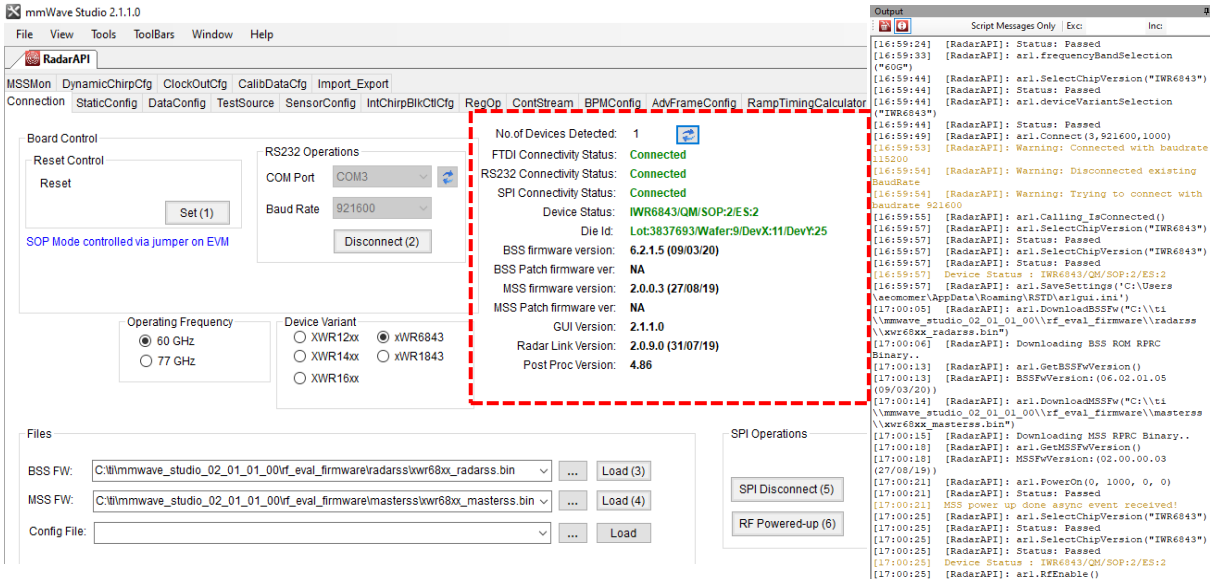

Figure 9.2: Full functionality of the original TI board as demonstrated by successfully passing all the connectivity configurations.

Next, the same debugging test was repeated on the mmWave Studio platform while connecting any of the five radar boards fabricated by AngusTech as depicted in Fig. 9.1. Remarkably, three boards namely B1, B2, and B3 were not able to achieve the full connectivity on the mmWave Studio as demonstrated in Fig. 9.3. Particularly, the BSS firmware was not accurately identified showing version 0.0.0.0 as indicted inside the red rectangle. Additionally, loading the MSS firmware into the board was stuck as shown by the freezing window.

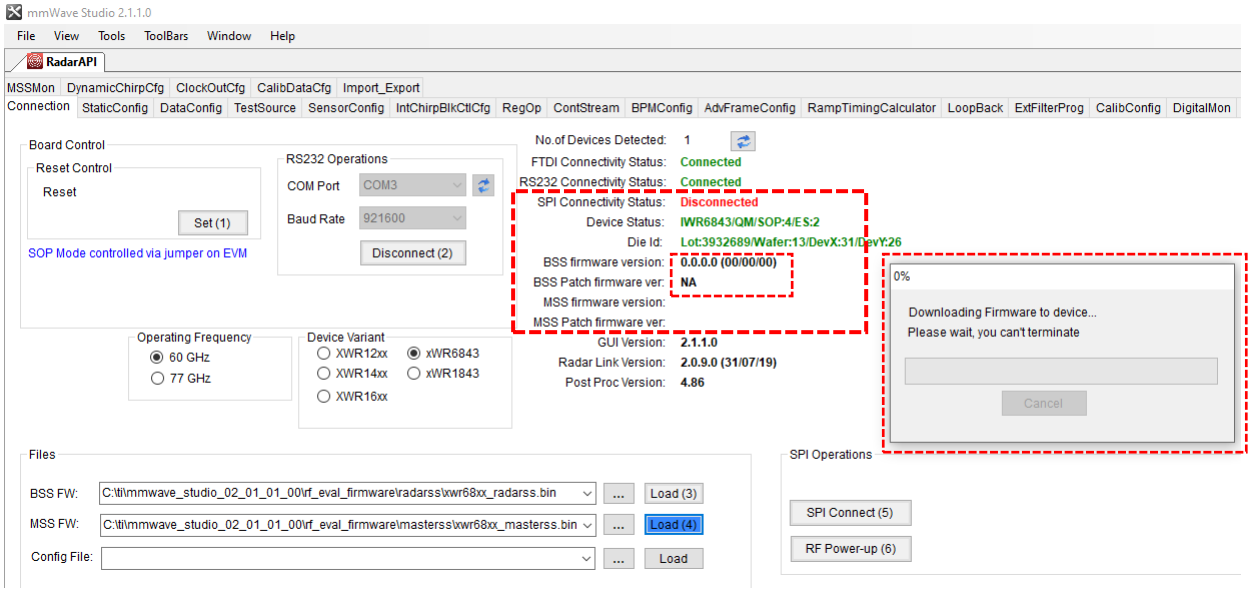

Figure 9.3: Defective functionality of three boards (B1, B2, and B3) that fail some connectivity configurations in the mmWave Studio.

The other two bards, namely, B4 and B5 were completely off and do not allow for RS232 connection as depicted in the following shot (Fig. 9.4) from mmWave Studio platform. User UART (COM3) was also not detected as shown.

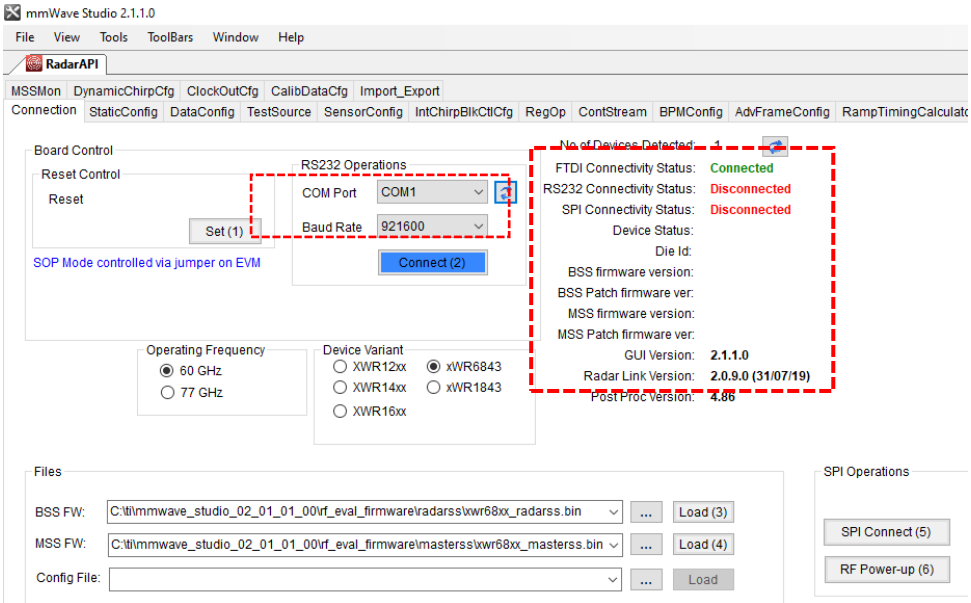

Figure 9.4: Defective functionality of the remaining two boards (B4 and B5) that fail all the connectivity configurations.

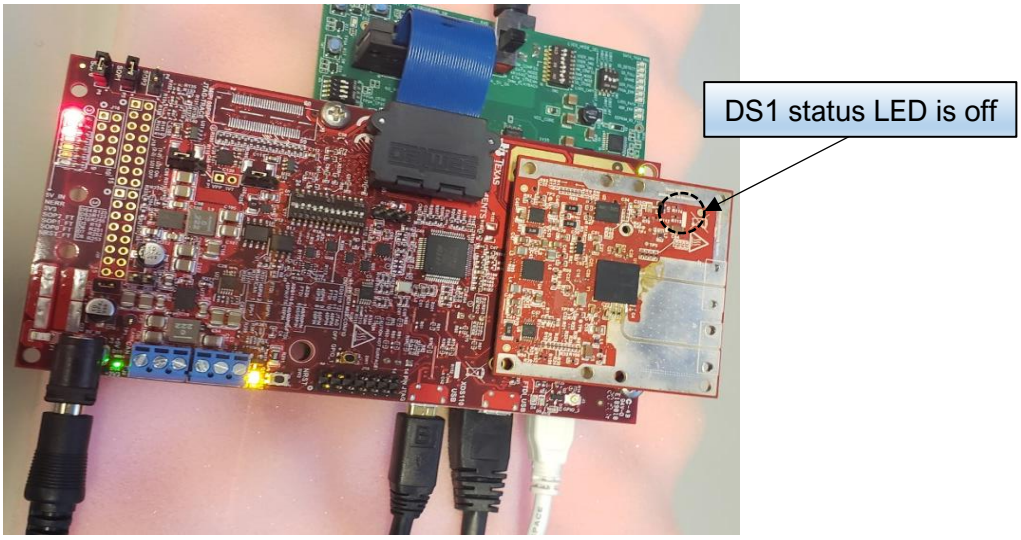

Figure 9.5: Fabricated boards (B4 and B5) integrated into the mm-wave system showing off state of connection when tested consecutively. DS1 LED is also shown off as highlighted.

Additionally, short tests were performed (using digital multi-meter) across some voltage paths for the designed supply decoupling capacitors. Particularly, the test measures the resistivity across many supply decoupling capacitors including those of RADAR 1V2, namely, C27, C28, C29, and C30 as shown in Fig. 9.6. The test was performed using a multi-meter device to indicate any shorts taking place across these paths as shown in Fig. 9.6. Short measurements were detected across the capacitor paths of board B4 and B5 as indicated by the resistivity values in yellow in Table 1.

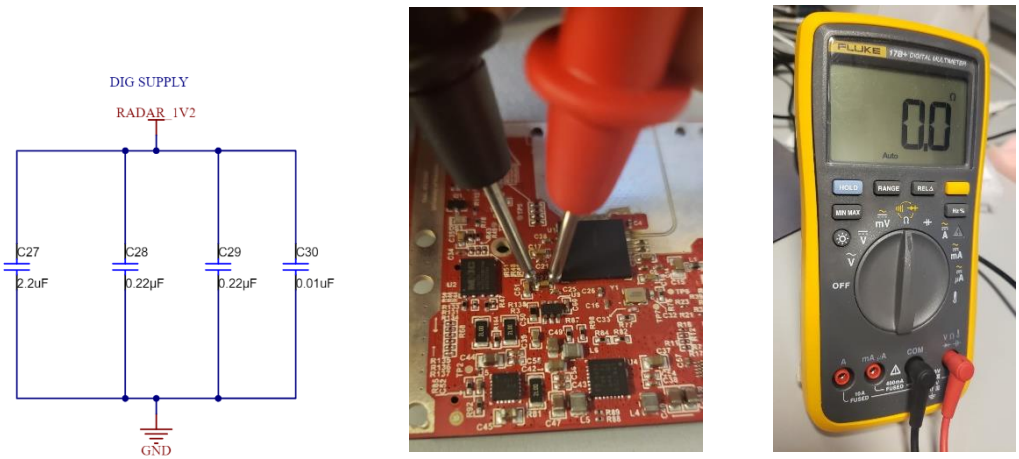

Figure 9.6: Short test across the supply decoupling capacitors in the five fabricated boards using a multi-meter device. Some short readings have been detected in the capacitors of board B4 and B5 as indicated by the zero measurements.

Table 9.1: Resistivity measurements across the supply decoupling capacitors in the five boards.

Board Number Measured path	Board 1	Board 2	Board 3	Board 4	Board 5
R_{C27}	287 Ohm	287 Ohm	373 Ohm	0.5 Ohm	0.0 Ohm
R_{C28}	284 Ohm	284 Ohm	365 Ohm	0.5 Ohm	0.6 Ohm
R_{C29}	340 Ohm	340 Ohm	354 Ohm	0.6 Ohm	1.4 Ohm
R_{C30}	280 Ohm	277 Ohm	286 Ohm	0.4 Ohm	0.6 Ohm

We suspect that the other three boards (B1, B2, and B3) also have some other manufacturing faults especially in the J1 and J2 60-Pin High Density (HD) connectors where tiny remnants of white pieces were found in dense amount inside and outside the pins of the connector. Another possibility of the manufacturing fault could be in the IWR6843 chip that was not initially installed in the first fabrication (IWR1843 was mistakenly printed instead). The outlook of the fabricated boards does not seem professional in many parts as one can see very clear in the area around the IWR6843 chip for example.